FERMILAB-TM-2491-AD-APC-CD-DI-FESS-PPD-TD

INTERNATIONAL LINEAR COLLIDER

A TECHNICAL PROGRESS REPORT

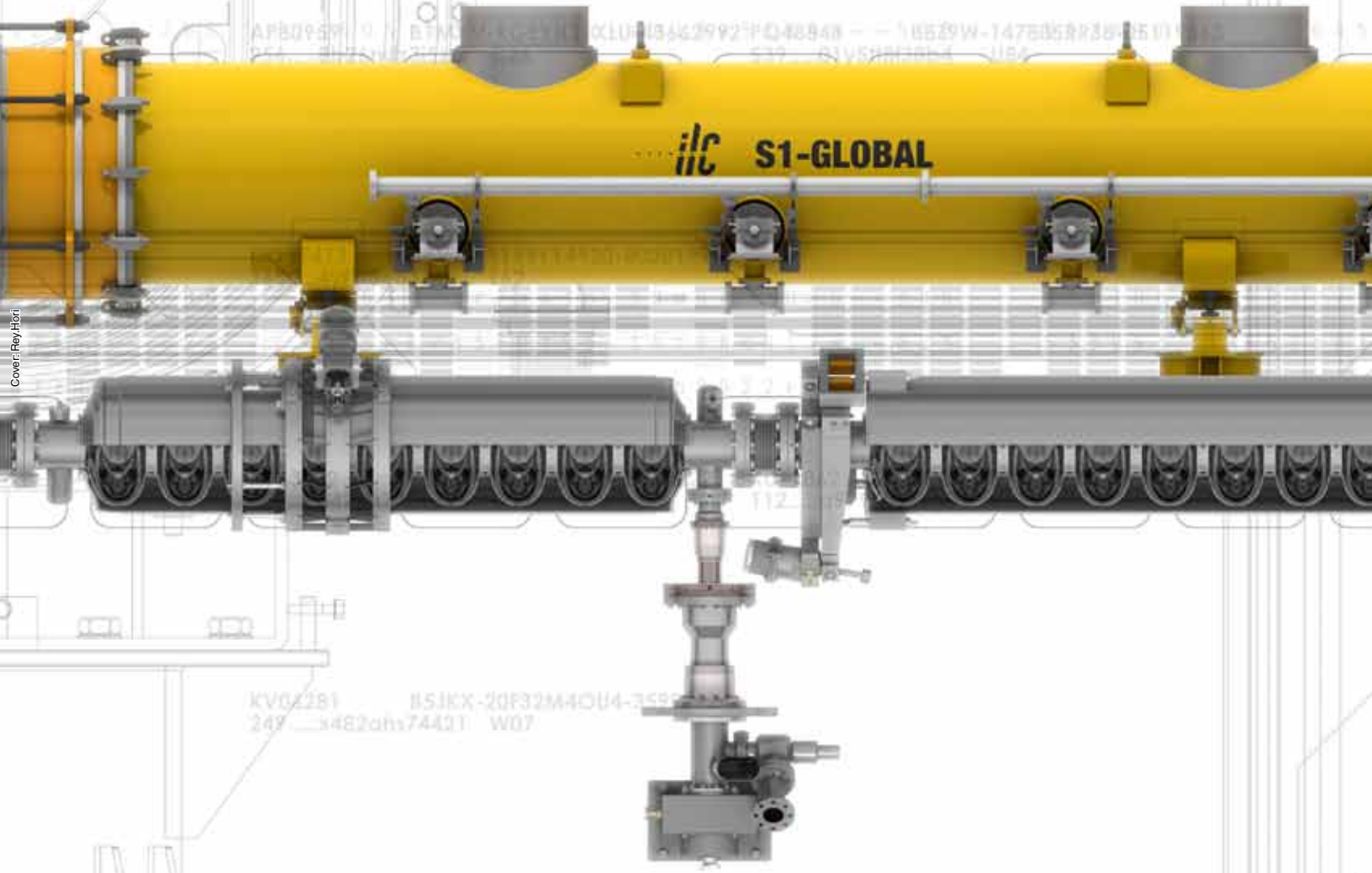

Cover: Rey Hori

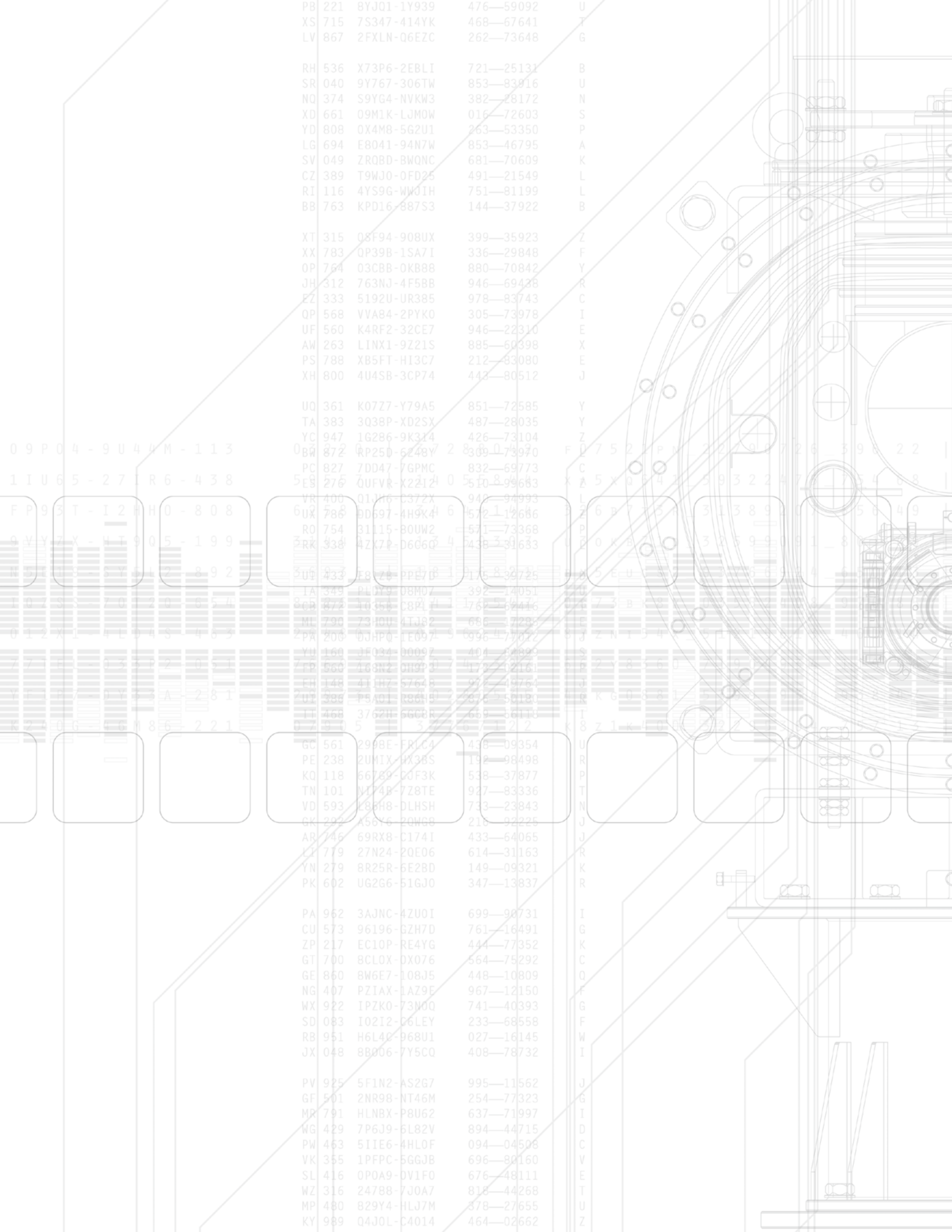

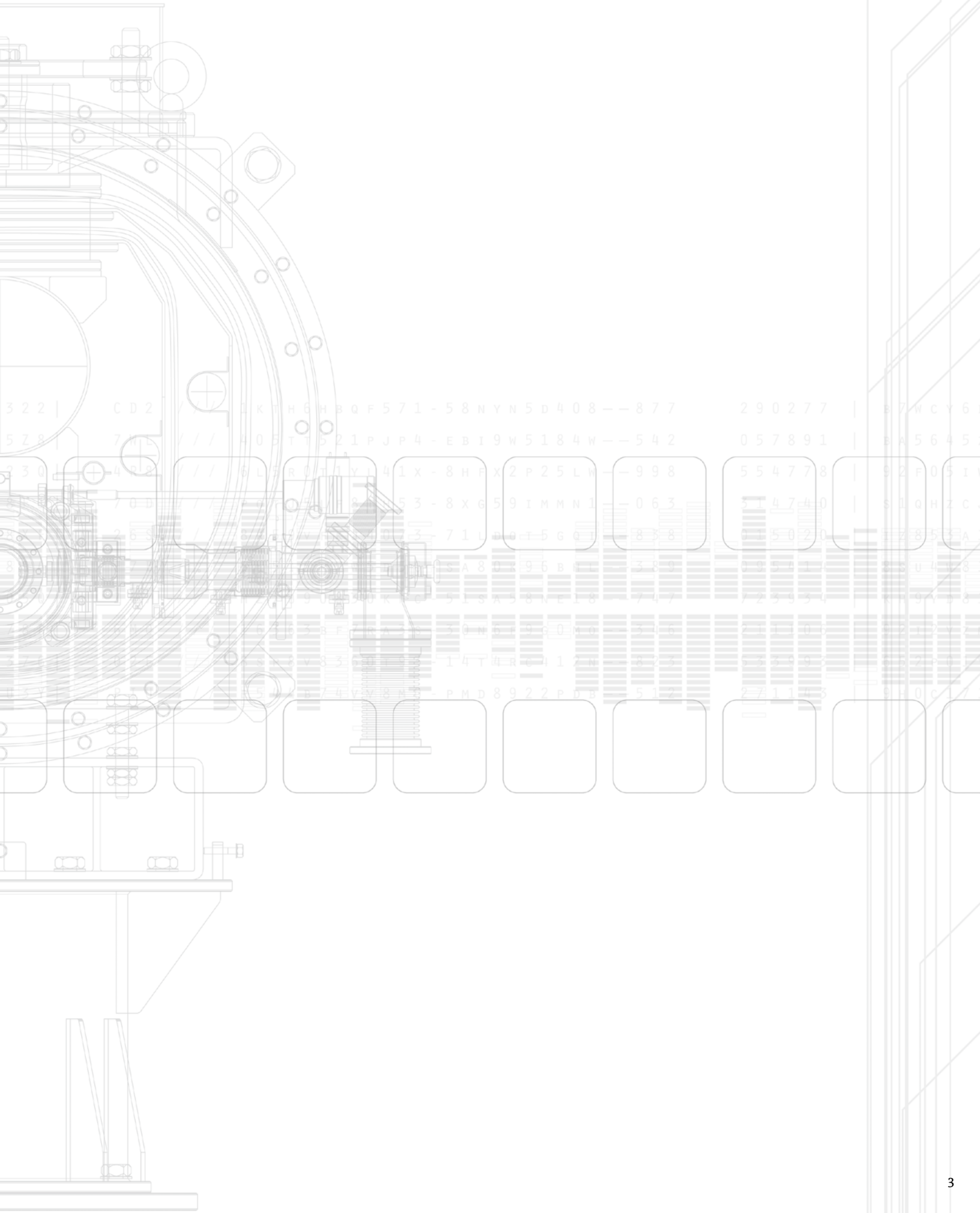

FOREWORD

The International Linear Collider: A Technical Progress Report marks the halfway point towards the Global Design Effort fulfilling its mandate to follow up the ILC *Reference Design Report* with a more optimised *Technical Design Report* (TDR) by the end of 2012. The TDR will be based on much of the work reported here and will contain all the elements needed to propose the ILC to collaborating governments, including a technical design and implementation plan that are realistic and have been better optimised for performance, cost and risk.

We are on track to develop detailed plans for the ILC, such that once results from the Large Hadron Collider (LHC) at CERN establish the main science goals and parameters of the next machine, we will be in good position to make a strong proposal for this new major global project in particle physics. The two overriding issues for the ILC R&D programme are to demonstrate that the technical requirements for the accelerator are achievable with practical technologies, and that the ambitious physics goals can be addressed by realistic ILC detectors.

This GDE interim report documents the impressive progress on the accelerator technologies that can make the ILC a reality. It highlights results of the technological demonstrations that are giving the community increased confidence that we will be ready to proceed with an ILC project following the TDR. The companion detector and physics report document likewise demonstrates how detector designs can meet the ambitious and detailed physics goals set out by the ILC Steering Committee. LHC results will likely affect the requirements for the machine design and the detectors, and we are monitoring that very closely, intending to adapt our design as those results become available.

There are too many people involved in important ways in the ILC programme to thank them individually. Nevertheless, I would like to express our ongoing appreciation of the support of funding agencies around the world, and of the major high-energy laboratories for their continuing support. I also want to note the importance of our oversight committees, the International Committee for Future Accelerators and the ILC Steering Committee for their steadfast advice and scientific oversight, and of the Funding Agencies for Large Collaborations, both for their support of our common fund, and their ILC R&D resource oversight.

Finally, as director of the GDE, I want to thank the dedicated group of accelerator scientists, engineers and technicians who continue to make such impressive progress in the face of the inevitable ups and downs of the overall project. This document is living proof!

Barry Barish, director, ILC Global Design Effort

EDITOR LIST

Eckhard Elsen
DESY, Germany

Mike Harrison
Brookhaven National Laboratory, USA

Leah Hesla
Fermilab, USA

Marc Ross
Fermilab, USA

Perrine Royole-Degieux
CNRS/IN2P3, France

Rika Takahashi
KEK, Japan

Nicholas Walker
DESY, Germany

Barbara Warmbein
DESY, Germany

Akira Yamamoto
KEK, Japan

Kaoru Yokoya
KEK, Japan

Min Zhang
IHEP, China

CONTENTS

01

INTRODUCTION & OVERVIEW

1.1 A global effort

In 2003, more than 2,700 scientists from around the world signed a published statement *Understanding Matter, Energy, Space and Time: the Case for the Linear Collider [1-1]*. The statement made clear the undisputed worldwide consensus that the next energy frontier machine after the Large Hadron Collider (LHC) should be an electron-positron linear collider with an initial centre-of-mass energy reach of 500 gigaelectronvolts (GeV), upgradable to 1 teraelectronvolt (TeV). In the same year, the International Committee for Future Accelerators (ICFA) commissioned the International Technology Review Panel (ITRP) to select from the then competing acceleration technologies a single technology that would be the basis for an international design effort towards a truly global project. The following year, 2004, the ITRP recommended to ICFA that the 1.3-gigahertz superconducting radiofrequency (SCRF) technology developed by the TESLA collaboration *[1-2]* should form the basis for the design of the International Linear Collider (ILC).

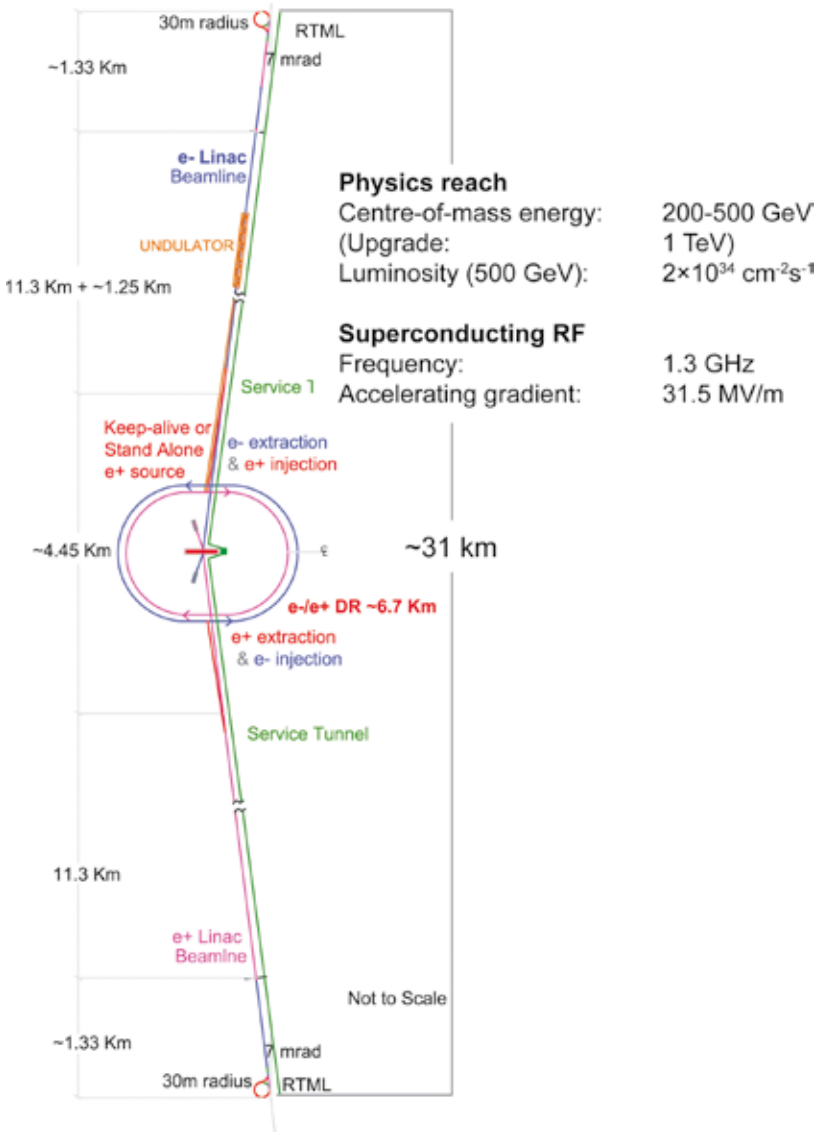

Figure 1.1. The layout of the ILC and its primary parameters as presented in the 2007 *Reference Design Report*.

Shortly after the ITRP decision, the International Linear Collider Steering Committee formally established the Global Design Effort (GDE) under the directorship of Barry Barish. Drawing on the resources of over 300 national laboratories, universities and institutes worldwide, the GDE produced the ILC *Reference Design Report* (RDR) *[1-3]* in August 2007. The report describes a conceptual design for the ILC reflecting an international consensus, together with an initial cost estimate of 6.70 billion ILCU[1] for capital equipment costs, and 14,200 person-years of institutional labour. The layout and principal parameters of the design as presented in the RDR is shown in *Figure 1.1.*

[1] 1 ILCU (ILC Unit) = 1 US 2007 $ (= 0.83 EUR = 117 Yen)

The first two years of the GDE leading up to the publication of the RDR were focused on ILC design activities and the cost estimate. The work done during the RDR phase identified many high-risk challenges that required R&D. The four highest-priority critical risk-mitigating R&D areas were prioritised as:

1. SCRF cavities capable of reproducibly achieving at least 35 megavolts/metre (MV/m).
2. A cryomodule consisting of eight or more cavities, operating at a gradient of 31.5 MV/m.
3. Linac 'string test' (or integration test) of more than one cryomodule linac with beam.
4. Development of models and mitigation techniques for electron cloud effects in the positron damping ring.

Other R&D areas (for example in the beam delivery system and the sources) were also identified, but were considered lower priority at the time of the RDR.

The first three priority R&D items all relate to the superconducting radiofrequency linear accelerator technology, the primary cost driver of the machine. Although it was noted by the International Technology Review Panel that TESLA SCRF technology was 'mature', the ILC gradient goal had only been achieved in a handful of cavities (one of which had accelerated beam at 35 MV/m in the TESLA Test Facility at DESY – a proof of principle). Furthermore, the R&D had been focused primarily in Europe centred at DESY, and a major goal for the GDE was to export this knowledge to the Americas and Asian regions. This had already begun during the RDR phase with the beginnings of development of the necessary SCRF infrastructure at Fermilab, Argonne National Laboratory and Jefferson Lab in the US, and KEK in Japan. Europe's own development has been driven by the design and construction of the European X-ray free-electron laser at DESY, which – although independent of the GDE – uses very similar technology and can be considered a large prototype for the ILC.

This report concentrates on the work subsequent to the RDR and the priority R&D identified therein. In 2007 the GDE began to restructure itself for an Engineering Design Phase, with the goal of producing an *Engineering Design Report* in 2010. Large funding cuts at the end of 2007 in the US and UK required the GDE management to rethink its strategy and timescale. With the loss of expected funding, it was clear that the originally planned engineering could not be done. Instead, it was decided to focus the remaining resources on the risk-mitigating R&D. The programme was also extended by two years to 2012 and renamed to the Technical Design Phase.

1.2 Beyond the *Reference Design Report*: primary goals for the Technical Design Phase

In 2008 the newly structured Global Design Effort technical project management published a five-year R&D Plan that outlined the scope, milestones and goals of the Technical Design Phase. The R&D Plan was intended to undergo regular revision and is now in its fifth version *[1-4]*. The plan clearly states the primary goals for the Technical Design Phase:

- results from critical R&D programmes and test facilities that either demonstrate or support the choice of key parameters in the machine design;
- one or more models for a Project Implementation Plan, including scenarios for globally distributed mass-production of high-technology components as in-kind contributions;
- an updated and robust VALUE estimate and construction schedule consistent with the scope of the machine and the proposed Project Implementation Plan;
- an updated technical description of the ILC technical design in sufficient detail to justify the associated VALUE estimate.

The Technical Design Phase will culminate in the publication of a *Technical Design Report* (TDR) at the end of 2012. The TDR and its supporting documentation is intended to show a robust design and form a sound basis for a 'proposal to host' the project. The TDR is expected to build on the solid base of the RDR, but emphasise the Technical Design Phase activities towards the goals stated above:

- **Results of critical R&D.** Unlike the RDR, which was primarily a design document, the TDR will focus on presenting the worldwide results of the technical R&D during the five-year Technical Design Phase along with an updated design and cost.
- **Project Implementation Plan.** The plan has no counterpart in the RDR. It will deal with issues pertaining to the international project itself, such as governance, project structure, finance models and in-kind contributions. Of critical importance is the development of globally distributed mass-production models, particularly for the SCRF technology. These models will go beyond the simplistic ones assumed for the RDR, and will not only relate to how the machine will get constructed, but will also factor significantly into the cost estimate.
- **Updated VALUE estimate.** During the RDR phase a bottom-up cost estimate for all technical systems and components was made. This estimate was subsequently successfully defended to an international review. For the TDR, a complete reworking of the estimate is not expected. However it is considered mandatory to review and update the costs associated with the primary cost drivers: SCRF technology and conventional facilities, including civil construction. In particular for the SCRF, the new estimates will reflect the five years of R&D in all three regions and must be consistent with the industrialisation models for globally distributed mass-production being developed. It is a stated goal of the Global Design Effort to make every attempt to produce a cost estimate in 2012 that does not significantly exceed the RDR estimate of 6.7 billion ILCU.
- **Updated design.** Again building on the solid base of the published 2007 *Reference Design Report,* an updated design will be presented in the TDR. This design will reflect not only the results of the risk-mitigating R&D, but also many cost-driven design modifications resulting in a more cost-effective solution. An additional important aspect will be the

further development of site-specific designs, taking into account the various differing constraints that individual sites may present. This is an important step forward from the RDR, which considered three conceptual generic sample sites from the standpoint of a single machine design. The resulting options will give potential hosts the flexibility in design needed to fulfil their specific site constraints.

The TDR will not be a complete engineered design and there will still be considerable engineering and design work to be done prior to start of construction. Identifying the scope of this remaining work – and the technical risk associated with it – is also an important task for the Technical Design Phase. However, the TDR will represent major technical progress over the RDR, and present a significantly mature design, including significant progress on industrialisation for the SCRF technology and site-specific development.

1.3 The halfway point

This document, coming close to the mid-term of the TD Phase (or the end of 'Technical Design Phase 1'), is a major deliverable for the Global Design Effort. It represents a snapshot of the R&D status: a large fraction of the R&D projects continue through to the publication of the TDR in 2012, and in some cases beyond.

Highlights from the Phase 1 R&D include:

- successful construction and commissioning, and/or further development of existing SCRF infrastructure at Fermilab, Argonne National Laboratory, Jefferson Lab and Cornell University in the US, KEK in Japan, and most recently the Institute of High Energy Physics, Chinese Academy of Sciences;
- identification of the preferred process for consistent production of 35-MV/m cavities (worldwide) and a successful demonstration of the Phase 1 goal of a 'production-like' yield of 50% (towards the final R&D goal of 90% for the TDR);
- as part of the above, and important for global mass-production, 'qualification' of new cavity vendors in the Americas and Asia to complement those already existing in Europe;
- construction and testing of more high-performance cryomodules (in particular at DESY as part of the preparation of the European X-ray Free-Electron Laser; this includes high-current beam tests at DESY's FLASH facility);
- international collaboration on the construction of a high-performance cryomodule at KEK, enabling plug-compatible design philosophies to be explored, as well as technology comparisons;
- start of developments towards SCRF mass-production models, including R&D for cost-effective industrialisation with an industrial R&D pilot plant at KEK;
- reconfiguration of the Cornell Electron Storage Ring (CESR) at Cornell University in support of the CesrTA electron cloud programme, phase 1 of which was successfully concluded at the end of 2010 with a recommendation on electron cloud mitigation technologies for the ILC positron damping ring;

- development of fast kicker technology for the damping rings, in particular tests in the Accelerator Test Facility (ATF) at KEK.
- Installation and commissioning of all subsystems and instrumentation of the final focus test beam at ATF2 at KEK;
- significant progress on the development of the machine-detector interface in support of the detector push-pull concept;
- progress on source R&D, in particular on development of prototype polarised electron gun; demonstration of a prototype undulator section for the positron source; initialisation of engineering design and key R&D on the positron target concepts and capture devices (ongoing).

In addition to the R&D outlined above, the overall design of the ILC has been critically reviewed with respect to the identified cost drivers, and in particular conventional facilities and siting. As part of the stated need to constrain the costs, a primary goal was to reduce the underground volume required by the machine (the underground civil construction also represents one of the highest risks in terms of cost and schedule). After approximately 18 months of study, several design modifications to the 2007 published reference design were proposed, including:

- a single-tunnel solution for the main linear accelerators (linacs), which includes two novel concepts for radiofrequency power generation and distribution in support of that solution;
- a reduction in the number of bunches per pulse from 2625 to 1312, facilitating cost savings via a reduction in the installed radiofrequency power and smaller damping rings, luminosity being in principle recovered by stronger focusing at the interaction point;
- moving the undulator-based positron production from the mid-point of the main electron linac (operating at a nominal 150 GeV) to the end, facilitating better integration into a consolidated 'central region' of the entire machine, which contains almost all the required systems other than the main linacs.

1.4 Design process

The above issues all have a direct impact on conventional facilities and siting. An accelerator design and integration team has been charged with developing a design based on these proposals. The goal is to achieve a consensus on the modified baseline early in 2011, which will then be used in Technical Design Phase 2 for further detailed design work and cost estimation. In order to facilitate a consensus-building mechanism, a Top-Level Change Control process was developed that focused on two workshops *(Table 1.1)*. These workshops – open to all stakeholders and especially to the physics and detector community – have been used to carefully review the design modifications and finally submit a consensus proposal to the director. With the modified baseline agreed upon, the emphasis of the work for Technical Design Phase 2 will shift to consolidating that design and the ongoing R&D towards producing the TDR in 2012.

Table 1.1 Baseline Assessment Workshops (BAW) used for defining the modified ILC baseline for the *Technical Design Report* as part of the Top-Level Change Control process.

BAW-I	September 2010, KEK *[1-5]*	1. Review of average accelerating gradient and allowed gradient spread 2. Single-tunnel option for main linacs and associated novel RF power schemes
BAW-II	January 2011, SLAC *[1-6]*	1. Relocation of the undulator-base positron production to the end of the main electron linac. 2. Reduction in bunch number and associated modifications to the damping rings, main linac RF and beam delivery system.

1.5 Structure of the Report

The remaining chapters of this report are intended to describe fully the Phase 1 achievements outlined above. Chapter 2 deals with the superconducting radiofrequency; chapter 3 deals with accelerator systems R&D (i.e., non-SCRF R&D); chapter 4 discusses the important work associated with the conventional facilities and siting (the second primary cost driver), and in particular the site-specific issues; chapter 5 discusses briefly the accelerator design and integration work and the updated baseline and parameters; and finally chapter 6 looks towards the remaining work and the publication of the TDR.

References

[1-1] http://physics.uoregon.edu/~lc/wwstudy/lc_consensus.html

[1-2] TESLA TDR: http://lcdev.kek.jp/TESLA-TDR/

[1-3] RDR: http://www.linearcollider.org/about/Publications/Reference-Design-Report

[1-4] TDP R&D Plan: http://ilc-edmsdirect.desy.de/ilc-edmsdirect/file.jsp?edmsid=*813385

[1-5] BAW-I indico site: http://ilcagenda.linearcollider.org/internalPage.py?pageId=5&confId=4593

[1-6] BAW-II indico site: http://ilcagenda.linearcollider.org/conferenceDisplay.py?confId=4612

02

SUPERCONDUCTING RADIOFREQUENCY TECHNOLOGY

2.1 Putting superconducting radiofrequency technology to the test for the ILC

2.1.1 SCRF development in the Technical Design Phase

R&D for superconducting radiofrequency (SCRF) technology is a very high-priority and global technical activity for the ILC in the Technical Design Phase (TDP) *[2-1, 2, 3]*. This activity builds on and extends the pioneering work done in the decade or so leading up to the International Technology Review Panel's choice of SCRF technology in 2004 *[2-4]*. In that decade, R&D on 1.3-gigahertz (GHz) technology done by the TESLA Technology Collaboration succeeded in reducing the cost per megaelectronvolt (MeV) by a large factor over the early 1990s state-of-the-art SCRF. The original goal was to reduce costs by increasing the operating accelerating gradient by a factor of five from 5 megavolts per metre (MV/m) to 25 MV/m, and reducing the cost per metre of the complete accelerating module by a factor of four for large-scale production *[2-1-5]*.

The pace of progress has continued during the TDP, with the state-of-the-art cavity performance now exceeding 40 MV/m in the vertical low-power test, approaching the physical critical field limit for niobium.

During the first half of the TDP, under the prioritised R&D guidance set by the Global Design Effort (GDE), the baseline cavity processing recipe was improved and optimised in most labs participating in the so-called S0 study programme (see section 2.3) to develop high-gradient superconducting cavities. Jefferson Laboratory (JLab) in the US reports that they have achieved repeatable cavity processing for cavities that can reach a gradient of more than 35 MV/m consistently. Argonne National Laboratory (ANL), Fermilab and KEK have started to demonstrate high-quality processing and cavity results. It is anticipated that a reliable process will be demonstrated in labs worldwide by the end of the TDP. This effort, along with the transfer of the processing technology to industry in all three regions, will put ILC cavity processing on a strong footing by the end of the TDP.

In the last three years, some 60 cavities were built for the purpose of demonstrating the ILC gradient. Of these, more than half were subjected to the defined standard process, while the others were used for developing the process or qualifying the equipment in use. The fraction of cavities manufactured using the standard process that meet or exceed the performance criteria can be used to estimate construction project performance (generally referred to as production yield).

Advancement in SCRF cavity performance has followed two tracks: the control of field emission typically caused by mechanical defects or contaminant particles and the reduction of localised heating caused by non-uniformities located near the cavity equator welds.

Major progress in both tracks was made before 2007, including the use of high-purity niobium material, the introduction of high-pressure water rinsing, and the development of electropolishing. Quality control and quality assurance in the production of the niobium starting sheet and in the fabrication of complete cavities, such as sheet scanning, have been introduced by DESY as well as by some other labs.

In view of this progress, a forward-looking gradient goal of 35 MV/m or higher in the low-power vertical test with 90% production yield was adopted for the reference design. This remains the primary goal to be demonstrated during the TDP.

Field emission is a major cause of variability in cavity performance. After the GDE's SCRF team had formed in 2007, it took the first step to suppress field emission following advice from the TESLA Technology Collaboration to introduce rinses intended to clear away the debris left behind by the electropolishing process *[2-6, 7]*. This has proved quite effective and the incidence of strong field emission has been greatly reduced after ethanol and degreaser chemical rinses were introduced.

The development of surface diagnostic techniques capable of quantitative evaluation of surface defects has proceeded in parallel. The most important of these is the development of the high-resolution 'Kyoto-KEK' camera. The camera can be precisely positioned inside the cavity and provides images of the electropolished mirror-like niobium surfaces that can be accurately referenced to external features.

A long-term goal of the cavity optical inspection development is to enable cavity performance predictions based on observed features prior to cavity RF testing at cryogenic temperatures. To meet this goal, a definitive correlation between camera image characteristics and external temperature-mapping measurements made during low-power tests as well as cavity quench behaviours need to be established. This work has just begun and already shows promising results; as a result of this R&D, we are now able to conclude that all observed hot spots that cause severe gradient limits (i.e., a gradient below 20 MV/m) have a corresponding internal surface defect. However, the converse does not appear to be true, that is, not all observed surface blemishes limit cavity performance. It is possible that more subtle details in the observed features control the quench behaviour. Optical inspection at higher resolution and in three dimensions is being explored at various labs to settle the issue. Further work on this topic will continue throughout TD Phase 2 and beyond; in particular, the mass production of the European-XFEL cavities will provide a large and valuable optical inspection dataset.

2.1.2 Main linac SCRF operational performance

Nowhere is the increased pace of progress more evident than in the expansion of global test infrastructures and in the fostering of cavity fabrication companies in each region. Halfway through the four-year Technical Design Phase, four institutional cavity process and test facilities (one in Europe, two in the Americas and one in Asia), are actively providing ILC cavities fabricated by four companies (two in Europe, one in the Americas and one in Asia). We expect to roughly double the number of qualified cavity fabrication vendors in the remaining half of the Technical Design Phase. Fully functional high-technology cavity production capability in each region is mandatory for providing the ILC project with a strong global technology basis.

In addition to fabrication and processing sites, the last few years have also seen the development of cryomodule assembly and SCRF linac beam test facility infrastructures in each region. These infrastructures make up the link between individual cavity testing and full linac performance. Following qualification in the low-power vertical test, cavities are connected in a string to allow the passage of the beam and are provided with coaxial power couplers. The string is placed in the 12-m-long cryomodules, which are in turn joined together in the accelerator enclosure tunnel. To characterise the performance of the finished linac complex we test the assembled cryomodules and groups of cryomodules with beam in test linac facilities. The GDE has established qualification performance criteria for each step of the cryomodule production through to a final linac system performance specification (average beam accelerating gradient). The criteria are summarised in *Table 2.1 [2-8]*.

Cost-relevant design parameter(s) for TDR	**ILC main linac cavity operational specification**	**R&D goal for cavity gradient in vertical test**
Gradient in vertical test, including the 2nd pass[1]	35 MV/m at $Q_0 \geq 8x10^9$, average with spread ≤ ±20%	35 MV/m at 90% yield, equivalent to ≥ 38 MV/m, average
Cavity-string gradient in cryomodule test	34 MV/m, average	
Main linac operational gradient	31.5 MV/m at $Q_0 \geq 1x10^{10}$ average, with spread ≤ ±20%	

Table 2.1 Cavity performance specification and R&D goals.

[1] Second-pass refers to a second surface process treatment of lower-performing cavities.

In the table, both the ILC main linac operational specification and the R&D goal are described in terms of an average cavity gradient to be achieved with an allowance for peak-to-peak gradient spread. Cavity performance is listed for two test stages: a vertical low-power test of individual cavities and a high-(pulsed-) power cryomodule test, after a cavity has been connected to a cavity string and inserted into a cryostat. The main linac operational gradient refers to the gradient at which the cavity can operate indefinitely following installation in the main linac. The table lists an R&D goal of not more than 3% deterioration of cavity gradient from vertical test to cryomodule test, assuming the 35 MV/m with the 90% yield to 34 MV/m on average, respectively. It also lists an R&D goal operational limit of not more than 1.5 MV/m below the limit seen in the cryomodule test and an operational controls margin gradient of not more than 3%.
The construction of ILC SCRF linac beam test facilities in each of the three regions is the largest investment in new SCRF infrastructure. These projects (section 2.6) will be complete or will be nearing completion by the end of the Technical Design Phase. These cornerstone facilities, listed in *Table 2.2*, complete the SCRF high-technology capability that provides the global basis for the ILC. In each case, the facility serves to advance regional projects, which are only indirectly related to ILC. This adds resources and strength and diversifies the development effort. Five cryomodules based on the ILC technology, along with 80 very similar cryomodules for the European XFEL, will be constructed during the period leading up to 2014. This includes the 'S1-Global' cryomodule recently built and tested at KEK with cavities contributed by institutions in each region (section 2.4).

Table 2.2 Regional ILC SCRF technology development and testing centres.

Region	Cavity development: fabrication, process and test	Cryomodule assembly/test	Linac beam test centres (beam on date)
Americas	Three industrial partners, and Fermilab/ANL, JLab and Cornell	Fermilab/SLAC	ILCTA–NML (2012)
Asia	Three industrial partners, and PKU, IHEP and KEK	KEK	Quantum-Beam/STF-2 (2011/2013)
Europe	Two industrial partners, and DESY and CEA-Irfu	CEA-Irfu/CNRS-LAL/DESY for FLASH and E-XFEL	FLASH (from 2005)

Table 2.2 summarises the number of cavity fabrication companies that are either qualified or expected to be qualified during the TDP, the institutional process and low-power testing centres that have throughput capability of dozens of cavities per year and the cryomodule assembly and high-power testing centres and linac beam test facilities, with expected initial operation date.

2.1.3 Challenges for SCRF technology

Underpinning the overall strategy of the SCRF R&D plan is the desire to produce the best possible cost-optimised solution for the main linac using state-of-the-art technology. Good progress has been made in TDP-1 towards these goals, and they remain fundamentally unchanged in TDP-2, which also sees a shift in emphasis towards the development of industrial mass-production models, (section 2.6). The milestones for the TD Phase SCRF goals outlined are summarised in *Table 2.3 [2-1]*.

Table 2.3 Milestones for the SCRF R&D programme.

Stage	Subjects	Milestones to be achieved	Year
S0	Nine-cell cavity	35 MV/m, maximum, at $Q_0 \geq 8\times10^9$, with a production yield of 50% in TD Phase 1, and 90% in TD Phase 2	2010/ 2012
S1	Cavity-string	31.5 MV/m, average, at $Q_0 \geq 10^{10}$, in one cryomodule, including a global effort, and 34 MV/m, average, in TD Phase 2	2010/ 2012
S2	Cryomodule-string	31.5 MV/m, average, with full beam loading and acceleration	2012

The interim TDP-1 R&D milestone of cavity production yield of more than 50% at 35 MV/m (including cavities which have undergone a second surface treatment and test process) has been achieved (section 2.3). We consider strategies for gradient improvement, categorising and prioritising tasks leading to the *Technical Design Report*. These are:

Short-term R&D goals:

- manufacturing process including quality control.
- preparation with surface treatment including a time- and cost-effective process.
- further studies towards the understanding and (further) reduction of field emission.

Long-term R&D goals:

- cost-effective mass production technology such as seamless hydro-forming, large-grain niobium with chemical polishing.
- further fundamental R&D to reach much higher gradient to be adaptable for a future upgrade towards 1 TeV, such as alternative cavity shapes.

For the latter, we expect to capitalise on the tremendous progress and investment of the last few years. In the coming months, we will outline the cost saving and performance-enhancing strategies to be implemented using the new infrastructure.

2.2 Development of worldwide infrastructure

2.2.1 Development of infrastructure at KEK, in Asia

The Asia region's effort for SCRF activity and infrastructure is centred at the Superconducting RF Test Facility (STF) at KEK *[2-9]*. It includes facilities for cavity surface process, cavity and cavity string assembly in cleanrooms, cryomodule assembly, cavity performance tests in the vertical position and cryomodule tests in the horizontal position in an undergrounded tunnel. The general layout is shown in *Figure 2.1*. Further efforts for new SCRF infrastructures have also progressed in laboratories in China and India.

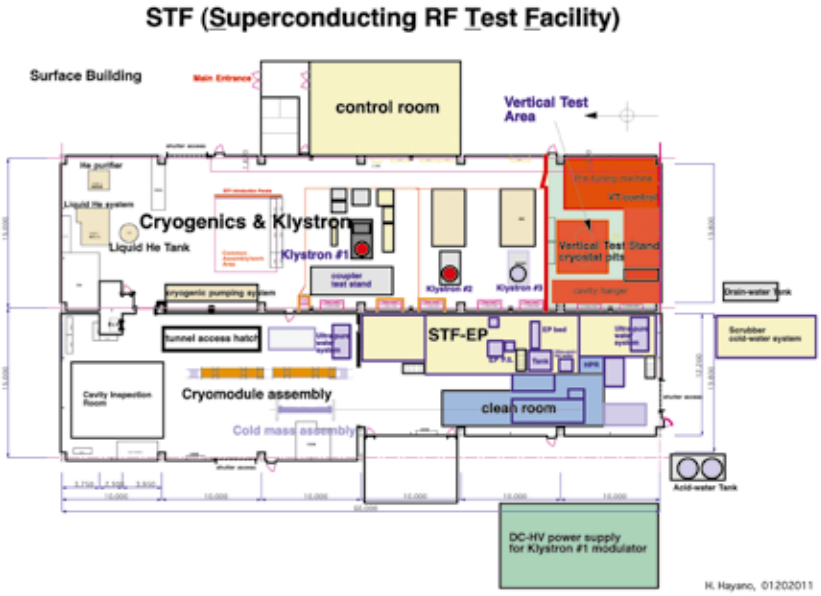

Figure 2.1 General layout of the Superconducting RF Test Facility at KEK.

For the cavity process and treatment at STF, a new electropolishing (EP) facility was constructed and became operational in 2008 *[2-10]*. The system includes the EP system, buffered chemical polishing utilities for small parts and flange surface etching, ultrasonic rinsing, a high-pressure rinsing system and a cleanroom for cavity assembly. Optimisation of the EP and high-pressure rinsing system has been a major continuing subject following initial commissioning. Various diagnostics are provided to monitor and record every EP treatment, the EP process itself and subsequent water rinsing in order to control the temperature to stay below 35 °C. A specific study examined the optimisation of the EP current density by setting a reasonably low current density (30 to 35 milliamperes (mA) per square centimetre (cm^2)) to suppress sulphur generation. The ultrasonic rinse solution was tested to ensure removal of precipitated sulphur particles from the cavity surface. As a result of the rinsing investigation, a 2% solution of commercially available FM-20 detergent has become a regular part of the process. Effluent water from the high-pressure rinse is routinely monitored by using a particle counter and a total organic component device for monitoring contamination. *Figure 2.2* shows the EP facility established at KEK during TD Phase 1.

Figure 2.2 The EP facility established at KEK-STF.

The vertical test stand for low-power cavity field testing was also commissioned in 2008. For the vertical test, the first 4-m-deep cryostat was installed in STF, assembled together with radiation shielding and helium pumping system. The test stand is now routinely operated once per week. It uses a 2,000-litre liquid helium supply with dewars for the cooling and cold test. *Figure 2.3* shows the vertical test facility at KEK-STF.

A monitoring system for full temperature and X-ray mapping is used for every vertical cavity test *[2-11]*. A total of 352 carbon-resistor temperature sensors and 142 PIN diode X-ray sensors are attached around each cell and end group higher order mode (HOM) coupler. Observed temperature rise and X-ray intensity data are summarised by a 'map plot' in real time in order to easily identify heat spots and to facilitate the connection with the surface inspection that follows each test.

Figure 2.3 The vertical test stand established at KEK-STF.

The development and subsequent upgrade of a cavity surface inspection camera system was done in collaboration with KEK and Kyoto University *[2-12]*. A newly developed high-performance complementary metal–oxide semiconductor (CMOS) camera combined with an LED illumination system resulted in a highly improved resolution, a ten-times increase in brightness and much longer-life illumination. Automated image capturing and defect-finding software was developed and is to be further optimised. *Figure 2.4* shows the cavity surface inspection camera system, together with an example of a high-resolution image of the electron-beam weld.

Figure 2.4 Left: Kyoto-KEK optical inspection camera system. Right: an example of automated image capture software.

In case a cavity has clearly visible defects inside and its performance is limited by these defects, a surface repair tool is useful. A miniature grinding mechanism with very small charge-coupled device (CCD) observation camera that fits within the 78-mm diameter of the cavity has been developed as shown in *Figure 2.4 [2-13]*. Recently, this device, combined with a technique to get precise internal defect information using a replica-mould technique, has been successfully used to repair a cavity at STF. One good example is the nine-cell cavity MHI-08. A pit-type defect (0.7 mm by 0.5 mm in size and about 115 micrometres (μm) in depth) was found using the inspection camera at precisely the 16 MV/m quench location indicated by the thermal monitor system. After grinding by using a local grinding machine developed at KEK *(Figure 2.5)* and ensuing 50-μm surface removal by EP, the cavity gradient performance was improved to 27 MV/m with no observation of heating at that location. After two additional EP cycles, a gradient of 38 MV/m was achieved in the fourth vertical test.

The installation of an automated cavity tuning machine is now operational at STF. It was originally developed at DESY and two additional sets have been fabricated in cooperation with DESY and Fermilab, as described later. The machine has the capability of field flatness tuning and cell-to-cell alignment correction through linked operation between the automated software, bead-pull, six-jaw cell deforming, and cavity eccentric measurement system.

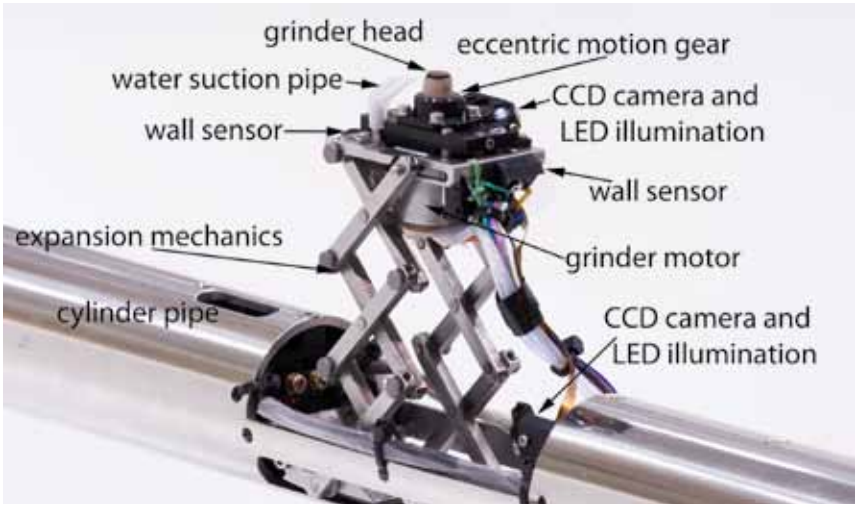

Figure 2.5 Local grinding tool with an expandable motor stage installed in a 50-mm-diameter cylindrical housing.

The development of a cavity fabrication facility (a pilot plant) is in progress at KEK to study cost-effective fabrication technology. To prepare for industrialisation, various R&D efforts are required, along with the initiative of researchers of the laboratories and in close cooperation with industry. The facility at KEK includes an electron beam welder, a trimming machine, a press machine and a chemical pre-process facility. *Figure 2.6* shows the general layout. The press machine and the trimming machine were already installed and commissioned in 2010. The electron beam welder is to be delivered to KEK in early 2011. The cavity fabrication study for forming cells and end group components was started. In order to simplify the machining steps, the use of a pressing technology for various fabrication processes is now under investigation. The close cooperation with industrial partners is much encouraged in these R&D efforts. The cavities to be fabricated by using the facility are expected to be installed into cryomodules and tested at STF between 2013 and 2014.

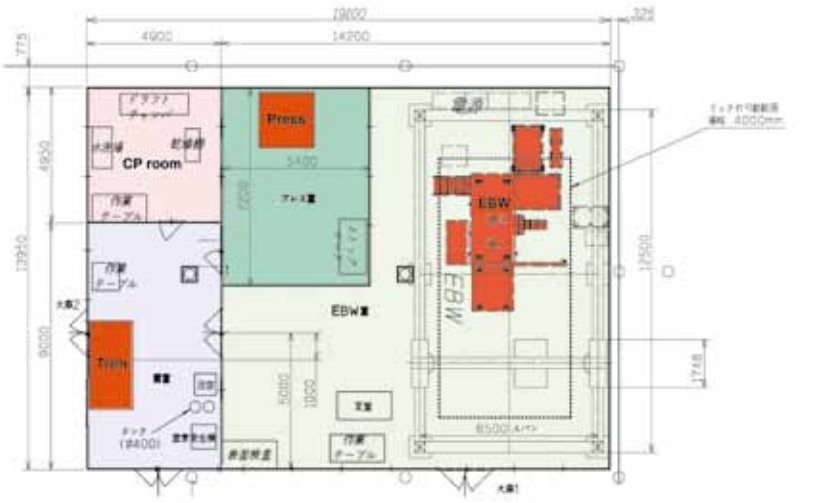

Figure 2.6 General layout of the cavity fabrication facility in progress at KEK.

2.2.2 Development of infrastructure in the Americas

Infrastructure development in the Americas has included a focus on new industrial capabilities to add to existing ones and the development of new diagnostic and test facilities at laboratories *[2-13, 14, 15, 16, 17, 18, 19, 20, 21]*. Nearly 100 nine-cell cavities sourced from industry in both Europe and the United States have been procured through the Americas regional team for the purposes of improving both infrastructure at the laboratories and capabilities in industry. The typical process for developing a vendor includes production and test of several single-cell prototypes and, after successful testing of these, progression to production of full nine-cell cavities. At the time of the RDR there was one vendor in the United States qualified to build nine-cell cavities; as of this writing not only has that vendor tuned up their production process to successfully make multiple nine-cell cavities, but a second vendor has recently had its first nine-cell cavity tested. It reached a gradient of 29 MV/m with no field emission. In addition, single cell cavities have been tested from a third Americas region vendor, and we have processed and tested single cell cavities fabricated in India as well.

In parallel with the cavity effort, processing facilities were developed at ANL and Fermilab, based strongly on the existing capabilities at JLab to develop the throughput capacity for both the cavities required for cryomodules and those being used for R&D. *Figure 2.7* shows the general layout of the ANL/Fermilab surface processing facility located at ANL *[2-22]*.

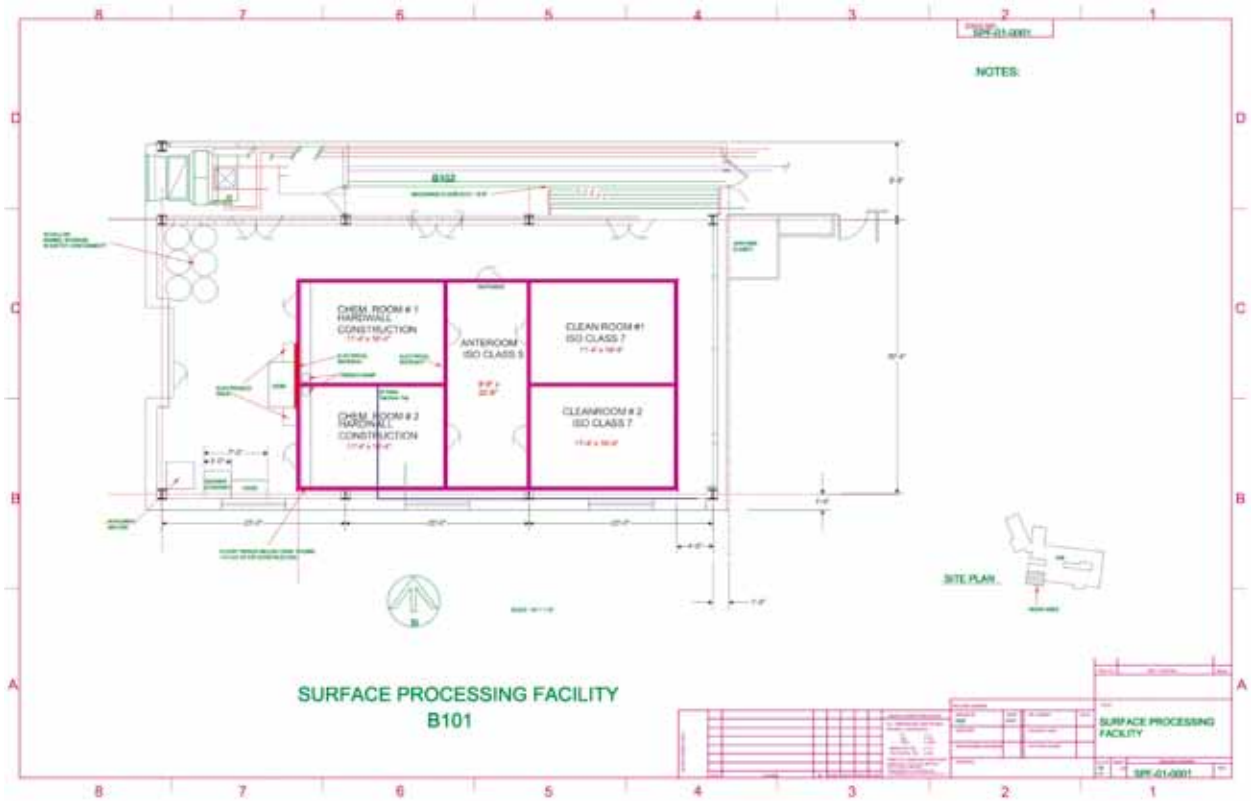

Figure 2.7 Layout of the ANL/Fermilab surface processing facility.

This has included the creation of EP and high-pressure rinsing systems and associated rooms at ANL that are now complete. The ongoing installation and commissioning of furnaces at Fermilab and Cornell removes the last large bottleneck in the production of cavities and allows capacity for further R&D. To operate the ANL/Fermilab facility, technicians were located and trained at JLab for extended periods. Throughout this effort, the processing and test of cavities at JLab has continued, and the performance of nine-cell cavities coming from JLab has been consistently excellent. The engineering of this processing facility, and the standardisation of the chemical processing steps, has now led to a chemical polishing facility being assembled in industry.

In 2007 the vertical test system at Fermilab was commissioned, and since has been used at an increasing rate such that two cool-downs per week are now possible, for either nine-cell or single-cell tests *[2-23]*. A unique facility in the Americas, the Horizontal Test Facility at Fermilab, used for the testing of dressed cavities, was brought online in 2008 and has been used since at a rate of approximately one test per month to qualify the cavity dressing process before assembly into an ILC-style cryomodule, known as CM-2 *[2-16]*. *Figure 2.8* shows the Horizontal Test Facility at Fermilab.

Figure 2.8 The Horizontal Test Facility at Fermilab.

Production, test and diagnostic facilities at the laboratories in the Americas region have been enhanced not only by propagation of tools developed elsewhere, such as the Kyoto-KEK camera system, but also through local efforts such as the creation of the controls system for the automatic tuning machine (since delivered to DESY and KEK and deployed at Fermilab), second sound quench detection location development, Questar optical inspection system development, automation and software development of the optical inspection process, development of a silicone moulding technique for the 3-D imaging of surface features, development and commissioning of a vertical EP facility and creation of a fast thermometry system for measurements of quench location and hot spots. Industrial X-ray tomography has been used to view voids in the cavity material, typically around the equator welds, that currently appear to be a leading indicator of fabrication difficulties that

could lead to quench limitations during tests. With respect to remediation efforts, laser re-melting has been shown to smooth single-cell cavity surfaces successfully and to be minimally invasive, while tumbling techniques are under continued study both as a remediation and a preventive measure. *Figure 2.9* shows the Fermilab tumbling process facility.

Figure 2.9 The Fermilab tumbling process facility.

In addition to cavity fabrication and processing, Fermilab hosts a full cryomodule assembly facility capable of a throughput of one cryomodule per month. *Figure 2.10* shows the cryomodule assembly facility at Fermilab. The design is strongly based on the system at DESY and has been used to date to assemble Cryomodule 1 (CM-1), and to dress multiple cavities currently undergoing testing in the horizontal test stand in preparation for CM-2 assembly.

Figure 2.10 The cryomodule assembly facility at Fermilab.

Leading up to the completion of the TD phase, the Americas region has additional vertical test stand and horizontal test facilities on order to increase capacity, and should be well positioned to process and test tens of cavities, finally assembling them into cryomodules in 2011 and beyond. Our diagnostic and test capabilities will continue to be used to diagnose faults earlier and earlier in the fabrication and processing chain, and to feed information back to our vendors.

Fermilab is currently constructing the SCRF Test Accelerator at the New Muon Lab (NML). NML consists of a photo-emitted RF electron gun, followed by a bunch compressor, low-energy test beamlines, SCRF accelerating structures, and high-energy test beamlines. *Figure 2.11* shows the general layout of NML. The progress of the system integration and tests is discussed in section 2.6.

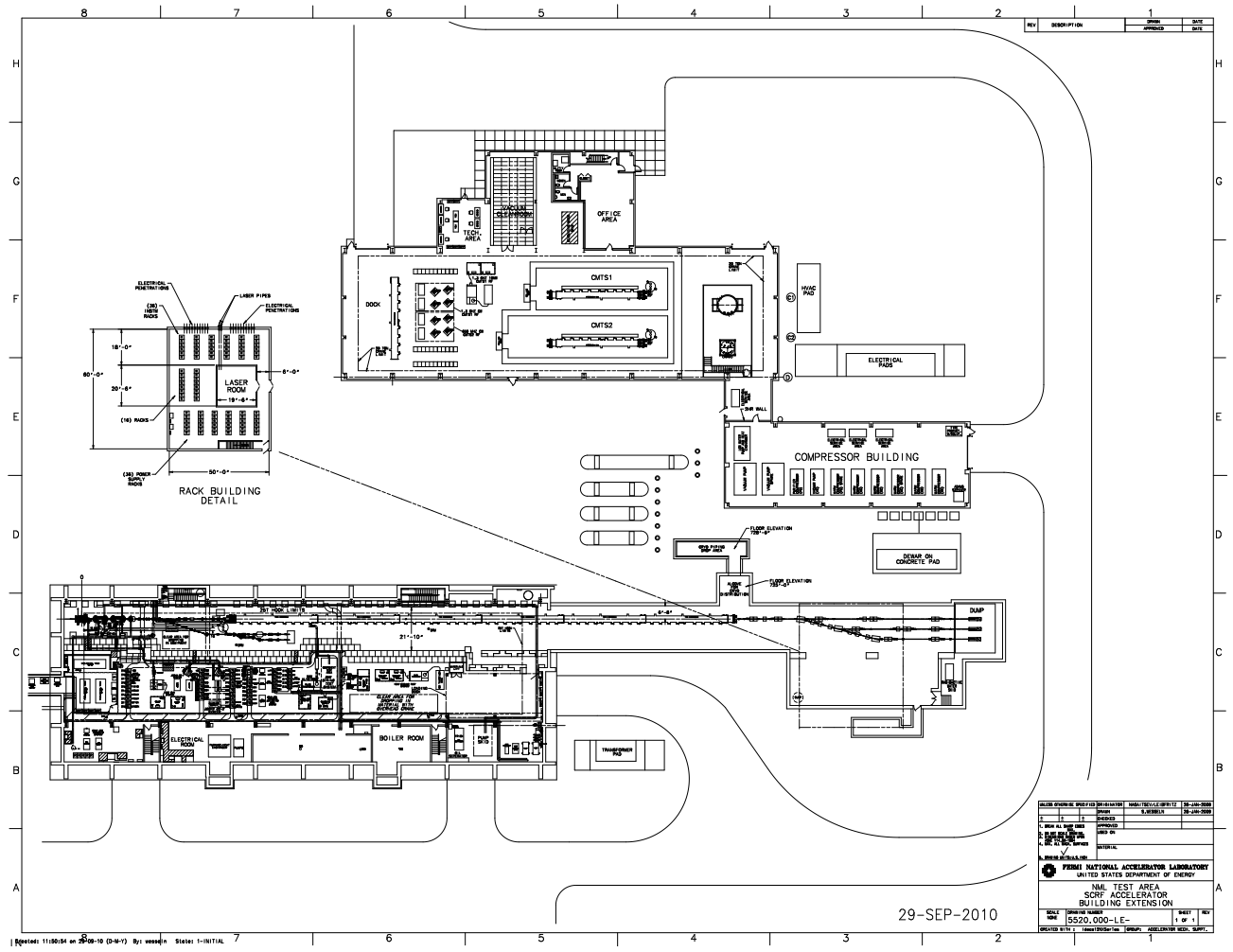

Figure 2.11 General layout of NML at Fermilab.

2.2.3 Development of infrastructure in Europe

The European SCRF activities are naturally centred on the imminent mass production for the European XFEL. The contracts for the production of some 600 cavities, couplers and tuners have been extended to industry. This development marks an important milestone since the cavity treatment process had to be agreed upon in all detail and specified for mass production. It is also an important milestone for the ILC since, although a higher operating gradient is required for the ILC, the manufacture with final electropolishing is deemed identical for European XFEL and ILC. Cryomodules have been produced by various vendors and performed excellently at the FLASH facility so that a sufficient industrial base has become available. Initial cold tests of the fabricated cavities will be made at DESY. RF couplers procured, tested and conditioned by CNRS/LAL (in Orsay, France) will be mounted at CEA/Irfu (in Saclay, France), who will also carry out the string and overall accelerator module assembly *[2-24]*. Subsequently the cryomodules will be returned to DESY for test and installation into the European XFEL.

The manufacturing contracts include 24 cavities that will be available for additional treatment for highest gradients and supplemented with couplers and tuners. These cavities are part of the ILC-HiGrade project that addresses the high gradient in the context of cavity mass production.

Surface preparation (polishing) of the cavities requires first a bulk removal process, followed by a final 'fine polishing'. The ILC specification requires that both bulk and final treatments be made using electropolishing. For the XFEL, electropolishing is used for the bulk treatment of all the cavities, but the final polishing process will be either electropolishing or buffered chemical polishing, depending on the vendor. The vendors are required to meticulously follow the process description and to document the individual steps. A comparison of the two techniques for final surface treatment can be done based on the statistics of several hundred cavities each.

Figure 2.12 Left: tool for room temperature RF measurement of half cells. Right: tool for field flatness tuning of completed cavities.

The two manufacturers selected in the tendering process will be supplied with European standards certified tools developed by DESY and Fermilab to assess the field and mechanically tune the individual cells for field flatness. These automated tools can be operated by non-RF experts and will provide a standardised log of the recorded data at the same time. The automation has considerably reduced the tuning time. *Figure 2.12* shows the automated RF measurement and the tuning machines.

The first cold test of the nine-cell cavity performance will be made at DESY. It will provide the first feedback on the achieved gradient after manufacture. All cavities, except for the ILC-HiGrade cavities, will be delivered with the helium vessel mounted. Much of the existing infrastructure at DESY has been developed at the time of the TESLA Technology Collaboration and has been used ever since. Evidently this infrastructure had to be augmented to allow for bulk testing. The Accelerator Module Test Facility has recently been built to allow for series test of cavities delivered from the manufacturer. *Figure 2.13* shows the general layout.

Figure 2.13 Layout of the Accelerator Module Test Facility hall at DESY.

Here four cavities at a time will be mounted on the so-called insert as shown in *Figure 2.14*. It is subsequently lowered into the vertical cryostat and individually tested for performance, which includes a test of peak field performance.

The facility has been planned for minimal physical handling of the cavities to guarantee high throughput and reproducibility. The test procedure was standardised and aims for rapid characterisation of the cavity performance. It is expected that most of the cavities will pass this test and fulfil the gradient requirement for the European XFEL of 22.4 MV/m. We estimate based on current understanding that the treatment of cavities of higher gradient will be no different. Cavities that fail the acceptance test will have to be diagnosed in detail and are subject to post-processing. The reason for failure is typically field emission from the inclusion of particulates in the niobium surface, or a quench resulting from surface irregularities. The vertical cryostats will be equipped with sensors, called oscillating superleak transducers, for detection of second-sound signals originating from the source of the cavity quench. The analysis of the second-sound propagation time enables the reconstruction of the quench origin by triangulation.

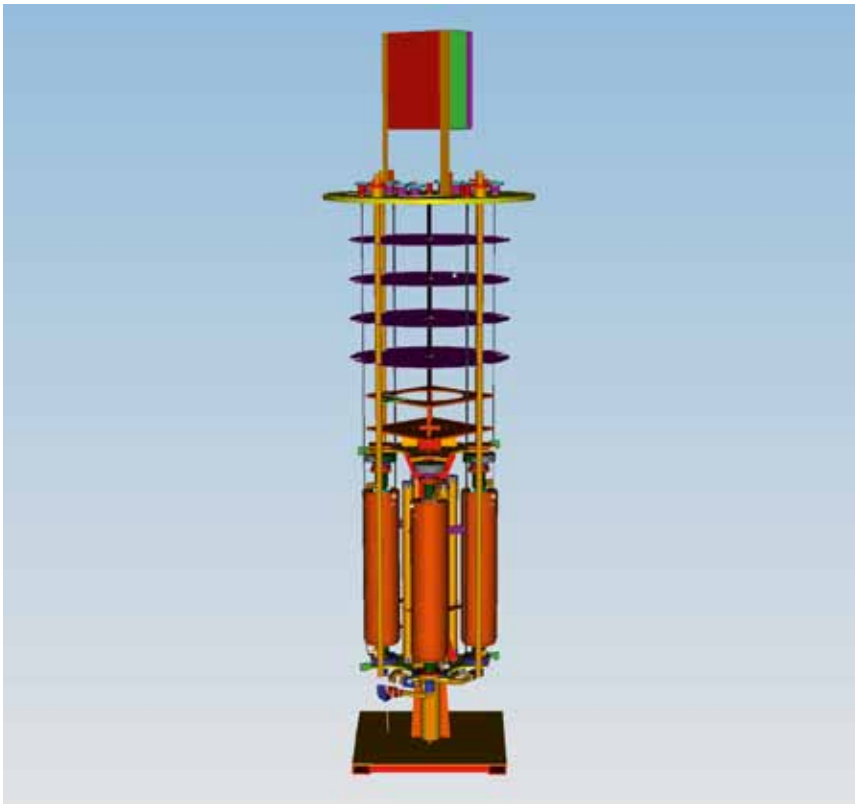

Figure 2.14 The cavity insert holds four cavities at a time for the test in the vertical cryostat.

ILC-HiGrade is also preparing an automated optical scanner, which will map the surface close to the electron beam weld of cell hemispheres and the iris between two cells. The optical scanner uses the Kyoto-KEK developed camera, as described above, which resolves surface features down to about 10 µm.

The long existing infrastructure at DESY has also been improved in order to facilitate the post-processing. The cleanroom standards have been raised and the handling steps have been streamlined. The failing cavities lend themselves to an additional short buffered chemical polish process, which removes a layer of niobium of around 10 µm from the surface. Specific action can be taken to address surface features located in the optical scan.

The accepted cavities will be shipped to CEA/Irfu for further assembly. The actual shipping procedure has been verified; the shipping tools have been developed and the forces on the cavities during transport have been measured and found acceptable.

The high-power couplers will be manufactured in industry and are delivered to CNRS/LAL for conditioning. Eight couplers will be conditioned per week with a maximum RF power of 5 megawatts (MW). *Figure 2.15* shows the layout of the coupler conditioning facility at LAL. After acceptance test the couplers will be shipped directly to the assembly site at CEA/Irfu.

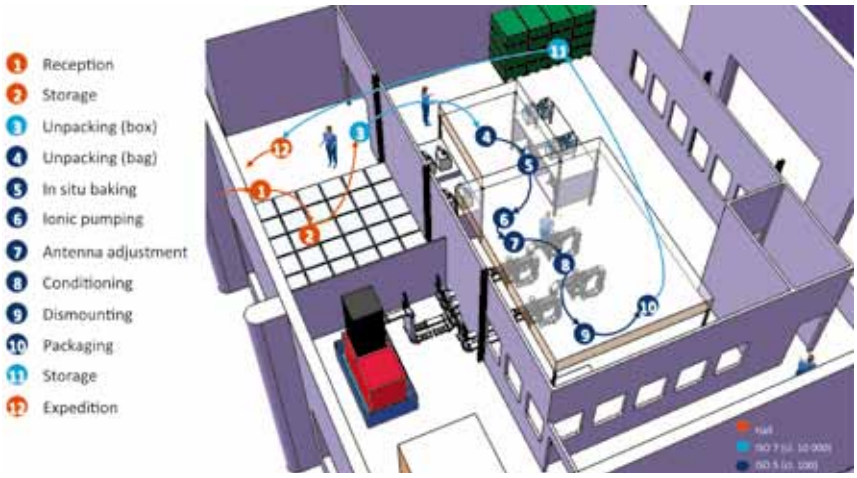

Figure 2.15 Layout of the coupler conditioning facility at CNRS/LAL.

The team at CEA/Irfu has equipped existing lab space to house the infrastructure for cryomodule assembly *[2-24]*. *Figure 2.16* shows the general layout. All components will be 'washed' before assembly. A large ISO 4 cleanroom and supplemental ISO 5 and ISO 7 cleanrooms have been installed to allow for mounting of the supplied couplers and for assembly of the cavities into a string. Once assembled, the string will be precision-aligned. The cantilever system will be used to insert the string into the cryomodule. The infrastructure will initially be used for the components for the SPIRAL2 project, and then for mass production for the European XFEL.

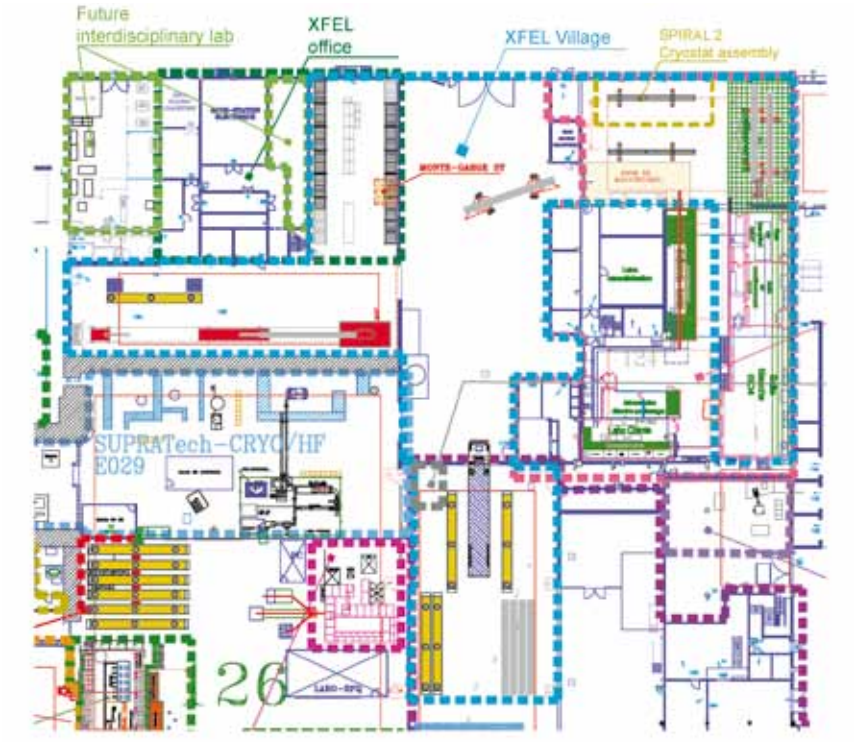

Figure 2.16 Layout of the cryomodule assembly facility at CEA/Irfu.

2.3 Progress towards manufacture of high-gradient cavities

2.3.1 Overview

The gradient choice for the ILC SCRF cavities is important for the beam energy reach and the machine cost. At the time of the RDR, a choice of 35 MV/m was made for cavity vertical qualification tests *[2-25]*. This choice was supported by the demonstration of a gradient of 35 MV/m or more in several nine-cell TESLA Test Facility (TTF)-shape cavities, results from the DESY-KEK collaboration. These cavities were surface-processed by electropolishing, heat treated at 600 – 800 °C in a vacuum furnace for hydrogen removal and baked at 120 °C for 48 hours after the final EP.

Achieving 35 MV/m in nine-cell cavities reproducibly is important, as the total number of cavities required for the ILC is far more than any SCRF-based machines built or planned. A global R&D programme called S0 was established in 2006 to address this challenge *[2-26]*. The S0 programme, coordinated by the GDE Cavity Group, has broad global participation from ANL, Cornell, DESY, Fermilab, JLab, and KEK. IHEP and Peking University are also going to participate in the programme. Significant progress in understanding the gradient limit and gradient scatter has been made by instrumented cavity testing at cryogenic temperatures and high-resolution optical inspection of the cavity RF surface. This is accompanied by steady progress in reproducibility at 35 MV/m and in improved practical gradient limit in nine-cell cavities. At the time of the RDR, Europe was the only region to have demonstrated 35-MV/m nine-cell cavity fabrication and processing. Today, 35-MV/m cavity fabrication and processing has also been demonstrated in the Asia and Americas regions. A solid SCRF technical base for the ILC on a global scale is now in place.

The global efforts in ILC gradient R&D are rewarded not only by improved gradient yield and reproducibility but also in the achievement of still higher gradients. By mid-2010, a major SCRF gradient R&D milestone of 50% yield at 35 MV/m was achieved as described below. The average gradient in the state-of-the-art nine-cell cavities is raised to around 40 MV/m, a steady increase compared to the state-of-the-art 35 MV/m in 2005.

2.3.2 Globally coordinated gradient R&D – the S0 programme

The ILC gradient R&D is a global effort with current participation of ANL, Cornell, DESY, Fermilab, JLab, and KEK. Information is exchanged monthly at the GDE ILC Cavity Group meetings. Diagnostic tools, production procedures and process parameters are at times verified by exchanging cavities across the labs and regions. There is growing interest and capability in cavity gradient R&D in other labs such as IHEP and Peking University in China, TRIUMF in Canada, and RRCAT and IUAC in India. Encouraging cavity results are emerging. Historically, these R&D initiatives usually drive industrial interest and capability for SCRF cavity manufacture and processing. A global SCRF industry is emerging, driven in large part by the demand for higher cavity gradient for the ILC.

2.3.3 Understanding the source of gradient limitation and scatter

The initial S0 effort focused on the issue of field emission, which was identified to be the main cause of gradient variability. Following the recommendation of the TESLA Technology Collaboration 2005 report, R&D priority was given to improved post-EP cleaning procedures *[2-27]*. Three methods are now established for effective field emission reduction: ethanol rinsing was successfully developed and applied at DESY, ultrasonic cleaning with detergent was introduced and optimised at JLab and fresh EP was found effective for field emission reduction at KEK. Some of the methods have been successfully transferred across facilities at different labs.

As a result of the R&D effort, sources of field emission are now understood *[2-27]*. Besides the traditional particulate field emitters, niobium oxide granule is found to be a major field emitter introduced by the electropolishing process itself. Wiping and brushing of end group components immediately after EP processing reduces niobium oxide granules (often accompanied by increased sulphur-bearing compounds) in the hidden areas where high-pressure rinse cleaning is less effective due to lack of direct water jet bombardment. Streamlined cleanroom assembly procedures are now routinely used, minimising recontamination by particulates generated by the assembly process itself. 'Field emission-free' performance up to 40 MV/m has been demonstrated in several electropolished nine-cell cavities. Efforts are continuing to develop improved and new cleaning techniques towards the goal of eradicating field emission up to the theoretical quench limit of a niobium cavity.

Our understanding of the source of limiting quench behaviour is much improved thanks to temperature mapping measurements and accompanying high-resolution optical inspection. Many of the thermometry and inspection instruments have been successfully adopted in most labs participating in the S0 studies. Kyoto-KEK cameras and Cornell oscillating superleak transducer systems are two examples. For the ILC nine-cell cavities, a quench limit at below 25 MV/m is found to be caused predominantly by highly localised geometrical defects in the zone adjacent to the electron beam weld seam at the cavity equator. These defects can be roughly categorised as circular pits or bumps with a typical diameter in the range of 200 to 800 mm. Detailed morphology of the defect can be quite complicated as revealed by replica mould measurements and by microscopic inspection of small samples cut out from real cavities. It is suspected that local magnetic field enhancement at sharp edges are usually observable on the RF surface of as-built cavities. This quench limit due to geometrical defects is insensitive to repeated EP, and there is emerging evidence to show that these geometrical defects already exist before any chemistry is done to the cavity surface. It is now generally recognised that, in order to overcome quench limits below 25 MV/m, improved quality assurance and control in material and fabrication are important.

Further studies are needed to understand the source of quenches at higher gradients in the nominal range of above 30 MV/m. It is clear that higher quench limits are also caused by highly localised defects near the equator electron beam weld, but unlike the geometrical defects, there is typically no observable feature at the predicted quench site. It has been suggested that locally suppressed superconductivity due to compositional irregularities may be responsible. Additional capabilities of compositional analysis in situ at the predicted quench location are expected to shed light on this issue, and offline microscopic analysis of small samples removed from the predicted quench location (as has been done at DESY) may also provide important information for further gradient improvement.

2.3.4 Gradient yield definition and global cavity result database

At the start of the Technical Design Phase, goals of a 50% process yield by 2010 and a 90% production yield at 35 MV/m, with a quality factor Q_o of greater than $8x10^9$, were defined. As the TDP progressed, the needs for a clearer definition of the production yield and for a globally consistent and available database for recording test results were recognised. In 2009 the GDE ILC Cavity Group proposed a clear definition of gradient yield, which adopted the concept of the first-pass and second-pass yield and established rules for cavity selection. In parallel the ILC Global Cavity Database Team was created as a part of the S0 effort *[2-28]*. The team includes members from Cornell, DESY, Fermilab, JLab and KEK, and took on the task of not only creating the database, but also defining the rules for how the data should be included and how the data would be presented. The result of this effort is a clear, objective, and publicly accessible database where the progress of cavity R&D can be tracked. In fact, the database group has presented status reports at each major ILC workshop, meeting or review since mid-2009.

The most recent results for first-pass and second-pass yields, presented in a time-phased manner at the IWLC2010 meeting in Geneva, Switzerland, are shown in *Figure 2.17 [2-29]*. By way of definition, plots only include results from a vendor-laboratory combination that has previously demonstrated through tests the ability to fabricate and process a cavity that achieves more than 35 MV/m in a vertical test. A first-pass result is one where the fabrication and processing have been completed according to the standard recipe leading up to the first test; a second-pass result sums up all first pass results greater than 35 MV/m and those results where a poorer-performing cavity had some remediation applied based on diagnostics from the first test. Apparent from the graphs is the improvement with time of the yield curves, particularly for second-pass results. This improvement is attributable to improved diagnostic and remediation tools that have been developed in the past years. Repeatability in EP processing, one of the methods that has been demonstrated, plays an important role in improving the second pass yield by raising the gradient performance of cavities quench limited between 25 and 35 MV/m. A smaller gain is seen in the first-pass results. This is consistent with our limited ability to recognise fabrication flaws early in fabrication by means other than vertical testing. Improvement of our understanding of the critical fabrication parameters and the development of predictive quality assurance checks are an R&D direction in the remainder of the TD phase.

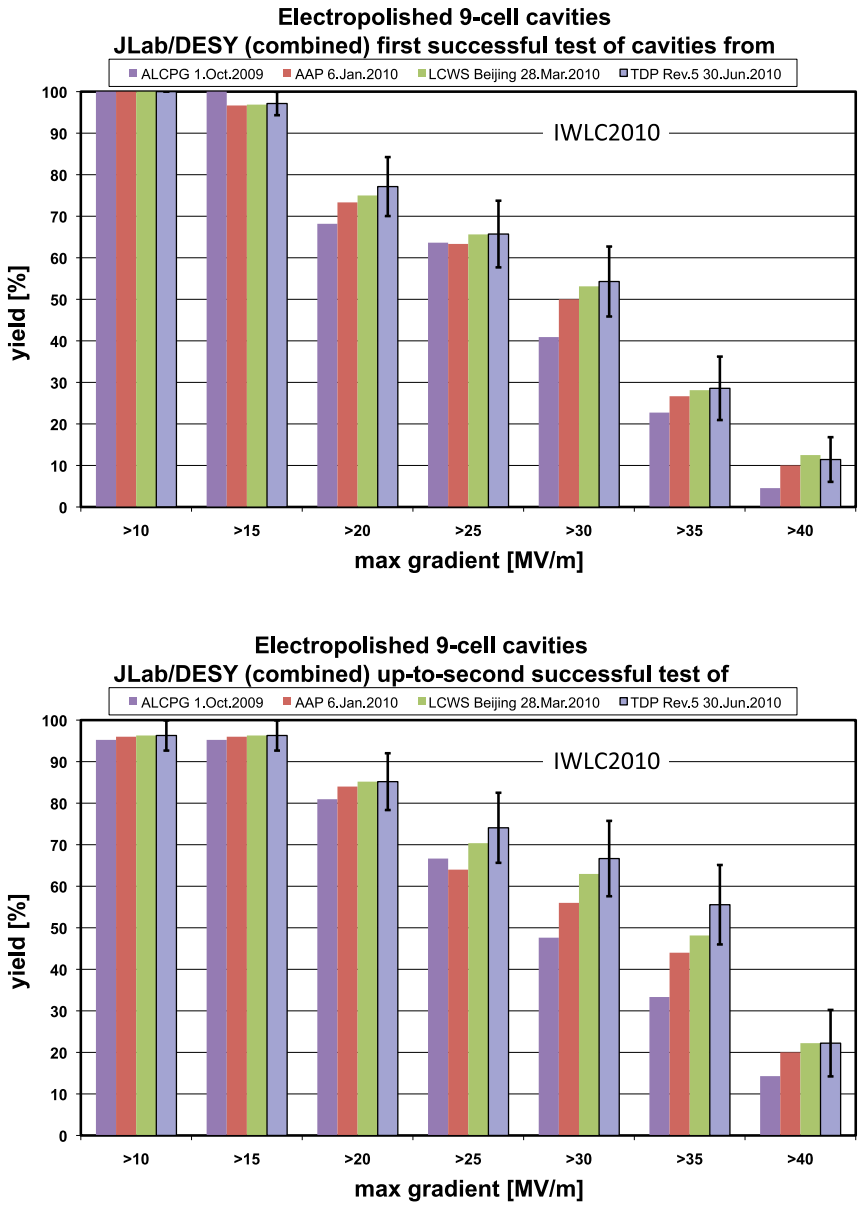

Figure 2.17 Cavity gradient performance with production yield for (top) the first pass and (bottom) the second pass.

2.3.5 Achieving the TDP-1 gradient milestone of 50% yield at 35 MV/m

The improved understanding of gradient limit goes hand in hand with the improvements achieved in cavity gradient yield. Field emission was much reduced due to the application of post-EP cleaning procedures such as ethanol rinsing and ultrasonic cleaning with detergent, with a further reduction in field emission achieved by applying the procedure of continued acid circulation after the EP voltage is turned off. This procedure reduces sulphur-bearing niobium oxide granules and hence reduces inherent contaminants on the as-polished surface. Optimised electropolishing and streamlined cleanroom assembly resulted in reproducible cavity processing and hence reproducible cavity gradient results. As a result of the continued

improvement and optimisation of the cavity processing and the continued understanding of the gradient limit, the TDP-1 gradient goal of a 50% production yield at 35 MV/m and at Q_0 greater than $8x10^9$ was accomplished in June 2010 as shown in *Figure 2.17*. Further highlighted individual institutional progress in the gradient R&D in 2010 is summarised in *Table 2.4*.

Joint effort	Progress
Research Instruments-JLab	Achieved 90% yield at ≥35 MV/m and Q_0 ≥$8x10^9$
Research Instruments-Fermilab/ANL/JLab	Achieved ≥35 MV/m and Q_0≥$8x10^9$
Research Instruments-Fermilab/ANL	Achieved 34.5 MV/m with tumbled cavity
Niowave-Fermilab/ANL	Achieved 28.8 MV/m with the first production cavity
KEK-Fermilab/ANL	Demonstrated local repairing: gradient improved from 11 to 30 MV/m
IHEP-KEK	Achieved 20 MV/m with the first IHEP cavity (LL, LG, no-end)
PKU-JLab	Achieved 28 MV/m with the PKU cavity (TESLA, FG, w/-end)
Hitachi-KEK	Achieved 35 MV/m with the first Hitachi cavity (TESLA-like, FG, no-end)
MHI-KEK	Achieved ≥35 MV/m and Q_0 ≥ $8x10^9$ with MHI-12 cavity
DESY/E-XFEL	600 cavities ordered; RI and Zanon awarded

Table 2.4 Globally highlighted gradient R&D progress in 2010.

2.3.6 Aiming at the TDP-2 gradient goal and 90% yield at 35 MV/m

After successful achievement of the 2010 goal of 50% second-pass production yield, the TDP-2 2012 goal remains a cavity gradient second-pass production yield of 90%. This is an ambitious goal, but appears possible. Recently, a 90% yield has been demonstrated based on very limited statistics (ten cavities built by one of the most experienced cavity manufacturers and processed and tested at JLab). Our efforts in TDP-2 will focus on two areas: at lower gradients, the modification of the production process to remove mechanical pits and other imperfections that now appear to be a leading cause of lower-gradient quench limitations; and at higher gradients, improvement of the processing and assembly techniques that result in improved surface homogeneity and reduced field emission. Though both of these efforts will start in our cavity R&D efforts with remediation of defects or emission seen in the first-pass results, the goal is to understand the problems well enough that our efforts can become predictive, rather than reactive. Our ultimate goal is to feed knowledge from labs back to industry for improved fabrication in industrial manufacturers.

For mechanical defects, use of inspection systems such as the Kyoto-KEK camera, silicone pit modelling or moulding, or X-ray tomography to locate and categorise defects early in production, and tracing of these defects to performance-limiting locations as seen by T-mapping or second sound, will require added inspection efforts over the next years to create a database of defects and a more detailed understanding of the parameters that directly limit performance. For processing errors, more detailed understanding

of the process itself is required, as is reasonable quality assurance checks to make sure the processes are executed successfully each time. This will include further tweaking of the standard process formula.

Finally, it should be noted that neither of the above R&D directions has been proven to be conclusively 'the' answer to the current yield limits. Current performance limitation could vary from vendor to vendor or from laboratory to laboratory. Continued incremental improvements will rely on continued extensive inspections, until the exact root causes are proven.

2.3.7 Long-term cavity R&D for a very high gradient beyond the TDR

Long-term R&D addresses the gradient need for the ILC 1-TeV upgrade *[2-27]*. With the improved cavity cell shapes and optimised material properties, one can expect nine-cell niobium cavities with gradients in the range of 40 to 60 MV/m. There are three proposed cell shapes with major efforts for very high gradients. The low-loss shape developed at KEK has shown excellent gradient results of around 50 MV/m in many single-cell cavities *[2-30]*. Several nine-cell cavities have been prototyped and gradients of more than 35 MV/m have been demonstrated in nine-cell cavities with and without end-groups. The re-entrant shape developed at Cornell has shown the record gradient of around 60 MV/m in a single-cell cavity *[2-31]*. The first nine-cell re-entrant cavity has been built and efforts are underway to push for very high gradient. A new 'low surface field' shape has been designed at SLAC. Planning is underway at JLab to prototype the first single-cell and multi-cell low surface field shape cavities.

In addition to the cell shape development, one can also expect benefits from continued optimisation of niobium material. There is evidence that heat treatment, at various stages such as post-forming or post-fabrication, may have significant room for improvement in achieving very high gradients. As the shape improvement and material improvement are two independent paths and as both are compatible with the EP processing procedure, one can expect significant gradient improvement toward the range of 40 to 60 MV/m by using the current baseline cavity processing procedures.

It is generally agreed that gradients up to 100 MV/m in superconducting RF cavities are theoretically possible by switching to other superconducting materials, but significant fundamental R&D is required. Active programmes now exist in this direction pursued by several groups at ANL, Cornell and JLab. It is recognised that the most promising path lies in the thin film coating of new material on copper or aluminium substrates pre-formed into suitable cavity shapes. Given the potential high return, R&D of new superconducting RF material and cavity system development should be intensified after the TDR in order to support the physics scenario of 1 TeV or more for the ILC.

2.4 Cryomodule design and development

Most of the effort and resources spent on ILC cryomodule activities since the publication of the RDR and the beginning of the Technical Design Phase have been devoted to the collaborative S1-Global programme *[2-32]*. Taking advantage of experimental activities at KEK in the framework of this worldwide effort, several ILC cryomodule design issues have been addressed, like the assessment of the thermal performance of the intermediate 5-kelvin (K) shields and the investigation of diverse tuner and magnetic shielding solutions. The experience gained from S1-Global, which integrates different variations of components (e.g., cavities, magnetic shielding, couplers and tuners) from several collaborating partners into a single cryomodule, is also very important for the assessment of all the 'plug-compatible' interfaces of the cryomodule for future ILC plans.

2.4.1 Progress in the S1-Global cryomodule development hosted at KEK

The ILC cryomodule design study mainly done at KEK is only briefly described here. (See 2.6.2 for details of the high-powered RF tests.) The cryomodule design work began in May 2008 with a joint team of Fermilab, INFN and KEK, and was completed by the end of 2008. For construction of the S1-Global cryomodule, KEK performed the modification of a half cryomodule, so-called Cryomodule-A, from one of the original STF modules *[2-33]* in 2009, while INFN and KEK cooperatively provided components for another half cryomodule, so-called Cryomodule-C. DESY, Fermilab and KEK provided and tested eight cavities and couplers needed for the S1-Global programme. The S1-Global cryomodule was assembled and installed in the KEK-STF tunnel between January and May 2010. The cold tests were performed between June 2010 and February 2011. Before starting the S1-Global cryomodule cold test, KEK completed the thermal test of the intermediate 5-K shield by using a half-length, 6-m-long STF cryomodule. The heat load to the 2-K region was measured with and without the 5-K shield and compared with calculations. The results are being applied on the thermal design of the ILC cryomodule. The thermal design guideline for the ILC cryomodule will be summarised below.

2.4.2 Progress in the European XFEL project hosted at DESY and R&D at Fermilab

The European XFEL project is now in its construction phase and the commissioning is expected in 2014 *[2-34]*. The XFEL superconducting linac consists of 80 cryomodules with a design derived from the TESLA Test Facility Type-3 on which the ILC module design concept is also based. The industrial vendors have been qualified, and the project is moving forward to the start of the serial production. The European XFEL project will therefore soon provide much experience from a relatively large series of production modules in an industrial context and that will bring valuable information for the industrialisation of the ILC cryomodules.

At Fermilab, CM-1, an ILC Type-3 cryomodule assembled using parts provided by DESY, INFN and Fermilab, has been cooled down and tests are underway at the NML test facility at Fermilab. Dressed cavities for CM-2 are being tested in Fermilab's Horizontal Test Cryostat. In addition, design work is in progress on cryomodules for Project X, a high-intensity proton linac proposed for Fermilab's next generation of neutrino experiments and other studies. Project X cryomodules, being a continuous wave and low beta design, differ in various ways from ILC-type cryomodules but will benefit greatly from the ILC experience.

2.4.3 ILC cryomodule design with plug compatibility

In order to develop an industrialised design of the ILC cryomodule, plug-compatible interfaces of the cryomodule have been defined as listed in *Table 2.5*. A detailed and more complete parameter list shall be established in future studies.

Table 2.5 Plug-compatible interfaces of cryomodule.

Interface	Item	Parameter
Cryomodule slot	Length	12,679.6 mm
Vacuum vessel	Length/Outer diameter/Support	11,830 mm / 965.2 mm / TBD
Vacuum bellow	Length	849.6 mm
Vacuum flange	Diameter/Thickness/Connection	TBD
Input coupler interface to vacuum vessel	Diameter/Thickness/Connection	Longitudinal pitch: 12,679.6 mm Others: TBD
Cavity support lug	Span/Lug width and thickness	750 mm / TBD
Cooling pipes	Position/Diameter/Material	Cooling pipe parameters are specified w/ cryogenic design.

2.4.4 Study of thermal balance with and without 5-K radiation shield

The specific heat loads in the three cryogenic circuits of one ILC cryomodule (at the temperature levels of 2 K, 5 K and 40 K) are listed in *Table 2.6*, calculated from the values of one RF unit as shown in the RDR *[2-35]*.

Table 2.6 Heat loads of one ILC cryomodule from RDR.

Load, in W	2 K	5 K	40 K
Static load	1.7	10.6	59.2
Dynamic load	9.7	4.4	94.3
Total load	11.4	15.0	153.5

In the 5-K circuit, the heat load by thermal radiation was evaluated to be at 1.41 W. The present ILC cryomodule scheme, derived from the TESLA Test Facility cryomodules *[2-36]*, has two thermal shields circuits. The '5-K circuit' contains helium pressurised above the 2.3-bar critical pressure, which warms from 5 K to 8 K through the circuit.

The 40-K circuit contains helium gas warming from 40 K to 80 K. When the 5-K thermal radiation shield is removed (this was investigated as a means to simplify the module and decrease the fabrication costs), thermal radiation from the 40-K screen would directly impinge into the 2-K region, increasing noticeably the module's 2-K heat load. However, by modifying the 40-K thermal shield flow scheme as shown in *Figure 2.18 [2-37]* and by rearranging the thermal intercept strategy, this additional contribution could be mitigated. The improvement is obtained by using the forward line to lower the temperature of the thermal shield from 74 K to 46 K while using the return (warmer) line to provide the thermal intercepts of input couplers and current leads, thus increasing the average intercept temperature from 54 K to 66 K.

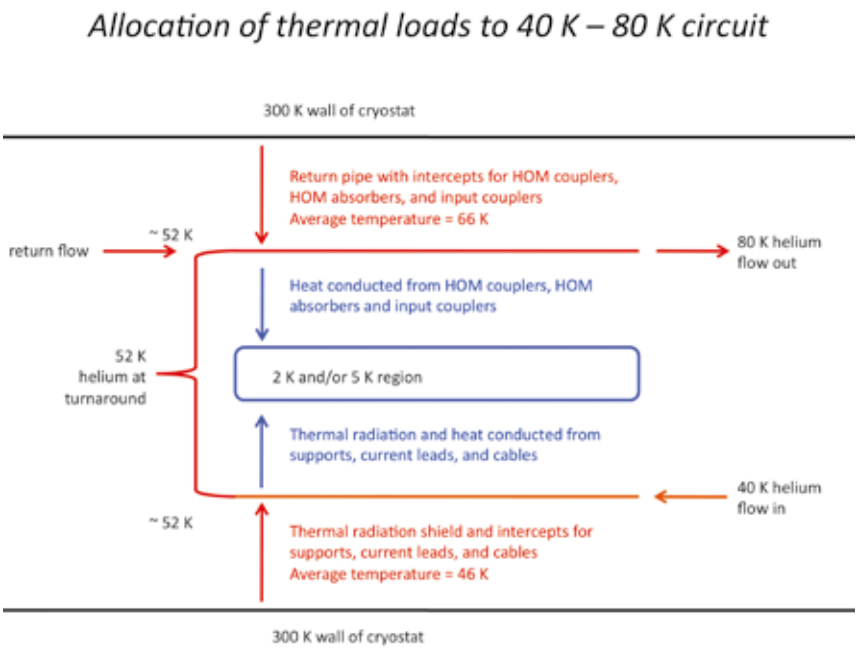

Figure 2.18 Cooling scheme and thermal balance for the ILC cryomodule's thermal design.

For future assessment of the ILC cryomodule's thermal design, the cost implications of eliminating the lower part of the 5-K shield needs to be carefully studied, particularly in the following aspects:

1. Capital and assembly cost reduction of the lower shield components
2. Capital and operational cost increase of the cryogenic system due to the additional heat load

The effect on the assembly time and costs for providing the 5-K thermal intercept to other components, such as main and HOM couplers, will be studied. For example, the cross-sections of the cryomodule with the 5-K shield and without the lower part of the 5-K shield are shown in *Figure 2.19*. In the proposed design, the cooling line at 5 K is preserved due to the need to provide the thermal intercepts of the input couplers, support posts and RF cables.

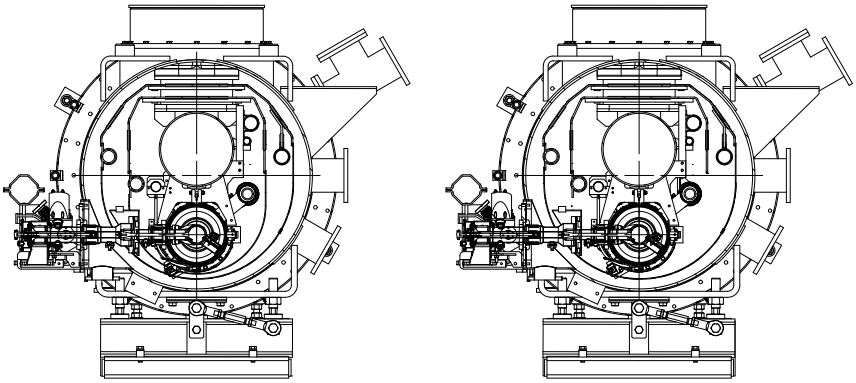

Figure 2.19 Cross-section of the cryomodule with (left) two thermal shields and (right) without the lower part of 5-K shield.

2.4.5 Study of the magnetic shield assembly

Different magnetic shield solutions are being developed by several institutions and are being studied from a viewpoint of the cryomodule assembly work. The magnetic shields of DESY and Fermilab (TESLA-type) cavities are designed to be assembled outside of the cavity jacket and require more numbers of split components. The magnetic shield of the KEK (TESLA-like) cavity is designed to be internally installed in the helium jacket and requires fewer split components. Both designs have been verified to work well through the S1-Global cavity string test. Further detailed design studies need to be carried out to find the best cost-effective magnetic shield design as a part of the best cost effective cryomodule design, satisfying the magnetic shield performance.

2.5 High-power radiofrequency development

In the *Reference Design Report* (RDR) *[2-38]*, the high-power radiofrequency equipment and layout had reached a fairly mature state. The klystrons, modulators and related equipment were housed in a parallel utility tunnel, connected every 38 m to the main linac tunnel by a penetration through which waveguides carried up to 10 MW of Lband (1.3 GHz) power, to be distributed along three cryomodules. Extensive ongoing work has been required, due mainly to the fundamental change in tunnel configuration. With the move to single-tunnel main linac housings, the production and distribution to the cavities of RF power had to be rethought. Two proposed options are currently being pursued by ILC R&D programmes. They are referred to by the acronyms KCS (klystron cluster scheme) and DRFS (distributed RF system).

2.5.1 Klystron cluster scheme

System description

In the KCS scheme *[2-39]*, RF production is moved to the surface. Unlike in the RDR, where it is brought down as alternating current (AC) wall-plug power, or the European XFEL, where it is brought down as direct current (DC) cable power to underground klystrons, with KCS, the power used to accelerate the beam is transported between the surface and the underground tunnel as RF. This approach of sending power down as RF follows the example of the SLAC linac, which served the only previous linear collider, the SLC. The differences arise both from having to accommodate a deep-bored (as opposed to cut-and-cover) tunnel, which makes shafts expensive, and from the need to minimise surface impact over what will be a much larger footprint.

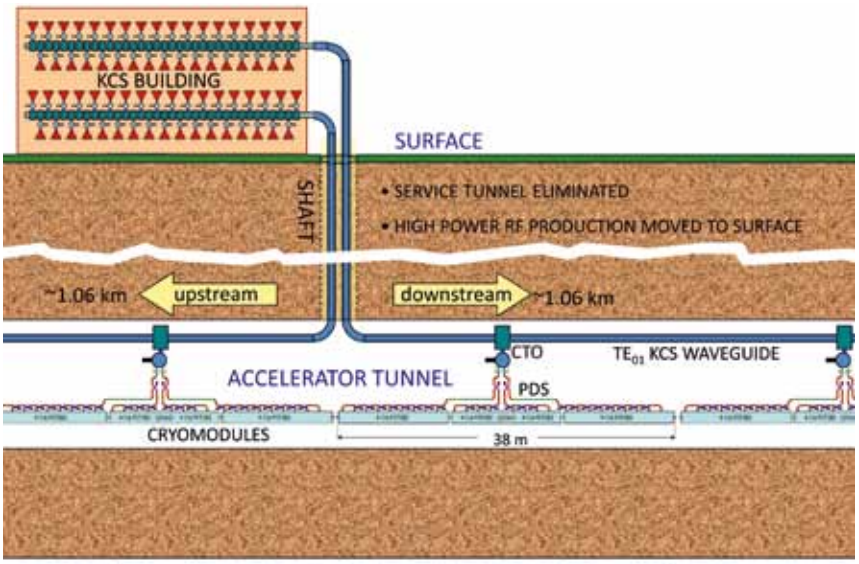

Figure 2.20 Basic layout scheme of the klystron cluster scheme. Many high-power RF sources in a surface building are combined into a large circular waveguide.

Thus the idea of clustering was adopted. Power from groups of approximately 34 10-MW klystrons is combined into a single low-loss, over-moded waveguide and transported down to the tunnel and along the linac as shown in *Figure 2.20*. This is sufficient, allowing for a few percent extra transmission loss, to power approximately 1.06 km of ILC linac. At 38-m intervals, partial power is siphoned from this main waveguide in 10-MW decrements. From each such tap-off, the RF is distributed to the cavities (26 in three cryomodules) through a WR650 waveguide system, just as it would be from a local klystron.

To minimise the number of buildings and shafts required, each houses two klystron clusters with one feeding upstream and the other downstream, powering over 2 km of linac per shaft. Besides the KCS main waveguide artery, some equipment from the service tunnel, such as front-end feedback electronics and beam instrumentation, is added to the linac tunnel in shielded crates below the cryomodules. No increase in tunnel diameter is foreseen. In addition to the civil construction cost savings associated with going to a single tunnel, this scheme brings the heat load associated with the RF production equipment to the surface, greatly facilitating cooling.

Klystrons and modulators

In the RDR, a 10-MW multi-beam klystron was identified as the ILC L-band power source. This choice was based on cost effectiveness, efficiency and relatively low operating voltage, and takes advantage of years of R&D for TELSA and the European XFEL. The prototypes were built by CPI, Thales, and Toshiba. The KCS option retains this source. A Toshiba tube is being operated at SLAC for reliability and lifetime studies.

The modulator requirements for the klystrons are 120-kilovolt, 140-A, 1.6-millisecond pulses at a 5-Hertz (Hz) repetition rate. As an alternative to the RDR baseline design, SLAC is pursuing a Marx-topology modulator to fulfil this requirement with a reliable and cost-effective approach *[2-40]*. A full-scale prototype, the SLAC P1 Marx is currently undergoing lifetime testing, driving the above-mentioned 10-MW Toshiba multi-beam klystron. In the accumulated 1,500 hours there have been no chronic problems. A second-generation Marx, the SLAC P2 Marx, is currently under development *[2-41]*.

The Marx is made up of many identical and, ideally, redundant cells. If a cell becomes inoperable, it can be bypassed. Increasing the applied charge voltage or turning on 'spare' cells allows the modulator to continue operation. In addition, a modular design allows better use of high-volume manufacturing techniques, thereby reducing costs. Finally, portable cells allow maintenance staff to quickly replace inoperable cells with pre-tested replacements, reducing the mean repair time.

The SLAC P1 Marx operates in air, has no output transformer, and is air-cooled as shown in *Figure 2.21*. The Marx utilises a field programmable gate array based control system. A diagnostic module on each cell, along with the ground station and a cell control board, coordinates the timing of the cells. The diagnostic card has four analog input channels monitored at 20 kilosamples per second with a resolution of 16 bits. A fast transient recorder can also be used at 30 megasamples per second with 8-bit resolution. In the SLAC P1 Marx, 16 11-kV Marx cells are arranged with a single 'Vernier' Marx.

The triggering sequence of the main Marx cells is designed to promptly turn on eleven cells, then stagger the turn-on of the remaining five cells to coarsely compensate the storage capacitor droop. The Vernier Marx (with cells charged to around 1 kV) staggers its turn-on and turn-off to further regulate the output to the specified level of ±0.5 %.

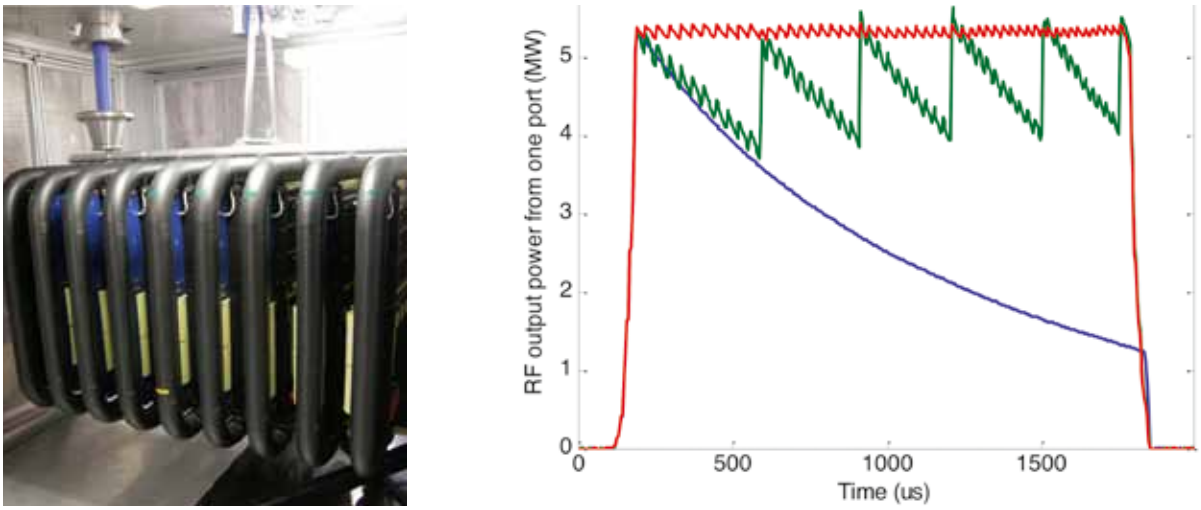

Figure 2.21 Left: SLAC P1 Marx modulator showing its cantilevered support structure, high-voltage grading rings, and 16 installed cells. Right: RF waveforms from one of the two klystron ports: no droop compensation (blue), with only delay cells (green), with delay cells and Vernier (red), producing a flat pulse with a 3% saw-tooth pattern.

Building upon the success of the P1 Marx, the SLAC P2 Marx is currently in the final stages of design. It includes 32 3.75-kV to 4-kV cells. This modulator will be able to produce the specified power with up to two of the cells offline. Three notable differences distinguish it from P1. First, a nested droop correction scheme is employed in the P2 Marx. Each cell individually regulates its output, removing the need for a separate compensation element (like the Vernier in the P1 Marx). Second, there is no arraying of solid-state switches within a cell, simplifying the control and protection schemes. Third, the modulator layout is redesigned to have a single-side access.

Main waveguide and tap-offs

For low transmission loss and robustness against RF breakdown, an overmoded circular waveguide operated in the TE01 mode is used as the main high-power RF conduit; the attenuation drops faster with radius for this mode than for others, and it has no electric fields terminating on the wall. The diameter chosen is 0.480 m, at which the added ohmic transmission loss along a KCS should be around 6.5%. With power levels on the order of 300 MW, this main transmission waveguide will likely be evacuated and thus needs sufficient wall thickness, about 1 cm. Mode conversion considerations suggest radius, roundness and alignment tolerances on the order of a millimetre and a straightness tolerance of half a degree. The flange joint between pipe sections will be designed to include sufficient longitudinal flexibility to take up local thermal expansion while maintaining concentricity and straightness. An insulation jacket and water cooling will be used to keep much of the main waveguide's heat load (averaging around 130 W/m) from the tunnel air.

An overmoded waveguide is not trivial to manipulate, as geometrical changes like bends tend to scatter power into parasitic modes. Each main waveguide will need to undergo probably three 90-degree bends, downward into the shaft, then towards and along the tunnel. These occur at maximum power between the last tap-in and the first tap-off, and will unavoidably have surface electric fields, so the design will be a challenge. They must have excellent port-to-port mode preservation and high-power handling without being excessively bulky. TE_{01} mode bends exist at X-band, and design options for KCS are currently under consideration.

For tapping off RF power from the main circular TE_{01}-mode waveguide without breaking the azimuthal symmetry and thus introducing surface electric fields in the very high-power region, a special waveguide component was designed, referred to as the coaxial tap-off *[2-42]*. The idea of this device involves stepping up the diameter from below to above the TE_{02} cut-off in such a way that roughly half the power is converted, creating a mixture of the two modes. The radial distribution of the electric field then varies longitudinally as the two modes beat as a result of their different guide wavelengths. At an appropriate distance, this beating is terminated by reintroduction of a wall at the original radius, separating the inner volume from a coaxial outer volume and dividing the power between the two in circular and coaxial TE_{01} modes.

To then extract the stripped power, the coaxial guide is shorted, and power is coupled through eight radial apertures into a wraparound waveguide and thence through two standard WR650 rectangular output ports as shown in *Figure 2.22*. The gap between the step and the dividing wall is varied over roughly 14 cm to achieve the many different fractional power couplings needed, ranging between 0.03 and 0.5, and a small customised ridge before the step is used to cancel any mismatch. The coaxial and wraparound region should never see more than about 10 MW, whereas the power in the inner region tops 300 MW. If the KCS is evacuated, a 5-MW pillbox window on each rectangular coaxial tap-off port will transition to the pressurised distribution waveguide.

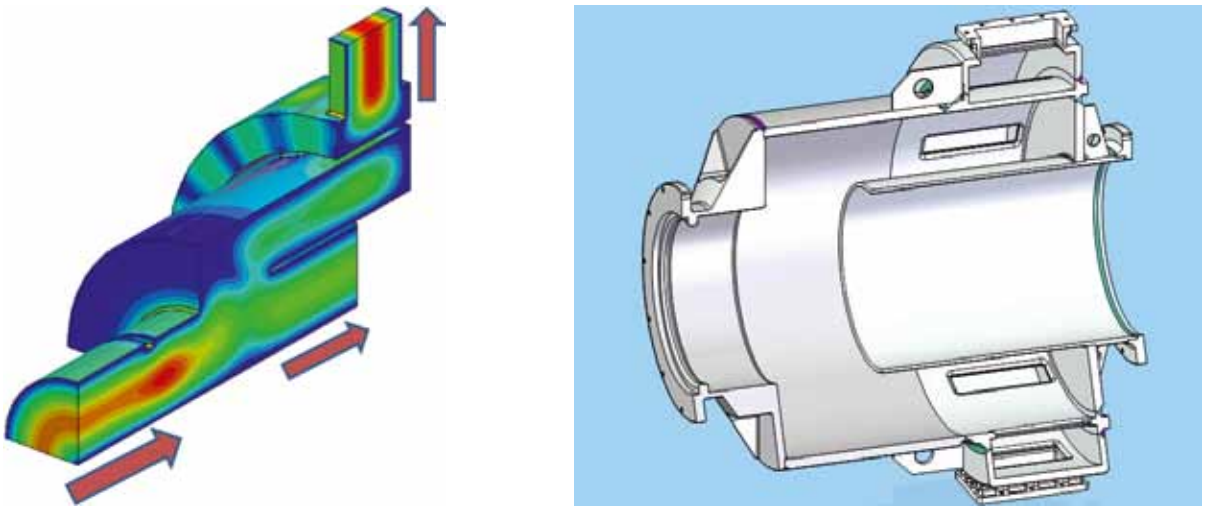

Figure 2.22 Left: simulation model with field plots (electric on cut plane, magnetic on surface). Right: mechanical design of a 3-decibel coaxial tap-off. For other couplings, only the gap length and matching ridge are modified.

In the surface building, tap-offs are also used in reverse for combining. At each one, proper phasing and relative amplitude ratio between the power flowing in the circular waveguide and the klystron power being added must be achieved for efficient combining. The diameter of the tap-offs' circular ports is smaller than that of the main waveguide. The two are interfaced by a matched double step taper at the end of the combining assembly and before and after each linac coaxial tap-off. These steps, as well as steps and edges in the coaxial tap-off, are radiused to ease pulsed heating.

A pair of 3-decibel (dB) coaxial tap-offs has been fabricated, as have been shorting caps which can be used as launchers, two diameter step tapers, a vacuum pump out spool and four 2.44-m sections of the 0.480-m diameter waveguide as shown in *Figure 2.23*. A back-to-back cold test of the tap-offs showed good transmission. High-power tests underway are aimed at resonating the waveguide to achieve field levels equivalent to a 300-MW travelling wave and demonstrating transmission at the 4- to 5-MW level available from our test setup's Thales klystron *[2-42]*. Initial tests with 14.5-pounds-force per square inch gauge (psig) nitrogen pressurisation are being done in the hope that evacuation may not be necessary after all. However, such a conclusion would have to wait until a bend, the likely bottleneck, is so tested.

Figure 2.23 KCS R&D hardware. Left: coaxial tap-off fed through a waveguide T and connected through a taper to the 0.480-m diameter circular waveguide. Right: a four-section 10-m run of the KCS main waveguide.

Local waveguide power distribution system

The RF power extracted from each coaxial tap-off along the linac tunnel is distributed to 26 cavities in three cryomodules (9-8-9, with a quadrupole magnet in the centre cryomodule), constituting an RF unit. The waveguide power distribution system (PDS) through which it flows has evolved since the RDR, as shown in *Figure 2.24*. The three-stub tuner has been eliminated, its dual functions now accomplished by phase shifters with a movable side wall and tunable coaxial fundamental power couplers, both of which are motorised. Feeding properly spaced cavities in pairs through a 3-dB hybrid allows the combined reflected power to be directed to a load on the hybrid's fourth port. Thus the expensive circulators can likely also be eliminated for most cavities. Finally, with the wide range of sustainable ILC cavity gradient limits (±20%) now to be accepted to increase production yield, power efficiency demands we tailor the distribution to the (sorted pairs of) cavities in each RF unit. Thus adjustable coupling from the main WR650 waveguide is included. This latter function can be provided by a novel waveguide component developed at SLAC called the variable tap-off *[2-43]*.

This adjustable directional coupler works by means of mode rotation of a circular TE_{11} mode accomplished via physical rotation of an oval middle section. A PDS incorporating four vertical tap-offs was built and high-power tested for the first cryomodule that will be tested at Fermilab *[2-44]*.

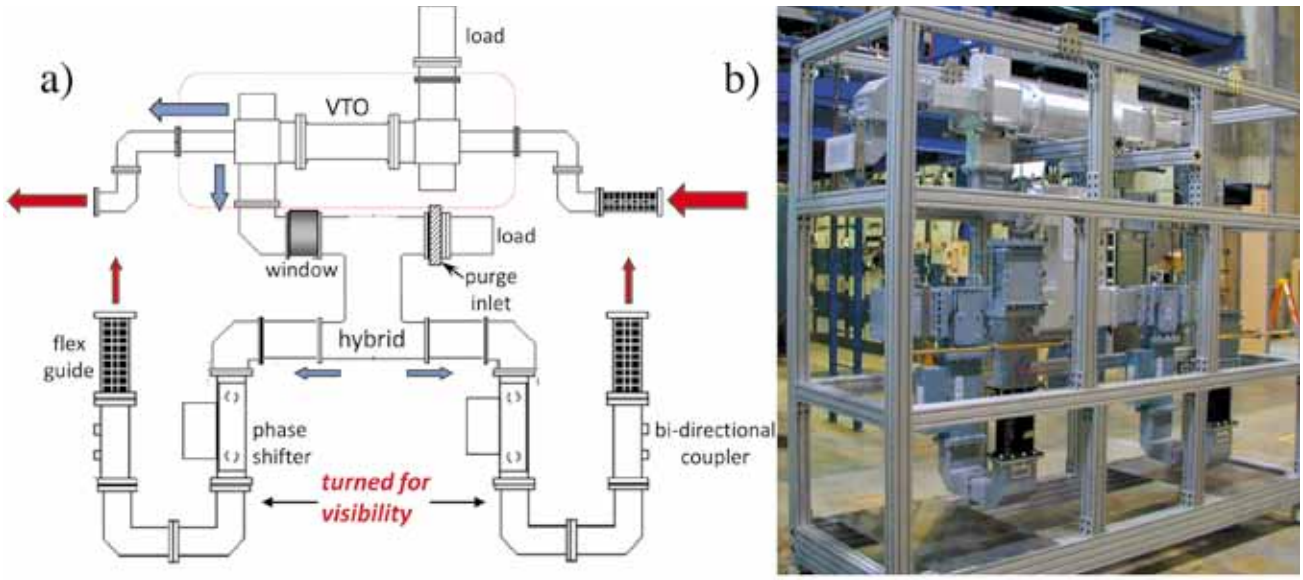

Figure 2.24 Left: updated modular PDS waveguide layout. Power for two cavities at a time is coupled from a main WR650 feed and divided through a hybrid. Reflections from the cavities combine into the hybrid load, allowing elimination of circulators (included after the hybrid in the 3-D view), except for the odd cavity in a nine-cavity cryomodule. Right: one of four PDS modules built and tested at SLAC for the first cryomodule of Fermilab's L-band NML test accelerator.

2.5.2 Distributed RF scheme

Basic concept of DRFS compared with the RDR

The distributed RF scheme (DRFS) was proposed as another possible cost-effective solution for a single main linac tunnel design in the proposal of SB2009 *[2-45]*. The basic concept of DRFS is illustrated in *Figure 2.25*. The salient feature of DRFS is a complete single-tunnel plan with no high-power RF components on the surface, utilising approximately 8,000 small modulating-anode (MA) klystrons of 800-kW output power, driven by DC power supplies and MA modulators. The RF power for two superconducting cavities is fed by a klystron through a rather simple PDS without employing a circulator. By contrast, the RDR presented a two-tunnel plan in which a 10-MW multi-beam klystron feeds power to 26 cavities through a complicated PDS using 26 circulators in RDR RF units comprising three cryomodules.

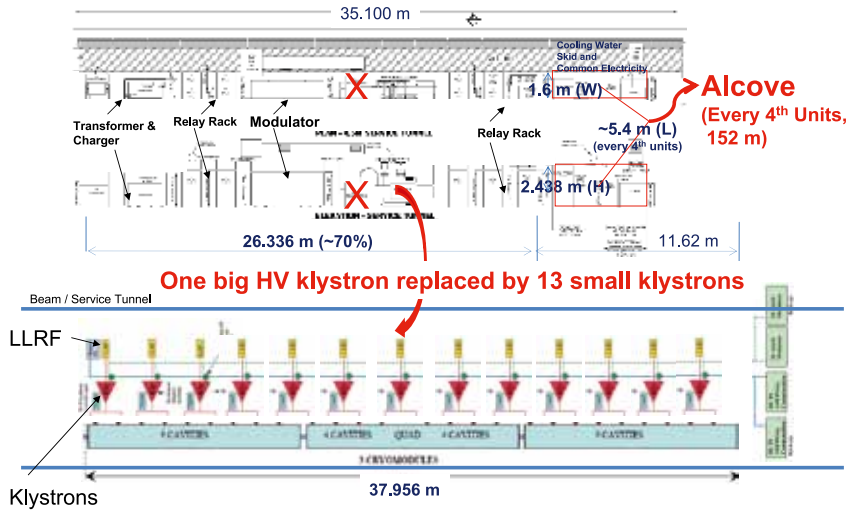

Figure 2.25 Schematic layout of the distributed RF scheme.

The advantage of the DRFS is that it represents a complete single-tunnel plan in which there are no high-power RF facilities on the surface. One klystron feeds power to only two cavities, facilitating optimised cavity performance. In the case of local superconducting cavity failures, it is easy to separate them from the operation, giving DRFS good operability. There is a small probability of big failures that prevent beam operation. There are also concerns about the construction cost, maintainability and heat loss problems, since all heat loads are also in the single underground tunnel (this will be described in a later section). Though it uses mature technology, DRFS is a newly proposed plan. The technical feasibility is being demonstrated in part of the S1-Global programme at KEK.

DRFS configuration in the tunnel

Since DRFS is a complete single-tunnel plan, its configuration strongly depends on the tunnel shape and the layout of cryomodule in the tunnel. If the tunnel cross-section is assumed to be circular, constructed by tunnel boring machine, two configurations are possible: in the first configuration the cryomodule hangs from the ceiling; in the second, the cryomodule is installed on the floor. The current likely configuration of DRFS is based on the latter, which is shown in *Figure 2.26*. The diameter of the tunnel cross-section is 5.7 m. The tunnel is divided into three horizontal regions: a cryomodule region, a passage and maintenance space including egress and a region of high-power RF equipment, separated from the other regions by a radiation shielding wall with access doors. It is shown that all required components, including standby power supply, are in the high-power equipment region. Waveguides of the PDS are laid under the floor. The tunnel is also divided into three regions in the vertical direction and accommodates all required functions, including water supply, ventilation and the space to exhaust an accidental helium leak. It is necessary to investigate this configuration in more detail to assure sufficient working space during installation and maintenance, and this will be done after optimisation of the RF component sizes.

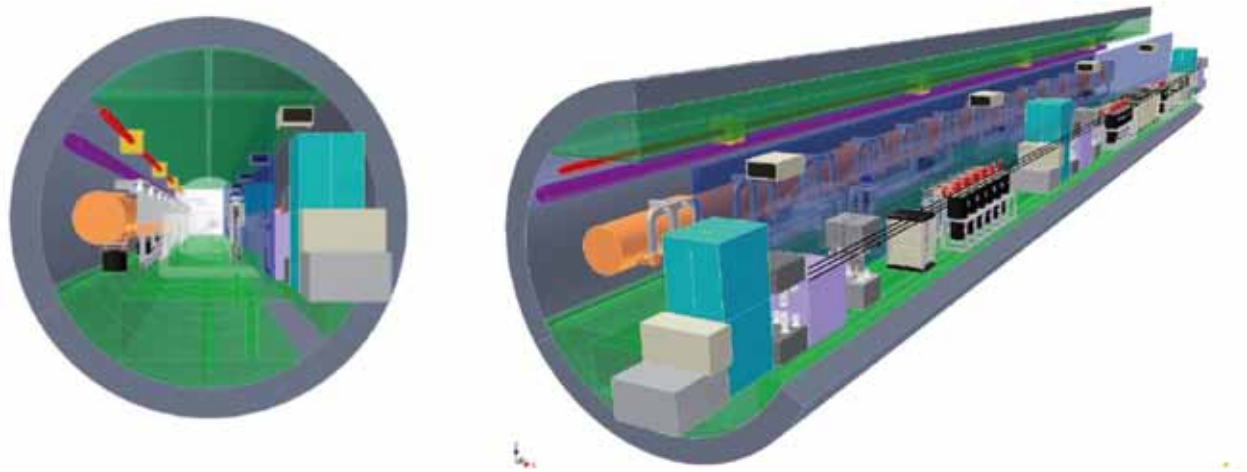

Figure 2.26 DRFS configurations in the tunnel shown in 3-D. Left: cross-section view. Right: three-quarters view.

Operability and availability of DRFS

Since DRFS can control two superconducting-cavity units with low-level RF, operability is better than foreseen in the RDR. Some of the advantages of the DRFS have already been described in an earlier section. Thirteen DRFS klystrons are operated on a common DC power supply and MA modulator, so the required applied high voltage is determined by the maximum power in the unit, if a fixed overhead for low-level RF control is assumed. From superconducting cavity manufacturing, a 20% variation in the accelerating gradient of 31.5 MV/m should be accepted, and in order to achieve an efficient system, sorting of the cavities is inevitable for DRFS. Assuming that 3,400 cavities are manufactured every year in the construction period and that they are sorted in bins with an 8%-range variation of field gradient, the resulting number in a bin is 680. These are sorted in an RDR unit (three cryomodules) with 4% higher power without sacrificing the field gradient. Therefore in DRFS, this kind of cavity sorting is prescribed. In order to achieve high availability in DRFS, we assumed 110,000 hours of mean time before failure for MA klystrons and introduced backup DC power supplies and MA modulators. This configuration is shown in *Figure 2.27*, in consideration of the DC power supply size and cost. In this case, the basic configuration of the DRFS baseline (or the high-current case) includes two regular DC power supplies and MA modulators plus another backup in two RDR units. So far, for other availability and installation issues, the basic scenario is kept to be the same as SB2009, as long as we employ the configuration of *Figure 2.27*.

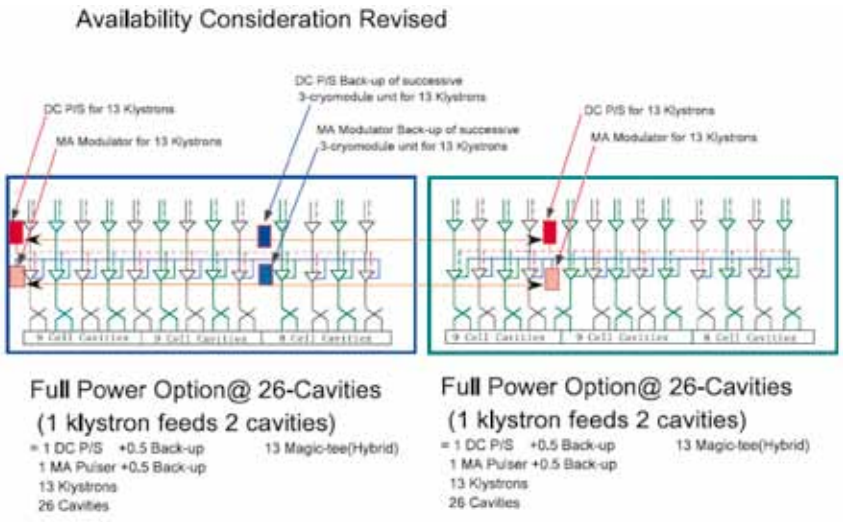

Figure 2.27 Two-RDR-unit system of DRFS in the baseline case is shown. Red boxes represent the DC power supplies. Pink boxes represent modulating-anode modulators for active components. Blue boxes represent the DC power supplies for backup components. Light blue boxes represent the modulating-anode modulator for backup components.

Another important issue for DRFS is radiation. There is a concern about semiconductor damage from the radiation in the high-power RF components. As shown in *Figure 2.27*, DRFS employs a radiation shield wall which has the same shield thickness investigated by DESY; it is planned to investigate the effect more precisely.

R&D status of DRFS

A DRFS demonstration to show feasibility is planned at KEK to extend over three consecutive years. The first demonstration is scheduled at the beginning of 2011. It will employ a two-unit DRFS in the S1-Global project in KEK *[2-46]*. The first prototype DRFS klystrons, a power supply and an MA modulator will be installed and operated to feed power to four cavities. Low-level RF control is a main R&D theme to evaluate the feedback technology when there are no circulators.

Prototype klystrons of DRFS were manufactured in 2010, and factory tests satisfied the required original specification: 750 kW, as shown in the left image of *Figure 2.28*. The output power is increased to 800 kW to accept the gradient variation of 32.5 MV/m ±20%; factory tests cleared this revised specification. Output characteristics of prototype klystrons are shown in the right image of *Figure 2.28*. The results for first klystron are an output power of 813 kW at 64.2 kV with an efficiency of 57.4% for micro-perveance of 1.36 and output power of 806 kW at 67.1 kV with an efficiency of 60.1% for micro-perveance of 1.15. Since the DRFS klystron is an MA klystron, beam perveance can be controlled by the ratio between cathode-to-MA electrode voltage and cathode-to-anode voltage. A prototype power supply and MA modulator have been delivered to KEK and are operated in an acceptance test. All DRFS high-power components were moved near to the cryomodule in the S1-Global tunnel and operated as the demonstration at the end of 2010. The configuration of test arrangement in S1-Global is shown in *Figure 2.29*.

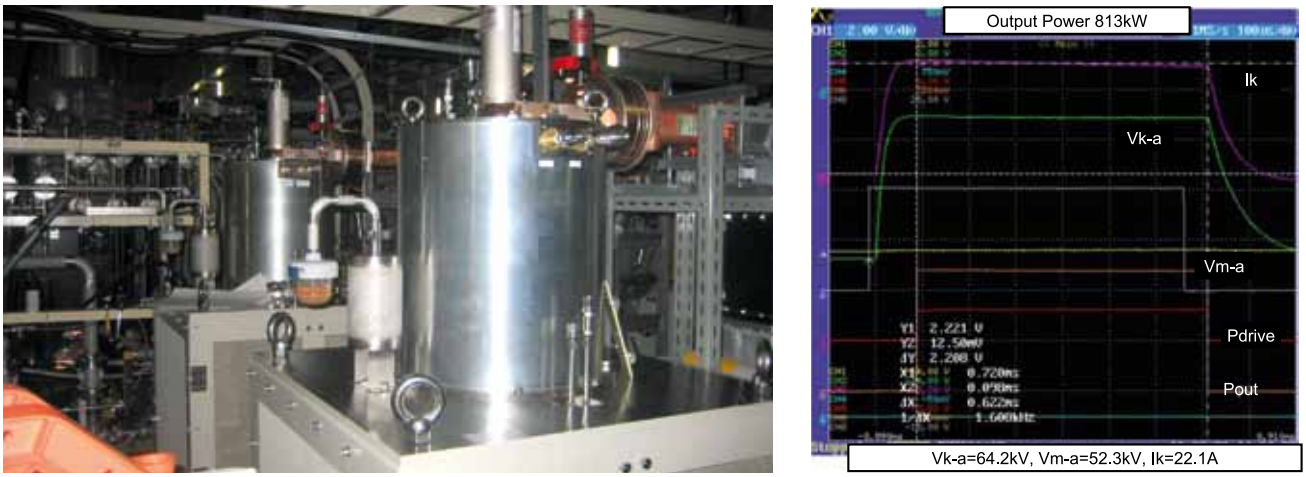

Figure 2.28 Klystrons (left) and waveforms in the test (right).

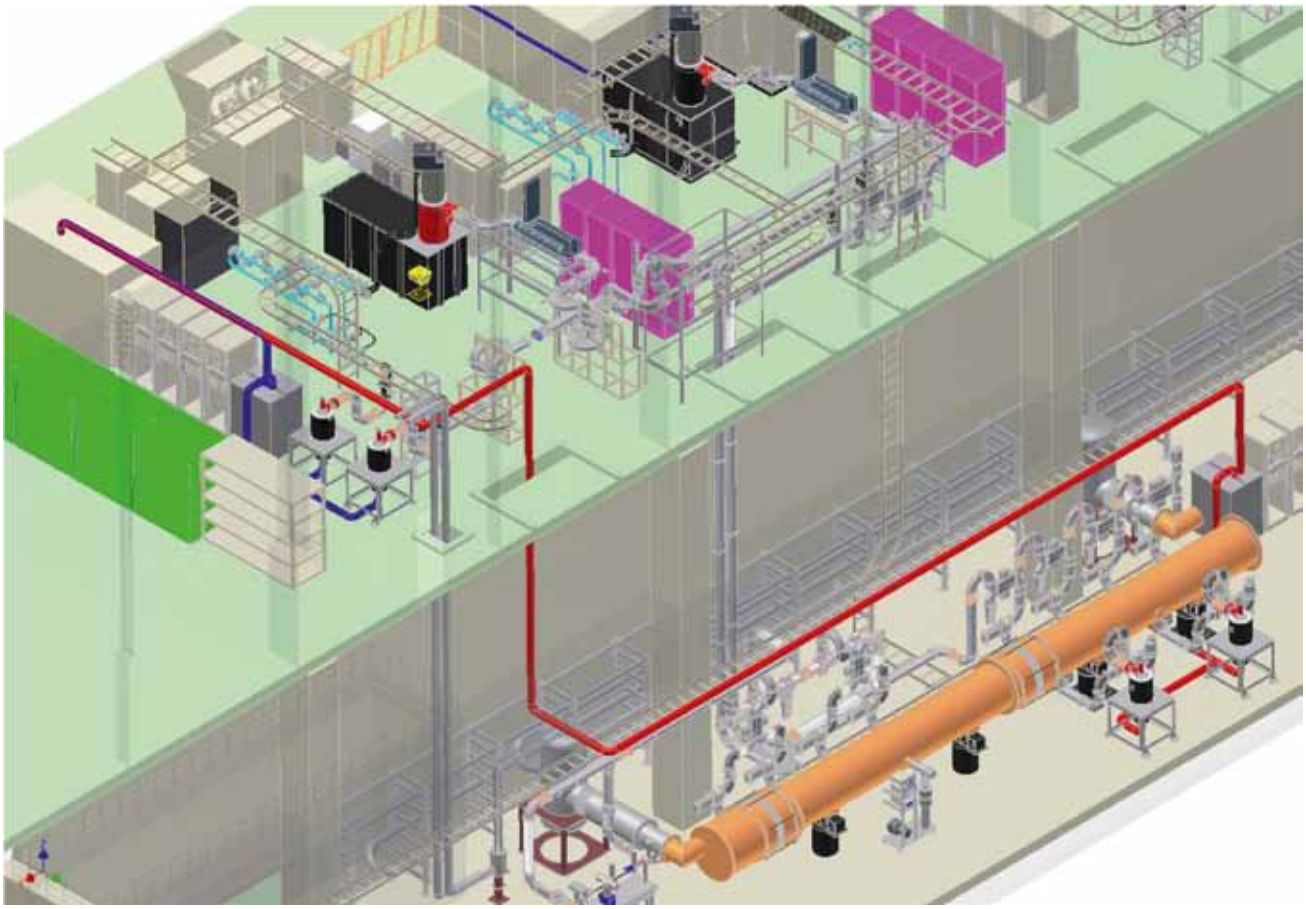

Figure 2.29 Layout of the DRFS test configuration in S1-Global. At first, high-power RF components are tested and evaluated on the first floor with a matched load on the PDS (shown in blue), and then systems are moved near the cryomodule in the tunnel (shown in red).

The second demonstration is a continuation to check the long-term stability by installing one of the above DRFS units in the 'quantum-beam project' at KEK. The third demonstration, planned for the years 2012 to 2013, entails the installation of a four-unit DRFS feeding RF power to eight cavities in the STF phase 2 project at KEK. During these R&D schedule periods, key elements of the DRFS high-power system components will be developed, including spark gap development in the crowbar circuit, high-voltage relay in the DRFS power supply system and permanent magnet R&D for the klystron. Some of this work has been already begun in collaboration with industry. Since the DRFS concept is well established and employed in many projects, we think there are no basic difficulties, but some problems need to be solved for system installation. The purpose of the R&D should be focused in this direction. R&D for cost reduction is another very important issue, and after successful operation, design efforts to reduce the cost of each component are strongly required.

2.5.3 RDR configuration in single tunnel as backup

SB2009 demands a single-tunnel configuration for the ILC main linacs in order to reduce project cost. Because the options described in the preceding two sections are in the R&D stage, a backup plan was put forward in which the equipment of the RDR high-power RF system, which is better studied, is incorporated into the linac tunnel. One possible RDR single-tunnel configuration is almost identical to that of the European XFEL, with pulse transformers, 10-MW multi-beam klystrons and power distribution systems in a single tunnel of a diameter of 5.2 m and modulators on the surface. Another single-tunnel plan for the RDR system has all high-power components in a single tunnel of a diameter of 6.5 m. For a mountainous site, this type of complete single-tunnel plan is preferable. The pros and cons of this latter option are largely shared with DRFS, since both are complete single-tunnel plans.

2.6 System integrations tests

2.6.1 Global progress in cavity and cryomodule string integration and tests

The cavity/cryomodule string integration and cold tests have made global progress in three major facilities of TESLA Technology Collaboration/FLASH at DESY in Europe, the New Muon Laboratory (NML) at Fermilab in the Americas region, and the Superconducting Test Facility (STF) at KEK in Asia *[2-47]*. TTC/FLASH has made much progress with beam acceleration by using a series of cavity/cryomodule strings *[2-48]*. NML construction started in 2007, and the first cryomodule installation and the associated facility was completed in 2010 *[2-49]*. The RF test is being prepared. STF construction start was in 2005, and the first cryomodule test was performed in 2007 without beam. Since spring 2010, the S1-Global cryomodule test has been carried out as a global cooperation programme *[2-50]*. *Table 2.7* summarises progress and plans for these facilities.

Table 2.7 Progress in cavity/cryomodule integration and tests for TTF/FLASH, NML, and STF.

Location	Year	Progress
TTF/ FLASH (DESY)	2005	TTF2/FLASH integration and test started
	2008	ILC 9-mA beam: first beam with 3-mA, 500-ms beam pulses
	2009	Operation with high-power ILC-like beam with 22-kW average power
	2011	Gradient-margin studies with long beam pulses
	2012	Studies of beam operation at the limits of gradient and RF power
NML (Fermilab)	2007	NML first cryomodule integration
	2010	Integration completed and cool-down started
	2012	Planned: NML accelerator system integration to be complete
	2013	Planned: Beam acceleration to start
STF (KEK)	2007	STF S-1: cavity/cryomodule system integration and test
	2010	S1-Global: cryomodule assembly and cold test
	2011	Planned: quantum beam integration and beam test to start
	2012	Planned: STF-2 accelerator system integration to be complete
	2013	Planned: STF-2 beam accelerator to start

2.6.2 Cavity/cryomodule string integration and test at NML, Fermilab

Fermilab is currently constructing the SCRF Test Accelerator at the New Muon Lab as described in section 2.4. The initial primary purpose of NML will be to test superconducting RF accelerating cryomodules for the ILC and for Fermilab's Project X, a proposal for a high-intensity proton source. The unique capability of NML will be to test these modules under conditions of high-intensity electron beams with ILC-like beam parameters. In addition NML incorporates a photo injector, which offers significant tunability and the possibility of generating an electron beam with a brightness comparable to state-of-the-art accelerators. This opens the exciting possibility of also using NML for fundamental beams research and tests of new concepts in beam manipulations and acceleration, instrumentation and the applications of beams.

Building infrastructure – cryogenics, electrical power, RF power, water cooling, electronics racks, shielding – is currently being installed. A single superconducting cavity is currently installed and tested, and a single SCRF cryomodule (type TTF III+) is being cooled down since November 2010. Beamline construction will start in late 2011 and we expect to start delivering beam in late 2012.

The NML injector beamline is shown in *Figure 2.30*. It consists of a 1.3-GHz RF photo-emitted electron gun, followed by two SCRF accelerating cavities, a bunch compressor and beam diagnostics. The primary injector beamline will operate at around 40 MeV and is some 22 m long. It will be capable of producing an ILC-like beam structure with a bunch charge of 3.2 nanocoulombs (nC), a 3-MHz bunch repetition rate, a bunch train length of 1 ms, a 5-Hz bunch train repetition rate, and peak current in excess of 10 kA. The single bunch charge can be well over 20 nC. In addition, there is floor space for two reconfigurable 40-MeV test beamlines for a variety of experiments.

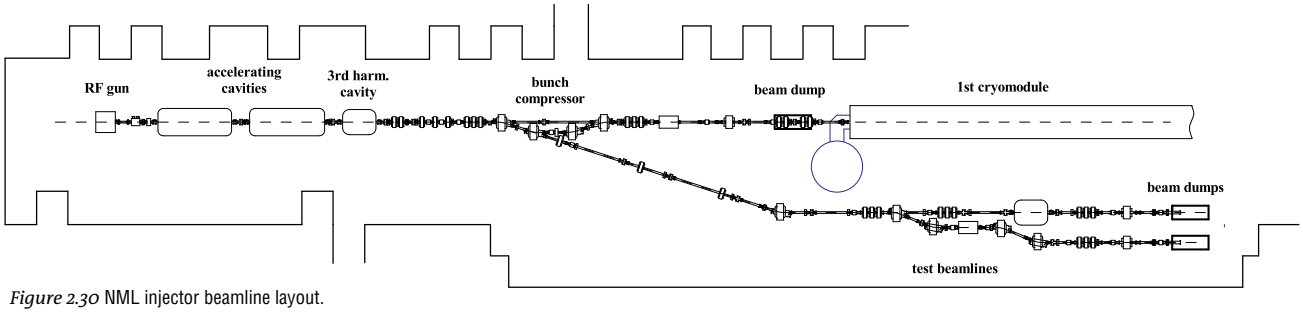

Figure 2.30 NML injector beamline layout.

The acceleration section will initially consist of three ILC-type SCRF cryomodules (a single ILC RF unit powered by a single 10-MW klystron) capable of accelerating beam to around 750 MeV. A building expansion, almost completed, will allow for a total of up to six cryomodules and up to 1,500 MeV of beam energy. A plan for the high-energy downstream beamlines is shown in *Figure 2.31.* There will be floor space and infrastructure available for up to three high-energy test beamlines (18 to 34 m in length) and a storage ring up to 10 m in diameter. High-energy beam dumps are being designed to absorb the 75 kW of beam power.

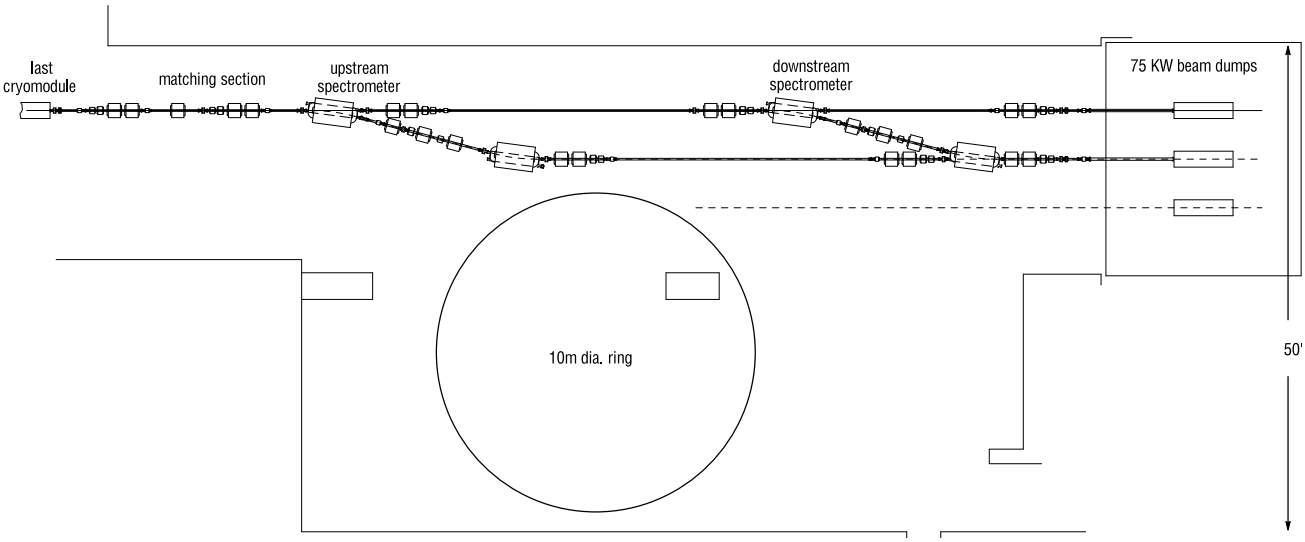

Figure 2.31 High-energy beamline layout at NML.

In summary, in addition to providing realistic tests of a new generation of RF cryomodules, the new NML facility offers excellent opportunities to advance ILC system integration tests, as well as accelerator science and technology on several fronts. Eventually, NML will become a truly open user facility with unique capabilities to advance accelerator research by groups from various institutions, to enhance accelerator education and to promote accelerator technology development for industrial applications.

2.6.3 Cavity/cryomodule integration and string test at KEK's STF

ILC cryomodule development, test and accelerator integration activities are done in STF at KEK. An accelerator tunnel of 100 m length is used for cryomodule test and system integration. The three high-power RF power stations and the cryogenics plant for the cryomodule are located in the nearby surface building, which measures 60 m by 30 m.

STF-1 Cavity/cryomodule test

The STF phase 1 test cryomodule consists of two 6-m horizontal cryostat units of half the length of the ILC design. Each of them can accommodate four cavities. The type-A cryomodule is designed to accommodate TESLA-like cavities, and the type-B cryomodule is for low-loss cavities *[2-51]*. A cool-down test was carried out for the TESLA-like cavities in Cryomodule-A and one low-loss cavity in Cryomodule-B in early 2008. Another cool-down test using four TESLA-like cavities in Cryomodule A followed in 2008. One cavity out of the four reached 31.5 MV/m, the nominal ILC operational gradient. The other three stayed around 20 MV/m. A study of Lorentz force detuning measurement and compensation was made, and the stabilisation of field amplitude and phase of cavities was demonstrated by digital feedback control using piezo actuator Lorentz force detuning compensation. An amplitude and phase stability of 0.04% root mean squared (rms) and 0.02-degree rms, respectively, was demonstrated. This stability performance is well within the ILC specification. Several tests of low-level RF and power distribution were performed, including simulated beam loading signal mixture, special filtering techniques and intermediate-frequency-mixture analogue-to-digital converter detection, as well as loaded Q-value control using waveguide shorts and phase shifters.

S1-Global cavity/cryomodule test

The primary goal of the S1-Global programme is the 'realisation of an average accelerating gradient of 31.5 MV/m with eight cavities' in the S1-Global cryomodule, which is composed of components contributed by the different collaborating partners *[2-47, 52]*.

The general plan for the S1-Global programme is summarised in *Table 2.8*. The S1-Global cryomodule consists of two 6-m cryomodules, Cryomodule-A and Cryomodule-C, shown in *Figure 2.32*. Four cavities from Fermilab and DESY are installed in Cryomodule-C, and four cavities in two different kinds of cavity jackets developed by KEK are installed in Cryomodule-A. The parameters of the two 6-m cryomodules are listed in *Table 2.8*. The contributions of the participating laboratories demonstrate the collaborative framework of S1-Global:

- DESY: two TESLA-type cavities including Saclay-type tuners and power couplers
- Fermilab: two TESLA-type cavities, power couplers and integration of the INFN blade tuners in the cavity packages
- KEK: four TESLA-like cavities, with two variations of tuner/jacket design, Cryomodule-A for KEK cavities, power distribution for Cryomodule-A, and infrastructure for tests
- INFN: design and construction Cryomodule-C in cooperation with KEK, and production of the blade tuners for the Fermilab cavities
- SLAC: two sets of VTO power distribution for Cryomodule-C, and processing of Fermilab couplers

In addition to the main target of demonstrating an average accelerating gradient of 31.5 MV/m with eight cavities during the cryomodule testing, the S1-Global programme has the following R&D goals:

- The operation at an average accelerating gradient of 31.5 MV/m in pulsed RF conditions at 5 Hz with 1-ms flat-top length under stable conditions: 0.07% rms amplitude variation and 0.35-degree rms phase variation
- Experience with the design, assembly and the alignment procedures for different types of cavity packages from participating parties
- The measurement and comparison of the cryogenic performance for each cavity package and cryomodule (in terms of heat loads to the 2-K environment) in the static and high accelerating field dynamic conditions
- The comparative studies of RF performances of the cavity packages (including tuner concepts) from the participating institutes
- Advancement in the implementation of the plug-compatible concept for the ILC activities

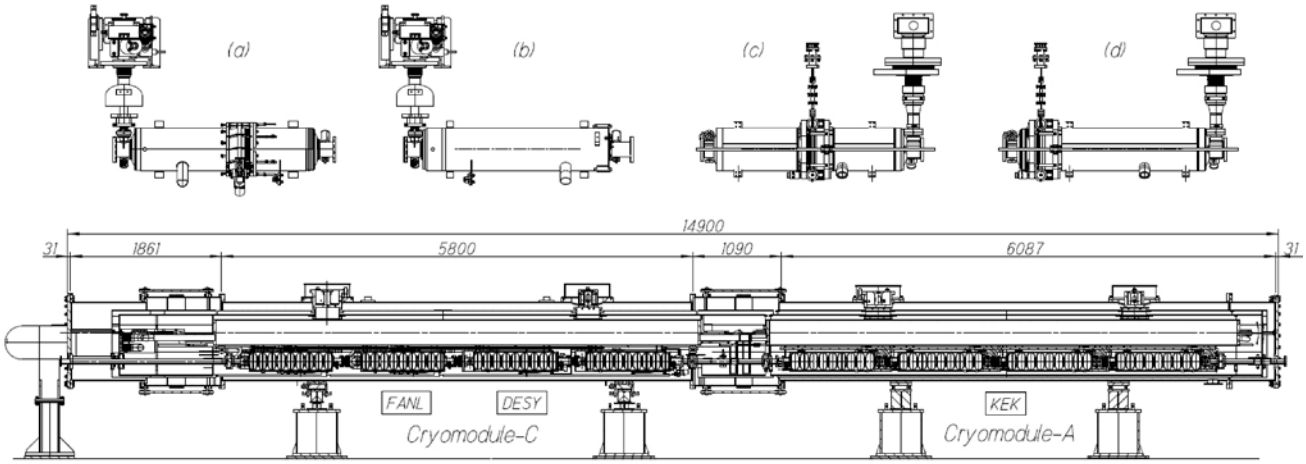

Figure 2.32 S1-Global cryomodule and cavity package of each laboratory. (a) Fermilab cavity with INFN blade tuner. (b) DESY cavity with Saclay-type tuner. (c) KEK-A cavity with slide jack tuner. (d) KEK-B cavity.

Table 2.8 S1-Global cryomodule parameters.

	Cryomodule-A	**Cryomodule-C**
Vacuum vessel length	6,087 mm	5,800 mm
Distance b/w couplers	1,337.0 mm	1,383.6 mm
Cavity package	KEK-A/KEK-B	Fermilab/DESY
Cavity type	TESLA-like	TESLA-type
Tuner type	Slide jack	Blade/CEA
Input coupler type	Disk window	Cylindrical window
Magnetic shield	Inside jacket	Outside jacket
Package length	1,247.6	1,247.4/1,283.4

Figure 2.33 Cooling characteristics of the S1-Global cryomodule with eight cavities in the second cooling test period.

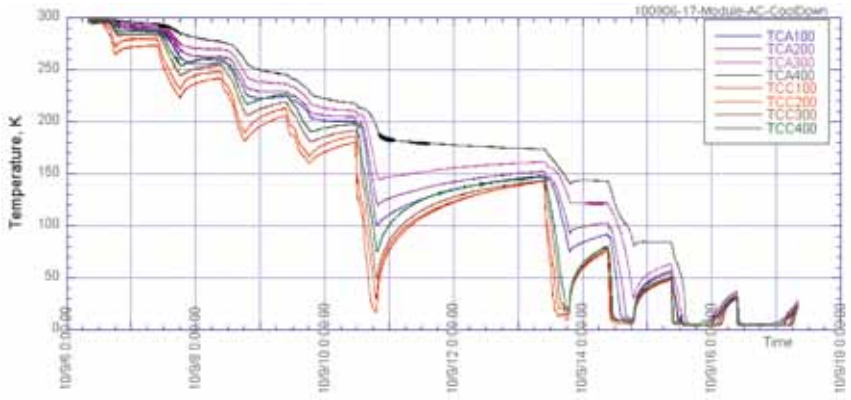

The S1-Global cryomodule has been cooled down to 2 K twice, as shown in *Figure 2.33*, and a series of experiments has progressed. The average maximum gradient of individual cavities was observed to be 27 MV/m, and the maximum gradient average in the seven-cavity string operation was observed to be 26 MV/m, compared to the maximum average gradient in each vertical test of 30 MV/m, as shown in *Figure 2.34*. The Lorentz force detuning characteristics for the four kinds of tuner systems were also measured for each cavity, and a new Lorentz force detuning compensation scheme was tried. The resulting experimental performance is now under analysis. The S1-Global cold test has successfully evaluated thermal performance, tuner performance, cavity high-gradient operation using vector-sum control, as well as Lorentz force detuning compensation, using both the RDR RF scheme and the DRFS system.

Figure 2.34 Cavity performance in the S1-Global cryomodule. Blue bars show the gradient measured for individual cavity in vertical tests. Red bars show the achieved gradient for each individual cavity in the S1-Global cryomodule test. Green bars show the average gradient for the seven-cavity string test in simultaneous RF operation. The average gradient is 30 MV/m, 27 MV/m and 26 MV/m, respectively.

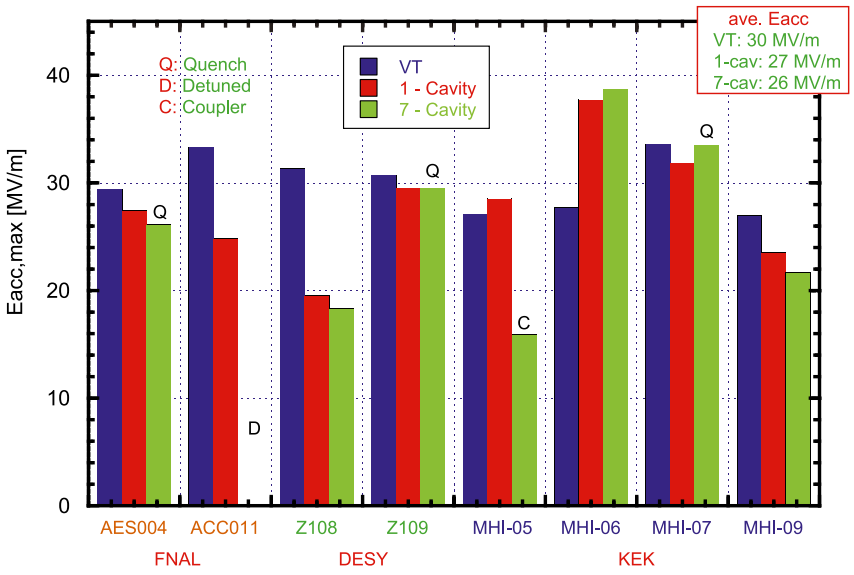

Development plans of STF phase 2

The planned STF phase 2 accelerator is illustrated in *Figure 2.35*. The new power scheme of DRFS, which is proposed for single-tunnel design in a mountainous site, will be demonstrated instead of the RDR power scheme. It consists of two ILC cryomodules driven by nine DRFS klystrons, a photocathode RF gun driven by a 5-MW klystron, and two nine-cell-cavity capture modules driven by a DRFS klystron. The current compact X-ray source development is included in the commissioning of the beam source as a part of the ILC test phase-2 accelerator.

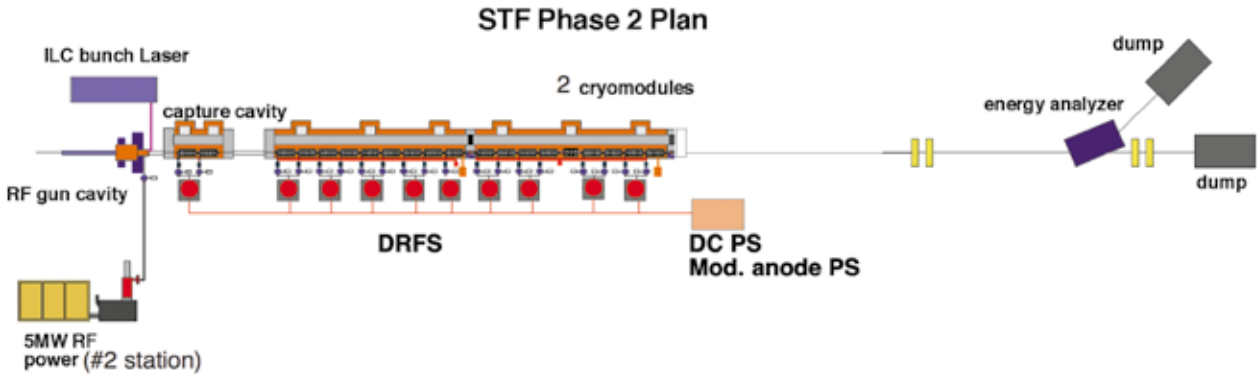

Figure 2.35 General layout of planned STF phase-2 accelerator. The RF gun, the capture cryomodule, two ILC-type cryomodules are aligned. The cavities will be powered by DRFS klystrons, while the RF gun will be powered by a 5-MW klystron. This accelerator is in the STF tunnel, which is 10 m below the STF building.

The production of two cavities for the capture section and nine cavities for the first cryomodule started in 2009 and will be completed in 2011. The beam source development to build the photocathode RF gun system took a major step forward in 2010. The RF gun cavity and the input coupler were fabricated and delivered to STF by the development of the DESY-Fermilab-KEK team through the US-Japan collaboration programme in November 2009. After minor modifications to the cavity water jacket and beam pipe flange, the pumps, solenoid, waveguide, RF window and the Cs2Te photocathode system were assembled into the gun cavity. RF processing of the cavity was performed up to 1.7-MW input without serious problems. The drive laser for the photocathode was also developed and delivered from the Institute of Applied Physics (IAP) in Nizhny Novgorod, Russia and the Joint Institute for Nuclear Research (JINR) in Dubna, Russia. The laser system is a collaborative development between KEK, IAP and JINR, begun in 2007. The laser generates 10-picosecond pulsed UV light (266 nm) with 3-MHz repetition during a 1-ms RF pulse with 5-Hz klystron repetition. The extracted electron charge in one bunch is designed to be 3.2 nC, which is the ILC specification. After finishing the X-ray generation experiment, the first ILC cryomodule will be installed in the STF tunnel by the end of 2012. The second run of the phase-2 accelerator is scheduled from January 2013 to July 2013. Parallel to this, a second cryomodule will be in preparation.

2.6.4 The TTF/FLASH '9-mA' experiment at DESY

The '9-mA' programme was proposed by the GDE in 2008 and subsequently taken up by DESY with a view to performing system tests in support of both the ILC S-2 beam test programme and the European XFEL development. Operationally, the programme is led by DESY, while the scientific programme is coordinated jointly by DESY and the GDE. International participation in the programme, notably from ANL, Fermilab and KEK, has concentrated on low-level RF and accelerator controls *[2-48]*.

The primary goal for TD Phase 1 was to demonstrate reliable operation of the TTF/FLASH linac with ILC-like high-power beams. Other specific goals are:

Long bunch train high beam loading demonstration

- 800-ms pulse: 2,400 bunches at 3 MHz, 3 nC per bunch
- vector sum control of up to 24 cavities
- +/- 0.1% energy stability
- beam energy from 700 to 1,000 MeV

Study operation at the limits

- determining energy stability limitations and trade-offs
- cavity gradient margins and RF power overhead

These goals broadly address linac integration and operation with ILC-like beams. Aside from the primary demonstration of reliable operation under ILC-like conditions, the critical R&D task is to assess operational requirements for gradient-margin and RF-power overhead, which provide direct input to the ILC main linac design parameters. In the following sections we will briefly describe the FLASH facility, results and accomplishments from the two main beam studies periods to date, and give an outlook for future 9-mA studies.

FLASH overview

The TESLA Test Facility at DESY was constructed by the international TESLA collaboration to demonstrate the feasibility of a linear collider based on superconducting accelerating structures of high performance and cost-competitiveness with conventional copper structures. Technical feasibility of superconducting accelerating structures was demonstrated in 2000 when an 800-ms-long 8-mA beam was accelerated through a single cryomodule to 168 MeV.

TTF has subsequently been upgraded several times. In 2005, TTF became FLASH (Free-electron laser in Hamburg), began operation as a free-electron laser (FEL) photon user facility and has since accumulated more than 25,000 hours of accelerator operation. The most recent upgrades in 2009/2010 included raising the maximum operating energy to 1.25 GeV.

The main elements of FLASH before the 2009/2010 upgrades, shown in *Figure 2.36*, are a 5-MeV laser-driven photo-cathode RF gun, two stages of bunch compression, and six cryomodules (ACC1 to ACC6), each containing eight TESLA-type 1.3-GHz superconducting RF cavities. Four klystrons supply RF power to the electron gun, eight cavities in ACC1, 16 cavities in ACC23, and 24 cavities in ACC456, respectively. Low-level RF controllers associated with each klystron regulate the vector sum of the fields in each group of cavities.

The RF unit comprising the 24 cavities in ACC456 is of particular interest for the 9-mA studies because of the close resemblance to the RF configuration in the ILC reference design. In this configuration, the beam energy at the end of the linac can be as high as 1 GeV. Electron bunches are then transported either through a series of undulators for FEL photon generation or through a bypass line, and then are finally transported to a high-power beam dump.

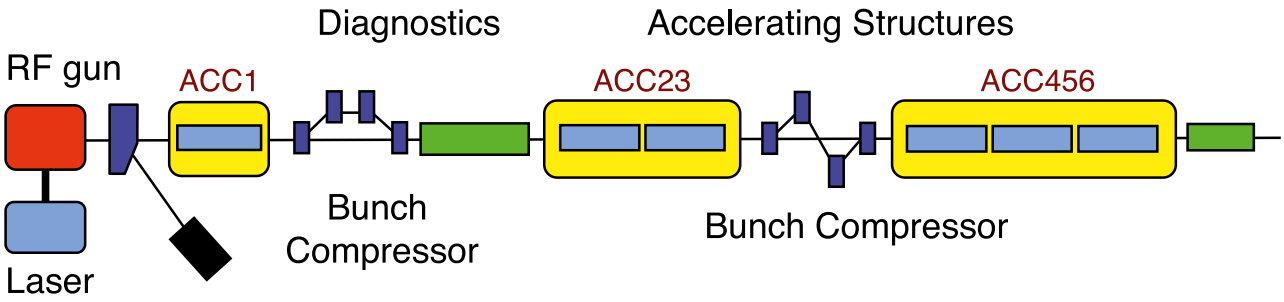

Figure 2.36 FLASH layout (2009).

Design beam parameters for FLASH are quite close to those of the ILC. Both are listed in *Table 2.9* together with design parameters for the European XFEL and performance goals for the 9-mA experiment itself. Even so, achieving these beam parameters is a major challenge for FLASH, since the average power and pulse length are well beyond typical parameters for FEL user operation (less than 30 bunches per pulse and less than 1 nC per bunch).

Extrapolation from the 9-mA experiment to the ILC involves not just beam parameters, but also operating gradients of the superconducting cavities. Gradient limits for the 48 FLASH cavities are shown in *Figure 2.37*. The gradient limits of the 24 cavities in ACC456 range from 23 MV/m to 32 MV/m, with the first four cavities in ACC6 all having gradient limits above 30 MV/m, and hence maximum operating gradients, are comparable to those planned for the ILC.

Parameter	**Design parameters**			**Goal**
	XFEL	ILC	FLASH	9-mA experiment
Bunch charge (nC)	1	3.2	1	3
Bunch repetition rate (MHz)	5	2.7	9	3
Number of bunches	3,250	2,625	7,200	2,400
Pulse length (ms)	650	970	800	800
Average current (mA)	5	9	9	9
Average beam power (kW)			36	36

Table 2.9 XFEL, ILC, and FLASH design parameters, and goals of the 9-mA experiment.

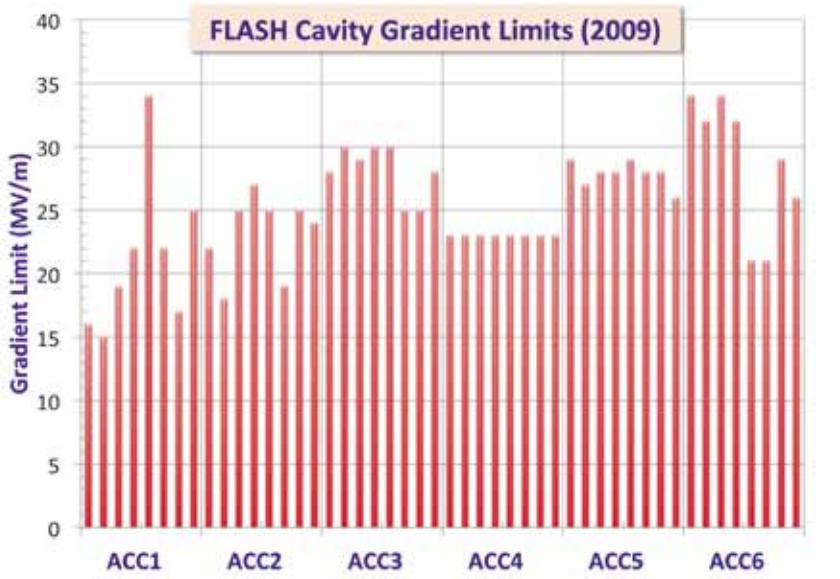

Figure 2.37 FLASH cavity gradient limits (2009).

Beam studies

There have been two periods of dedicated 9-mA studies with high-power beams: 48 hours in September 2008 and a two-week period in September 2009.

In September 2008, the linac operated at a 1-MHz bunch repetition rate with 3 nC per bunch, and pulse lengths of 550 bunches were reached before the studies were cut short by a vacuum event in the final section of the beam transport line. This vacuum event prompted DESY to develop several new diagnostics for monitoring the beam position and monitoring beam spill. Beam position monitors using in-air magnetic loops and diamond/sapphire blades were installed immediately before the beam dump, and four-quadrant beam loss monitors using Cerenkov fibres and ion chambers were installed along the last several metres of the beam transport line. These new diagnostics were installed immediately prior to the two-week 9-mA study period in September 2009. It was during these two weeks of studies that the primary study goal for TD Phase 1 was achieved. Highlights of the studies results and achievements are described in the next section.

Achievements during TD Phase 1

A major milestone was reached during the September 2009 studies when high-power beam operation was demonstrated over a range of beam currents and pulse lengths. The highlighted progress is summarised in *Table 2.10*.

Metric	Goal	Achieved
Bunches per pulse	800 x 3 nC (1 MHz)	800 x 3 nC
	2,400 x 3 nC (3 MHz)	1,800 x 3 nC 2,100 x 2.5 nC ~2,400 x 2 nC
Charge per pulse	7,200 nC @ 3 MHz	5,400 nC @ 3 MHz
Beam power	36 kW (7,200 nC, 5 Hz, 1 GeV)	22 kW (5,400 nC, 5 Hz, 800 MeV)

Table 2.10 Goals and results achieved in the FLASH 9-mA experiment.

In summary, the following machine parameters were achieved:

- 15 continuous hours of running with 3 mA and 800-µs bunch trains
- Running at around 9 mA with bunch trains of 500 to 600 µs for several hours
- Full pulse length (800 µs, around 2,400 bunches) at around 6 mA for shorter periods
- Energy deviations within long bunch trains: less than 0.5% pulse-pulse at 7 mA
- Energy jitter pulse-pulse with long bunch trains: around 0.13% rms at 7 mA

Reaching and operating the linac with high-power levels was unquestionably challenging, particularly with respect to minimising bunch-by-bunch fractional beam loss and with regard to exception handing. These, however, are operational issues, and are not indicative of any fundamental issues associated with operating a high-power superconducting linac. On the contrary, the test results achieved in September 2009 are considered by the GDE to be sufficient to have demonstrated the feasibility of a high-power superconducting electron linac. The requirement to minimise beam scraping plays into many different operational aspects, since beam scraping can occur from wrong steering, energy changes, beam size and beam stabilisation.

Energy stability

The beam energy must be stabilised over two timescales: long-term pulse-to-pulse stability over minutes and hours and energy deviations within a bunch train. Representative measurements of energy stability over both timescales are summarised above.

The main challenge for stabilising energy deviations within the bunch train is the compensation of transients from beam loading and Lorentz force detuning, which are a function of beam current and cavity gradient respectively. Both effects are largely repetitive from pulse to pulse: they can be compensated using ‘iterative learning feed-forward’ to progressively modify the RF power feed-forward drive waveforms to minimise the repetitive transients on the cavity field vector sum. Examples of energy deviations within long bunch trains for 3 mA and for 7.5 mA currents are shown in *Figure 2.38*.

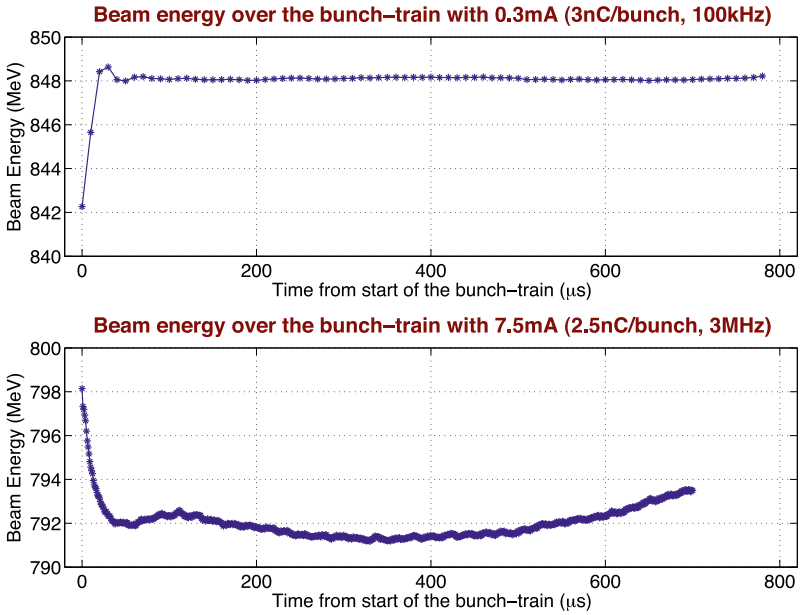

Figure 2.38 Achieved energy stability during bunch train at different currents.

Effects of beam loading

The effect of beam loading on individual cavity gradients can be seen in *Figure 2.39* for 3 mA and 7.5 mA. Although the vector sums are flat, the individual cavities charge or discharge at a rate that depends on the beam current. These gradient 'tilts' can minimised by tailoring individual cavity forward power ratios and loaded Qs to the operating gradient and beam current. The extent to which this can be accomplished will be a subject of study during TD Phase 2. Examples of energy stability over the bunch train at 3 mA and 7.5 mA are shown in *Figure 2.39*.

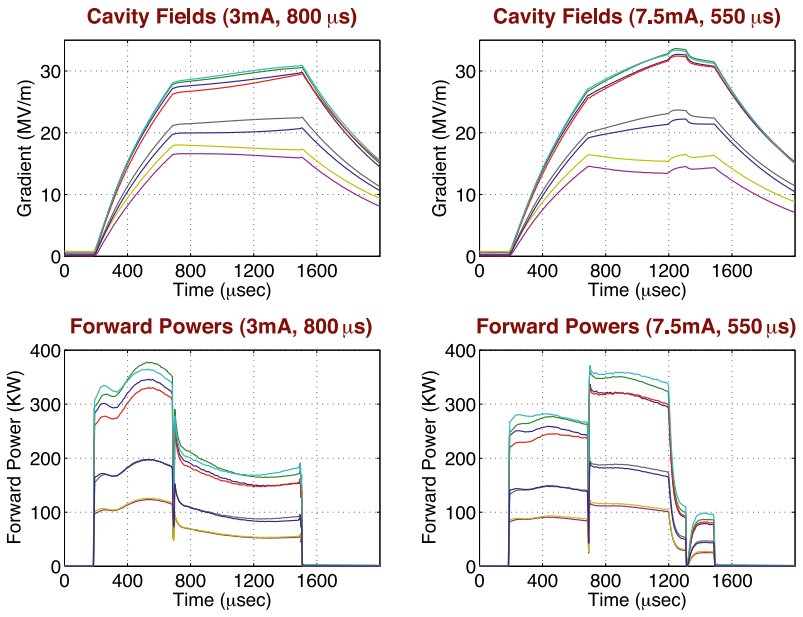

Figure 2.39 Beam loading-induced gradient tilts at different currents.

Outlook

Since September 2009, there have been several major upgrades to the FLASH accelerator to increase the reach and performance of FEL user operation. Upgrades included installation of a seventh cryomodule to raise the maximum energy to 1.25 GeV and a third-harmonic cavity in the injector to linearise bunch compression and increase the peak bunch current. Significant upgrades have also been made to the low-level RF systems, with the introduction of fast beam-based feedback during the bunch trains, improvements in pulse-to-pulse learning feed-forward and beam loading compensation, and expansion of exception handling. The 9-mA studies will reap substantial benefit from these upgrades and the resulting performance improvements, such as the more than ten-fold reduction in rms energy jitter as shown in *Figure 2.40*.

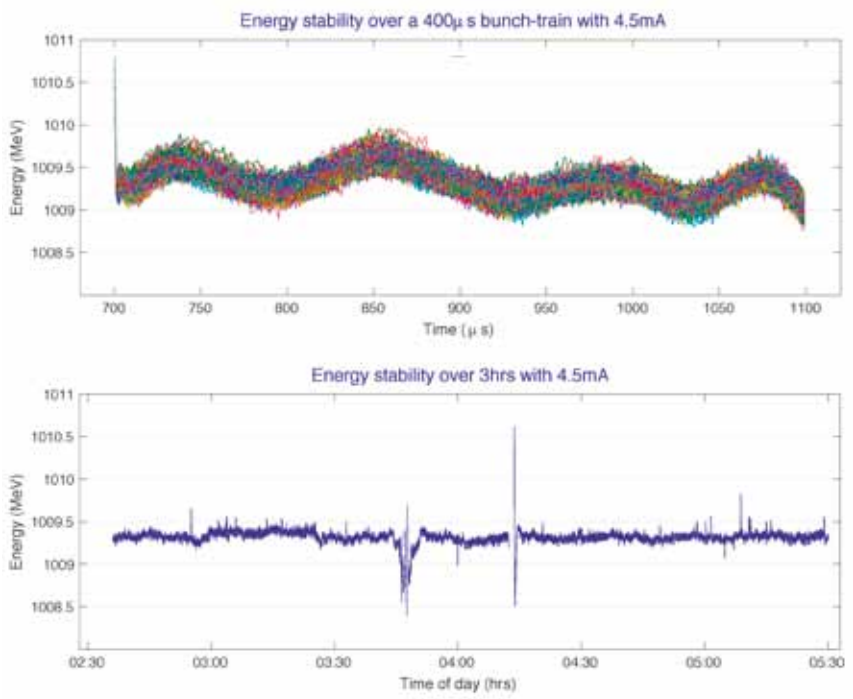

Figure 2.40 Energy stability during February 2011 studies.

During TD Phase 2, 9-mA studies will shift emphasis from demonstrating feasibility of operations to studying 'operation at the limits,' such as required gradient margins and RF power overhead. Key issues will be tight control of beam-loading-induced gradient tilts, accurate compensation of Lorentz force detuning using fast piezo tuners, and tight control of beam loading-induced transients.

In summary, accomplishments during TD Phase 1 have demonstrated reliable operation of the FLASH linac with high power ILC-like beams, and hence the primary 9-mA experiment goals for TD Phase 1 have been achieved. Future 9-mA studies will be directed towards characterising operation with these high-power beams, and in particular, to assess the minimum gradient margin and RF power overhead required for reliable operation of the ILC.

References

[2-1] ILC-GDE Technical Design Phase R&D Plan (Rel. 5, 2010): http://ilcdoc.linearcollider.org/record/15442

[2-2] A. Yamamoto for the ILC-GDE SCRF collaboration, "Global R&D effort for the ILC SCRF LINAC Technology," Proc. EPAC-08, Genova, (2008).

[2-3] A. Yamamoto for the ILC-GDE SCRF collaboration, "Superconducting RF cavity development for the International Linear Collider," IEEE Trans. Appl. Supercond. 19 No. 3, p. 138 (2009).

[2-4] ITRP report: (2004). http://www.fnal.gov/directorate/icfa/ITRP_Report_Final.pdf

[2-5] TESLA TDR edited by F. Richard et al. (2001): http://flash.desy.de/tesla/tesla_documentation/#e1509

[2-6] J. Wiener et al., TTC Report 2008-2 (2008).

[2-7] G. Ciovati et al., TTC Report 2008-5 (2008): http://flash.desy.de/reports_publications/tesla_reports/tesla_reports_2008/

[2-8] A. Yamamoto, presented at the1st Baseline Assessment Workshop (BAW1): http://ilcagenda.linearcollider.org/conferenceOtherViews.py?view=standard&confId=4593

[2-9] H. Hayano, "Asian Region Laboratory Plans," presented at the Superconducting RF Cavity Technology and Industrialization Workshop (A Satellite Workshop at IPAC-10, Kyoto, 2010): http://ilcagenda.linearcollider.org/conferenceDisplay.py?confId=4530

[2-10] K. Ueno et al., "Development of electro-polishing facility in KEK," Proc. of 5th Japanese Accelerator Society meeting (2008).

[2-11] Y. Yamamoto et al., "Summary of results and development of online monitor for T-mapping/X-ray-mapping in KEK-STF," Proc. IPAC-10, Kyoto (2010).

[2-12] Y. Iwashita et al., Phs. Rev. ST Accel. Beam, 11, 093501 (2008).

[2-13] K. Watanabe et al., "Repair techniques of superconducting cavity for improvement cavity performance at KEK-STF," Proc. IPAC-10, Kyoto.

[2-14] R. Kephart, "American Region Laboratory Plans," presented at the Superconducting RF Cavity Technology and Industrialization Workshop (A Satellite Workshop at IPAC-10, Kyoto, 2010): http://ilcagenda.linearcollider.org/conferenceDisplay.py?confId=4530

[2-15] J. Ozelis, "Initial Results from Fermilab's Vertical Test Stand for SCRF Cavities," Proc. 13th International Workshop on RF Superconductivity (SRF2007), Beijing (2007).

[2-16] A. Hocker et al., "Commissioning and early operating experience with the Fermilab horizontal test facility," Proc. 13th International Workshop on RF Superconductivity (SRF2007), Beijing (2007).

[2-17] R. Carcagno et al., "Control System Design for Automatic Cavity Tuning Machines," Proc. 2009 Particle Accelerator Conference, Vancouver (2009).

[2-18] Jan-Hendrik Thie et al., "Mechanical Design of Automatic Cavity Tuning Machines," Proc. 14th International Workshop on RF Superconductivity (SRF2009), Berlin (2009).

[2-19] D. Reschke et al., "Preparatory Procedure and Equipment for the European X-ray Free Electron Laser Cavity Implementation," Phys. Rev. ST Accel. Beams 13, 071001 (2010).

[2-20] T. Arkan et al., "Superconducting RF Cryomodule Production and Testing at Fermilab," Proc. XXV Linear Accelerator Conference (LINAC10), Tsukuba, Japan, 2010.

[2-21] C.M. Ginsburg, M.P. Kelly et al., "Superconducting RF Cavity Production Processing and Testing at Fermilab," Proc. XXV Linear Accelerator Conference (LINAC10), Tsukuba (2010).

[2-22] A. Rowe, "ANL/Fermilab SCPF EP/HPR Processing Status and Plans," Linear Collider Forum of the Americas, (2009).

[2-23] M. Kelly et al., "Surface Processing Facilities for Superconducting RF Cavities at ANL," LINAC-08 (2008).

[2-24] O. Napoli, "E-XFEL cryomodule production plan and model," presented at the Superconducting RF Cavity Technology and Industrialization Workshop (A Satellite Workshop at IPAC-10, Kyoto, 2010): http://ilcagenda.linearcollider.org/conferenceDisplay.py?confId=4530

[2-25] L. Lilje, "R&D in RF superconductivity to support the International Linear Collider," Proc. PAC-08, Albuquerque, p. 2559 (2007).

[2-26] See an appendix of the TTC Report 2008-05, "ILC R&D Board Task Force on high gradient (S0/S1)," (2006).

[2-27] R. Geng "Long-term cavity R&D overview," presented at Int. Workshop on Linear Collider 2010, IWLC2010, Acc-WG3, 10-10-21, Geneve (2010).

[2-28] See *ILC Newsline,* http://www.linearcollider.org/newsline/readmore_20091029_ftr1.html

[2-29] C. Ginsburg and A. Yamamoto presented at Int. Workshop on Linear Collider 2010, IWLC2010, Acc-WG3, 21 October 2010: http://ilcagenda.linearcollider.org/conferenceOtherViews.py?view=standard&confId=4507

[2-30] K. Saito et al., "Gradient yield improvement efforts for single and multi-cells and progress for very high gradient cavities," SCRF-07, Beijing, TU202 (2007).

[2-31] R. Geng, "Review for new shapes for high gradients," Physica C 441 p. 145 (2006).

[2-32] N. Ohuchi, et al, LINAC10, Tsukuba, September 2010, MO302, http://jacow.org

[2-33] N. Ohuchi, et al., EPAC08, Genoa, June 2008, MOPP144, p. 892 (2008), http://jacow.org

[2-34] http://www.xfel.eu

[2-35] N. Phinney, et al., ILC RDR Accel., ILC-Report-2007-001, p.III-171, (2007): http://ilcdoc.linearcollider.org/record/6321/files/ILC_RDR_Volume_3-Accelerator.pdf?version=4

[2-36] C. Pagani, et al., "TESLA Cryogenic Accelerator Modules," TESLA Report 2001-36.

[2-37] T. Peterson, "Cryomodule Thermal Intercept Optimization Strategy," TILC08-Sendai, March 3-6, Sendai, 2008: http://ilcagenda.linearcollider.org/conferenceOtherViews.py?view=standard&confId=3154

[2-38] Reference Design Report, Accelerator, ILC-Report-2007-001, 2007: http://lcdev.kek.jp/RDR/RDRall.pdf

[2-39] Christopher Nantista and Chris Adolphsen, "Klystron Cluster Scheme for ILC High Power RF Distribution," presented at the 2009 Particle Accelerator Conference (PAC09), Vancouver (2009); SLAC-PUB-13696.

[2-40] C. Burkhart, et al., "ILC Marx Modulator Development Program Status," presented at the 1st International Particle Accelerator Conference (IPAC10), Kyoto, (2010).

[2-41] M.A. Kemp, et al., "Status Update on the Second-Generation ILC Marx Modulator Prototype," IEEE Power Modulator Conference, Atlanta, (2010).

[2-42] Chris Adolphsen, "ILC RF System R&D," presented at the 1st International Particle Accelerator Conference (IPAC10), Kyoto, Japan, May 23-28, 2010.

[2-43] Christopher D. Nantista and Chris Adolphsen, "A Variable Directional Coupler for an Alternate ILC High-Power RF Distribution Scheme," presented at the 2006 Linear Accel. Conf. (LINAC06), Knoxville,(2006); SLAC-PUB-12372.

[2-44] Christopher Nantista et al., "Progress in L-Band Power Distribution System R&D at SLAC," presented at the XXIV Linear Accelerator Conference (LINAC08), Victoria, (2008); SLAC-PUB-13438.

[2-45] S. Fukuda, "DRFS design and R&D status, and Installation strategy," presented at the 1st Baseline Assessment Workshop (BAW-1), KEK, Tsukuba (2010): http://ilcagenda.linearcollider.org/conferenceOtherViews.py?view=standard&confId=4593
[2-46] S. Fukuda, "DRFS test preparation for S1-Global," presented at Int. Workshop on Linear Collider, IWLC2010, Geneva, (2010): http://ilcagenda.linearcollider.org/conferenceOtherViews.py?view=standard&confId=4507
[2-47] A. Yamamoto, "ILC SCRF Update," presented at the Int. Workshop on Linear Collider, Geneva, (2010): http://ilcagenda.linearcollider.org/conferenceOtherViews.py?view=standard&confId=4507
[2-48] N. Walker, et al, "Operation of the FLASH Linac with Long Bunch Trains and High Average Current," (PAC 2009): http://accelconf.web.cern.ch/AccelConf/PAC2009/papers/we6pfp109.pdf
[2-49] R. Kephart, "American Region Laboratory Plans," presented at the Superconducting RF Cavity Technology and Industrialization Workshop (A Satellite Workshop at IPAC-10, Kyoto, 2010): http://ilcagenda.linearcollider.org/conferenceDisplay.py?confId=4530
[2-50] H. Hayano, "Asian Region Laboratory Plans," presented at the Superconducting RF Cavity Technology and Industrialization Workshop (A Satellite Workshop at IPAC-10, Kyoto, 2010): http://ilcagenda.linearcollider.org/conferenceDisplay.py?confId=4530.
[2-51] STF group, "STF Phase-1 Activity Report," KEK Report 2009-3, April 2009:
[2-52] N. Ohuchi, et al, "S1-Global collaborative efforts 8-cavity-cryomodule: 2 Fermilab, 2 DESY and 4 KEK," Proceedings of LINAC 10, Tsukuba, Japan, 2010.

03

ACCELERATOR SYSTEM R&D

3.1 The electron cloud R&D programme at CesrTA and other laboratories

3.1.1 Introduction

One of the principal R&D issues for the positron damping ring of the ILC is to ensure that the build-up of the electron cloud in the vacuum chambers can be kept below the levels at which electron cloud-induced emittance growth and beam instabilities occur. During Phase I (2008-2010) of the ILC Technical Design Phase (TDP) a focused effort to study methods of suppressing the electron cloud as well as measuring its impact on ultra-low emittance beams was undertaken at the Cornell Electron-Positron Storage Ring Test Accelerator (CesrTA). In addition, work has also been underway at various laboratories around the world to develop better techniques to mitigate the build-up of the electron cloud. Section 3.1.2 describes the research effort being carried out at Cornell University with the CesrTA collaboration *[3-1, 2]*, while section 3.1.3 describes the work that is in progress at various other laboratories around the world. As part of this coordinated global programme, a major emphasis has been placed on developing and benchmarking simulation tools as well as measurement techniques. In October 2010, the ECLOUD10 Workshop was held at Cornell University *[3-3]*. The workshop presentations provide a comprehensive overview of the recent activities.

In order to incorporate the research results into the ILC damping ring design, an ECLOUD Working Group has been formed whose main objective is to provide recommendations on the electron cloud mitigation techniques to apply to the damping ring design based on the results of the R&D programme *[3-4, 5]*. This objective has recently been achieved in a dedicated Working Group meeting *[3-6]* during the ECLOUD10 Workshop, with a significant level of participation by the experts attending the workshop. The preliminary recommendations are summarised in section 3.1.4.

3.1.2 The CesrTA R&D programme

The CesrTA research programme was approved in late 2007 to carry out electron cloud R&D in support of the ILC technical design. The first dedicated experiments using the Cornell Electron-Positron Storage Ring (CESR) began in March 2008 at the conclusion of 28 years of colliding beam operations for the CLEO experiment *[3-7]*. Two principal goals were specified for the programme. The first was to characterise the build-up of the electron cloud in each of the key magnetic field regions of the accelerator, particularly in the dipoles and wigglers, and to study the most effective methods of suppressing it in each of these regions. This required the design and installation of detectors to study the local build-up of the cloud in each of these environments as well as a supporting simulation programme to fully characterise and understand the results. The second goal was to study the impact of the electron cloud on ultra-low emittance beams. The ILC damping ring design targets a geometric vertical emittance of 2 picometre radians (pm·rad); no positron ring has been operated in this emittance regime. By benchmarking electron cloud instability and emittance growth simulations in a regime closer to that specified for the damping ring, confidence in projections of the final damping ring performance can be significantly improved. This in turn will determine whether further R&D is required to achieve the necessary design specifications.

In order to carry out these measurements, CESR had to be reconfigured as a damping ring and upgraded with the necessary beam instrumentation for low-emittance optics correction and characterisation of the resulting beams.

Conversion of CESR to a damping ring test accelerator configuration

Modification of CESR into a damping ring configuration involved three main thrusts:

1. Relocation of six of the twelve CESR-c damping wigglers *[3-8, 9]* to the Lo straight section to enable ultra-low emittance CesrTA operation *[3-7]*.
2. Upgraded beam instrumentation to achieve and characterise ultra-low emittance beams. This included deployment of a high-resolution beam position monitoring system *[3-10]* and X-ray beam-size monitors for both positron and electron beams *[3-11]*.
3. Addition of vacuum system diagnostics for characterisation of local electron cloud growth in a range of vacuum chambers. Local electron cloud diagnostics include retarding field analysers *[3-12, 13]*, transverse-electric-wave transmission hardware *[3-14]* and shielded pickups for time-resolved measurements *[3-15]*

Table 3.1 shows the CesrTA lattice parameters for operation at 2 and 5 gigaelectronvolts (GeV). At 2 GeV, 90% of the synchrotron radiation power is provided by the twelve damping wigglers and a horizontal emittance of 2.6 nanometre radians (nm·rad) is obtained *[3-16]*. During Phase I of the CesrTA programme, a vertical emittance target of less than 20 pm·rad (ten times the ILC damping ring vertical emittance target) was specified. A key element of the R&D programme is the flexibility of CESR operation. CESR allows operation between 1.8 and 5.3 GeV with both positron and electron beams. The ability to operate over a wide range of energies, bunch spacings and bunch intensities enables systematic studies of primary photoelectron and secondary electron contributions to electron cloud build-up in the vacuum chambers, which are not feasible at any other facility.

Table 3.1 2-GeV and 5-GeV lattice parameters for CesrTA.

Energy		**GeV**	**2.085**	**5.0**
Number of wigglers			12	6
Wiggler field		T	1.9	1.9
Horizontal tune	Q_x		14.57	
Vertical tune	Q_y		9.6	
Longitudinal tune	Q_z		0.075	0.043
RF voltage	V_{RF}	MV	8.1	8
Horizontal emittance	ε_x	nm·rad	2.6	35
Damping time constant	$\tau_{x,y}$	ms	57	20
Momentum compaction	α_p		6.76×10^{-3}	6.23×10^{-3}
Bunch length	σ_l	mm	9.2	15.6
Relative energy spread	σ_E/E		0.81%	0.93%
Bunch spacing	t_b	ns	≥4, steps of 2	

A novel element of the CesrTA upgrade has been the development of a high-resolution X-ray beam size monitor capable of single-pass measurements of each bunch in a train. *Figure 3.1* shows one of the indium-gallium-arsenide detectors wire-bonded to its circuit board along with a single-pass fit of data acquired using pinhole imaging with a 1-milliamp (mA) bunch. In addition to pinhole imaging, coded aperture and Fresnel zone plate optics have also been installed in both the positron and electron beam lines. These detectors are our principal tools for verifying the vertical beam size in the ultra-low emittance machine optics.

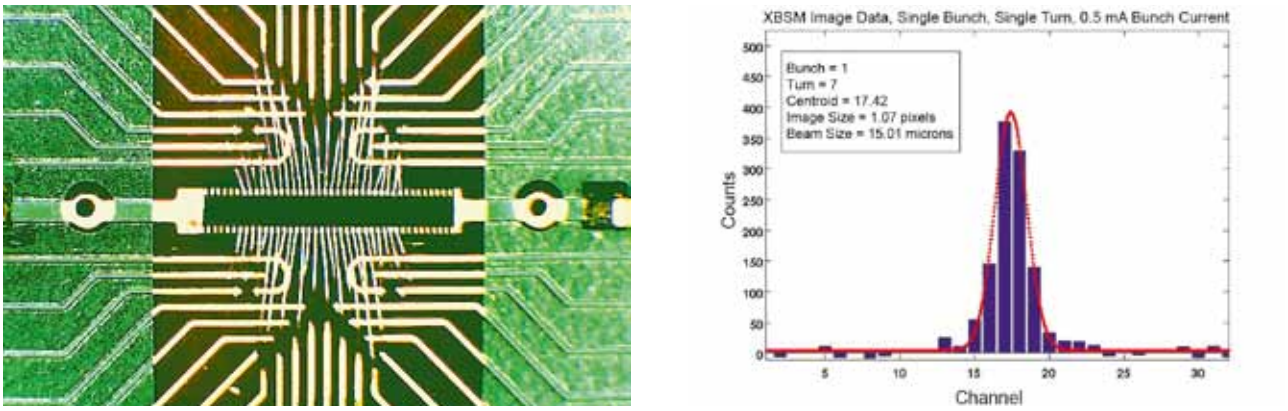

Figure 3.1 Left: an X-ray beam size monitor detector, an indium-gallium-arsenide diode array, mounted on its circuit board. 32 diodes of 400-micrometre width and 50-micrometre pitch are utilised in each detector. Right: a single-turn fit to data acquired from a bunch with 0.8×10^{10} particles (at 2.1-GeV beam energy) using a heavy-metal slit as the X-ray imaging optic.

Figure 3.2 shows the layout of the L0 straight section after installation of the wiggler string. This region is one of four dedicated CesrTA electron cloud experimental areas. It is equipped with extensive diagnostics to study the growth and mitigation of the electron cloud in wigglers. A second electron cloud experimental region was installed on the opposite side of CESR in the L3 straight section.

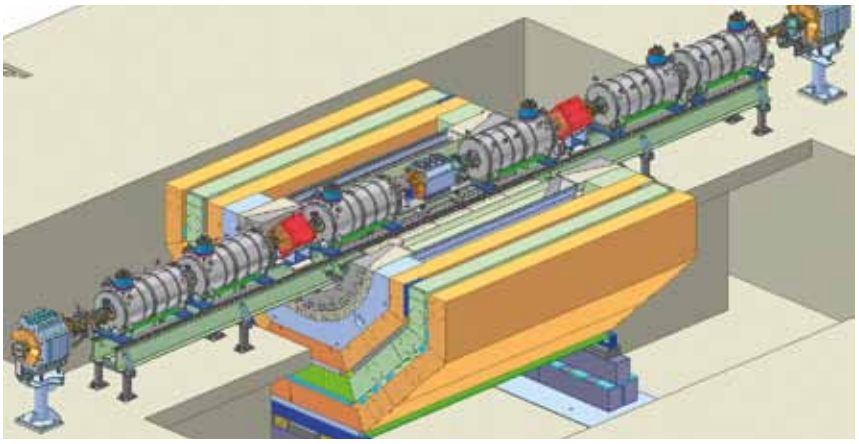

Figure 3.2 Layout of the CESR L0 wiggler straight and electron cloud experimental region with a cutaway view of the CLEO detector. Six superconducting CESR-c type wigglers are deployed in the straight, which is configured for zero dispersion operation. The straight section includes extensive vacuum diagnostics: retarding field analysers, residual gas analyser, and transverse electric wave measurement hardware.

Figure 3.3 shows the layout of the L3 region. It supports four electron cloud experiments: a large bore quadrupole housing a test chamber; the Positron Electron Project (PEP) II chicane for dipole chamber tests, which was relocated from SLAC after the early termination of PEP II operations; a drift chamber test section currently configured for testing titanium-zirconium-vanadium (TiZrV) (NEG) test chambers; and an in situ secondary-electron yield measurement station, which supports studies of the processing rates and equilibrium secondary electron yield properties of various technical surfaces. In addition to the L0 and L3 experimental regions, two arc sections were configured for flexible installation of experimental drift chambers to study the performance of various mitigations in the photon environment of the CESR arcs.

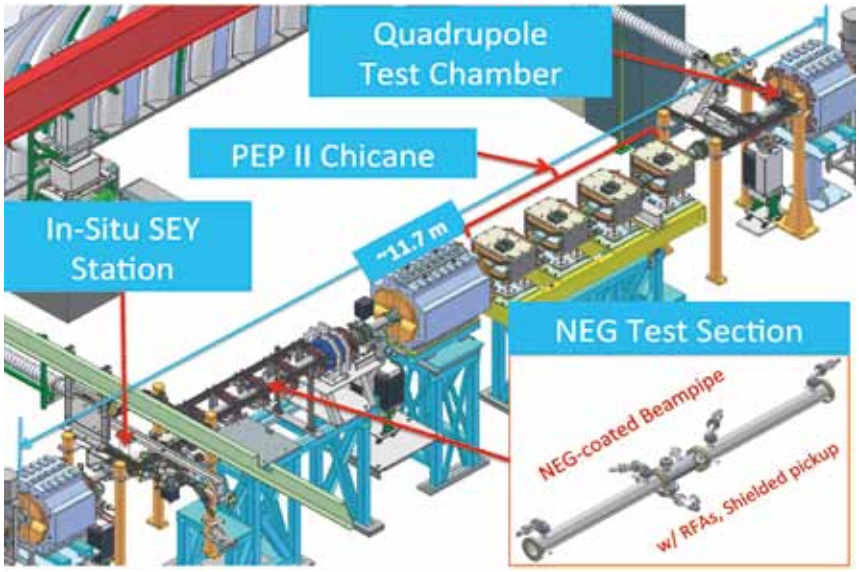

Figure 3.3 Layout of the CESR L3 straight and electron cloud experimental region. Tests of electron cloud mitigations in drift, dipole and quadrupole chambers are possible in this region. Additionally, an in situ secondary-electron-yield station is also installed, which allows characterisation of the rate of processing and equilibrium secondary electron yield properties of various vacuum system technical surfaces.

Electron cloud build-up and mitigation studies

Retarding field analysers deployed at approximately 30 locations around CESR have enabled the detailed study of local cloud build-up in variety of vacuum chambers under a range of experimental conditions *[3-17, 18]*. The analysers provide a time-averaged current readout at each location. The majority of deployed retarding field analysers utilise a segmented design to provide geometric information about the cloud build-up around the azimuth of the vacuum chamber. Analyser data taken in vacuum chambers fabricated with cloud mitigations provides the foundation for comparison of the efficacy of different electron cloud mitigation methods. An active effort is underway to model this analyser data in order to determine the secondary-electron yield and photoelectron yield parameters of the vacuum chambers treated with mitigations *[3-18, 19, 20]*. In addition to the retarding field analyser studies, transverse-electric-wave transmission methods *[3-21]* are also being used to characterise the build-up around the ring and a significant simulation effort is underway to take full advantage of these results *[3-22, 23, 24]*. A final method to study local cloud build-up is shielded pickup measurements *[3-25]*, which are providing additional constraints on the vacuum chamber surface parameters for the chambers in which they are installed.

Table 3.2 summarises the range of chamber surfaces and mitigation methods that were prepared for testing during Phase I of the CesrTA R&D programme. *Figure 3.4* shows a comparison of the performance of various chamber surfaces in a dipole field along with a plot of the evolution of the transverse distribution of the electron cloud that develops in the dipole chamber as a function beam current. While coating with a low secondary electron yield material such as titanium nitride significantly reduces the growth of the cloud in this environment, the use of a grooved surface with titanium nitride coating is clearly superior.

Mitigation	Drift	Quadrupole	Dipole	Wiggler	Institutions providing chambers
Al	√	√	√		CU, SLAC
Cu	√			√	CU, KEK, LBNL, SLAC
TiN on Al	√	√	√		CU, SLAC
TiN on Cu	√			√	CU, KEK, LBNL, SLAC
Amorphous C on Al	√				CERN, CU
Diamond-like C on Al	1/2011				CU, KEK
NEG on SS	√				CU
Solenoid windings	√				CU
Fins with TiN on Al	√				SLAC
Triangular grooves on Cu				√	CU, KEK, LBNL, SLAC
Triangular grooves with TiN on Al			√		CU, SLAC
Triangular grooves with TiN on Cu				1/2011	CU, KEK, LBNL, SLAC
Clearing electrode				√	CU, KEK, LBNL, SLAC

Table 3.2 Vacuum chambers fabricated for testing during Phase I of the CesrTA R&D programme. Checks indicate chambers for which data has already been acquired. Dated entries indicate scheduled installation times for chambers yet to be tested. CU stands for Cornell University.

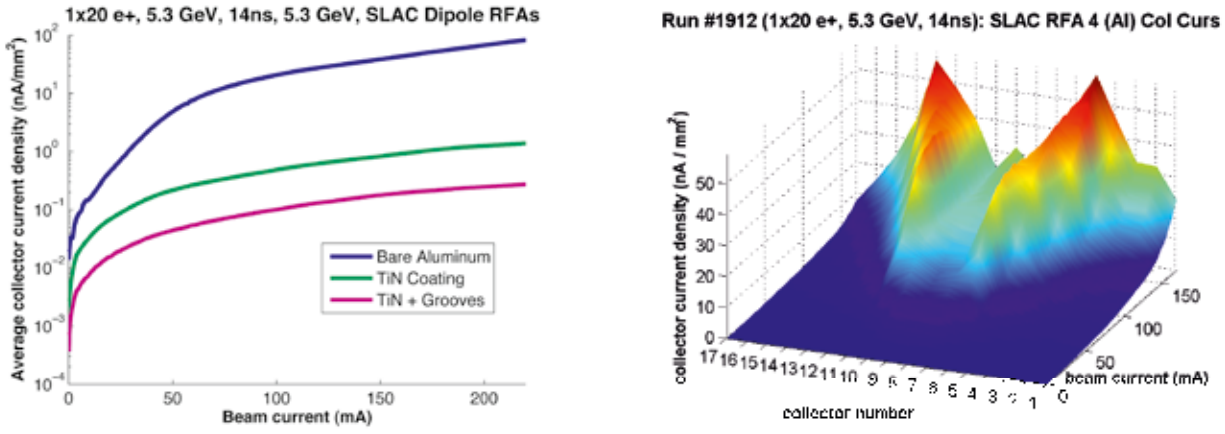

Figure 3.4 Left: the measured retarding field analyser current in a dipole versus beam current with a 20-bunch positron train for a bare aluminium surface, titanium nitride-coated surface and a grooved surface with titanium nitride coating. The efficacy of the grooved surface for suppressing the electron cloud is clearly evident. Right: the transverse shape of the electron cloud signal in the dipole retarding field analyser (aluminium chamber surface) as a function of beam current.

Figure 3.5 shows two of the mitigation methods that have been tested in the CesrTA high-field damping wigglers: triangular grooves and a clearing electrode. The clearing electrode is a very thin structure developed at KEK *[3-26]* that offers very good thermal contact with the vacuum chamber and minimal impact on the chamber aperture (see also section 3.1.3). A bare copper surface and a titanium nitride-coated copper surface have also been tested. The left plot in *Figure 3.6* shows a comparison of the electron cloud growth as a function of beam current with each of these surfaces. The data indicate that the best cloud suppression in the wiggler region is obtained with the clearing electrode. One additional comparison remains: the testing of a grooved surface with titanium nitride coating. This test chamber has recently been installed in CESR and tests will take place over the next few months.

Figure 3.5 Left: a grooved copper insert with 21.8° triangular grooves having 1-mm pitch for testing in a CesrTA wiggler. Right: a thin clearing electrode applied with a thermal spray method to the bottom half of another CesrTA experimental wiggler chamber.

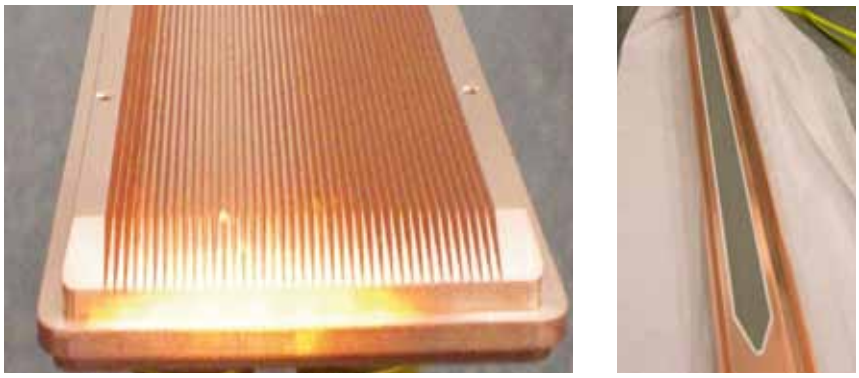

The right plot in *Figure 3.6* shows the transverse distribution of the cloud present in the vertical field region of the wiggler (copper surface) as a function of the retarding grid voltage, which probes the energy spectrum of the electron cloud.

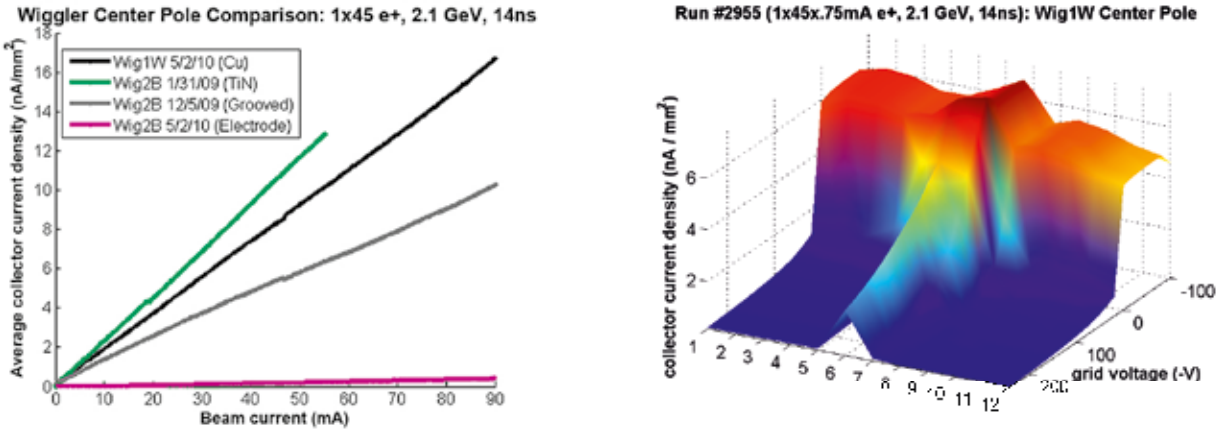

Figure 3.6 Left: the measured retarding field analyser current in a wiggler versus beam current with a 20-bunch positron train for a bare copper surface, a titanium nitride-coated copper surface, a grooved copper surface and a clearing electrode. The efficacy of the clearing electrode for suppressing the electron cloud is clearly evident. Right: the transverse shape of the electron cloud signal in the wiggler retarding field analyser as a function of retarding voltage.

Studies of the electron cloud build-up in drift and quadrupole regions have also yielded important results. Drift measurements have been used to compare the performance of various coatings. A new coating of significant interest is amorphous carbon coating developed at CERN *[3-27]* for use in the Super Proton Synchrotron (SPS). Tests at CesrTA have afforded the opportunity to study the performance of this coating in the presence of synchrotron radiation. Initial studies show that the electron cloud mitigation performance of amorphous carbon is quite comparable to that of titanium nitride and that its vacuum performance is quite reasonable in an environment with significant photon flux. Continued testing will provide information about the long-term durability of this very promising coating. Vacuum chambers in quadrupole magnetic fields can show quite significant cloud build-up. Concerns about long-term trapping of the cloud in quadrupole fields *[3-28]* requires that cloud mitigation be incorporated into the ILC damping ring quadrupole vacuum chambers. Tests in CesrTA have demonstrated the effectiveness of titanium nitride coating in this region.

Low-emittance programme and studies of electron cloud-induced beam dynamics with low-emittance beams

The CesrTA low-emittance tuning effort provides the basis for studying the emittance-diluting effects of the electron cloud in a regime approaching that of the ILC damping rings. As of early 2010, the low-emittance tuning programme had resulted in reliable operation at or below the CesrTA Phase I vertical emittance of 20 pm·rad *[3-29]* for both single- and multi-bunch operation as confirmed by X-ray beam size monitor measurements of the vertical beam size *[3-30]*. As of the end of 2010, vertical emittances less than 10 pm·rad have been achieved.

A number of beam dynamics studies have been conducted in order to fully characterise the impact of the electron cloud on beams in CESR. As the electron cloud builds up along a bunch train, the focusing effect of the cloud on the beam causes the natural frequency of oscillation of each bunch (i.e. the horizontal and vertical betatron tunes) to shift with respect to the preceding bunch. Measurements of this electron cloud-induced coherent tune shift *[3-31, 32]* for trains of electron and positron bunches, as well as for witness bunches at various positions behind a leading train, have provided an important probe of the integrated effect of the cloud around the ring. Systematic measurements over a wide range of beam conditions (varying beam energy, emittance, bunch current, bunch spacing and train lengths) are being used to validate our electron cloud models more thoroughly and have led to improved simulations, for example, for the ring photon propagation model *[3-33]*, which are now being applied to the ILC damping ring.

A principal deliverable of the CesrTA programme is the characterisation of instability thresholds and emittance-diluting effects in the regime of ultra-low vertical emittance *[3-34, 35, 36]*. *Figure 3.7* shows the observed beam motion spectrum for each bunch along a train obtained in these conditions. As described in the preceding paragraph, the development of the horizontal and vertical tune lines, denoted by F_h and F_v, along the bunch train provides information about the electron cloud density experienced by each bunch. For a positron train, the attractive force of the bunch pinches the cloud into the bunch and can lead to the development of an oscillation of the bunch tail with respect to the head. This head-tail instability is expected to induce

characteristic sidebands in the bunch motion spectrum. In *Figure 3.7*, the onset of the spectral lines denoted by $F_v \pm F_s$ part way along the bunch train indicate where the cloud density build-up has become sufficient for the onset of the instability.

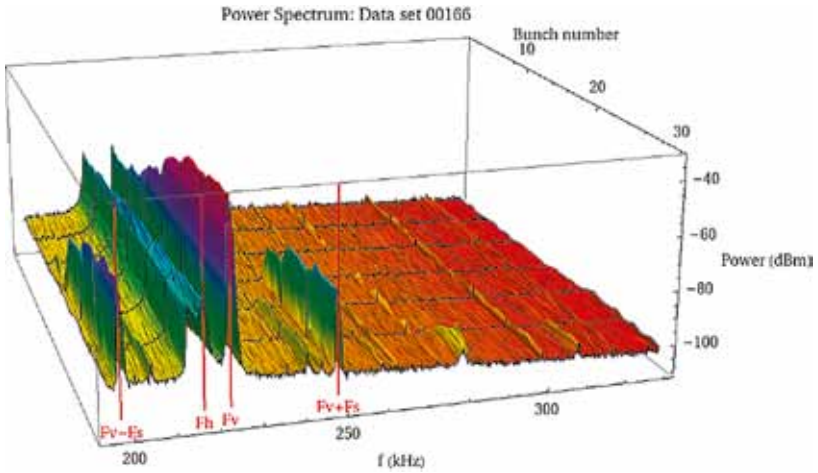

Figure 3.7 Bunch-by-bunch power spectrum for a positron train with a nominal bunch current of 0.75 mA/bunch. The horizontal (F_h) and vertical (F_v) tunes are clearly visible for all bunches. The onset of the sidebands labelled as $F_v \pm F_s$ are consistent with the onset of a head-tail instability around bunch number 15 in the train.

A second observable associated with this instability is a growth in the vertical beam size as measured along the train. *Figure 3.8* shows bunch-by-bunch beam size development along bunch trains with three different intensities. As the bunch currents are increased, the bunch number in the train at which beam size blow-up occurs moves earlier in the train due to the more rapid build-up of the electron cloud. By studying both the spectral and beam size information as a function of various parameters (bunch intensity, vertical emittance, bunch spacing, chromaticity, feedback conditions, and beam energy) and comparing with simulation *[3-37, 38]*, we will be able to validate the simulations in a regime approaching that of the ILC damping ring to ensure that our projections of the expected positron damping ring performance are accurate.

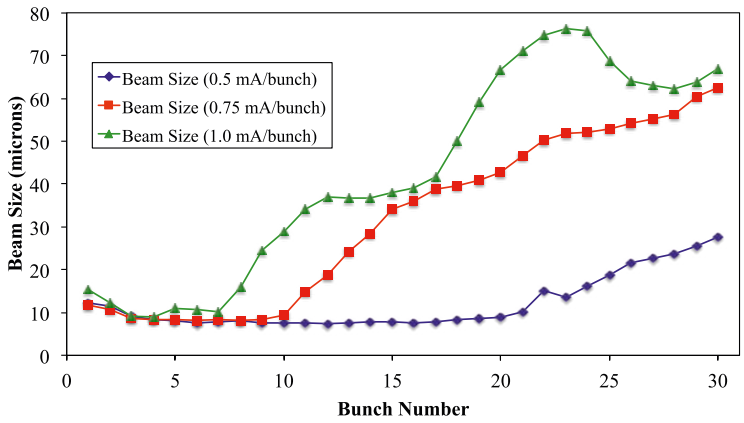

Figure 3.8 Bunch-by-bunch beam sizes based on turn-by-turn fits for each bunch for 30 bunch trains of varying current (0.8, 1.2, and 1.6×10^{10} particles/bunch). As the bunch currents are increased, the point in the train at which the electron cloud density is high enough to cause emittance and beam size growth moves to earlier points in the train.

Incorporation of CesrTA results into the ILC damping ring technical design

The results from the first two-and-a-half years of the CesrTA R&D programme are currently being integrated into the ILC damping ring technical design *[3-39]*. In particular, the observed efficacy of grooved chamber surfaces in the dipoles as well as that of the clearing electrode in the high-field wigglers provide confidence that practical electron cloud mitigations can be prepared for the arc and wiggler straight regions of the ILC positron damping ring. The importance of cloud mitigation in the damping ring quadrupole chambers has also been demonstrated. New coating technologies to suppress the secondary electron yield offer great promise. However, there is still the issue of studying the long-term performance and durability of these coatings. This will be a subject of study during Phase II of the CesrTA programme. Perhaps most importantly, the flexibility of CESR operations supports a systematic programme of electron cloud build-up and electron cloud-induced beam-dynamics studies. By benchmarking our physics models and simulations against these studies, our confidence in being able to make valid projections of the expected ILC positron damping performance has been significantly enhanced.

3.1.3 Electron cloud R&D at other laboratories

During 2007 and 2008 in the Positron Low Energy Ring of the PEP II accelerator, a magnetic chicane and special vacuum chambers were installed to study electron cloud effects in an accelerator beamline *[3-40, 41]*. A special chamber was used to monitor the secondary electron yield of titanium nitride and titanium-zirconium-vanadium (NEG) coating, copper, stainless steel and aluminium under the effect of electron and photon conditioning in situ in the beam line. A drastic reduction of the secondary electron yield to approximately 0.95 for titanium nitride and a still-high value for aluminium of greater than 2.0 after exposure in the accelerator beamline has been measured. Other vacuum-chamber materials including NEG coated samples have also been measured. In magnetic field-free regions, chambers have been installed with rectangular groove profiles meant to reduce the secondary electron generation at the surface. The electron signals in the grooved chambers, when compared to signals in smooth chambers, were significantly reduced. From the electron cloud chicane tests, two important results in dipoles are reported: 1) the titanium nitride coating reduces the cloud density by several orders of magnitude with respect to a bare aluminium surface and 2) a new resonance phenomenon has been observed that results in the modulation of the electron wall flux, and hence, one presumes, of the electron cloud density. After the PEP II shutdown the magnetic chicane and the test chambers were installed in the CesrTA ring (see section 3.1.2) to continue the cloud mitigation studies.

Tests of coated chambers, grooves and clearing electrodes have been carried out at KEK in order to mitigate the electron cloud instability in an intense positron ring *[3-26, 42, 43, 44]*. Aiming for the application in a dipole-type magnetic field, various shapes of triangular grooved surfaces have been studied. In a laboratory, the secondary electron yields of small test pieces were measured using an electron beam in the absence of magnetic fields. The grooved surfaces clearly had low secondary electron yield compared to flat surfaces of the same materials. The grooves with sharper vertices had smaller secondary electron yield.

A test chamber installed in a wiggler magnet of the KEK-B positron ring was used to investigate the efficacy of the grooved surface in a strong magnetic field. In the chamber, a remarkable reduction in the electron density around the beam orbit was observed compared to the case of a flat surface with titanium nitride coating.

An electron-clearing electrode with an ultra-thin structure has been developed. The electrode was tested with a positron beam of the KEK-B. A drastic reduction in the electron density around the beam was demonstrated in a wiggler magnet with a dipole-type magnetic field of 0.78 tesla (T). No discharge or extra heating of the electrodes and feedthroughs was observed after using the latest connection structure. The same type of electrode was also successfully tested in a CesrTA wiggler (see section 3.1.2). The clearing electrode has also been applied to a copper beam pipe with antechambers in preparation for its application in the wiggler section of Super-KEKB. Simulations indicate a small impedance for the thin structure of this electrode design.

At the INFN Frascati National Laboratories in Italy, clearing electrodes to mitigate the electron cloud instability have been installed in all the dipole and wiggler chambers of the DAΦNE positron ring, covering approximately 16% of the circumference *[3-45]*. All the electrodes have been inserted, leaving the chambers in place. Tests of the electrodes' effectiveness at high positron current will be done shortly.

At CERN, amorphous carbon thin films have been applied to the liners in the electron cloud monitors and to vacuum chambers of three dipole magnets in the SPS *[3-27]*. The electron cloud is completely suppressed for LHC-type beams in the liners even after three months of air venting, and no performance deterioration is observed after one year of SPS operation. Following the positive preliminary results obtained at the SPS it was decided to test these types of coatings in a high synchrotron radiation environment in a lepton machine at CesrTA (see section 3.1.2).

3.1.4 Preliminary recommendations of the ILC Electron Cloud Working Group

A working group has been set up to evaluate the electron cloud effect and instability issues for the ILC positron damping ring and to recommend mitigation solutions. The collaborating institutions are Argonne National Laboratory, CERN, Cornell University, INFN, KEK, Lawrence Berkeley National Laboratory and SLAC. The first task of the working group was to compare the electron cloud effect for two different damping ring designs with 6.4-kilometre (km) and 3.2-km circumferences, respectively, and to investigate the feasibility of the shorter damping ring with respect to the electron cloud build-up and related beam instabilities. We compared the instability thresholds and the electron cloud formation assuming 6-nanosecond (ns) bunch spacing in both configurations, that is, in the same beam current. Both ring configurations were found to exhibit very similar performances. The risk associated with the adoption of the 3.2-km damping ring design, while maintaining the same bunch spacing, was deemed low and the 3.2-km ring was found to be an acceptable baseline design choice.

Field region	Baseline mitigation recommendation		Alternatives for further investigation
Drift*	TiN coating	Solenoid windings	NEG coating
Dipole	Grooves with TiN coating	Antechambers for power loads and photoelectron control	R&D in the use of clearing electrodes
Quadrupole*	TiN coating		R&D in the use of clearing electrodes or grooves with TiN coating
Wiggler	Clearing electrodes	Antechambers for power loads and photoelectron control	Grooves with TiN coating

Table 3.3 Summary of baseline electron cloud mitigation recommendations developed at the Electron Cloud Working Group meeting held as part of the ECLOUD10 Workshop on 13 October 2010.

* Where drift and quadrupole chambers are in arc or wiggler straight regions of the machine, the chambers will incorporate features of those sections, that is, antechambers for power loads and photoelectron control.

The preliminary mitigation recommendations for the ILC damping rings are the result of the working group discussions held during a number of workshops and regular online meetings. The working group met at Cornell University on 13 October 2010 as a satellite meeting to the ECLOUD10 Workshop held from 8 to 12 October. The workshop was devoted to hearing the results of detailed studies of a range of mitigation options. Input from the workshop participants was included in the evaluation. The results of the evaluation were presented at the IWLC2010 workshop at CERN *[3-46]*. *Table 3.3* provides a brief summary of the recommendations.

3.2 The ATF2 final focus test beamline at KEK

3.2.1 Introduction

The challenge of colliding nanometre-sized beams at the interaction point involves three distinct issues:

- creating small emittance beams.
- preserving the emittance during acceleration and transport.
- focusing the beams to nanometres before colliding them.

The Accelerator Test Facility (ATF) at KEK in Japan is a prototype damping ring, which has succeeded in obtaining emittances that come close to satisfying ILC requirements. ATF is now used as a beam injector for the ATF2 final focus test beamline, constructed in 2008. The primary goals for ATF2 address the challenge of the beam size:

- achieving a 37-nanometre (nm) vertical beam size at the interaction point.
- stabilising the beam at that point at the nanometre level.

The main parameters of ATF2 are given in *Table 3.4*, together with the corresponding values for the ILC.

Table 3.4 Main design parameters for ATF2 compared with those for ILC. The ATF2 37-nm beam size (at the interaction point) includes residual effects from uncorrected higher-order optical aberrations.

Parameter			ATF2	ILC
Beam energy	E	GeV	1.3	250
Effective focal length	L^*	m	1	3.5 – 4.5
Horizontal emittance	ε_x	nm	2	1.0 (damping ring)
Vertical emittance	ε_y	pm	12	2 (damping ring)
Horizontal IP β function	β^*_x	mm	4	21
Vertical IP β function	β^*_y	mm	0.1	0.4
Horizontal IP angular dispersion	η'		0.14	0.0094
Relative energy spread	σ_E	%	~0.1	~0.1
Chromaticity			$\sim 10^4$	$\sim 10^4$
RMS horizontal beam size	σ^*_x	μm	2.8	0.655
RMS vertical beam size	σ^*_y	nm	37	5.7

The layout of the ATF-ATF2 facility and the design optical functions of the ATF2 beamline are displayed in *Figures 3.9* and *3.10*, respectively. The optics system – based on a local chromatic correction scheme that affords a compact geometry – is a scaled-down version of the ILC design.

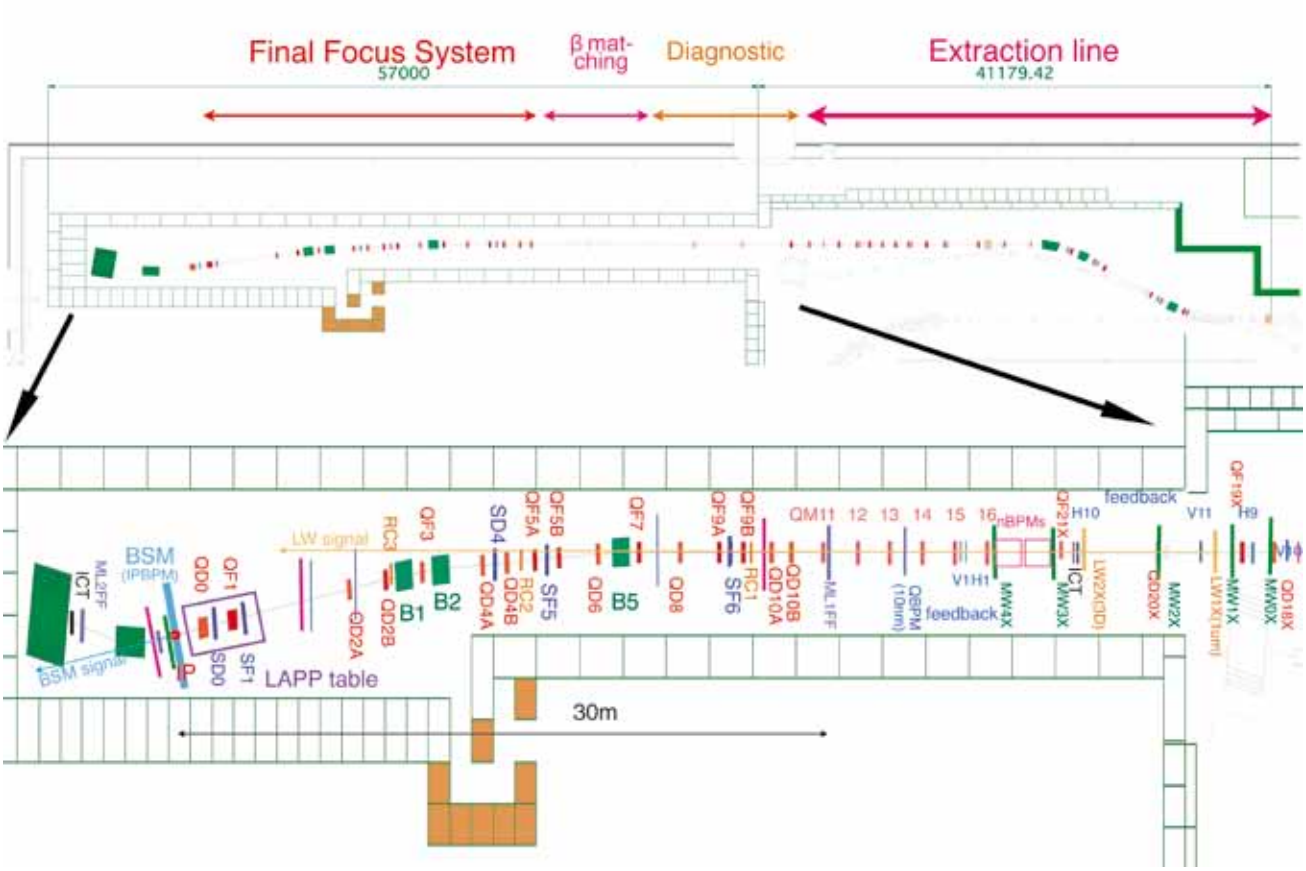

Figure 3.9 Top: the ATF2 beam line. Bottom: an enlargement of the final focus system.

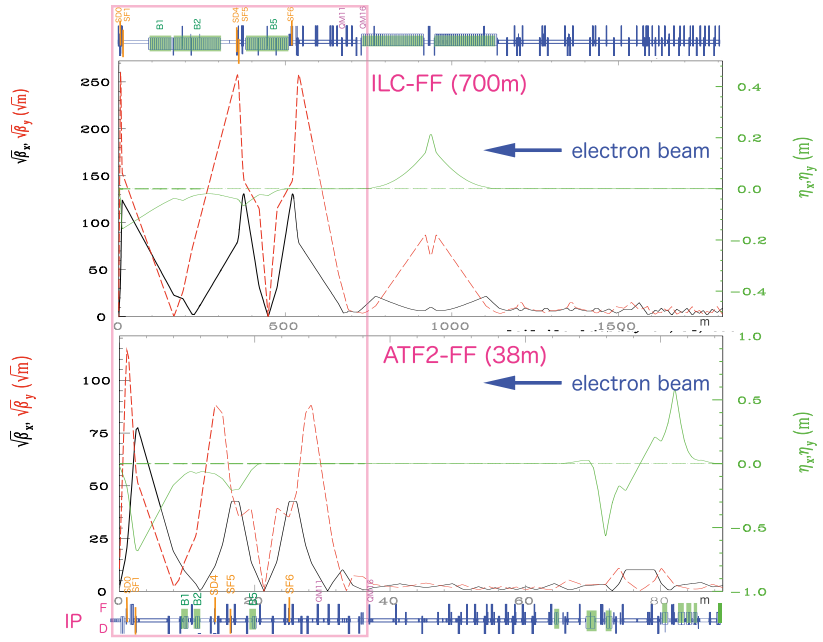

Figure 3.10 Top: ILC beam delivery system optics from the exit of main linac on the right to the interaction point on the left. Bottom: ATF2 optics from the ATF damping ring extraction point on the right to the interaction point on the left.

3.2.2 Status of ATF2 systems

Magnets and magnet mover

The ATF2 beamline extends over about 90 m from the beam extraction point in the ATF damping ring to the interaction point (see *Figures 3.9* and *3.11).* Many quadrupoles and some dipoles were fabricated for ATF2 by IHEP in China, while others were reused from the old ATF extraction beamline and from the Final Focus Test Beam at SLAC. Among those from the latter were the two quadrupole and two sextupole magnets that make up the strong-focusing final doublet system just before the interaction point. The apertures of the final doublet quadrupole magnets needed to be increased to accommodate the larger β function values in the ATF2 optics design.

Figure 3.11 View looking downstream along the final focus section of the ATF2 beamline.

Anticipating gradual movements of supports and magnets due to thermal variations or slow ground motion, 20 quadrupole and five sextupole magnets in the final focus were mounted on remote-controlled three-axis movers recycled from the Final Focus Test Beam experiment. The movers have a precision of 1 to 2 micrometres (μm) for transverse motion (horizontal and vertical), and 3 to 5 microradians (μrad) for rotations about the beam axis.

Overall alignment precisions of 0.1 millimetres (mm) (displacement) and 0.1 milliradians (mrad) (rotations) have been achieved using conventional alignment and metrology techniques. The final alignment of the magnets is achieved via beam-based alignment techniques.

Final doublet

The final doublet is composed of two quadrupole and two sextupole magnets (labelled QD0, QF1, SD0, SF1 in *Figure 3.9)*. These magnets must be supported in a way that ensures that their vertical vibration amplitude relative to the interaction point is smaller than 7 nm rms above 0.1 hertz (Hz); this limits unwanted effects on the measured beam size at the interaction point to less than 5% of the total size. For vibrations below 0.1 Hz, beam-based feedback methods can be used to limit those effects. A rigid support was chosen since it strongly suppresses the relative motion of the final doublet and the interaction point. Vibration measurements with the table fixed to the floor and with all magnets and movers installed were performed in the laboratory for validation, including checking for potential effects from cooling water flowing in the magnets. Additional measurements after installation of the final doublet confirmed that the residual motions of the magnets relative to the interaction point were within tolerance. The whole final doublet system is shown in *Figure 3.12*.

Figure 3.12 View of the final doublet installed on its rigid mechanical support system.

Cavity beam position monitors

The ATF2 beamline is instrumented with 32 C-band (6.5 gigahertz) and four S-band (2.8 GHz) high-resolution cavity beam position monitors, fabricated by Pohang Accelerator Laboratory and Kyungpook National University in Korea. There are also four C-band and one S-band reference cavities to monitor beam charge and beam arrival phase. In the diagnostics and final focus sections, every quadrupole and sextupole magnet is instrumented with a cavity beam position monitor. The final doublet magnets use S-band beam position monitors, while the other quadrupoles are equipped with C-band monitors. The usable measurement range of the cavity beam position monitors was found to exceed the mechanical range of quadrupole movers (±1.5 mm). A resolution of 200 to 400 nm for the C-band beam position monitors has so far been demonstrated.

Interaction point beam size monitor

Measuring transverse beam sizes of tens of nanometres at the interaction point requires specialised beam instrumentation, in particular a laser interferometer-based beam size monitor, also referred to as a Shintake monitor. This beam size monitor is based on inverse Compton scattering between the electron beam and a laser interference fringe pattern.

For the ATF2 beam energy, the energy of the generated gamma rays is typically rather low compared to the main component of detector backgrounds, Bremsstrahlung photons (these are emitted when electrons in the transverse tails of the beam interact with apertures and start showering). In the monitor designed for ATF2, the signal is separated from this high-energy background by analysing the signal's longitudinal shower profile, measured with a multilayered detector (located a few metres after the interaction point, downstream from a dipole magnet). The laser wavelength is 532 nm, the second harmonic of the Nd:YAG (neodymium-doped yttrium aluminium garnet) laser, which provides a suitable fringe pitch to measure the target vertical size of 37 nm. Four laser beam crossing modes of 2-, 8-, 30- and 174-degree angles are available to provide a broad dynamic range of up to several micrometres, allowing the initial beam size to be tuned down to the nominal beam size or smaller. In addition, a single 'laser wire' mode can be used for horizontal beam size measurements.

Other beam line instrumentation

The instrumentation from the old ATF extraction line (strip line beam position monitors, integrated current transformers, optical transition radiation, screen profile monitors and wire scanners) is reused in the reconfigured beamline. There are five wire scanners with tungsten and carbon wires of 10-µm and 7-µm diameters, respectively, located in the diagnostic section upstream of the final focus section (see *Figure 3.9)*. They are used to measure the horizontal and vertical beam emittances after extraction from the damping ring. An additional wire scanner is installed just downstream of the interaction point for beam size tuning and has tungsten and carbon wires of 10-µm and 5-µm diameters, respectively. Screen monitors are located right after the extraction, in the middle of the beamline and before and after the final doublet. An optical-fiber beam loss monitor is installed all along the beamline to measure and localise beam losses. Four optical transition radiation monitors with an improved resolution of 2-µm have been installed in the extraction line, close to the wire scanners. These monitors are used for single-bunch beam size as well as fast emittance measurements.

Commissioning status

Emittance in the damping ring

Figure 3.13 shows recent results of the vertical emittance measured by three different devices at the damping ring. The vertical emittance of 10 pm required for ATF2 was routinely obtained with the standard beam tuning procedures for the damping ring.

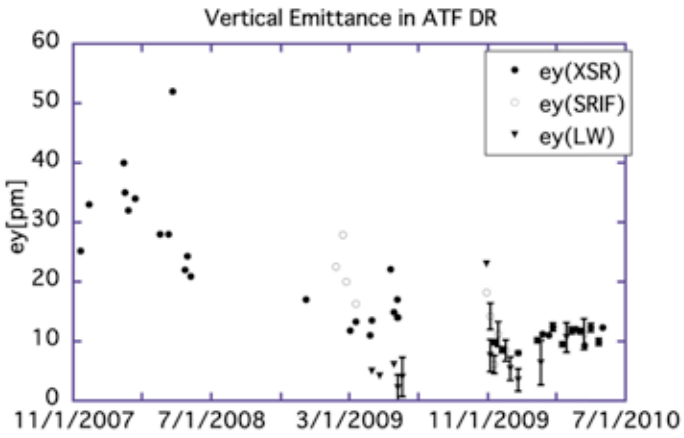

Figure 3.13 Recent measurements of vertical emittance at the damping ring, where XSR, SRIF and LW are values by X-ray profile of synchrotron radiation, interference pattern of synchrotron radiation and the laser wire, respectively.

Beam tuning strategy

Focusing the low-emittance beam extracted from the ATF damping ring to the specified interaction point beam size requires correcting trajectory and optics distortions induced both by imperfections along the beamline and by mismatch of the beam phase space at damping ring extraction. While final corrections must be performed at the interaction point, it is still important to keep mismatches under control at the entrance of the final focus in order to limit distortions of the linear optics in the carefully tuned chromatic correction section. It is also important for minimising Bremsstrahlung backgrounds in the beam size monitor. These arise from electrons driven to large amplitudes, which then cause showers at the limiting apertures.

To focus the low-emittance beam, all the magnets except for the dipoles must first be aligned with respect to the beam using the beam position monitors. In the final focus section, the positions of most magnets were adjusted using their mechanical movers; steering magnets were used to centre the beam in the upstream magnets. In the extraction line, two quadrupole magnets (labelled QF1X and QF6X – see *Figure 3.9)* and two skew-quadrupole magnets (labeled QS1X and QS2X) were used to correct horizontal and vertical dispersions at the end of the extraction line.

There are five sextupole magnets in the final focus system (SF6FF, SF5FF, SDFF, SF1FF and SDoFF), which are primarily required for correction of chromatic and geometric optics aberrations. By adjusting linear combinations of the horizontal and vertical displacements of these magnets using their magnet movers, the beam waist positions, dispersions and cross-plane coupling at the interaction point can be orthogonally tuned.

The final doublet quadrupole strengths are also used for fine-tuning. The primary tuning diagnostic is the beam size monitor together with the mechanical wire beam size measurements at the interaction point.

Overview of commissioning runs

Commissioning ATF2 with beam began in late 2008 and continued throughout 2009. Most of the early commissioning was focused on hardware and software commissioning. To reduce the beam size in the final doublet, and therefore background rates, during initial commissioning of the instrumentation (most notably the beam size monitor), the initial optics used a lower demagnification than the goal optics. Interaction point β functions of 8 centimetres (cm) in both the horizontal and vertical planes – factors of 20 and 800 higher, respectively, than design – were used. Under these conditions, initial interaction point beam sizes of 12.5 mm (horizontal) and 1 to 2 mm (vertical) were measured with the beam size monitor in laser wire mode.

After this initial success, the vertical interaction point β function was reduced from 8 cm to 1 cm, corresponding to a theoretical vertical beam size of approximately 500 nm. (The horizontal β function was left unchanged.) Further development of the instrumentation at this time included additional interaction point diagnostics (a screen monitor, wire scanners and a knife-edge monitor) and an upgrade to the interaction point beam size monitor, replacing the laser with a more powerful one (four times greater in intensity). With the stronger focusing optics, the first detailed measurements of the lattice response and optics functions were made *(Figure 3.14)*. Towards the end of 2009 another major milestone was achieved with the first beam size monitor measurements in interference mode, where a vertical beam size of 3.3 mm in the 3-degree crossing mode was observed.

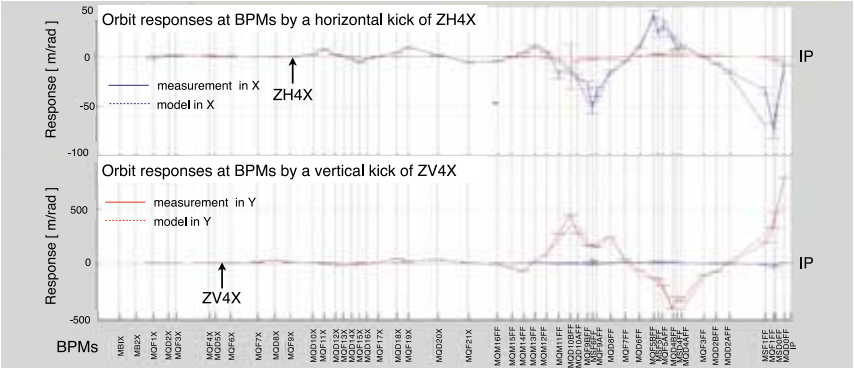

Figure 3.14 The beam position monitor model (lattice) response measured by steering beam at a horizontal corrector magnet ZH4X (top) and at a vertical corrector magnet ZV4X (bottom) in the extraction line. Both measured and simulated data are shown.

In early 2010, another significant step in demagnification was made with the interaction point β functions now only 1 mm high and 4 cm wide (ten times larger than the design). This level of demagnification required the use of the sextupoles for the first time to correct the chromatic aberration at the interaction point. With the beam size monitor and beam position monitor systems now fully commissioned, application of the interaction point beam size tuning algorithms could be made for the first time, squeezing the beam size down to the expected value.

Figure 3.15 shows the raw beam size monitor measurement, corresponding to a vertical beam size of 310 ±30 (statistical) ±30 (systematic) nm – almost three times the value of the expected size of 110 nm, with a vertical emittance of 12 pm. Two possible sources of error were identified: alignment roll error of the final doublet quadrupoles, and insufficient commissioning time for the interaction point beam size (Shintake) monitor using the 30-degree mode required for beam size measurements less than 300 nm. The final doublet roll has been subsequently confirmed by mechanical inspection and realigned. One major issue for small beam size operation is high-order multipole components (aberrations) in the quadrupole magnets. A retuned optics has been proposed to mitigate the (simulated) effects of these multipole components. Currently, a new optics is being implemented with the design demagnification in the vertical plane (vertical interaction point β function of 0.1 mm), but with a still relaxed horizontal demagnification by a factor of 2.5 (horizontal interaction point β function of 10 mm). The optics includes the proposed mitigation for the quadrupole multipole components.

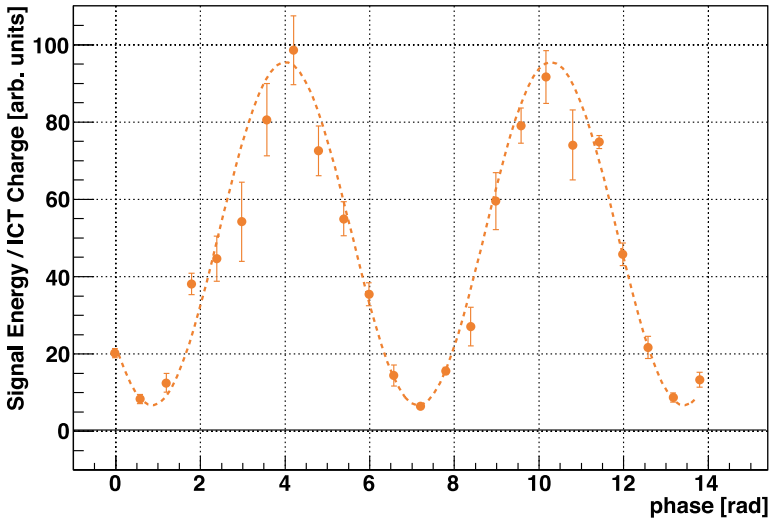

Figure 3.15 The best modulation measured to date by the beam size monitor (Shintake monitor) with the 8-degree crossing angles in the continuous run, taken May 2010. The measurement corresponds to a beam size of 310 ±30 (statistical) ±30 (systematic) nm.

3.2.3 ATF2 outlook and plans

The remainder of Technical Design Phase 2 (and beyond) will see a concerted effort to achieve the goal of 37-nm vertical beam size. In parallel to this, several R&D activities related to the second ATF2 goal – stability – are being actively pursued:

- feedback on a nanosecond time scale
- nanometre resolution of the interaction point beam position monitor
- fast nanosecond rise-time kicker
- cavity beam position monitor optimised for monitoring angular variations of the beam near the interaction point with high accuracy
- development of robust laser wire diagnostics

The most recent results of feedback on a nanosecond (ns) time scale are shown in *Figure 3.16*, where a measurement of the beam offset at the first of a three-bunch train is used to correct (feed back on) the subsequent two bunches. Bunch separation is 151.2 ns. The data clearly indicates a reduction of the beam jitter by a factor of five from the first to the second bunch. The achieved 2.1-μm rms scales to 2.6 nm at the interaction point, assuming the demagnification of the optics.

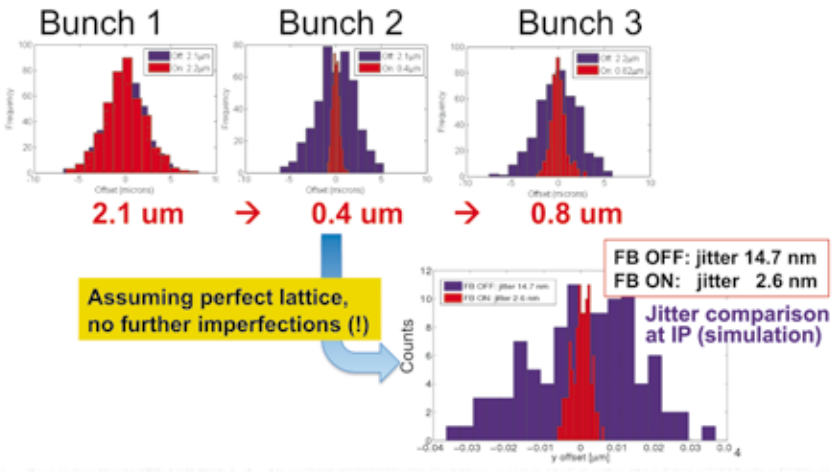

Figure 3.16 Recent results of feedback on a nanosecond time scale. The above three plots are experimental results. The bottom one is a simulated result to demonstrate the nanometre stabilisation at the interaction point, assuming a perfect lattice in the final focus beam line.

Plans to upgrade the performance of ATF2 on the time scale of a few years, after the main goals of ATF2 have been achieved, are also under consideration. In particular, optical configurations with ultralow β^* values (two to four times smaller than the current nominal values in the horizontal and vertical planes), relevant to both the CLIC design and to some of the alternative ILC beam parameter sets, are actively studied. In order to allow beam-based stability studies, there is also a proposal to upgrade the final doublet with superconducting magnets built using the foreseen ILC direct-wind technology. An R&D programme to develop a tunable permanent magnet suitable for the final doublet is also pursued in parallel, with an initial goal to construct a prototype for initial beam testing in the upstream part of the ATF2 beamline.

3.3 Accelerator systems R&D

3.3.1 Polarised electron source

Currently, the R&D for the ILC polarised electron source focuses on two aspects. The first is to build a prototype of the source laser system with the goal of generating an electron beam with ILC beam parameters *(Table 3.5)*. For this demonstration of the ILC beam, SLAC's ILC Injector Test Facility will be used. This facility comprises the laser facility, the US Stanford Linear Collider electron gun with associated diagnostics, including a Faraday cup for bunch charge, and a Mott polarimeter for electron polarisation measurements. At a later stage, it is planned to move the laser system to US Jefferson Laboratory's injector facility to allow beam demonstration with a higher-voltage electron gun (160 to 200 kilovolts (kV)), which is currently under construction.

The second aspect of R&D is aimed at the electron gun itself. The goals are to achieve the ILC specification for a gun voltage of 200 kV while maintaining a low dark current to ensure a long cathode lifetime.

Table 3.5 ILC electron source beam parameters.

Parameter	Symbol	Value
Number of electrons per bunch at gun exit	n_e	$4x10^{10}$
Number of electrons per bunch at damping ring injection	n_e	$2x10^{10}$
Number of bunches	N_e	2,820
Bunch repetition rate	$F_{\mu b}$	3 MHz
Bunch train repetition rate	F_{mb}	5 Hz
Bunch length at source	Δt	2 ns
Peak current in bunch at source	I_{avg}	3.2 A
Energy stability	S	< 5% rms
Polarisation	Pe	≥ 80%
Photocathode quantum efficiency	QE	0.5%
Drive laser wavelength	Λ	780-810 nm (tunable)
Single-bunch laser energy	E	5 µJ

Currently, no photocathode R&D is being conducted. Results from previous R&D projects have demonstrated that materials are available that can provide the ILC beam charge and polarisation. It is anticipated that the ILC source will use a strained gallium arsenide phosphide (GaAsP) highly-doped photocathode. *Figure 3.17* illustrates the performance of such a cathode. The last remaining question is the surface charge limit at microsecond timescales. The laser system currently under development will answer this question.

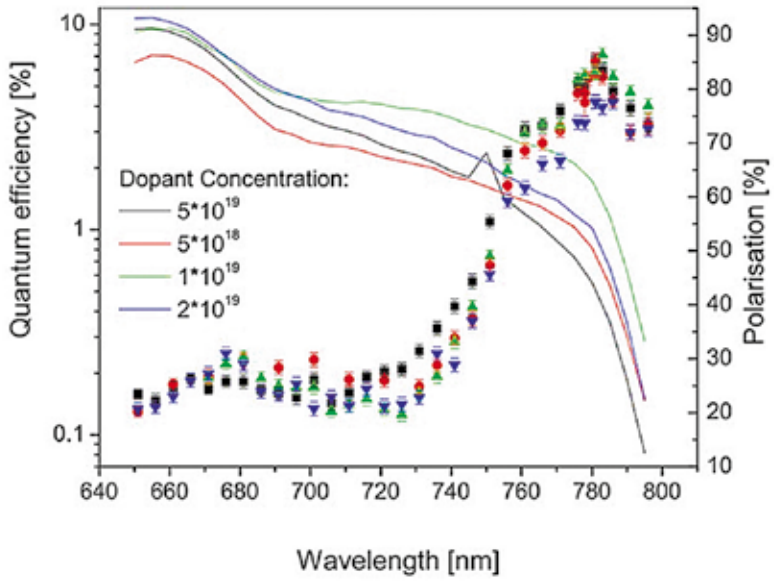

Figure 3.17 Performance of strained layers of GaAsP photocathodes at different doping levels.

Laser system development

A laser system is being developed for the ILC polarised injector that is capable of generating the ILC bunch train. The laser wavelength must match the band gap of the cathode material. For GaAsP, a wavelength of approximately 800 nm is necessary. The laser system must provide the time structure of the ILC pulse train. One basic component of this laser system is the mode-locked oscillator that operates at a harmonic frequency of the micro-bunch repetition rate, which can be locked to an external reference frequency. For efficient amplification of the pulse train, a regenerative amplifier is used *(Figure 3.18)*.

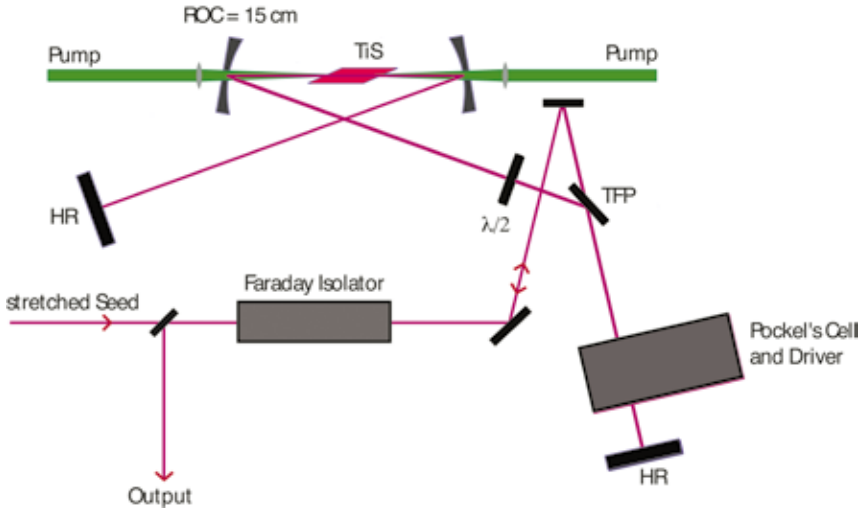

Figure 3.18 Optical layout of the regenerative amplifier.

A key component of this amplifier is the cryogenic cell containing a titanium-sapphire crystal. Cryogenic technology allows large pump power and efficient amplification, minimising the effects of thermal lensing in the amplifying medium. The micro-bunch structure (3-megahertz (MHz) pulse train) is controlled by injection and extraction of the regenerative amplifier using a high-repetition-rate Pockel's cell system. The macro-bunch structure (5 to 10 MHz) is generated by electro-optical switching of the amplified beam. At SLAC, two such laser systems are being built: a SLAC version and a second similar system that was constructed by a commercial laser company, Kaptayne Murnane Laboratories, Inc.

Direct current gun

The main goal of R&D towards a direct current gun for polarised electron generation is to increase the high-voltage capability while maintaining or reducing the dark current. A higher voltage is desirable to reduce the space charge forces that the electrons experience at low energy before further acceleration. The reduction of space charge forces is desirable to lower the transverse and longitudinal emittance of the generated electron bunches. A low dark current is necessary to maintain the negative electron affinity properties of the photocathode, thereby increasing the lifetime of the electron source. The most important issue is to reduce field emission within the gun, which is the fundamental source of dark current. The ILC gun R&D is being carried out at Jefferson Lab and focuses on new materials for the anode and cathode electrodes. New surface-polishing techniques are being investigated and compared. Some examples are traditional diamond-paste polishing, electropolishing and buffer chemical polishing. Promising results have been achieved for chemical-buffered polished niobium electrodes *(Figure 3.19)*.

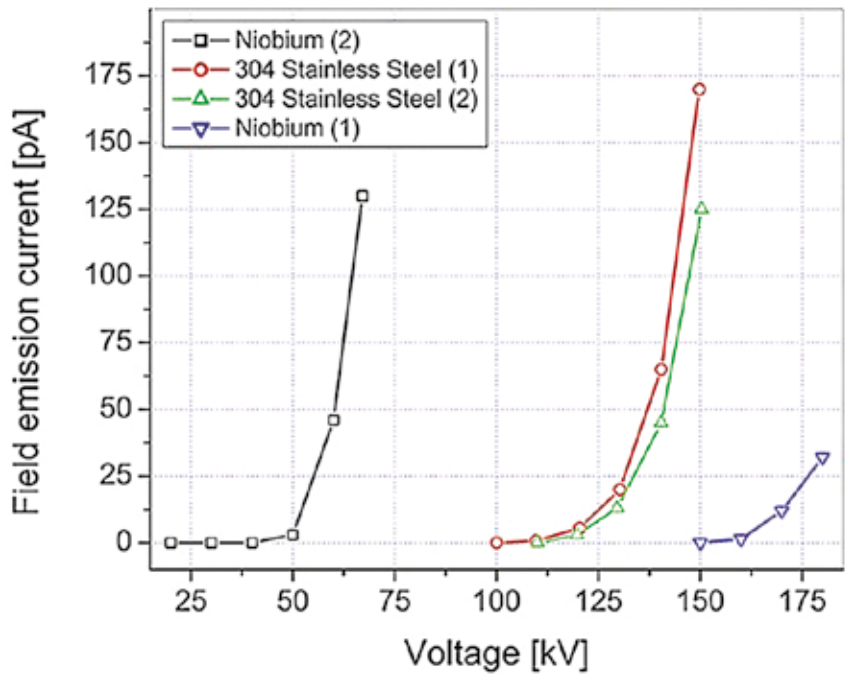

Figure 3.19 Comparison of field emission versus high voltage for stainless steel and niobium electrodes.

The onset of dark current is significantly higher compared to stainless steel electrodes (150 kV vs. 100 kV). Additional work focuses on an alternative gun design, the so-called inverted gun, to improve the high-voltage performance. *Figure 3.20* shows a niobium electrode for an inverted gun design, which replaces a conventional ceramic insulator with an inverted insulator. This design eliminates the need of sulphur hexafluoride, used in the traditional design to achieve appropriate high-voltage conditions and to ensure no high-voltage breakdown can occur outside the electrode chamber.

Additional emphasis is placed on developing conditioning methods to achieve ultra-high vacuum conditions, which is crucial for successful operation of the gun and improved cathode lifetime.

Figure 3.20 Niobium electrode of inverted gun design.

3.3.2 Positron source

The ILC baseline for positron production uses the primary high-energy electron beam to generate photons in a long undulator, which subsequently generates electron-positron pairs in a thin target *[3-48]*. There is a very active R&D programme associated with the positron source. This system is challenging and novel. As the R&D has progressed, the design and performance of the source has increased substantially, with many legitimate concerns being dealt with in a systematic manner. Whilst progress has been made in virtually all subsystems, the three key areas of the helical undulator, the conversion target and the flux concentrator have rightly received the most attention as these were previously singled out as higher-risk areas.

Helical undulator

At the time of the *Reference Design Report* (RDR), short superconducting helical-undulator prototypes using niobium-titanium superconductors had been successfully fabricated and tested by groups at Rutherford Appleton Laboratory (RAL) in the UK and at Cornell University *[3-49, 50]* in the US. This gave confidence that the undulator period and field strength selected for the ILC were feasible. Since that time the RAL group has successfully fabricated two identical long undulators, each 1.75 m in length, which have been magnetically tested and proven easily to achieve the field strength required. In fact, both exceeded the magnetic field specification by more than 30% *[3-51]*. The quench training for the two magnets is shown in *Figure 3.21*.

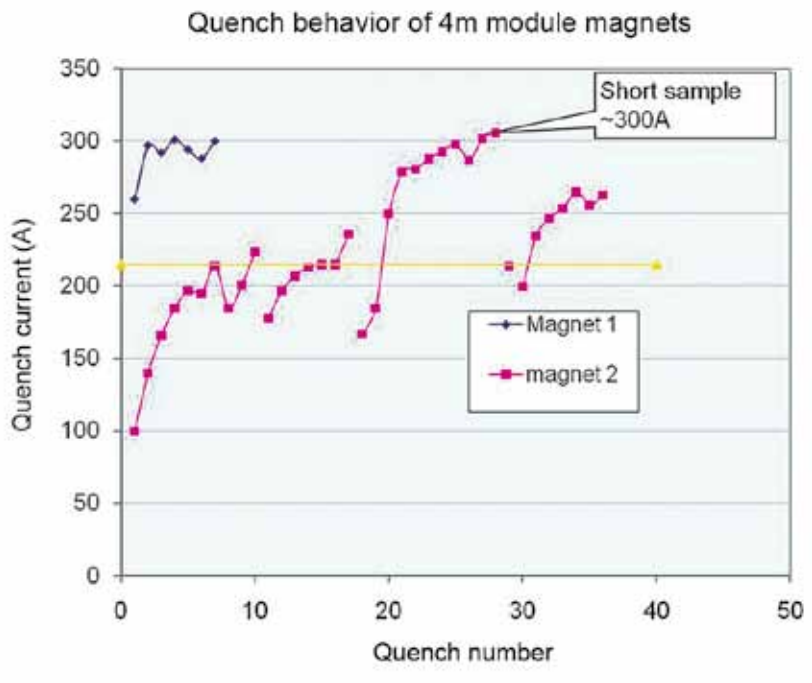

Figure 3.21 Quench history of the 3-m prototype superconducting helical undulator.

In addition the subsequent analysis of the magnetic field results by staff at Daresbury Laboratory in the UK has shown that both undulators have a very high field quality, certainly more than sufficient to provide the intense source of gamma photons that is required. The RAL team has since incorporated both of these undulators into a single 4-m-long cryogenic module (which operates at -269 °C) of the design required by the ILC, and has proven that both undulators can be powered simultaneously at the field levels required *[3-52]*. A photo of the complete undulator cryomodule is shown in *Figure 3.22.* In the future it would be valuable to install the module into an electron beam test line to measure the photon properties of the light generated by the undulators.

Figure 3.22 The 4-m prototype superconducting helical undulator under test at Rutherford Appleton Laboratory.

The RAL team is now investigating the use of a more advanced superconducting material, niobium tin, which should enable even higher field strengths to be generated. If this is proven to be the case in practice it will enable the period of the undulator to be reduced further, which will allow the positron source to generate the required positron yield at lower electron drive-beam energies, a considerable advantage to the ILC project. Currently the team is winding short prototypes to gain experience with this technically more challenging material and also to allow a direct comparison with the other prototypes built using niobium titanium *[3-53]*.

Conversion target

The conversion target is a 1-m-diameter wheel of titanium alloy that rotates at 100 m/s at the rim. To increase the positron yield, the target rim passes through a strong magnetic field. Unfortunately, this then induces unwanted eddy currents in the wheel, causing the wheel to heat up. The level of heating that can be tolerated limits the usable magnetic field. Several groups have tried to model the eddy current heating but inconsistent results were obtained from the different simulation codes they used *[3-54, 55]*. Consequently a full-scale prototype target has been built at the Cockcroft

Institute in the UK to benchmark the simulation codes. A full-size target wheel was fabricated from the required titanium alloy and was rotated over a range of rim velocities in a strong magnetic field *(Figure 3.23)*. The results of this unique experiment have accurately quantified the eddy current effects and have confirmed which simulations were correct *[3-56]*. Furthermore, the experiment has proven that the magnetic field level assumed by the positron source design at the target wheel is feasible, with the eddy current heating being easily tolerated.

Figure 3.23 Prototype rotating target setup for eddy current tests at Daresbury Lab. Copyright STFC.

The target wheel also has to operate inside a vacuum chamber whilst the motor is in air. This means that a rotating vacuum seal is required that is capable of operating at high velocity, near a magnet and in a high radiation environment – quite a demanding challenge. The team has identified a commercial vacuum seal that, the manufacturers claim, is suitable for ILC conditions. To confirm the long-term performance of the seal, a relatively simple test is currently being planned by staff at Lawrence Livermore National Laboratory (LLNL) in the US. Initially, an equivalent load to the target will be rotated in a vacuum and the performance of the seal evaluated by monitoring the vacuum level within the chamber. Later the full-size target wheel that is currently at the Cockcroft Institute will be delivered to LLNL, and be rotated at the speeds required by the ILC under vacuum. The engineering design concept for this test is shown in *Figure 3.24*.

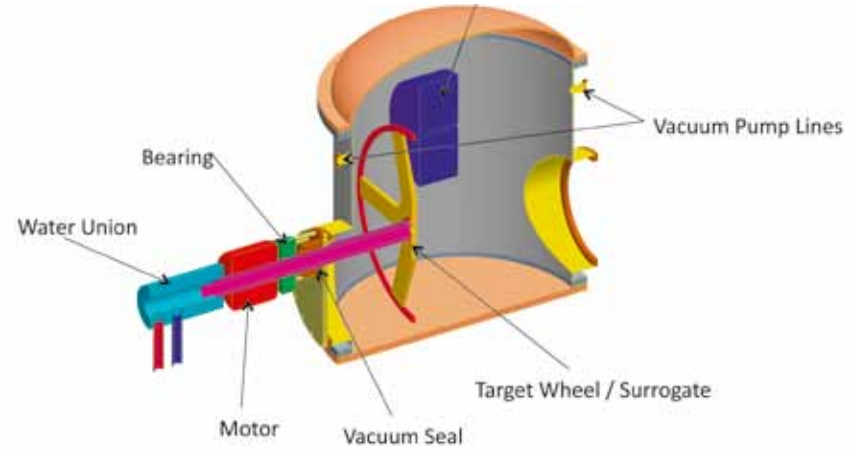

Figure 3.24 Schematic of the engineering design for the in-vacuum rotating target.

Another issue for the target that has been studied in detail is the effect of the shockwave on the target as a consequence of being struck by the intense pulses of gamma photons generated by the undulator *[3-56]*. Concerns were raised over possible material damage to the target itself on a shot-by-shot basis. Simulations with a numerical code at LLNL suggested that the effect is not significant. This has since been confirmed with a detailed analytical study, carried out at Durham University in the UK *[3-57]*.

Flux concentrator

The flux concentrator is the pulsed magnet that generates the strong magnetic field close to the target wheel in order to enhance the positron yield. Many of these have been used successfully in the past but the parameters of the ILC require a more technically challenging device. A detailed R&D study has been initiated at LLNL to confirm the feasibility of the proposed magnet and later to build a suitable prototype to demonstrate the design performance. The team has shown that the flux concentrator must be operated at around -200 °C using a liquid-nitrogen cooling system so that the electrical conductivity of the very high current-carrying copper disks do not generate too much resistive heating. The design is now well advanced (see *Figure 3.25)* and the simulations predict excellent performance of the magnet *[3-58]*. The next step is a phased prototyping of the magnet to demonstrate the key features of the design. The first tests will be carried out at room temperature and at low repetition rates. These will confirm the magnetic field strength and profile is as required. The next step will be to cool the magnet with liquid nitrogen and to confirm reliable operation at 5 Hz over an extended period.

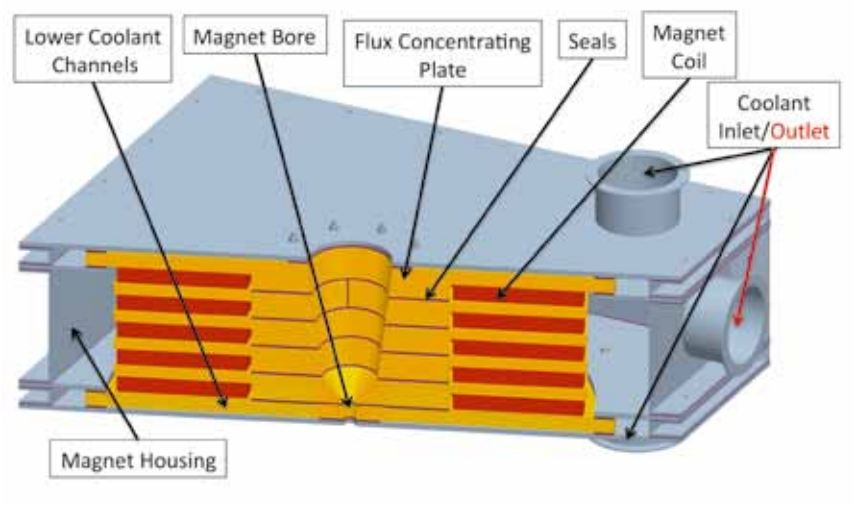

Figure 3.25 Section of the prototype design for the pulsed flux concentrator.

Performance simulations

The parameters for source subsystems and the determination of the source performance can only be quantified using complex simulations. These simulations quite often require the combination of several sophisticated computer codes. The primary performance figure of merit is the yield, defined as the number of positrons captured in the acceptance of the damping ring per electron passing through the undulator. (Ideally a yield of 1 is required, but the design goal is set at 1.5 to allow a 50% safety factor.) The second figure of merit is the polarisation of the captured positrons, which depends on additional parameters such as the collimation aperture of the photon beam before the target. *Figure 3.26* shows an example of integrated performance simulation *[3-59]*.

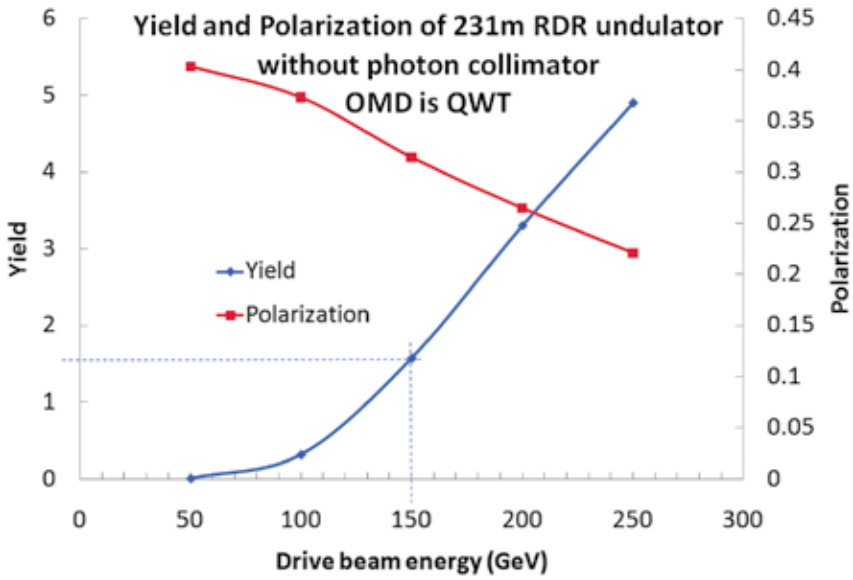

Figure 3.26 Integrated simulation results of positron yield and polarisation as a function of electron drive-beam energy.

Alternative sources

Since the undulator-based source represents a novel concept, more conventional options using an electron beam on a thick target are also being investigated as possible backup solutions. In the first such option, the positron beam is produced by a few-GeV electron beam from a normal-conducting linac with a beam pulse length of approximately 1 μs and a repetition rate of around 300 Hz. The total 2,630 positron bunches required are produced in 60 ms (as opposed to a single 1-ms pulse for the undulator source) to reduce the peak target heat load. In this case the flux concentrator technology is less demanding owing to the shorter (1 μs) pulse length. As a second option, a system with multiple targets could be used, but a more elegant solution would be a single liquid-lead target system, a prototype of which is currently being tested at KEK-ATF *[3-60]*. A third possible electron-driven scheme is the 'hybrid-target system' in which a photon beam is produced from a few-GeV electron beam at an enhanced rate by using a crystal target. The charged particles produced by the crystal target are swept out by a magnetic field, leaving only the photon beam to irradiate a second amorphous target to produce positrons. A basic experiment is being done at KEK using the KEK-B linac *[3-61]* (see *Figure 3.27)*.

The common disadvantage of electron-driven sources is that the positron beam is unpolarised. As a possible future advanced scheme for polarised positron production, methods using laser Compton scattering are also under study *[3-62]*.

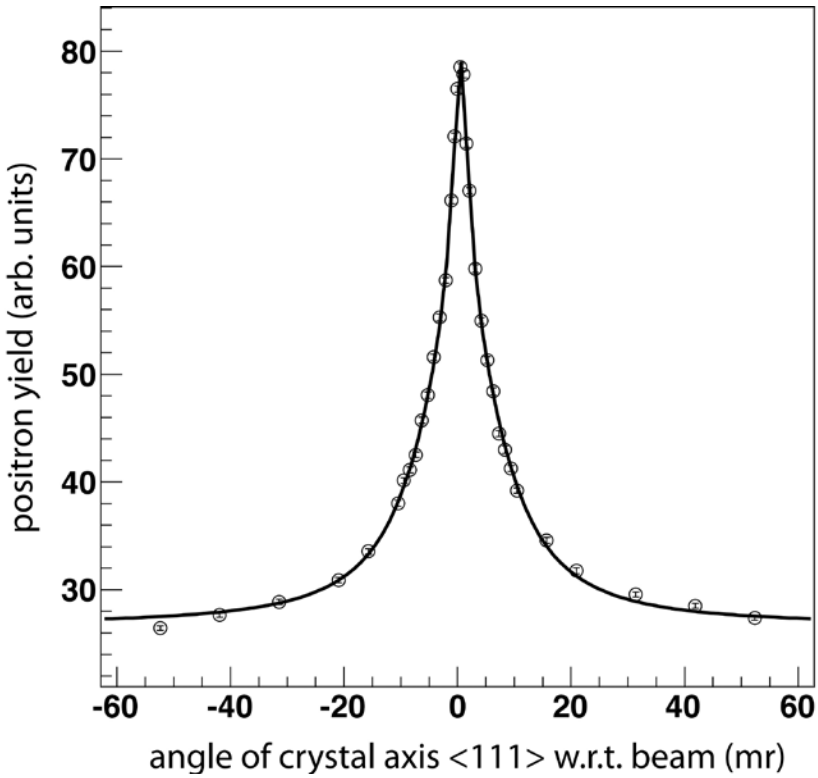

Figure 3.27 Observed positron yield as a function of the incident beam angle with respect to the crystal axis. An enhancement of a factor of approximately 3 is seen at the correct orientation.

3.3.3 Damping ring

The ILC R&D programme identified the key areas for work during the Technical Design Phase:

1. developing methods to suppress the electron cloud instability
2. demonstration of ultra-low vertical emittance operation (vertical emittance of 2 pm)
3. demonstration of fast injection/extraction kickers performance.

Two dedicated test facilities were identified for this effort: CesrTA at Cornell University and ATF at KEK. Both programmes have managed large collaborations, with contributors from institutions worldwide working on simulation, experiment and design.

Electron cloud mitigation

The R&D effort on electron cloud mitigation involves the large international collaboration gathered around the CesrTA programme plus the effort that is in progress at other laboratories.

This successful damping ring R&D endeavour is described in more detail in section 3.1 on the CesrTA programme.

Ultra-low emittance operation

The demonstration of ultra-low emittance was carried out in the framework of the CesrTA and ATF collaborations, but important results have also come from the synchrotron light sources community.

Diagnostics for low-emittance beams at ATF

The ATF damping ring achieved a vertical emittance as low as 4 pm before the publication of the RDR and has supported a wide range of important research for many years: low-emittance tuning and intrabeam scattering studies, studies of the fast ion effect and fast kicker tests. Now the damping ring's main focus is the production of an extracted beam with the required characteristics for the ATF2 programme (see section 3.2) and the development and test of low-emittance beam diagnostics. Instrumentation development includes laser wire, optical transition radiation, optical diffraction radiation, and a high-resolution X-ray monitor *[3-63]*.

Diagnostics and tuning algorithms at CesrTA

The low-emittance tuning effort provides the foundation for studies of the emittance-diluting effects of the electron cloud in a regime approaching that of the ILC damping rings. The vertical emittance goal for the initial phase of the CesrTA programme is less than 20 pm. Low-emittance tuning efforts have focused on the systematic elimination of optical and alignment errors that are the sources of vertical emittance degradation *[3-64]*. Techniques have been developed to eliminate beam position monitor systematic errors, measuring gain variation among the four button-electrodes on each beam position monitor, and to centre the monitors with respect to the adjacent quadrupole. Work has also been carried out to optimise the sextupole design, thus minimising sources of emittance coupling. During the most recent experimental run, this effort resulted in measurements of the vertical emittance consistent with having achieved the target vertical emittance of 20 pm in both single-bunch and multi-bunch operations.

An X-ray beam size monitor has been developed and successfully demonstrated at CesrTA. It is able to measure both integrated and single-bunch turn-by-turn beam sizes at positions for monitoring the progress of the low-emittance tuning of the machine and for beam dynamics related to instabilities driven by the electron-cloud *[3-65, 66]*.

Demonstration of vertical emittance below 2 pm at synchrotron light sources

A step forward in the demonstration of very low vertical emittance has been achieved at some synchrotron light sources, where they operate low-emittance storage rings with characteristics very similar to the ILC damping ring and have developed alignment procedures, machine modelling, tuning algorithms, and orbit stabilisation for coupling correction and low vertical emittance tuning *[3-67]*. In particular, the Diamond Light Source in the UK, the Swiss Light Source and the Australian Synchrotron storage ring have achieved betatron coupling correction down to 0.1% and vertical emittances below 2 pm *[3-68, 69, 70]*. Significant progress has been made in the development of diagnostic systems for the measurement of such small vertical emittances *[3-71, 72, 73]*. The Low Emittance Ring workshop, held at CERN in January 2010 and organised by the joint ILC-CLIC working group on damping rings, was very successful in strengthening the collaboration within the two damping ring design teams and with the rest of the low-emittance rings community, including synchrotron light sources and B-factories.

Performance of fast injection/extraction kickers

ILC-like multi-bunch extraction at ATF

The injection/extraction kickers act as the bunch-by-bunch beam manipulator to compress and decompress the bunch spacing into and from the damping ring. The kickers require high repetition frequency, 3 (or 6) MHz, and very fast rise and fall times of the kicker field: 6 ns for the nominal configuration and 3 ns for a proposed luminosity upgrade. The tolerance on horizontal beam jitter of the extracted beam is approximately 10% of the beam size, which requires the extraction kicker amplitude relative stability to be below 7×10^{-4}.

A rise and fall time of 3 ns has been already demonstrated in the ATF using a 30-cm-long strip-line kicker together with a semiconductor high-voltage pulse source *[3-74]*. The time response of the strip-line kicker was observed by measuring the resulting betatron oscillation amplitude of the stored electron beam.

An ILC-type beam extraction experiment using two strip-line kickers has been carried out at KEK-ATF *[3-75]*. The length of the strip-lines is 60 cm and the gaps of the two electrodes are 9 mm and 11 mm. Two pairs of pulsers with a peak amplitude of 10 kV, a rise time of 1.5 ns and a repetition rate of 3.3 MHz are used to drive the strip-lines. The strip-line kicker system produced a 3-mrad total kick angle for the 1.3-GeV beam. The rise time of the kick field is less than 5 ns.

The multi-bunch beam stored in the damping ring with 5.6-ns bunch distance was successfully extracted with 308-ns bunch spacing in the extraction line *(Figure 3.28)*. No deterioration of the extracted vertical beam size was observed (as measured with the laser wire). The resynchronisation circuit used for precise timing adjustment worked stably. The relative angle jitter of the single bunch beam extraction was 3.5×10^{-4} rms, which is better than the requirements for ILC damping ring extraction. For multi-bunch beam extraction a trigger timing circuit is needed to compensate the time drift of the pulser. Very recently, 30-bunch extraction with an rms angle jitter about 10^{-3} has been achieved. This value can be further reduced by precisely tuning of the timing system or by using a feed-forward system.

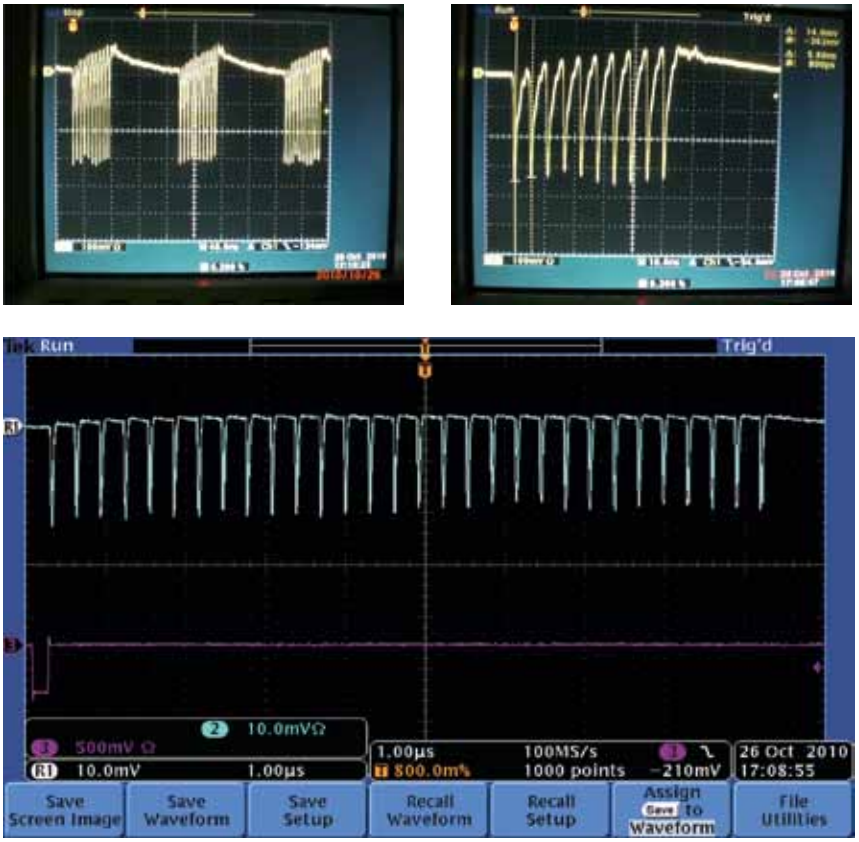

Figure 3.28 ATF damping ring. Top: three trains of ten bunches with 5-ns spacing (right image is a close-up of waveforms seen in the left image). Bottom: 30 bunches extracted with 308-ns spacing.

Strip-line kicker design at DAΦNE

The design of the new, fast strip-line kickers for the injection upgrade of the DAΦNE Φ-factory is based on strip-line tapering to obtain a low-beam impedance device and an excellent uniformity of the deflecting field in the transverse plane *(Figure 3.29) [3-76]*. These characteristics are essential also for the ILC damping ring, and the experience gained with the new DAΦNE injection system will be applied to the damping ring injection system design. The rise and fall times of the kickers are all less than 6 ns, corresponding to the damping ring requirement for the nominal configuration.

The coupling impedance measurements and simulations have pointed out the absence of trapped higher-order modes in the longitudinal and horizontal planes when at least two ports are loaded by 50 watts *[3-77]*. In the vertical plane only four trapped higher-order modes were found. The instability growth rates of these resonances (in the worst case) were well below the damping rates provided by the DAΦNE feedback systems. After installing the injection system, no instability effects due to the kickers were observed and the DAΦNE broadband impedance arising from this and other vacuum chamber modifications made at the same time was reduced by about 50% *[3-78]*.

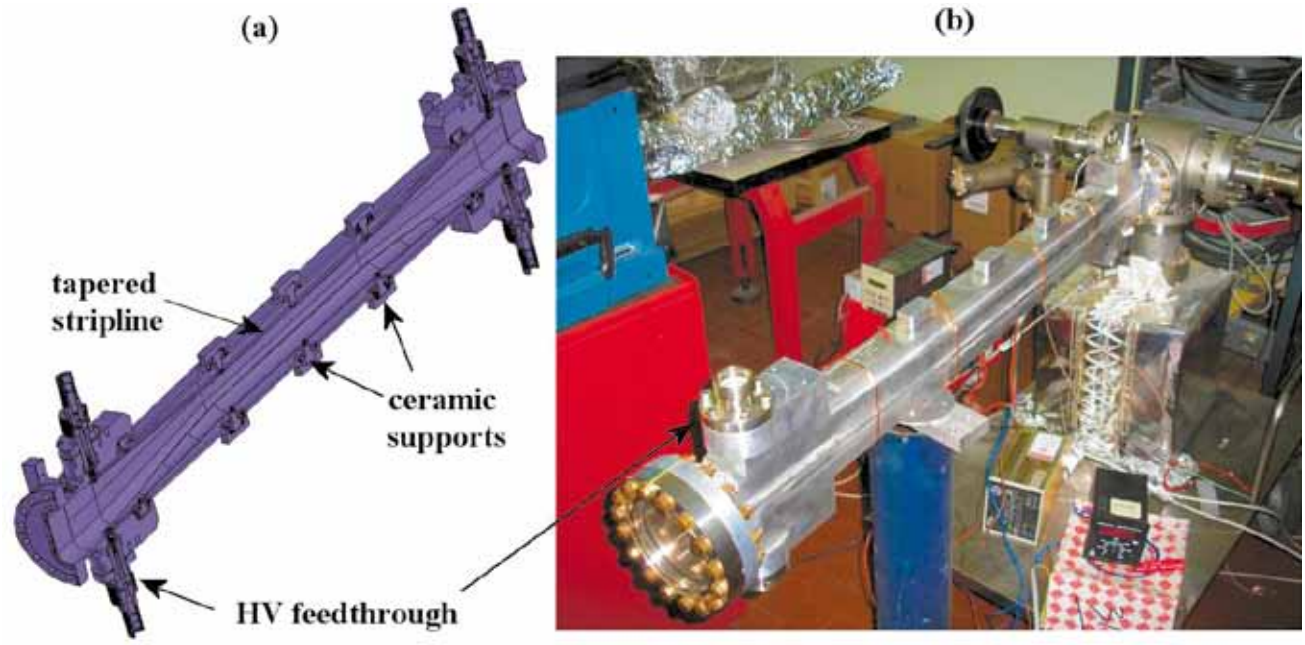

Figure 3.29 DAΦNE strip-line kicker.

SLAC pulser modulator

At SLAC, two related paths to meet the ILC kicker driver requirements are being studied: a transmission line adder topology, which combines the output of an array of ultra-fast MOSFET (metal-oxide-semiconductor field-effect transistor) switches and a drift step recovery diode (DSRD) approach.

For the adder topology, an ultra-fast hybrid MOSFET/driver, recently developed at SLAC, has achieved 1.2-ns switching of 33 amperes at 1,000 volts with a single power MOSFET die *[3-79]*. A transmission-line adder has been designed based on the ultra-fast hybrid MOSFET/driver switching module. The initial test demonstrated that the adder can combine pulses with 1.4-ns switching time without any degradation *[3-80]*. The programme continues to extend the system to the ILC parameters.

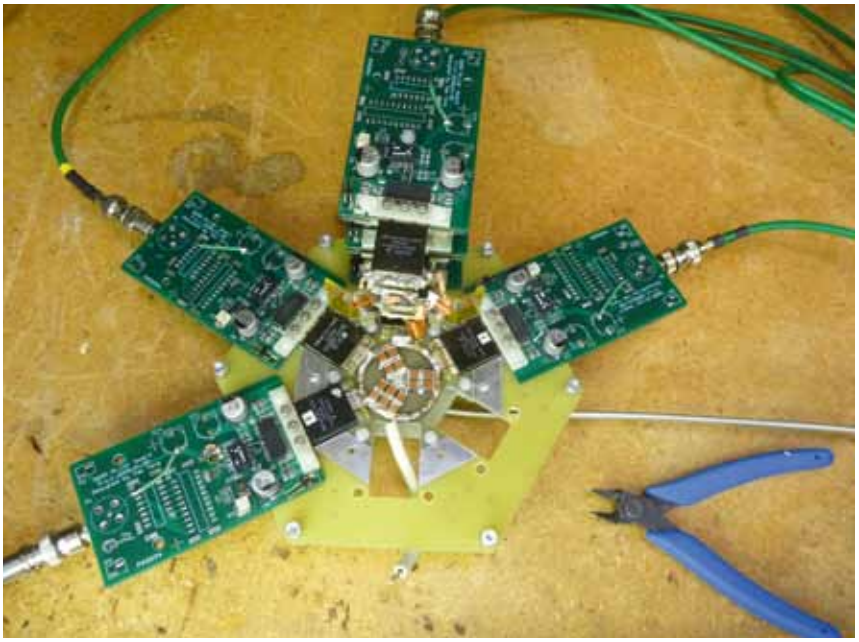

Figure 3.30 A partially assembled drift step recovery diode circuit of a SLAC kicker modulator.

For the DSRD programme, development of a fully capable DSRD kicker driver is proceeding well, with excellent results obtained from the first commercially produced DSRDs, and from a refined circuit for the MOSFET driver *[3-81]*. A prototype with 2-ns pulse length and 1-MHz pulse train has been demonstrated *(Figure 3.30)*. A recent success was to eliminate the post-pulse, which is unacceptable for the ILC kicker driver since it affects the bunches adjacent to the kicked bunch *[3-82]*. The plan is now to build a demonstration modulator for beam testing at ATF.

3.3.4 Beam delivery system

Final doublet design and prototyping

The interaction region magnets are one of the most challenging systems. Design and prototyping of the final-doublet magnets is proceeding and is illustrated in *Figures 3.31* and *3.32*. One particular difference of the present final doublet design with respect to the RDR version is that the last 2-m-long coil defocusing quadrupole (QD0) is split into two separate coils, which allows introduction of a mechanical support point in the middle of the quadrupole cold mass. This modification was found to be necessary during prototyping of the long coil for the final doublet, and will also benefit a proposed modular approach for optimising the optics for low-energy running (shorter QD0). Cryostats have been designed to house the magnets, providing the necessary stable support of the magnet, while being compatible with the requirements of the push-pull arrangement of the detectors.

Figure 3.31 Final doublet magnet design and prototype of the long coil.

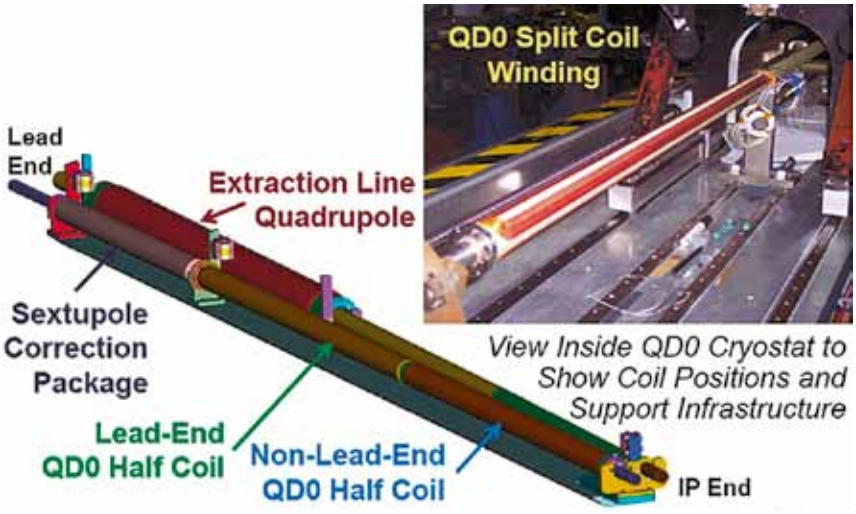

Figure 3.32 Details of design of the final doublet cryostat.

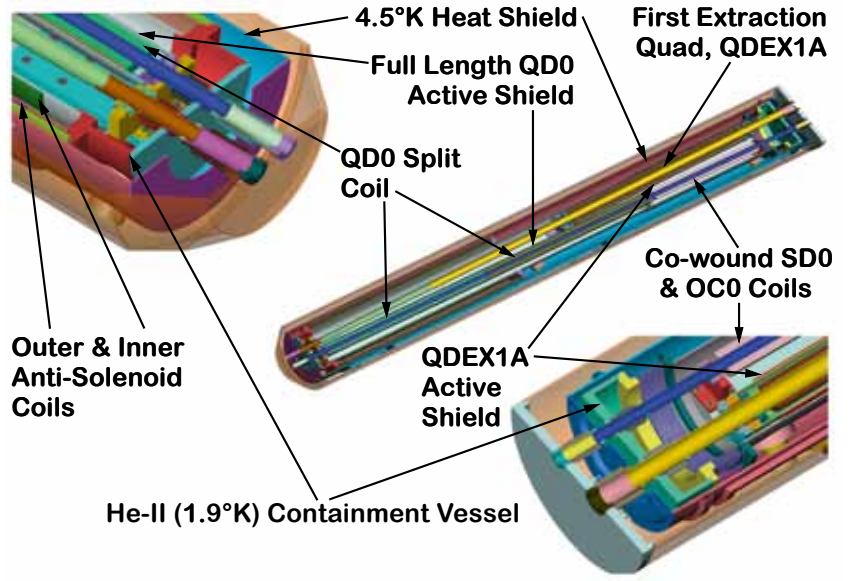

Machine-detector interface

The push-pull system for the two detectors was only conceptual at the time of the publication of the RDR, and since then the engineering design has progressed significantly. A time-efficient implementation of the push-pull model of operation sets specific requirements and challenges for many detector and machine systems, in particular the interaction region magnets, the cryogenics, the alignment system, the beamline shielding, the detector design and their overall integration. The minimal functional requirements and interface specifications for the push-pull interaction region have been successfully developed and published *[3-83]*, to which all further related design work on both the detectors and machine sides are constrained.

The push-pull design needs to accommodate the two detector concepts, the International Large Detector (ILD) and the Silicon Detector (SiD), which are different in their designs, dimensions and mechanical characteristics (such as mechanical rigidity). The different sizes provide particular challenges for the beamline shielding elements, collectively referred to as the pacman shielding. An example of a design of the pacman shielding that ensures compatibility with both detectors is illustrated in *Figure 3.33*.

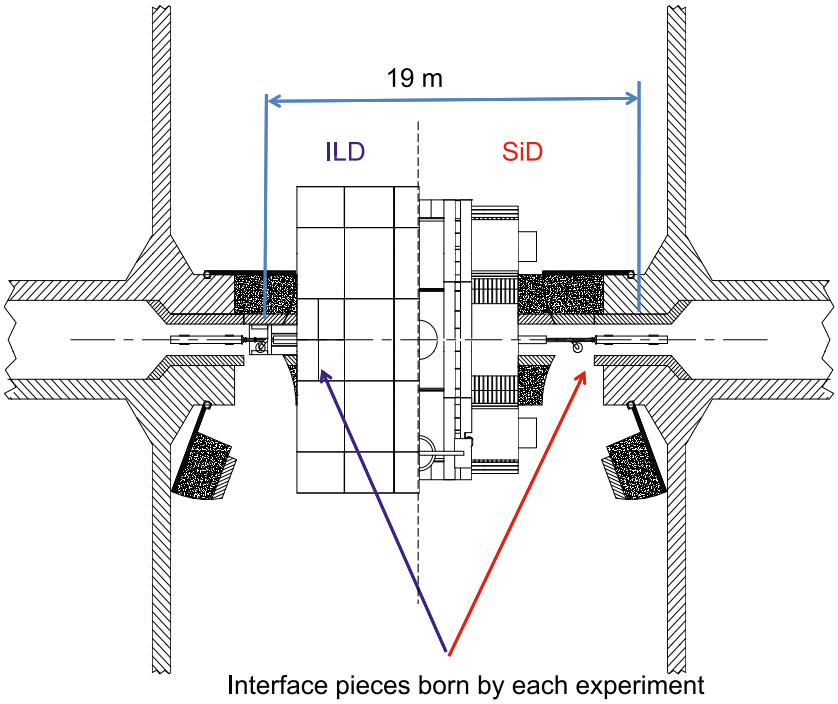

Figure 3.33 Design of the beamline shielding compatible with two detectors of different sizes.

The detector motion and support system has to be designed to ensure reliable push-pull operation, allowing a hundred moves over the lifetime of the experiment while preserving internal alignment of the detector's internal components and ensuring accuracy of detector positioning. The motion system must be designed to preserve structural integrity of the collider hall floor and walls. Moreover, the motion and support system must be compatible with the tens-of-nanometre-level vibration stability of the detector. If the collider is built in a moderate or high seismic region, the system must also be compatible with earthquake safety standards. Two different approaches for the detector support system are currently being considered. The ILD detector is somewhat larger than SiD and is also designed to be assembled from slices in a way similar to the LHC Compact Muon Solenoid detector. The ILD motion system will thus benefit greatly from the use of a rigid platform on which the entire detector can be placed. The platform will preserve detector alignment and will distribute the load evenly onto the floor. Such an approach is illustrated in *Figure 3.34*. The more compact and rigid SiD can be supported naturally by an eight-leg structure as shown on *Figure 3.35*.

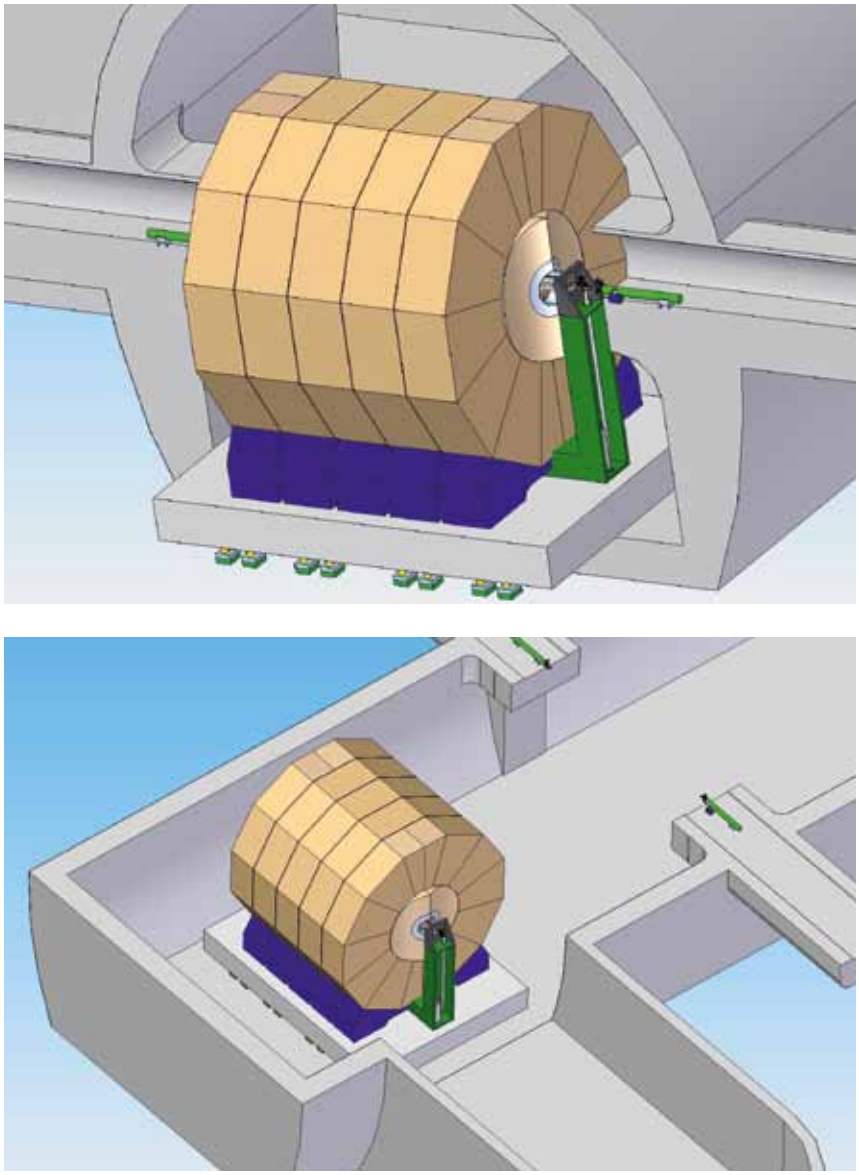

Figure 3.34 Possible platform support concept for the ILD. Left: detector is positioned on the beamline. Right: detector is off the beamline.

The approach for the design of the detector motion system and in particular the use of a platform is currently being investigated. The criteria for selection of the common design will be based on vibration stability analysis of the entire system (detector together with its support and motion system). The selection is planned to happen in the near future.

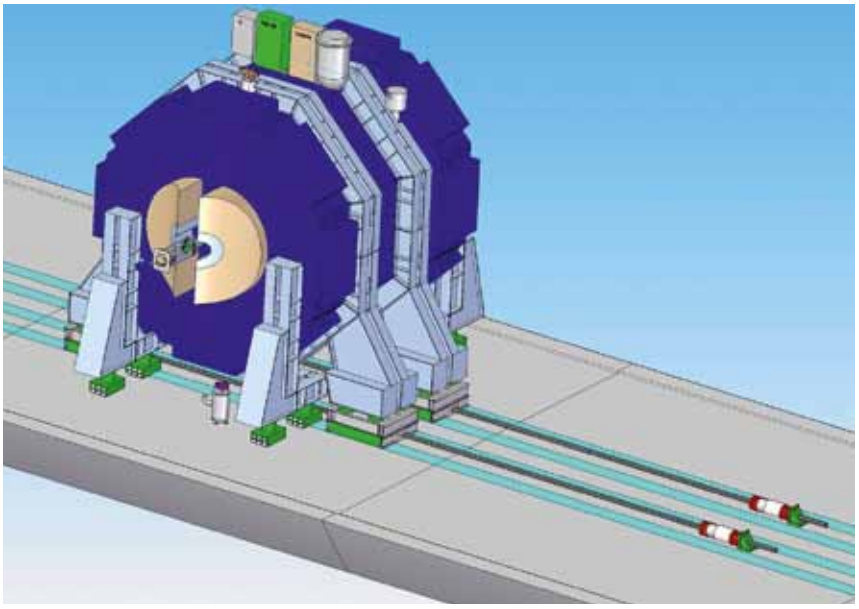

Figure 3.35 Possible detector motion system for SiD.

High-power beam dump systems

High-power beam dumps are essential components of the beam delivery system. The main beam dumps are located at the end of the post-interaction point extraction lines. A further two dumps located further upstream (before the final focus beamlines) are envisaged as tune-up and commissioning dumps. The pressurised water dumps must be capable of dissipating up to 18 megawatts (MW) of average beam power (to accommodate the energy upgrade to 1 TeV centre-of-mass).

The dump design for the beam delivery system is based on the 2.2-MW direct-convection dump developed and successfully operated for the Stanford Linear Accelerator. Water is injected azimuthally with an appropriate velocity near the outer periphery through a water header located parallel to the beam propagation, which gives rise to a vortex flow. The water is collected in a header located along the axis of beam dump. The beam enters the dump off-axis at a location of high-vortex flow. The length of the beam dump is determined by the energy deposited by the beam in the end plate of the dump. The design parameters are chosen to prevent a temperature rise of the water that would result in boiling. A further critical design item is the beam dump window, which needs to be thin enough to survive the beam passage while supporting the water pressure in the dump. The detailed design of the complete beam dump system, including window and cooling system, is currently being developed *[3-84]*. The work includes detailed hydrodynamic simulations of the dump, of which an example is given in *Figure 3.36*. The approximately 1-ms beam pulse is assumed to be rastered by a system of magnets upstream of the dump, which smears the energy distribution in the water and in particular over the millimetre-thin window.

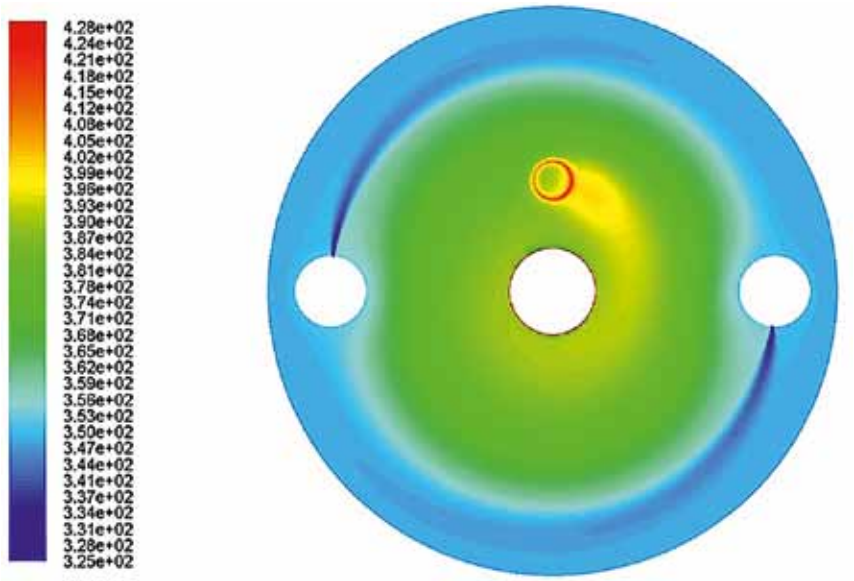

Figure 3.36 Temperature distribution at the shower maximum of the beam in the dump just after passage of the beam train. The colour bar shows temperature in kelvins, with the maximum temperature equal to 155 °C. The water inlets and sink are shown by white areas.

Crab cavity system

A final critical component of the beam delivery system is the crab cavity system, which effectively provides head-on bunch collisions at the interaction point by compensating for the 14-mrad interaction region crossing angle. The radiofrequency (RF) transverse deflecting cavity 'tilts' the bunches at the interaction point. Design and prototyping of the crab cavity has recently demonstrated that the key performance characteristic of the system – the relative phase stability between electron and positron crab-cavities – can be achieved. RF tests of the prototype system have demonstrated an rms phase stability better than 0.1 degrees *[3-85]*, which is already close to the required ILC specification (0.08 degrees). Further improvements have been identified.

3.3.5 Beam dynamics and simulation

The luminosity performance of the ILC relies heavily on the ability to preserve the ultra-low emittances produced in the damping rings as the beams are transported and accelerated to the interaction point. The major sources of performance degradation arise from component alignment and instrumentation errors. Quantifying the expected performance can only be made via sophisticated simulations, ideally of the whole accelerator, which include models of the various tuning algorithms to be applied in the real machine.

The work continues with refinement of the models, and inclusion of new effects. In this way the simulation models become more realistic, and confidence is gained in the projected performance. Since publication of the *Reference Design Report,* many design modifications have also been proposed and accepted (see chapter 4), and the impact of these modifications on the beam dynamics generally needs re-evaluation.

For the ring-to-main-linac system, two major changes in configuration have been considered: a single-stage bunch compressor instead of the two-stage bunch compressor considered for the RDR, and lattice modification in the central area necessitated by the new layout of damping rings. Additional beam dynamics effects extensively studied since the RDR include coupler wakefield and RF kicks in the superconducting cavities *[3-86, 87, 88]*.

During the studies for the RDR, the effort's main focus was on the main linacs and the beam delivery system. The ring-to-main-linac – which includes the long transport line from the damping rings, a 180-degree turnaround, spin rotation sections and bunch compressor – had not been studied in any great detail, but this has since been rectified. The results of emittance preservation studies for the section of the ring-to-main-linac up to but not including the bunch compressor are shown in *Figure 3.37.* The final average vertical emittance growth is 5.36 nm, or approximately 27% of the damping ring extracted emittance of 20 nm.

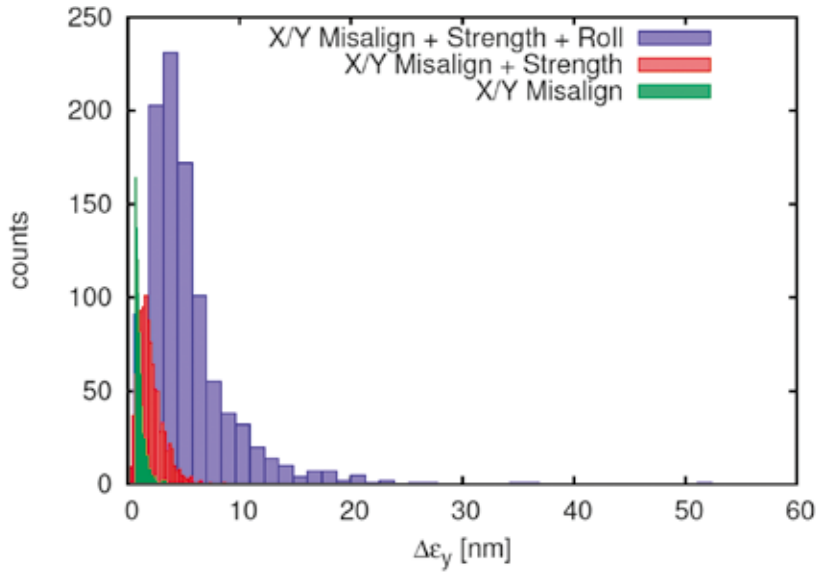

Figure 3.37 Histogram of final vertical rms emittance growth (1,000 random seeds of alignment errors), with the inclusion of the specified errors: X/Y transverse offsets only (green); addition of magnet strength errors (red); addition of magnet roll (alignment) errors (blue). The simulation model is based on realistically achievable error specifications; the results reflect the achieved performance after application of beam-based tuning algorithms.

The average vertical emittance growth in the single-stage bunch compressor itself (including all errors) is 2.3 nm, after application of dispersion-free steering, dispersion-generating trajectory bumps and small adjustments to the cryomodule tilt in the RF sections of the compressor. The vertical emittance growth for the entire ring-to-main-linac does not exceed 7.6 nm on average in the current simulations.

The effect of possible time-varying stray magnetic fields in the long transport line was found to be quite significant; uncorrected field variations of about 5 nanoteslas rms results in vertical beam jitter of about 50 percent of the beam size. This induces emittance growth of about 1 nm in the turnaround, though the orbit jitter downstream will be corrected after feed-forward correction *[3-89]*. Experimental data shows that stray field at frequencies above 1 Hz can be controlled at this level, but more studies are needed on this issue *[3-90]*.

For the main linacs, the impact of static uncorrelated random errors has been well studied using simulations for the RDR, with the average emittance growth typically measuring around 5 nm *[3-91]*. There is possible scope to reduce this further with the application of additional tuning strategies. More recent studies on long-range alignment- and survey-correlated errors *[3-92]* have indicated potential problems, but these appear to be strongly dependent on the survey and alignment models used and are currently inconclusive.

Effects of coupler wakefield and RF kicks have also been studied in the main linacs. The effects are much less than in the bunch compressors because of the shorter bunch length and are not considered serious.

Effects of dynamic (i.e., time-dependent) errors have been studied as well. Assumed dynamic errors and expected orbit change and emittance growth due to each of the errors are summarised in *Table 3.6*.

Table 3.6 Simulated effects of some dynamic (i.e., time-dependent) errors in the main linacs

	Assumption	**Beam jitter at linac exit**	**Emittance dilution at linac exit**
Quad offset change (vibration)	100 nm	1.5 s	0.2 nm
Magnet strength jitter	10^{-4}	1 s	0.1 nm
Cavity tilt change	3 mrad	0.8 s	0.5 nm
Cavity-to-cavity strength change	1%	0.8 s	0.5 nm

The significance of a change in the accelerating voltage of individual cavities in combination with mechanical tilt of the cavity (static alignment error) – particularly within the approximately 1-ms pulse – has recently become a focus of attention. The effect leads to trajectory errors of individual bunches in a bunch train. While these trajectory errors (which are relatively slow over the 1-ms pulse) can easily be corrected with feedback (or feed-forward) at the end of the linac, the variation in trajectories in the main linacs gives rise to emittance growth of individual bunches (in accordance with the numbers in *Table 3.6)*. With the assumption of 300-mrad rms random cavity tilts, the voltages in the individual cavities need to be corrected to the level of a few percent over the pulse, which is quite challenging[1]. *Figure 3.38* shows the simulated average emittance growth along a main linac, assuming 5% rms accelerating voltage jitter with 300-mrad rms static cavity tilt error, both in the cases without orbit correction and with orbit correction at 50-GeV beam energy *[3-93]*.

[1] Note that the radiofrequency feedback control corrects the sum energy gain of many cavities to a 0.1% level, but not the individual cavity voltages themselves.

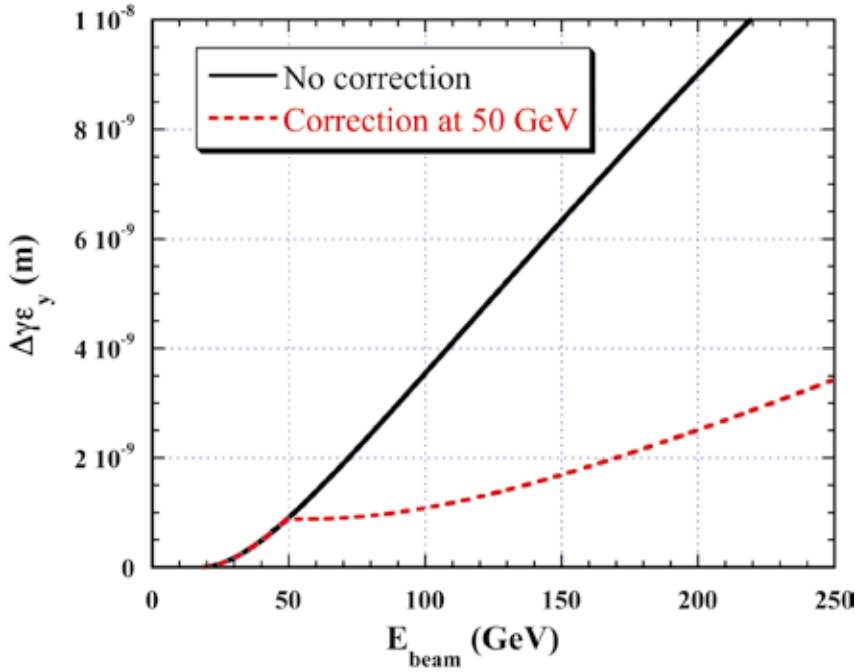

Figure 3.38 Calculated average emittance growth along a main linac, assuming 5% rms random cavity accelerating voltage jitter, with 0.3-mrad rms static cavity tilt random error. The solid line indicates the expected vertical emittance growth for the entire linac, while the dashed line shows the impact of having an additional fast trajectory correction at the nominal 50 GeV point.

An example of the beam delivery system luminosity tuning simulation for static errors is shown in *Figure 3.39*. Vertical emittance at the entrance of the beam delivery system was assumed to be 34 nm, which also assumes an emittance growth of 15 nm for the ring-to-main-linac and main linacs combined. The results show that, for the given assumptions on static errors and input conditions, all random seeds exceed the design luminosity after application of the beam-based tuning algorithms. (Similar simulations have been performed for ATF2, where the results will be experimentally verified.)

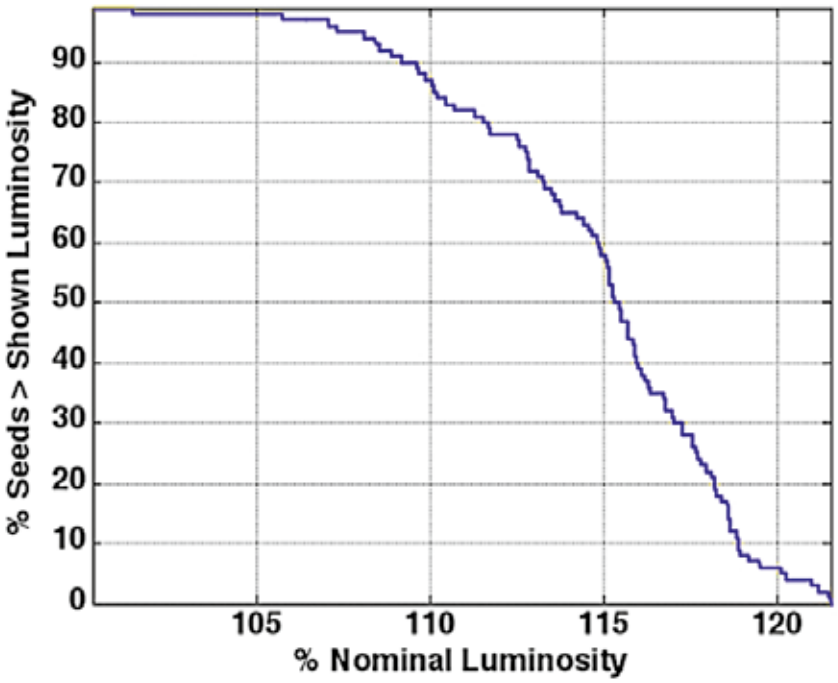

Figure 3.39 Results of simulation of the luminosity tuning in the beam delivery system. The vertical axis indicates the ratio of the random seeds simulated that results in a relative luminosity greater than values in the horizontal axis [3-94].

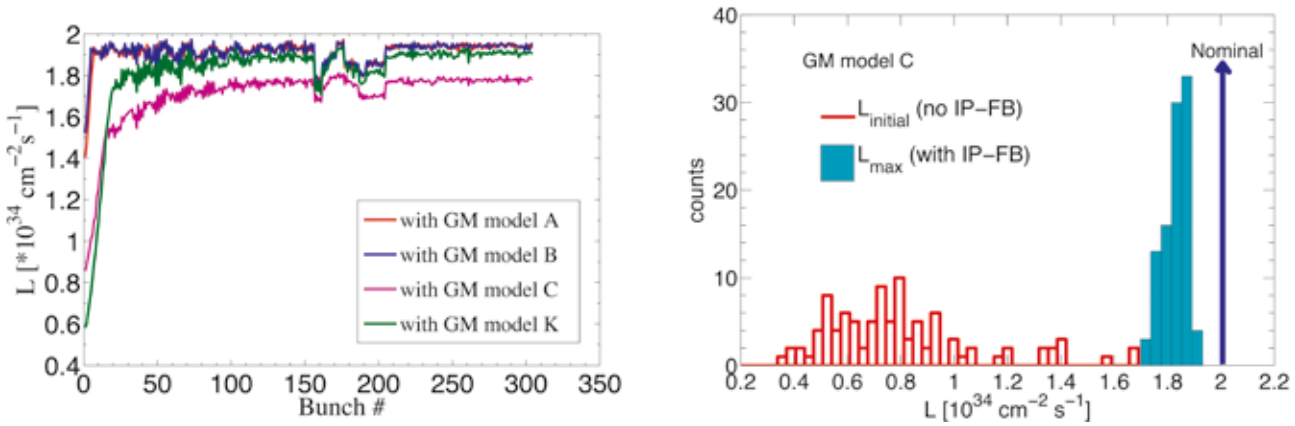

Figure 3.40 Time-dependent luminosity modelling in the beam delivery system. Left: the luminosity is shown as a function of bunch number for the first 300 bunches of a pulse for various ground motion (vibration) models. The luminosity is quickly recovered by the beam-beam fast feedback. Right: a histogram of the results of 100 seeds, assuming model C, as referenced in the left graph, for the ground motion, with and without intra-pulse orbit feedback [3-95].

Effects of dynamic (time-dependent) errors have been also simulated in the beam delivery systems. For example, *Figure 3.40* shows the luminosity performances for specific models of ground motion and vibration. The primary effect is a beam-beam offset at the interaction point, which is quickly compensated for by the intratrain fast feedback

A key parameter is the maximum allowed vibration of the final doublet. This is primarily set by the limitations of the interaction-point fast feedback, which becomes increasingly ineffective for larger beam-beam offsets. *Figure 3.41* shows the luminosity as function of rms offset of both final-doublet cryomodules. The allowed rms final doublet offset tolerances has been conservatively specified as 50 nm.

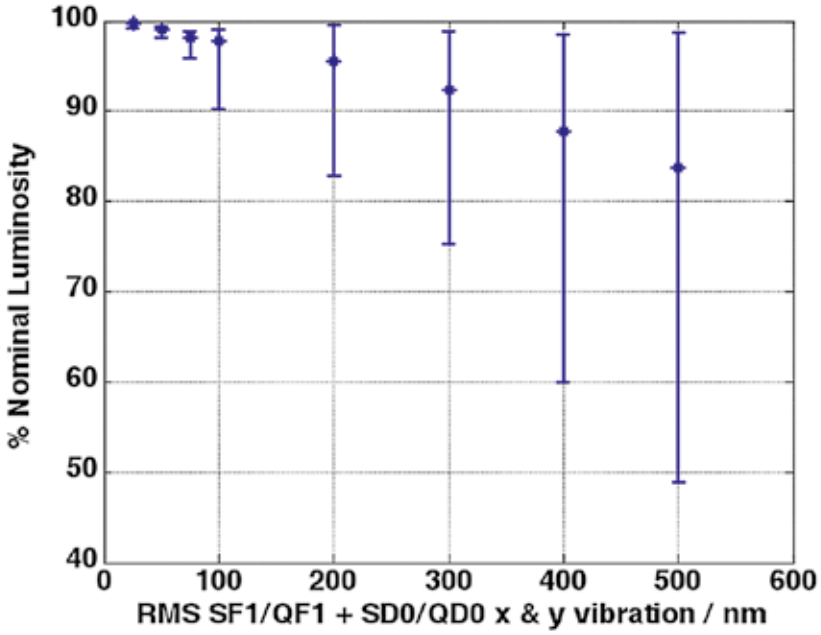

Figure 3.41 Simulated luminosity as function of rms offset of both final doublet cryomodules. Mean and standard deviation from tracking simulation are shown [3-94].

While work continues on a complete integrated simulation, including all static and dynamic effects and tuning and feedback, the current results suggest that the goal luminosity is likely to be achievable to within 10%, providing the alignment tolerances and other input assumptions in the simulations can be realistically achieved.

References

[3-1] M.A. Palmer, et al., "Electron Cloud at Low Emittance in CESRTA," Proceedings of IPAC'10, Kyoto, Japan (2010) and references therein.

[3-2] The CesrTA Collaboration includes senior researchers from the following institutions: ANL, Australian Synchrotron, BNL, California Polytechnic State Univ., Carleton Univ., CERN, the Cockroft Institute, FNAL, INFN-LNF, KEK, LBNL, Purdue University, SLAC and Technion-Haifa.

[3-3] http://www.lns.cornell.edu/Events/ECLOUD10/WebHome.html

[3-4] https://wiki.lepp.cornell.edu/ilc/bin/view/Public/DampingRings/WebHome#Working_Group_on_Electron_Cloud

[3-5] M.T.F. Pivi, et al., "Recommendation for the Feasibility of More Compact LC Damping Rings," Proceedings of IPAC'10, Kyoto, Japan (2010).

[3-6] http://www.lns.cornell.edu/Events/ECLOUD10/ILCDampingRingsSatelliteMeeting.html

[3-7] M.A. Palmer, et al., "The Conversion and Operation of the Cornell Electron Storage Ring as a Test Accelerator (CESRTA) for Damping Rings Research and Development," Proc. of PAC09, Vancouver, Canada (2009), and references therein.

[3-8] Y. Li, et al., "CesrTA Vacuum System Modifications," Proceedings of PAC09, Vancouver, British Columbia, Canada (2009).

[3-9] D. Rice, "CESR-c: A Wiggler-dominated Collider," Proceedings of PAC07, Albuquerque, New Mexico, USA (2007).

[3-10] M.A. Palmer, et al., "CESR Beam Position Monitor System Upgrade for CesrTA and CHESS Operations," Proceedings of IPAC10, Kyoto, Japan (2010).

[3-11] J. Alexander, et al., "CesrTA X-Ray Beam Size Monitor Design," Proceedings of PAC09, Vancouver, British Columbia, Canada (2009).

[3-12] M.A. Palmer, et al., "Design, Implementation and First Results of Retarding Field Analyzers Developed for the CesrTA Program," Proceedings of PAC09, Vancouver, British Columbia, Canada (2009).

[3-13] Y. Li, et al., "Design and Implementation of CesrTA Superconducting Wiggler Beampipes with Thin Retarding Field Analyzers," Proceedings of PAC09, Vancouver, British Columbia, Canada (2009).

[3-14] S. De Santis, et al., "The TE Wave Transmission Method for Electron Cloud Measurements at CesrTA," Proceedings of PAC09, Vancouver, British Columbia, Canada (2009).

[3-15] M.G. Billing, et al., "Techniques for Observation of BeamDynamics in the Presence of an Electron Cloud," Proceedings of IPAC'10, Kyoto, Japan (2010).

[3-16] D. Rubin, et al., "CesrTA Layout and Optics," Proceedings of PAC09, Vancouver, British Columbia, Canada (2009).

[3-17] J.R. Calvey, et al., "CesrTA Retarding Field Analyzer Measurements in Drifts, Dipoles, Quadrupoles and Wigglers," Proceedings of IPAC'10, Kyoto, Japan (2010).

[3-18] J.R. Calvey, et al., "Electron Cloud Mitigation Investigations at CesrTA," to be published in the proceedings of the ECLOUD'10 workshop, Ithaca, New York, USA (2010).

[3-19] J.R. Calvey, et al., "CesrTA Retarding Field Analyzer Modeling Results," Proceedings of IPAC'10, Kyoto, Japan (2010).

[3-20] J.R. Calvey, et al., "Methods for Quantitative Interpretation of Retarding Field Analyzer Data," to appear in the Proceedings of the ECLOUD10 Workshop, Ithaca, New York, USA (2010).

[3-21] S. De Santis et al., "Characterization of Electron Clouds in the Cornell Electron Storage Ring Test Accelerator using TE-Wave Transmission," Phys. Rev. ST Accel. Beams 13:071002 (2010).

[3-22] G. Penn, J-L. Vay, "Theoretical Studies of TE-Wave Propagation as a Diagnostic for Electron Cloud," Proceedings of IPAC'10, Kyoto, Japan (2010).

[3-23] K. Sonnad, et al., "Simulations Using VORPAL on the Effect of Imperfections and Nonuniformities in TE Wave Propagation Through Electron Clouds," to appear in the Proceedings of the ECLOUD10 Workshop, Ithaca, NY, USA (2010).

[3-24] S. Veitzer, et al., "Modeling Electron Cloud Buildup and Microwave Diagnostics Using Vorpal," to appear in the Proceedings of the ECLOUD10 Workshop, Ithaca, NY, USA (2010).

[3-25] J. Crittenden, et al., "Electron Cloud Modeling Results for Time-resolved Shielded Pickup Measurements at CesrTA," to appear in the Proceedings of the ECLOUD10 Workshop, Ithaca, NY, USA (2010).

[3-26] Y. Suetsugu, et al., "Demonstration of Electron Clearing Effect by Means of Clearing Electrodes and Groove Structures in High-Intensity Positron Ring", proc. of PAC09, Vancouver, Canada (2009).

[3-27] C. Yin Vallgren, et al., "Amorphus Carbon Coatings for Mitigation of Electron Cloud in the Cern SPS," Proceedings of IPAC'10, Kyoto, Japan (2010).

[3-28] L. Wang and M.T.F. Pivi, "Electron Trapping in Wiggler and Quadrupole Magnets of CesrTA," Proceedings of IPAC'10, Kyoto, Japan (2010).

[3-29] J.P. Shanks, et al., "CesrTA Low Emittance Tuning," Proceedings of IPAC'10, Kyoto, Japan (2010).

[3-30] D.P. Peterson, et al., "CesrTA X-Ray Beam Size Monitor Operation," Proceedings of IPAC'10, Kyoto, Japan (2010).

[3-31] J. Crittenden, et al., "Studies of the Effects of Electron Cloud Formation on Beam Dynamics at CesrTA," Proceedings of PAC09, Vancouver, British Columbia, CA (2009).

[3-32] J. Crittenden, et al., "Progress in Studies of Electron Cloud – Induced Optics Distortions at CesrTA," Proceedings of IPAC'10, Kyoto, Japan (2010).

[3-33] G. .Dugan, et al., "Synrad3D Photon Propagation and Scattering Simulation," to appear in the Proceedings of the ECLOUD10 Workshop, Ithaca, NY, USA (2010).

[3-34] G. .Dugan, et al., "CesrTA EC-Induced Beam Dynamics," to appear in the Proceedings of the ECLOUD10 Workshop, Ithaca, NY, USA (2010).

[3-35] J.W. Flanagan, et al., "Measurement of Low-Emittance Beam with Coded Aperture X Ray Optics at CesrTA," Proceedings of IPAC'10, Kyoto, Japan (2010).

[3-36] J.W. Flanagan, et al., "xBSM Bunch-by-Bunch Measurements in EC Conditions at CesrTA," to appear in the Proceedings of the ECLOUD10 Workshop, Ithaca, NY, USA (2010).

[3-37] K. Ohmi, et al., "Electron Instability in Low Emittance Rings, CesrTA and SuperKEKB," to appear in the Proceedings of the ECLOUD10 Workshop, Ithaca, NY, USA (2010).

[3-38] M.T.F. Pivi, et al., "ILC Damping Ring Electron Cloud R&D Effort and Single-Bunch Instability Simulations Using CMAD," to appear in the Proceedings of the ECLOUD10 Workshop, Ithaca, NY, USA (2010).

[3-39] M. Palmer, et al., "CesrTA Preliminary Recommendations for the ILC Positron Damping Ring," to appear in the Proceedings of the ECLOUD10 Workshop, Ithaca, NY, USA (2010).

[3-40] M. T.F. Pivi, et al, "Secondary Electron Yield Measurements and Groove Chambers Update Tests in the PEP-II Beam Line," 691, proc. of EPAC08, Genova, Italy, 2008.

[3-41] M. T.F. Pivi, et al., "A New Chicane Experiment in PEP-II to Test Mitigations of the Electron Cloud Effect for Linear Colliders," 688, proc. of EPAC08, Genova, Italy, 2008.

[3-42] Y. Suetsugu, et al., Nucl.Instrum. Methods A598 (2008) 372.

[3-43] Y. Suetsugu, et al., "Experimental Studies on Grooved Surfaces to Suppress Secondary Electron Emission," Proceedings of IPAC'10, Kyoto, Japan, 2010.
[3-44] Y. Suetsugu, et al, "Beam Tests of a Clearing Electrode for Electron Cloud Mitigation at KEKB Positron Ring," Proceedings of IPAC'10, Kyoto, Japan, 2010.
[3-45] D. Alesini, et al., "Design and Test of the Clearing Electrodes for e- cloud Mitigation in the e+ DAFNE Ring," Proceedings of IPAC'10, Kyoto, Japan, 2010.
[3-46] M. Pivi, "Recommendation for the ILC DR EC mitigations," slides 20-49, IWLC2010 Workshop, CERN, October 2010, http://ilcagenda.linearcollider.org/materialDisplay.py?contribId=544&sessionId=83&materialId=slides&confId=4507
[3-47] P. Bambade et al., Phys. Rev. ST Accel. Beam 13, 042801 (2010), and references therein.
[3-48] V. Balakin and A. Mikhailichenko, Preprint INP-79-85, 1979. See also K. Flöttmann, DESY-93-161, 1993.
[3-49] Y. Ivanyushenkov et al, PAC 2007, Albuquerque, p2865.
[3-50] A. Mikhailichenko, PAC 2007, Albuquerque, p1974.
[3-51] E. Baynham et al, PAC 2009, Vancouver.
[3-52] J. A. Clarke, http://ilcagenda.linearcollider.org/getFile.py/access?contribId=462&sessionId=77&resId=0&materialId=slides&confId=4507, IWLC 2010, Geneva.
[3-53] G. Ellwood, http://indico.cern.ch/getFile.py/access?contribId=6&resId=0&materialId=slides&confId=109166, EUCARD-WP7-HFM collaboration meeting, Nov 2010, CERN.
[3-54] S.P. Antipov et al., PAC 2007 Albuquerque, p2909.
[3-55] I.R. Bailey et al., EPAC 2008, Genoa, p715.
[3-56] I.R. Bailey et al., IPAC 2010, Kyoto, p4125.
[3-57] I.R. Bailey, http://ilcagenda.linearcollider.org/getFile.py/access?contribId=485&sessionId=83&resId=0&materialId=slides&confId=4507, IWLC 2010, Geneva.
[3-58] J. Gronberg et al, IPAC 2010, Kyoto, p4137.
[3-59] Wanming Liu and Wei Gai, IPAC 2010, Kyoto, p4134.
[3-60] T. Omori, http://ilcagenda.linearcollider.org/getFile.py/access?contribId=475&sessionId=77&resId=1&materialId=slides&confId=4507, IWLC 2010, Geneva.
[3-61] T. Takahashi, http://ilcagenda.linearcollider.org/materialDisplay.py?contribId=471&sessionId=77&materialId=slides&confId=4507, IWLC2010, Geneva.
[3-62] V. Yakimenko, http://ilcagenda.linearcollider.org/getFile.py/access?contribId=487&sessionId=83&resId=1&materialId=slides&confId=4507, and T. Omori, http://ilcagenda.linearcollider.org/getFile.py/access?contribId=486&sessionId=83&resId=0&materialId=slides&confId=4507, IWLC2010, Geneva.
[3-63] J. Urakawa, "Results From DR and Instrumentation Test Facilities," Proceedings of PAC2005, Knoxville, Tennessee, 2005
[3-64] J. P. Shanks, D. Rubin, D. Sagan, "CesrTA Low Emittance Tuning," Proceedings of IPAC'10, Kyoto, Japan, 2010.
[3-65] D.P. Peterson et al., "CesrTA x-Ray Beam Size Monitor Operation," Proceedings of IPAC'10, Kyoto, Japan, 2010.
[3-66] J.W. Flanagan et al., "Measurement of Low-Emittance Beam with Coded Aperture X Ray Optics at CesrTA," Proceedings of IPAC'10, Kyoto, Japan, 2010.
[3-67] R. Bartolini, "Performance and Trends of Storage Ring Light Sources," Proceedings of EPAC08, Genoa, Italy, 2008
[3-68] R. Bartolini, "Light Sources Trends and Common Design Issues with Low Emittance Rings," LER10, Low Emittance Rings Workshop, CERN 12-15 Jan. 2010. http://indico.cern.ch/materialDisplay.py?contribId=92&sessionId=21&materialId=paper&confId=74380
[3-69] M. Böge et al., "The Swiss Light Source a "Test-bed" for Damping Ring Optimization," Proceedings of IPAC10, Kyoto, Japan, 2010
[3-70] R. Dowd, et al., "Emittance Coupling Control at the Australian Synchrotron," Proceedings of PAC09, Vancouver, BC, Canada, 2009.
[3-71] G. Rehm, "Recent Development of Diagnostics on 3rd Generation Light Sources," Proceedings of EPAC08, Genoa, Italy, 2008
[3-72] C. Thomas et al., PRSTAB, 13, 022805, 2010
[3-73] A. Andersson, et al, Nucl. Instrum. Methods Phys. Res., Sect. A 591, 437, 2008.
[3-74] T. Naito et al., "Development of a 3ns rise and fall time strip-line kicker for the International Linear Collider," NIM A571(2007) 599-607.
[3-75] T. Naito, et al., "Multi-Bunch Beam Extraction Using Strip-Line Kicker at KEK-ATF," Proceedings of IPAC'10, Kyoto, Japan, 2010.
[3-76] D. Alesini et al., "Design and Tests of New Fast Kickers for the DAFNE Collider and the ILC Damping Rings," Proceedings of EPAC 2006, Edinburgh, Scotland, 2006.
[3-77] F. Marcellini, et al., "Tests and Operational Experience with the DAFNE Stripline Injection Kicker," Proceedings of PAC09, Vancouver, BC, Canada, 2009.
[3-78] F. Marcellini, et al., "Coupling Impedance of DAFNE Upgraded Vacuum Chamber," Proceedings of EPAC08, Genoa, Italy, 2008.
[3-79] T. Tang, C. Burkhart, "Hybrid MOSFET/Driver for ultra-fast switching," IEEE Trans. on Dielectrics and Electrical Insulation, Aug. 2009, in press.
[3-80] T. Tang, C. Burkhart, "Development of an Adder-Topology ILC Damping Ring Kicker Modulator," Proceedings of PAC09, Vancouver, BC, Canada
[3-81] F. Arntz et al., "A Kicker Driver Exploiting Drift Step Recovery Diodes for the International Linear Collider," Proceedings of EPAC08, Genoa, Italy, 2008
[3-82] C. Burkhart, et al., "Ultra-Fast Damping Ring Kicker Modulator Development at SLAC," IWLC2010 Workshop, CERN, October 2010.
[3-83] ILC-NOTE-2009-050
[3-84] BARC references
[3-85] Crab cavity Cockcroft Institute reference
[3-86] N. Solyak et al., "Final Results on RF- and Wake- Kicks Caused by the Couplers in the ILC Cavity," ICAP 2009, San-Francisco
[3-87] A.Latina et al., "Emittance Dilution Caused by the Couplers in the Main Linac and in the BC of the ILC," PAC 09
[3-88] Dirk Kruecker, ILC-LET Workshop, SLAC, Dec.2007
[3-89] A.Latina, ILC-CLIC Workshop, Geneva, Oct. 2010
[3-90] K. Kubo, ILC-Asia Note 2006-05, 2006
[3-91] Dmitri Sergatskov, ILC-CLIC LET Beam Dynamics Workshop, CERN, June 2009
[3-92] John Dale, ILC-CLIC LET Beam Dynamics Workshop, CERN, June 2009
[3-93] K. Kubo, ILC-CLIC Workshop, Geneva, Oct. 2010
[3-94] G.White, ILC-LET Workshop, SLAC, Dec.2007
[3-95] J. Resta-Lopez, ILC-CLIC Workshop, Geneva, Oct. 2010

04

ACCELERATOR DESIGN & INTEGRATION

4.1 Evolving design beyond the *Reference Design Report*

The design of the ILC continues to evolve from the 'conceptual design' presented in the *Reference Design Report* (RDR) *[4-1]* towards a more mature 'technical design'. The ongoing modifications to the design are based on the results of continuing R&D on technical systems, on engineering design of these systems and their integration with the civil engineering layouts, designs and supporting services.

At the time of the RDR's publication in 2007, it was envisaged that an *Engineering Design Report* could be completed by late 2010. However, by early 2008 it became clear that the resources required were not available, so the two-stage technical design phase shifted its focus to risk-mitigating R&D (see chapter 1). Many technical system designs at the time were already evolving with improved performance, and many ideas for perhaps lower-cost schemes were being proposed for study. In order to consolidate and prioritise these developments in an integrated fashion, it was proposed that a modified formal baseline design be developed by the end of Technical Design Phase 1. The new baseline will form the basis of the technical work and updated cost estimate to be published in the *Technical Design Report* at the end of 2012.

The accelerator design and integration studies in Technical Design Phase 1 have evolved into a total design review of the older RDR parameters, technical and civil system designs and their integrated layouts. The supporting technical R&D programmes are described in chapters 2 and 3 and development of the civil system designs in section 5. The proposed integrated design and layout is described below in section 4.3.

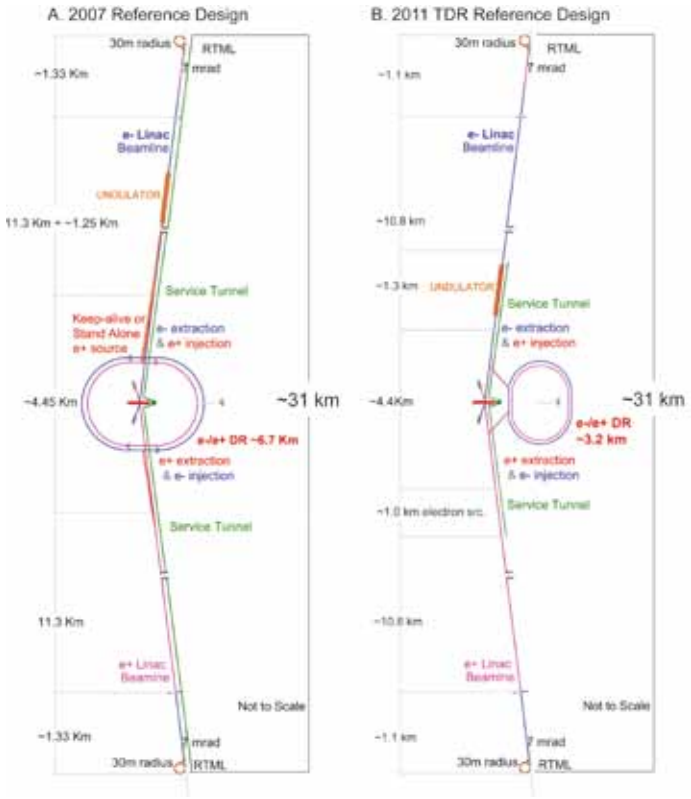

Figure 4.1 Schematics of (a) the 2007 published *Reference Design Report* and (b) the modified reference baseline for the *Technical Design Report.* Most prominent is the modified damping ring geometry and the integration of both positron (undulator) and electron sources into the central region. Removal of the main linac service tunnel is also indicated.

4.2 Layout and Design

4.2.1 Main linear accelerators

Schematics of the ILC layout are shown in *Figure 4.1* as (a) proposed in the RDR and (b) with the proposed technical and civil engineering changes for 2010. The primary system parameters that have not changed are those of the main electron and positron linacs, which remain the same length, a reflection of the fact that after extensive review, there is no proposed change in the maximum average accelerating gradient of 31.5 megavolts per metre (MV/m). The linear accelerators, or linacs, also remain oriented to provide the 14-milliradian (mrad) crossing angle between the two particle beams required at the interaction point.

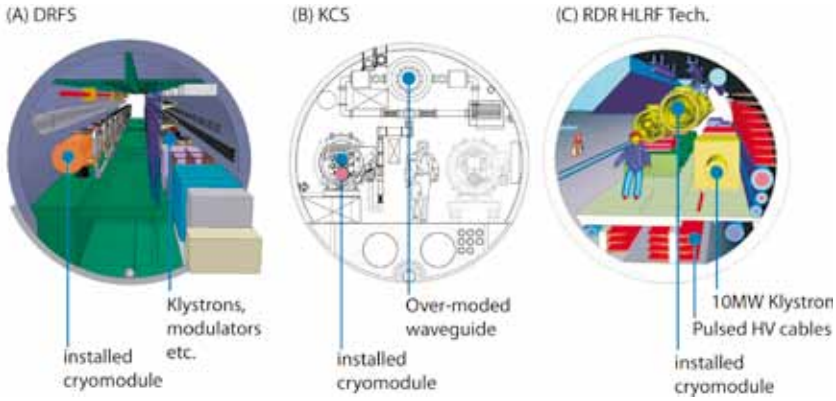

Figure 4.2 Single-tunnel solutions for the main linacs: (a) distributed radiofrequency sources, where many small modular 800-kilowatt klystrons, modulators and associated power supplies are all installed in the tunnel; (b) klystron cluster system, where no active RF is installed in the tunnel, and the RF power is brought to the accelerator via long high-power over-moded waveguide system; and (c) the solution adopted for the European X-ray Free Electron Laser (ILC backup solution), where the 10-MW klystrons are installed in the tunnel, but driven by surface-located modulators connected via many high-voltage pulsed cables.

The major change is the removal of the separate so-called service tunnel for the main linacs, in which the radiofrequency (RF) power sources, power supplies and electronics were originally located. This is a significant reduction in underground tunnel volume that benefits both costs and construction schedules. Two novel solutions for the RF power systems have been proposed in support of the single tunnel solution: the distributed radiofrequency sources scheme and the klystron cluster scheme – both of which are described in section 2.5. The two schemes represent quite different solutions for the single-tunnel design and have emerged due to detailed considerations of differing site-specific constraints (see *Figure 4.2).* Both solutions offer an efficient use of space for the RF power sources and associated power supplies, either in the accelerator tunnel itself (in the case of the distributed radiofrequency sources system), or in surface buildings (klystron cluster scheme). Although these alternate RF power designs appear practical, there is ongoing R&D to demonstrate their performance and cost. As a risk-mitigating measure, a single-tunnel solution based on the RDR/European X-ray Free Electron Laser-type solution is still considered as a backup.

4.2.2 Particle sources

The electron source remains unchanged from that outlined in the RDR as it has the capability of providing any of the electron bunch train patterns or repetition rates being considered in the new baseline options.

The changes in the positron systems are more extensive and are coupled to the layout of the central region, which includes injectors (both electron and positron), damping rings and final focus systems. In the RDR the undulator-based positron production, capture and acceleration systems that accelerate the beam to 400 megaelectronvolts (MeV) were incorporated in an approximately 1.5-kilometre (km) insertion in the electron linac at the nominal 150 gigaelectronvolts (GeV) point (the approximate mid-point). The produced 400-MeV positron beam was then transported 6 km to the central region (see section 4.2.4) before being accelerated to 5 GeV and injected into the damping ring. This change was considered necessary to maintain an adequate positron yield for operation at centre-of-mass energies of less than 300 GeV. An almost duplicate low-charge conventional source (the 'keep-alive source') was originally located in the central region along with the positron and electron 5-GeV booster injectors. Moving the undulator and target systems to the central region, and integrating it with a built-in low-current auxiliary linac source that uses the same target and capture section reduces the total component count and tunnel length.

In addition, going from a linac that has a large acceptance in energy and transverse phase space into such a complex insertion with small acceptance requires beam collimation and machine protection systems ahead of the insertion. These same systems are also required at the ends of the main linacs in the central region to similarly protect the beam delivery systems. Moving the positron system to the central region allows both protection systems on the electron side to be combined into one single system.

Moving the whole positron production to the end of the linac benefits the electron linac operation and civil designs, but the benefits come with trade-offs that require alternative methods of boosting positron yield for lower-energy running. The proposed solution is to run the electron injector and electron linac at 10 Hz with alternating pulses at 5 Hz, producing either positrons that are sent into the damping ring or electron beams that are sent to the interaction point for collisions. This can be done at low energies with almost no modifications to the electron systems and with electrical power consumption equal to or less than that required at full energy. The original damping time in the damping rings has to be reduced by a factor of two, which can be achieved with the introduction of more wiggler magnets and RF cavities (and power); the new flexible damping ring design (section 4.2.3) can accommodate these modifications with no changes in the layout of the other systems in the central region.

4.2.3 Damping rings

In the RDR the 6.4-km circumference damping rings had six-fold symmetry. There were difficulties in stacking the two (electron and positron) rings in one tunnel because of physical interferences of components such as wiggler magnets and RF systems. The design rather quickly evolved into a racetrack-shaped design with two 1-km straight sections that contained RF stations, long wiggler magnets and injection and extraction systems. This design allowed many different options for the damping ring layouts and their integration with the other central region systems. For example, in the RDR, to maintain a compact footprint of the central region, the damping rings, including their 5-GeV injector boosters, were in a plane separated vertically by 10 m from the plane of the linac and final focus. With the racetrack design, everything can remain in one plane, with the injection/extraction straight section close to and parallel to the final focus beamline, simplifying the civil engineering.

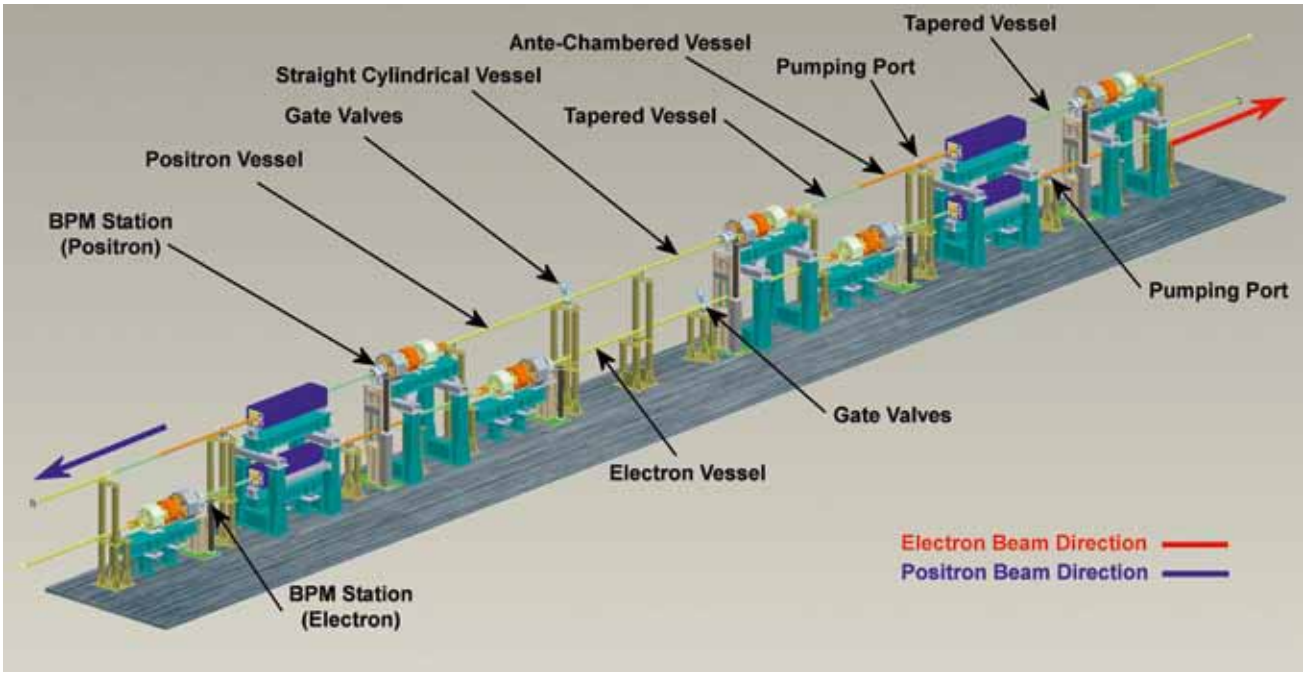

Figure 4.3 Engineering design for the DCO4 damping ring arc cell.

A low and flexible momentum compaction lattice has provided RF system and bunch length optimisation. The 6.4-km DCO4 lattice design is quite mature. It satisfies the main damping ring requirements and has been the basis of a large amount of technical design work *(Figure 4.3) [4-2]*. At present two lattices for the 3.2-km ring are under study *[4-3, 4]* based on the same racetrack design as the DCO4 and with very similar straight sections, in order to take advantage of the technical design already done. Studies have been carried out to compare the performance of the 3.2- and 6.4-km lattices with respect to the electron cloud instability (see section 3.1).

One large advantage of the present racetrack approach is that it is relatively straightforward to exchange in the design the two different circumference rings being considered, since both have the same 1-km injection/extraction straight sections. This provides a common interface to the central region integrated layout, which is now independent of the choice of damping ring design. The detailed design of the damping rings will continue to evolve with technology and engineering development as described in sections 3.1 and 3.3.3.

4.2.4 Central region

The central region, the central 6 km of the 30-km-long 500-GeV machine, contains all the different ILC systems except the linacs and the ring-to-main-linac transport and bunch compressors. In the RDR layout there were three interconnected tunnels, not counting the damping rings. One tunnel contained the beam delivery systems consisting of complex beamlines and instrumentation, which included several hundred metres of spent-beam transport (after the interaction point) to the main beam dumps. A second tunnel contained the electron and positron (keep-alive) sources, the 5-GeV booster linacs and the injection and return lines to and from the damping rings. The third tunnel was the support tunnel for all of the equipment in the other two tunnels and contained RF equipment, power supplies and instrumentation. This required a complex civil design, which at the time of the RDR was very conceptual.

Today the same equipment, with the undulator source and target replacing the keep-alive positron source, shares a single beam tunnel with the beam delivery system. With respect to the optics and layout of the system, the most significant difference involves modification of the beamline sequence and features for the electron side, primarily to incorporate the positron source (see *Figure 4.4)*. The beam delivery system sacrificial collimators are now protecting the undulator and are placed upstream. The new dogleg needed to separate the gamma beam from the main beam is designed in such a way to minimise beam emittance growth for the beam energy up to 0.5 TeV/beam. The fast abort capability is located in front of the undulator while the tune-up extraction beamline retains only DC extraction.

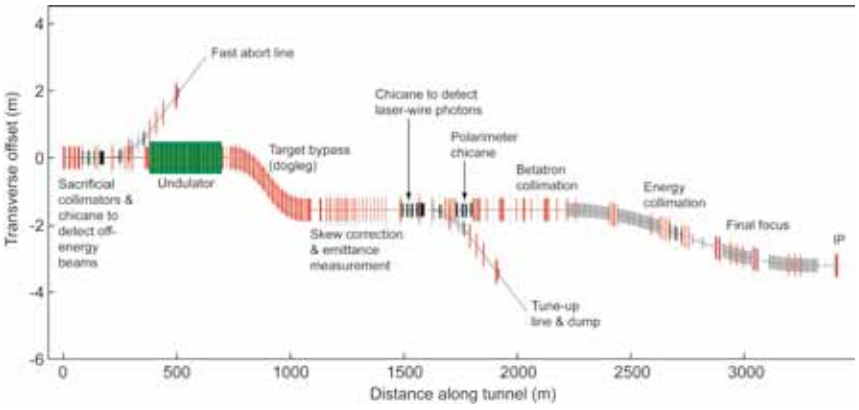

Figure 4.4 Updated design of the electron beam delivery system, compatible with integration requirements.

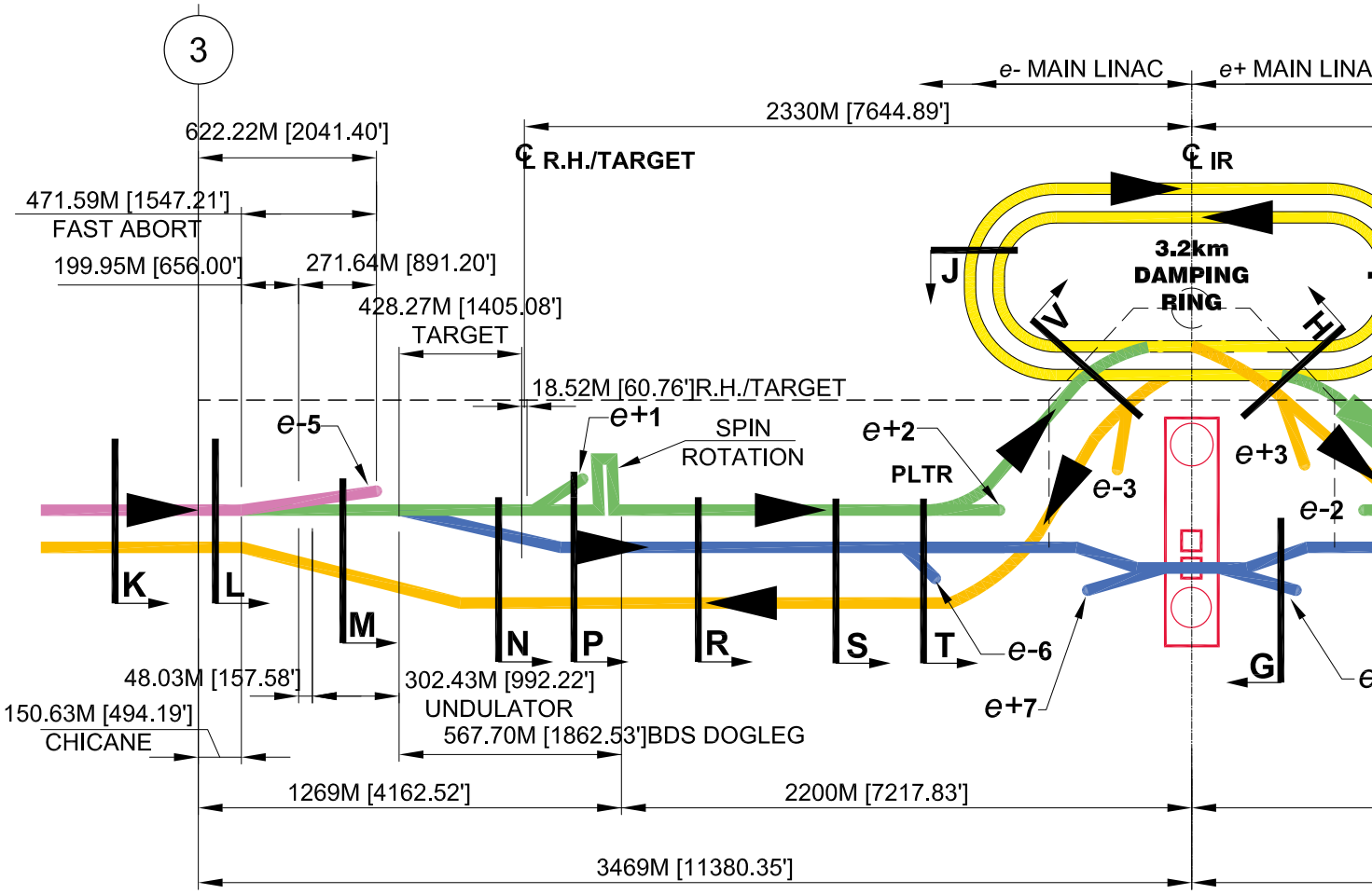

A second equipment support tunnel exists as before and everything is in one plane. There is less underground volume than previously but the central region still has the most complex layout and civil engineering of any section of the ILC (see *Figure 4.5)*.

To achieve practical satisfactory designs, integration of three-dimensional computer-aided design (CAD) modelling of civil engineering and beamline components (geometry) is required. The 3-D CAD work, along with several iterations of technical and civil designs in special GDE workshops, brings us to the present baseline layout. Designs for the whole ±3 km of the central region now exist as a baseline for final civil engineering. An impression of a few hundred metres of the central region is shown in *Figure 4.6*.

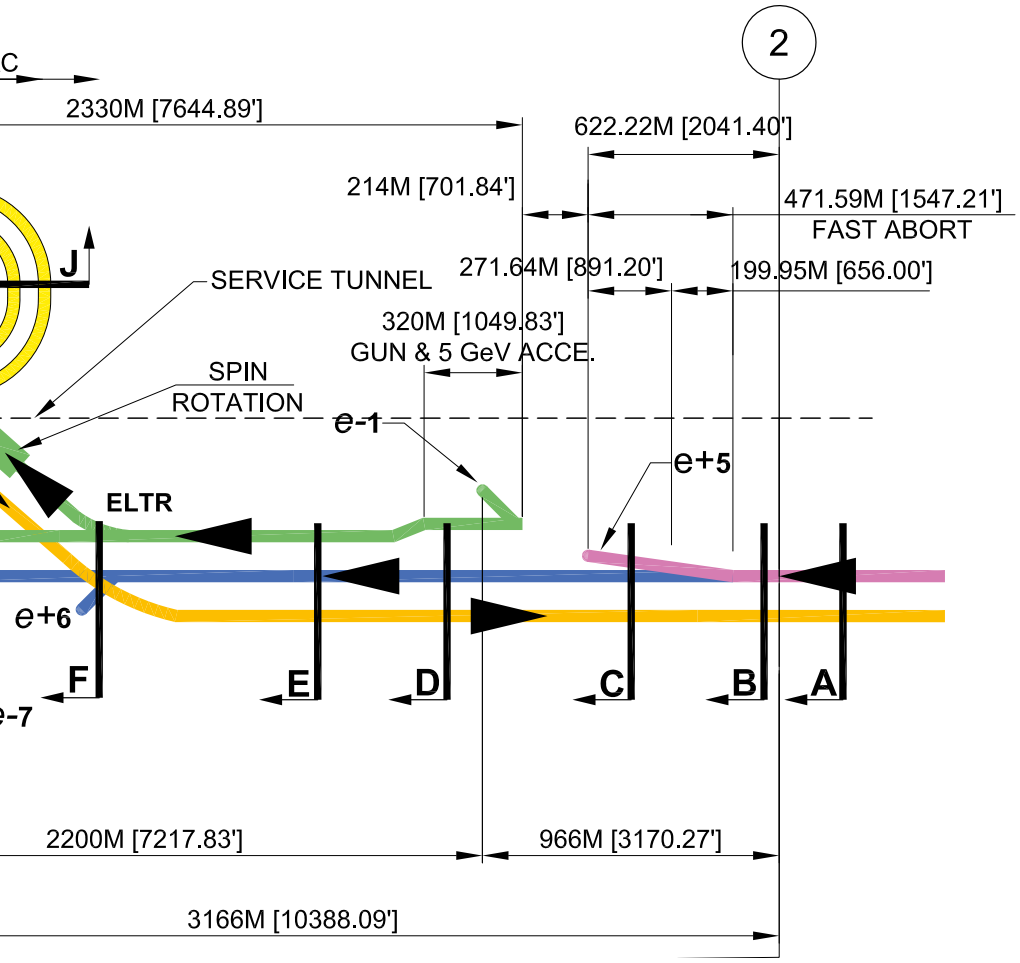

Figure 4.5 Schematic of the various beamlines in the central region, approximately five kilometres from the interaction point (not to scale).

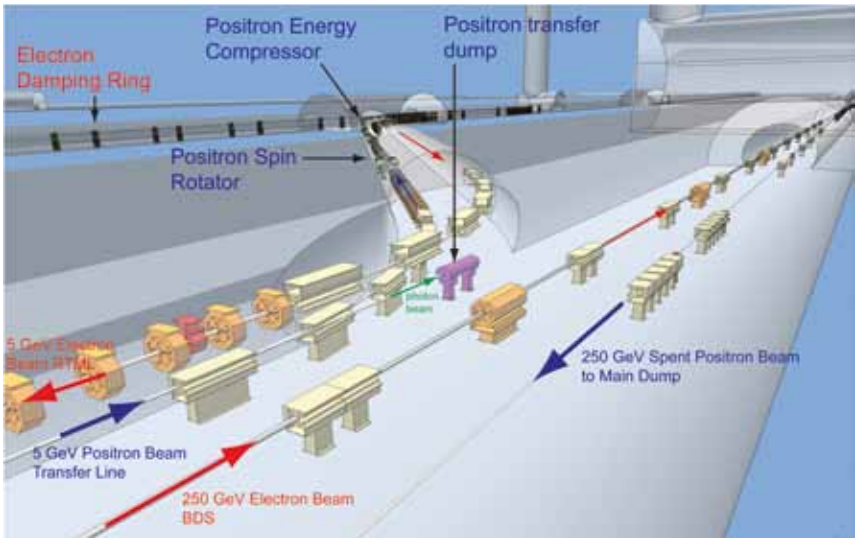

Figure 4.6 Example of a 3-D layout of part of the central region.

4.3 Parameters

In addition to studying a more cost-effective layout and configuration for the machine as outlined in the previous sections, the accelerator design and integration studies also examined the parameter space of the published reference design with a view to understanding the RDR cost drivers. The performance of the machine design at centre-of-mass energies lower than the nominal 500 GeV has also for the first time been studied in detail. In particular, physics-relevant parameter sets have been developed for centre-of-mass energies of 200, 230, 250 and 350 GeV, reflecting the physics case centred around a possible light Higgs and the top quark. A modified parameter set that has a reduced beam power has also been developed. This supports a significant cost saving in both RF power generation and the size of the damping rings. Luminosity is restored by more aggressive focusing at the interaction point (beam-beam). *Table 4.1* gives the top-level parameters for each of the identified centre-of-mass energies of interest.

	Centre-of-mass energy	**E_{cm}**	**GeV**	**200**	**230**	**250**	**350**	**500**	**upgrade 1,000**
	Collision rate	f_{rep}	Hz	5	5	5	5	5	4
	Electron linac rate	f_{linac}	Hz	10	10	10	5	5	4
	Number of bunches	n_b		1,312	1,312	1,312	1,312	1,312	2,625
	Electron bunch population	N_-	$x10^{10}$	2	2	2	2	2	2
	Positron bunch population	N_+	$x10^{10}$	2	2	2	2	2	2
	Main linac average gradient	G_{av}	MV/m	12.6	14.5	15.8	22.1	31.5	>31.5
	RMS bunch length	σ_z	Mm	0.3	0.3	0.3	0.3	0.3	0.3
	Electron RMS energy spread	$\Delta p/p$	%	0.22	0.22	0.22	0.22	0.21	0.11
	Positron RMS energy spread	$\Delta p/p$	%	0.17	0.15	0.14	0.1	0.07	0.04
	Electron polarisation	P_-	%	80	80	80	80	80	80
	Positron polarisation	P_+	%	31	31	31	29	22	22
	IP RMS horizontal beam size	σ_x^*	nm	904	843	700	662	474	554
	IP RMS vertical beam size	σ_y^*	nm	9.3	8.6	8.3	7	5.9	3.3
	Luminosity	**L**	**$\times 10^{34}$ cm^{-2}s^{-2}**	**0.47**	**0.54**	**0.71**	**0.86**	**1.49**	**2.7**
	Fraction of luminosity in top 1%	$L_{0.01}/L$		92.20%	89.80%	84.10%	79.30%	62.50%	63.50%
	Average energy loss	δE_{BS}		0.61%	0.78%	1.23%	1.75%	4.30%	4.86%
Using	IP RMS vertical beam size	σ_y^*	nm	6	5.6	5.3	4.5	3.8	2.7
Travelling	**Luminosity**	**L**	**$\times 10^{34}$ cm^{-2}s^{-2}**	**0.64**	**0.73**	**0.97**	**1.17**	**2.05**	**3.39**
Focus	Fraction of luminosity in top 1%	$L_{0.01}/L$		91.60%	89.00%	83.00%	77.90%	60.80%	62.30%
	Average energy loss	δE_{BS}		0.61%	0.79%	1.26%	1.78%	4.33%	4.85%

Table 4.1 Selected top-level parameters assumed for the *Technical Design Report*. These parameters will be adjusted as the R&D continues. In particular, the impact of emittance dilution from the main linacs and the beam delivery systems (collimator wakefields) still need to be assessed and included in this table.

Two sets of luminosity parameters are supplied:

- The first set assumes a straightforward reduction in the vertical beam size at the interaction point, pushing the vertical beta (β) function close to the nominally accepted limit of the bunch length. This pushes the vertical disruption parameter to a level close to the instability threshold (approximately 25), but to one that is still considered achievable. This configuration achieves about 75% of the nominal RDR luminosity (2×10^{34} $cm^{-2}s^{-1}$).
- The second set assumes application of the so-called travelling focus *[4-5]*. Travelling focus allows the beam to be focused down beyond the traditional limit of the bunch length. Adjustment of the longitudinal position of the focal point (optical waist) of individual longitudinal segments of the bunch effectively compensates the luminosity-diluting effects of the hourglass effect. The technique potentially allows 100% of the RDR luminosity, but at the cost of a relatively unstable collision due to the intense beam-beam effect, which will result in tighter vibration tolerances and more demanding specifications on beam-based feedbacks. The travelling focus configuration will be studied in more detail during the remainder of the Technical Design Phase.

At centre-of-mass energies of 200, 230 and 250 GeV, the corresponding beam energies are less than the minimum 150 GeV required to generate the design positron bunch charge (3.2 nanocoulombs). For these energies, the electron linac is run at 10 Hz, with one pulse used to generate a 150-GeV beam to produce positrons, as described in section 4.2.2. (Other alternatives such as a short-period undulator are also under consideration.)

Finally, a tentative parameter set for the 1-TeV upgrade has been added. The current working assumption is that the full RD beam power (2,625 bunches) will either be restored in parallel to the energy upgrade or will have already been implemented. Restoration of the full RDR bunch number assumes a doubling of the installed RF power (by klystrons and modulators) and that the damping rings can accommodate the increased bunch number. The major bottleneck for the latter is likely to the electron cloud effects in the positron damping ring. Because of this uncertainty, space is assumed in the current design to facilitate the construction of a second positron ring.

References

[4-1] ILC Reference Design Report, Vol. 3, Accelerator.

[4-2] A. Wolski et al., "ILC Damping Ring Design Studies at the Cockcroft Institute," ILC-NOTE-2010-057.

[4-3] S. Guiducci, M. E. Biagini, "A Low Emittance Lattice for the ILC 3 km Damping Ring," Proceedings of IPAC 2010, Kyoto, Japan, 2010.

[4-4] D. Wang, J. Gao, Y. Wang, "A New Design for ILC 3.2 km Damping Ring Based on FODO Cell," Proceedings of IPAC 2010, Kyoto, Japan, 2010.

[4-5] V.E. Balakin, Travelling Focus Regime for Linear Collider, VLEPP Proc. 77th ICFA Workshop on Beam Dynamics, May 13-16, Los Angeles, 1991.

05

CONVENTIONAL FACILITIES AND SITING

5.1 Global conventional facilities design

During the Technical Design Phase, the conventional facilities design has continued as a global enterprise coordinating the work in the Americas, Asian and European regions. Over the first two years of this phase, the conventional facilities design has matured from relatively similar generic solutions for sample sites in each of the three regions to more detailed designs adapted to specific site conditions. In all cases, designs are based on requirements that apply to the construction of all modern accelerators: stable geologic conditions for the support of the accelerator complex, suitable radiation shielding, life safety and egress considerations, appropriate infrastructure for the transport of equipment and components and ample utility support. Since a site has not been preselected, the design development in each region has led to differences in the design approach and resulting configuration. These differences will be well documented, cost-estimated and carefully reviewed to understand the distinctions among the regional design solutions.

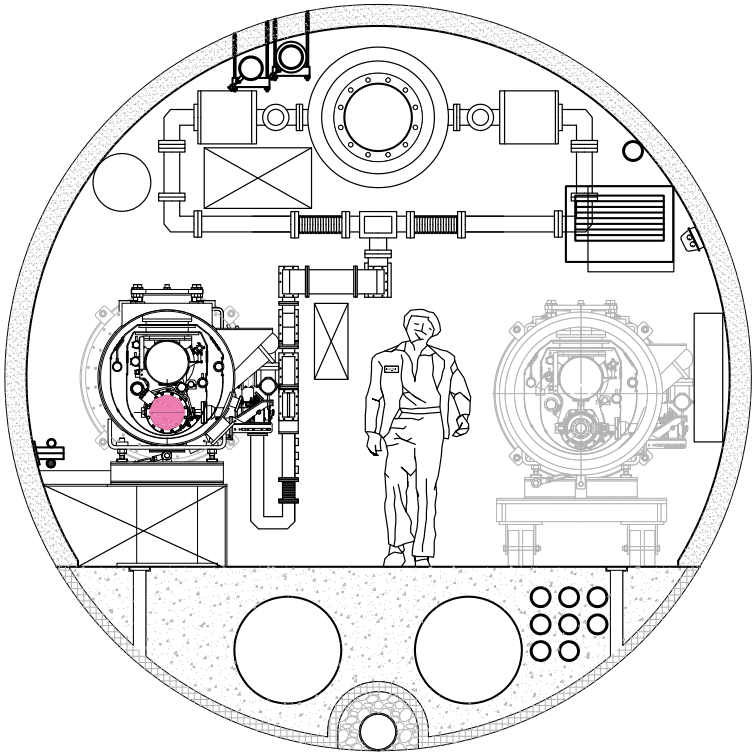

Figure 5.1 Main linac tunnel cross-section for the Americas region. The klystron cluster scheme waveguide is shown.

In *Figure 5.2*, the overall ILC layout is depicted in schematic form with the path of the electron and positron beams indicated by directional arrows. In all regions, the machine layout and configuration remain consistent. However, regional conditions have prompted differing solutions for tunnel construction as well as the choice of high-level radiofrequency power supply systems. The Americas and European regions have selected a klystron cluster radiofrequency system to facilitate a single-tunnel main linear accelerator (linac) configuration.

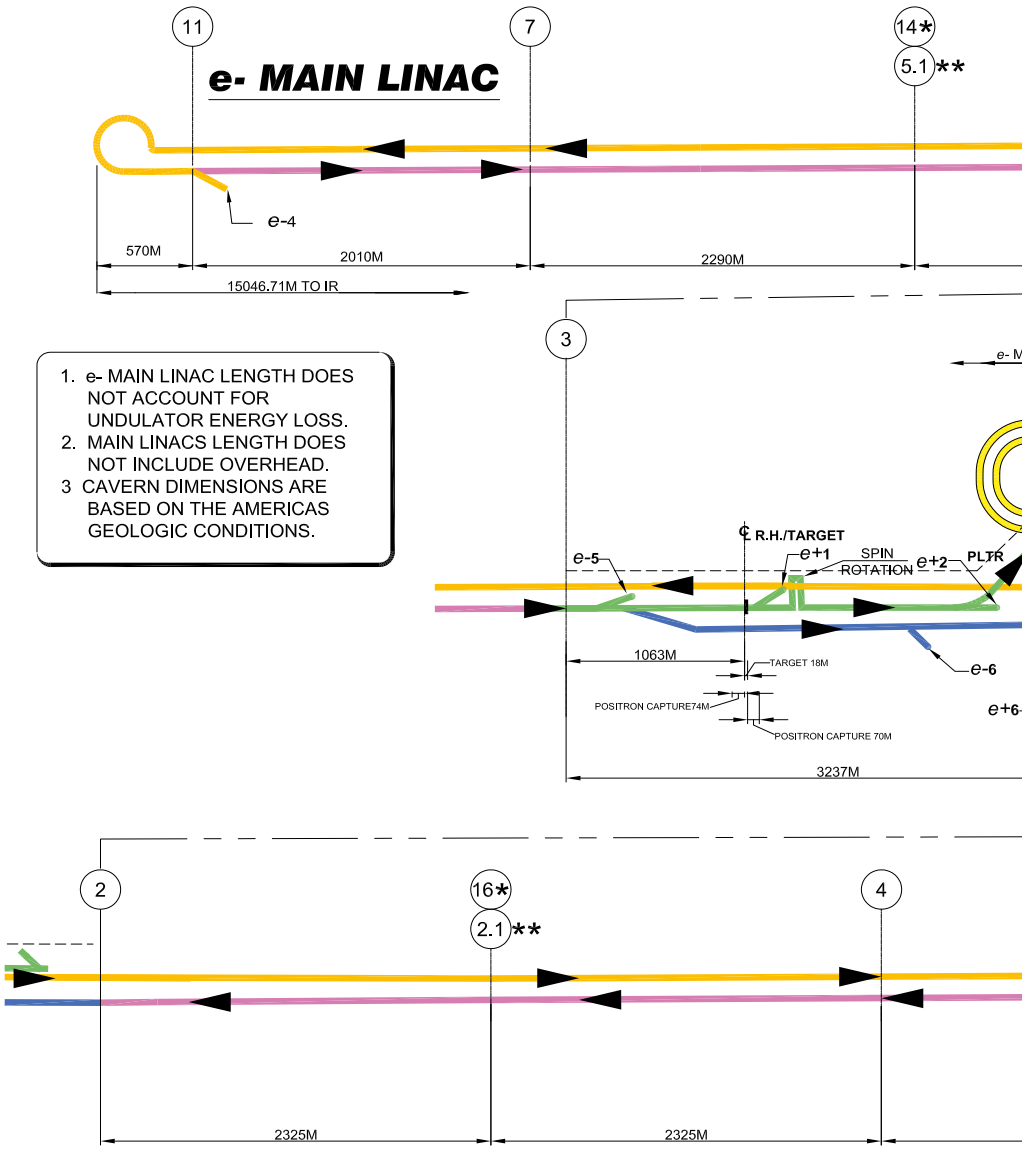

Figure 5.2 ILC beamline schematic.

This system allows the klystrons that supply the radiofrequency (RF) power to the accelerating cavities to be grouped in surface buildings located at approximately 2.5-kilometre (km) intervals. Due to regional conditions at sites being considered for the Asian region in Japan, a distributed RF system has been selected for that region. In that system, smaller klystrons are being developed to support only two cavities; these are to be located in the tunnel near the cryomodules. In all regions the primary main linac tunnel diameter is determined by three fundamental dimensions: the space needed for the installed main linac cryomodule, the space needed for transport of replacement equipment and the space required for emergency exit, even in the event that replacement equipment is being transported through the tunnel at the time of an incident.

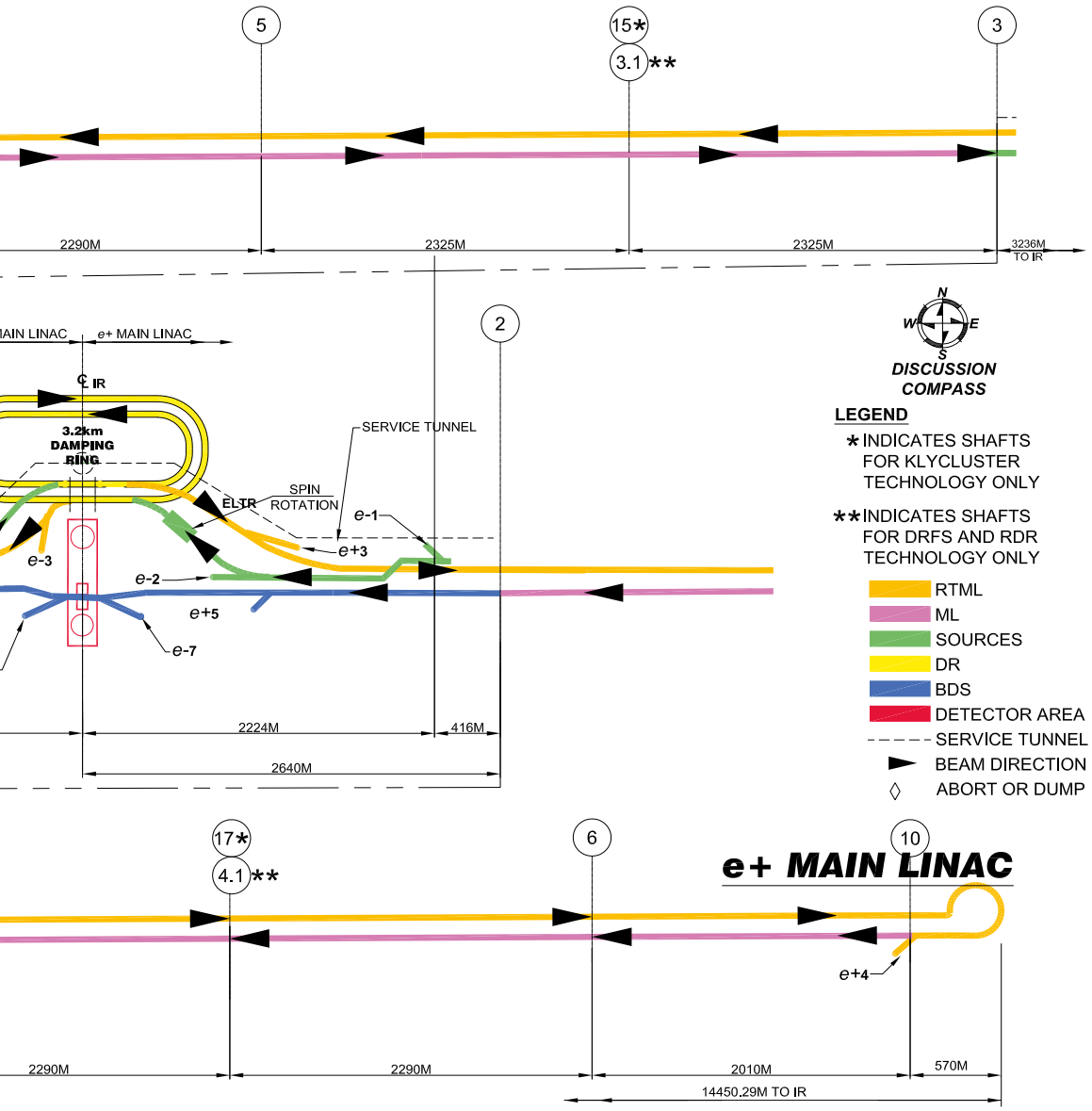

Figure 5.1 shows the cross section of the Americas region main linac, which uses the klystron cluster RF system. At the crown of the tunnel, the large circular waveguide is shown along with the associated waveguide connections to the installed, floor-mounted cryomodule on the left. Space is provided in the centre of the tunnel for personnel access and a replacement cryomodule in transit is indicated on the left side of the tunnel in shaded tone. The area directly below the main linac cryomodule shows dedicated space for the installation of low-level RF electronics for the main linac cryomodules. In addition, the cast-in-place concrete floor mass contains a drainage system to control ground water inflow, conduits for high-voltage power cable distribution and supply and return air ducts to provide fresh air to dedicated safety alcoves spaced at 600-m intervals throughout the underground tunnel complex. Life safety requirements for the various regions will be described later in this section.

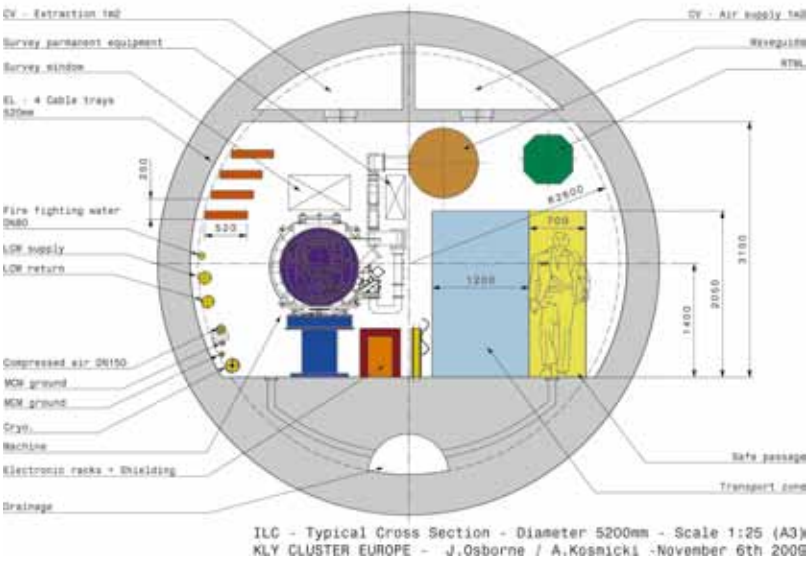

Figure 5.3 Main linac tunnel cross-section for the European region showing KCS waveguide.

The European main linac tunnel cross-section, *Figure 5.3*, uses a similar approach to tunnel configuration and also uses the klystron cluster RF system. The main linac cryomodule is floor-mounted and the large waveguide is also mounted at the tunnel ceiling. The personnel access way and equipment transport space is reversed in position. The main differences between the two cross-sections are the two large supply and return air ducts that are formed at the tunnel crown. The European approach to underground life safety requires a 'compartmentalised' approach in which the underground space is divided into increments of 500 m and requires the provision for fresh air supply and return for each 'compartment'.

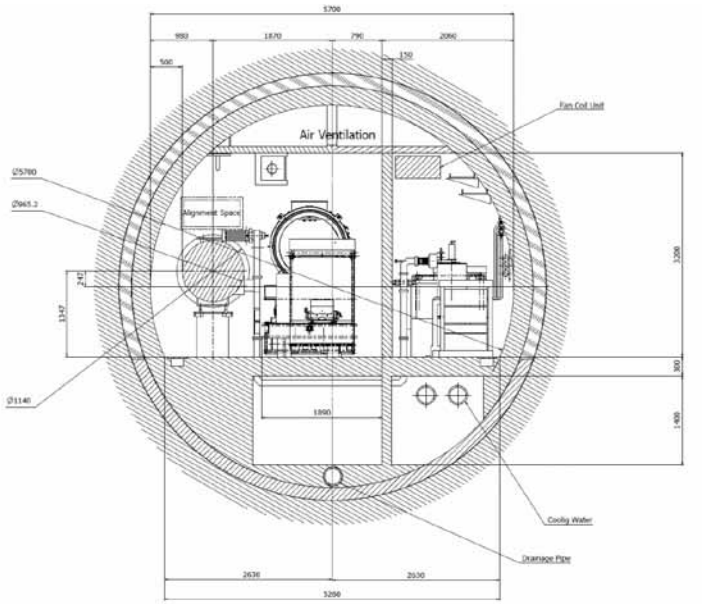

Figure 5.4 Main linac tunnel cross-section for the Asian region showing distributed radiofrequency system installation.

The Asian main linac tunnel cross-section, shown in *Figure 5.4*, uses a 'compartmentalised' approach to life safety very similar to the European solution. At the crown of the tunnel two large supply and return air ducts are indicated. The Asian main linac tunnel configuration has one major distinction from that of the Americas and European regions. The sites being considered for the ILC in Japan are in mountainous areas and are not suitable for a klystron cluster system approach with large surface buildings. The Asian tunnel cross-section shows the configuration of the distributed RF system. On the left side of the tunnel, the main linac cryomodule is floor-mounted. The centre portion of the tunnel shows an equipment transport vehicle and minimum space for personnel passage. On the right side of the tunnel, the distributed RF system, the small klystrons and related support equipment is indicated. This equipment is separated from the main accelerator space by a wall for radiation shielding. The space below the floor is also utilised for a drainage system to control ground water inflow, process water piping and electrical power cable distribution. The Japanese sites being considered have additional unique features that affect the underground tunnel configuration. These will be discussed later in the site-specific section of the conventional facilities & siting portion of this report.

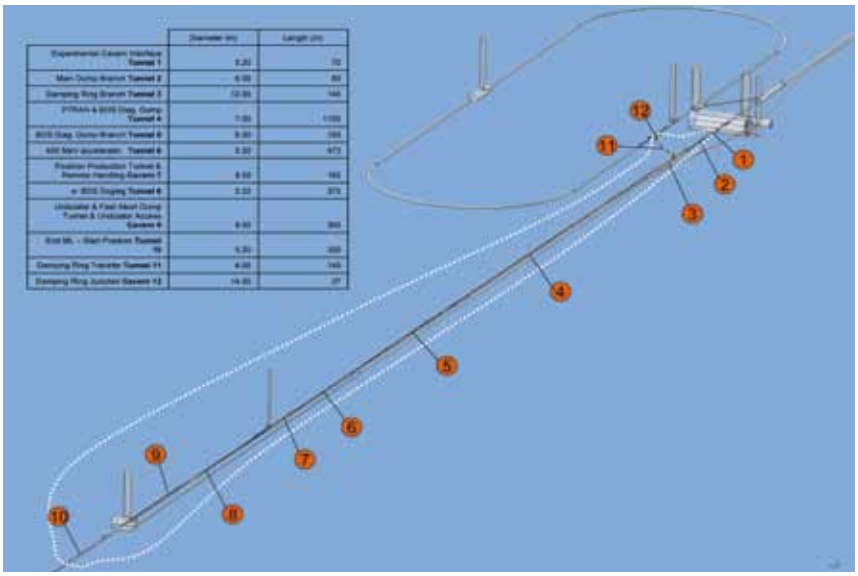

Figure 5.5 An isometric view of the Central Region tunnel schematic.

While the ILC main linacs represent a considerable portion of the underground construction for the project, there are several other requirements for underground space. Both the electron and positron main linacs extend for a length of approximately 10 km each. However, the 'central region' of the project also occupies a similar overall length of 10 km and contains the electron and positron sources, the damping rings and the electron and positron beam delivery systems, which lead to the interaction region where two detectors alternate positions in the beamline for data gathering (see *Figure 5.2)*. The electron and positron sources are located in an enlarged enclosure that also accommodates the beam delivery systems. The damping ring is located offset from the interaction region in a racetrack

shape that has a circumference of 3.2 km. In addition the ring-to-main-linac, which transfers the electron and positron beams from the damping rings to the start of the main linacs, it also occupies space in both the beam delivery system and main linac enclosures. Needless to say, the central region design and construction will require attention to the requirements of each individual system as well as to all aspects of initial installation and ongoing operations and maintenance processes.

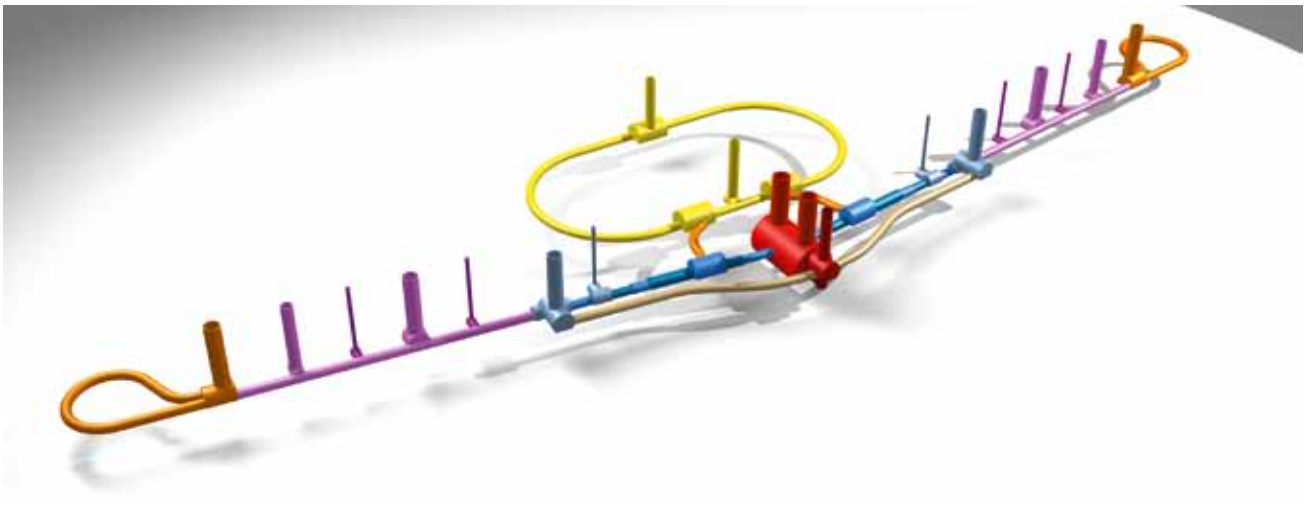

Figure 5.6 An overall view of the linac collider tunnel schematic showing access shafts.

Figure 5.5 is a 3-D isometric drawing of the electron beam delivery system, damping ring and interaction region. *Figure 5.6* is an overview of the entire ILC underground configuration. It is likely that the enclosures for the beam delivery system on each side of the interaction region will have to be enlarged beyond the nominal main linac tunnel diameter to accommodate the accelerator equipment required to occupy this area.

Figure 5.7 An isometric view of the Central Tunnel schematic showing the detector hall.

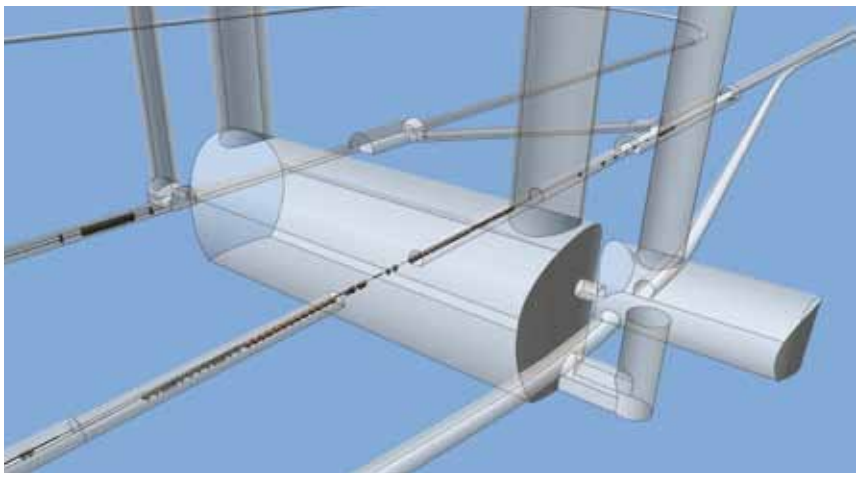

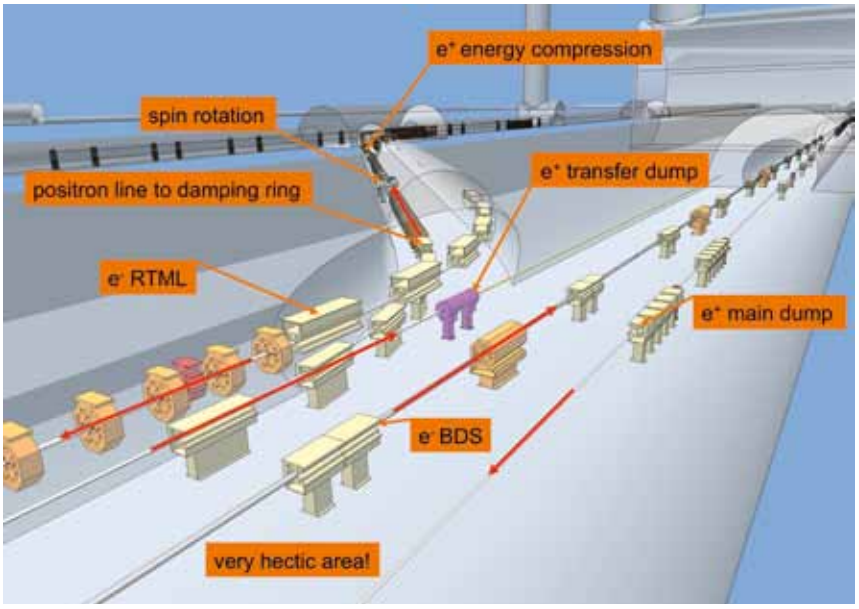

Figure 5.8 A detail of the Central Region tunnel showing typical beamline installation.

Figure 5.7 shows an enlarged depiction of the interaction region and adjacent damping ring and ring-to-main-linac connections to the beam delivery system enclosure. *Figure 5.8* shows one of the more congested areas of the entire underground complex. This is a view looking towards the interaction region from the end of the electron main linac. At the right side of the drawing is the positron beam transfer line from the interaction region to the main positron absorber. To the left, the electron beam delivery system carries the electron beam to the interaction region. To the left of the electron beam, and floor-mounted, is the low-energy positron transfer line from the positron source to the damping ring. Finally, above the positron transfer line, the electron ring-to-main-linac transfer line from the damping ring to the start of the electron main linac is indicated positioned at ceiling height above the other beam lines. Red directional arrows indicate the direction of travel for each of the beam lines. A similar condition exists on the opposite side of the interaction region at the end of the positron main linac. These 3-D drawings are an essential tool for the conventional facilities effort. Work continues in all three regions to use the 3-D drawings to understand potential interferences, evaluate installation and maintenance techniques and develop workable design solutions for the entire range of underground enclosures from the simplest to the most complex.

5.2 Life safety and infrastructure support

While the underground tunnels, enclosures and caverns constitute the largest component of the conventional facilities design, the safety of personnel and the configuration of supporting utilities are also very important parts of the overall design. When the accelerator complex is operating, only a few underground areas are accessible to personnel. However, during initial installation and ongoing maintenance periods, there is likely to be a good deal of activity in many parts of the underground space. It is for these times that proper precautions must be taken to ensure the safety of workers underground in general. People's safety and stable machine operation also depend on a variety of utility support systems. An accelerator with the magnitude and complexity of the ILC requires a stable temperature environment, a process water system for component cooling and a high-voltage electrical distribution system to supply the power needed to operate the machine.

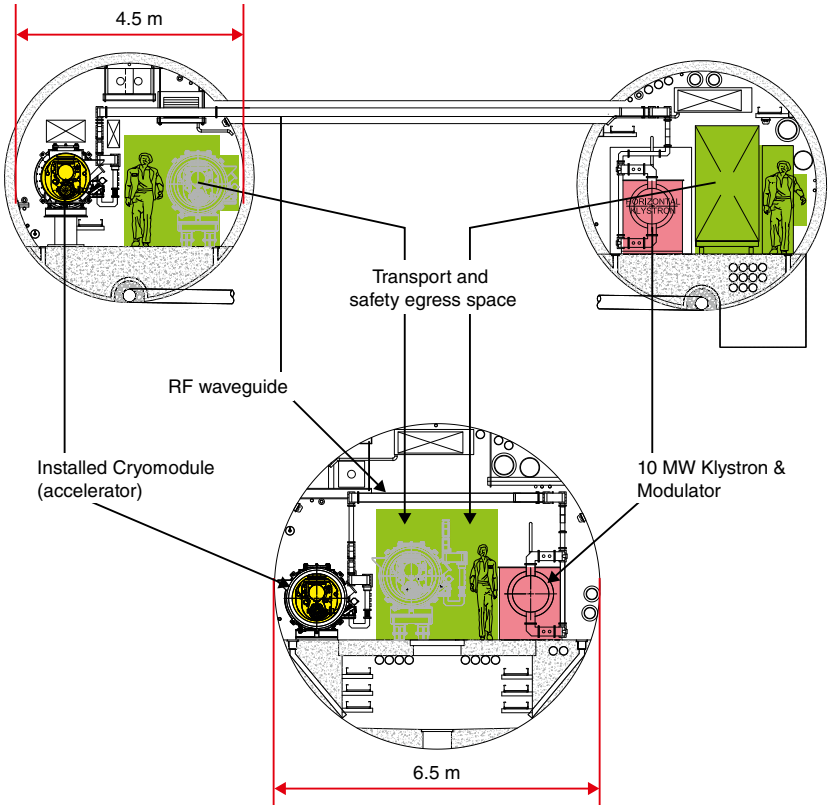

Figure 5.9 The main linac tunnel design has been modified from a two-tunnel to a single-tunnel scheme.

An important part of the Technical Design Phase was the decision to move from the *Reference Design Report* (RDR) twin-tunnel configuration to a single-tunnel configuration for the main linacs. The damping ring also has a single-tunnel configuration while the beam delivery systems retain an adjacent service tunnel configuration due to requirements for support equipment. *Figure 5.9* illustrates the transition from the twin-tunnel RDR scheme for the main linacs to an RDR-type single-tunnel solution. Other solutions for a single tunnel have been developed based on different RF

system configurations and local geologic conditions. But fundamental to all of these alternative single-tunnel solutions was the need to develop sensible life safety and egress solutions for a single-tunnel configuration that were compliant with prevailing codes and regulations. The twin-tunnel configuration allowed a fairly straightforward approach to life safety and egress. If a fire or other hazard occurred in one of the tunnels, the second tunnel could be isolated and used as the emergency escape route. With a single-tunnel configuration, the issue of emergency personnel egress had to be studied. Varying regulations in the three regional areas has led to two different solutions to the problem.

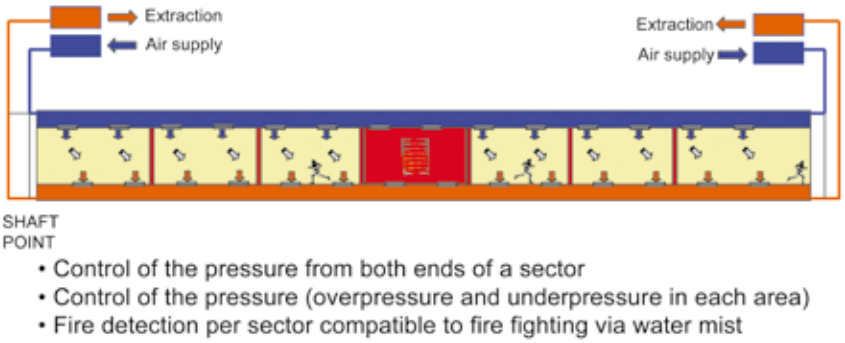

Figure 5.10 A scheme of the exit plan for the main linac tunnel if the ILC were built in the European region.

The Asian and European regions have both developed a similar approach to the life safety and egress issue. Their solution divides the single-tunnel portions of the main linacs and damping ring into 500-m increments or 'compartments' that are separated by fire walls and automatic fire doors that can isolate areas that may be involved in a fire or other incident. *Figure 5.10* is a schematic drawing that shows how this compartmentalisation scheme can isolate a hazardous area. Another important part of this approach is the control of airflow in an emergency. As the drawing indicates, a continuous duct for air supply and extraction extends along the entire length of the single-tunnel enclosure (see previous tunnel cross-section drawings in section 5.1). Under normal operation, supply conditioned fresh air to the tunnel enclosure is returned for conditioning and air change through the extraction duct. In the event of a fire, the affected area can be sealed by firewalls and doors. Dampers will close in the supply duct, preventing fresh air from contributing to the fire and controlling smoke from permeating beyond the affected area. In this way the unaffected areas of the tunnel can be used for personnel egress to the surface and for emergency response personnel to access the affected area.

In the Americas region a different approach is required due to stipulations in the prevailing regulations for underground construction. Instead of dividing the underground space into small areas, the containment is based upon the enclosure of the highest-hazard areas with fire-rated walls. This highest-hazard equipment is actually not the accelerator itself, but in some of the equipment required to support accelerator operation. Oil-filled electrical equipment, water pumps, motors and other utility equipment constitute the highest potential for fire. This equipment is located in the caverns at the base

of the vertical access shafts located along the single-tunnel enclosures. In the Americas region solution, these local areas are isolated by fire-rated walls and doors, which leave the main tunnel enclosure available for personnel egress to the surface. It is required to have a fire-protected area of refuge at intervals of 1,200 m along the length of the single tunnel to provide an intermediate safe area for injured personnel or to await emergency response assistance. *Figure 5.11* is a schematic drawing showing the areas of refuge with respect to the adjacent vertical shafts.

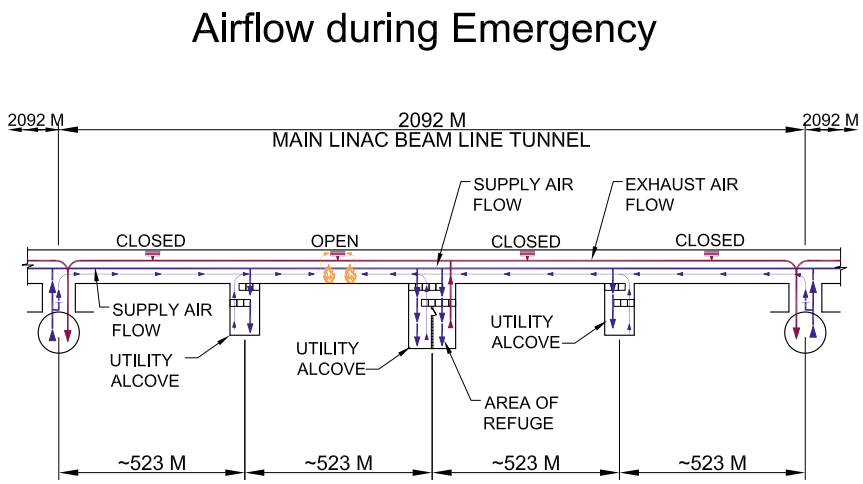

Figure 5.11 Ventilation scheme for the main linac tunnel.

It is important to note that both approaches to life safety and egress are the direct result of extensive analysis of regional requirements supported in part by independent consultant review. Work to date has provided confidence that a single-tunnel solution can be constructed that will provide a safe working environment when people are underground performing machine installation and maintenance activities. When an actual site is selected for the project, the details of a final design solution can be developed in conjunction with local code requirements.

Another continuing focus within the conventional facilities design effort is the optimisation of the designs for the utility systems that support the accelerator operation. After the underground civil construction, the mechanical systems, including air handling and ventilation systems and process cooling water systems, are the second largest cost driver in the conventional facilities cost, with the process cooling water being the largest component. At the time of the RDR, the major portion of the process water system design was completed in the Americas region and adopted for use in all three regions. During the first two years of the Technical Design Phase, the Americas regional team completed a formal value engineering review of the process water system. The value engineering process involves identifying major drivers to the existing design and identifying alternatives for evaluation and possible inclusion into the design to improve efficiency and reduce costs. During this process it was determined that the process cooling water design developed as the reference design was based on criteria provided independently from all of the contributing parts of the ILC machine. In many cases these criteria were

optimised for each specific part of the machine, or area system, which resulted in a varied set of requirements and produced a very complicated and expensive process water system design. One of the most important outcomes of the value engineering review was to identify specific extreme criteria that were complicating the process water design and work with the various area systems to relax some of the more stringent criteria. In doing so, a more uniform and simplified process water system design was achieved and costs were reduced.

5.3 Site-specific design efforts

In the conventional facilities work that led to the development of the ILC *Reference Design Report,* no specific site investigation was included. Instead, each region identified a generic sample site and used a common overall machine layout and underground configuration on which to base the initial cost estimate. During the current Technical Design Phase, preliminary site investigation has been started in varying degrees and in all regions. In the Asian region, two specific sites have been identified in Japan as possible locations to be considered for the construction of the ILC. In the European region, the sample site location at the CERN laboratory in Switzerland as well as a possible site in Dubna, Russia, near the Joint Institute for Nuclear Research are undergoing preliminary site investigation as well. In the Americas region, although specific site investigation has not begun, studies for surface building arrangement at shaft locations have been completed. In the Asian region the down-selection to two specific sites in Japan as candidate sites for the location of the ILC project marks the most mature of the site-specific investigation efforts. The Asian conventional facilities and siting group has been working jointly with the Japanese Advanced Accelerator Association Promoting Science & Technology (AAA) in the development of preliminary design for these sites. The member corporations of the AAA have a great deal of cumulative experience in the construction of tunnels in Japan, primarily for car and rail traffic. Both of the selected sites, one located in the northern part of Japan and one located in the southern region, are in mountainous areas and as such present unique challenges for the construction of large underground complexes.

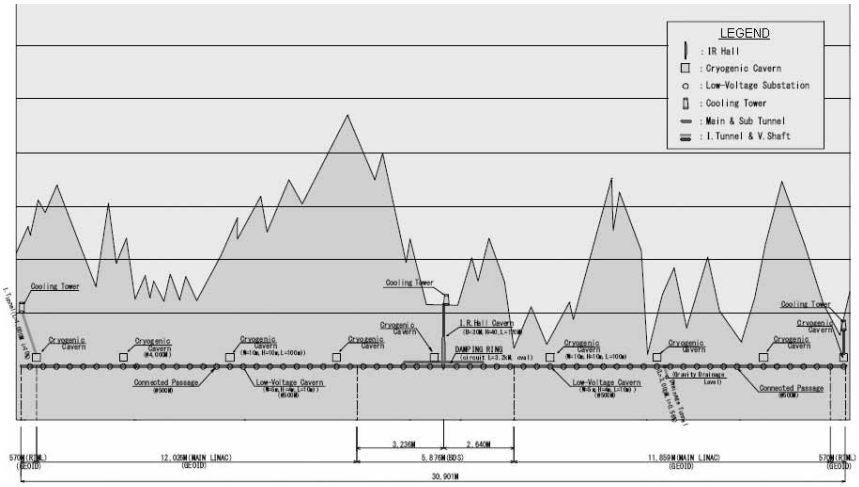

Figure 5.12 Schematic of a mountainous region tunnel provided by the Japanese Advanced Accelerator Association Promoting Science & Technology.

Figure 5.12 is a schematic transverse section of one of the selected sites; both sites have a similar mountainous profile. In a mountainous region, vertical shaft access to the surface and the corresponding surface facilities are in most cases unworkable solutions, so gently inclined horizontal tunnels will be used to provide access to most parts of the underground accelerator complex. The geology for both of the sites being considered in Japan is primarily granite, which affords the possibility of tunnel construction using either tunnel boring machines or the drill and blast method.

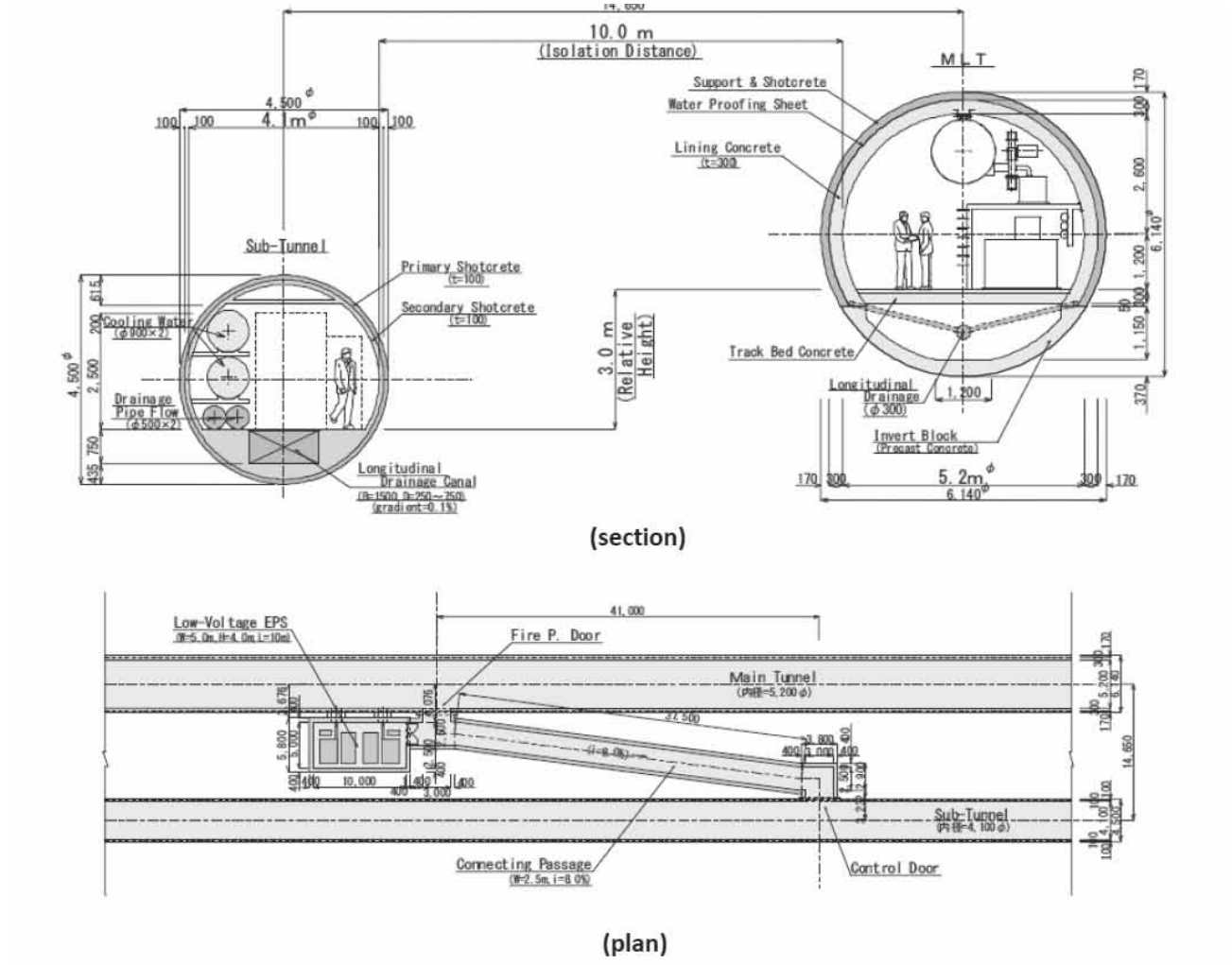

Figure 5.13 A cross-section of a mountainous region tunnel provided by the Japanese Advanced Accelerator Association Promoting Science & Technology.

A unique aspect of the design approach in Japan's mountainous regions is the construction of a smaller-diameter pilot tunnel ahead of and slightly below the level of the main accelerator tunnel. This approach is used for most traffic tunnels in Japan and the benefit of the pilot tunnel is two-fold. First, water inflow in this type of construction is expected and the pilot tunnel provides a means to dewater the main tunnel during both construction and operational use. Second, the pilot tunnel can also be used

as an additional means of egress in the event of an emergency or hazardous event. *Figure 5.13* shows a typical cross-section through the main linac tunnel with the lower pilot tunnel as well as a plan view of the two-tunnel configuration with a connecting passage between the two tunnels. In the case of the ILC, the pilot tunnel can also be used for support equipment in addition to ground water control and egress. While mountainous sites require most of the accelerator complex to be housed in underground tunnels and caverns, some major support installations will still be required to be located on the surface. These installations will likely be adjacent to one or more of the adits of the horizontal access tunnels. *Figure 5.14* is a schematic layout for the main substation that will supply the electrical power needed to support the accelerator complex. This substation layout is likely to be applicable to any site being considered to host the ILC project.

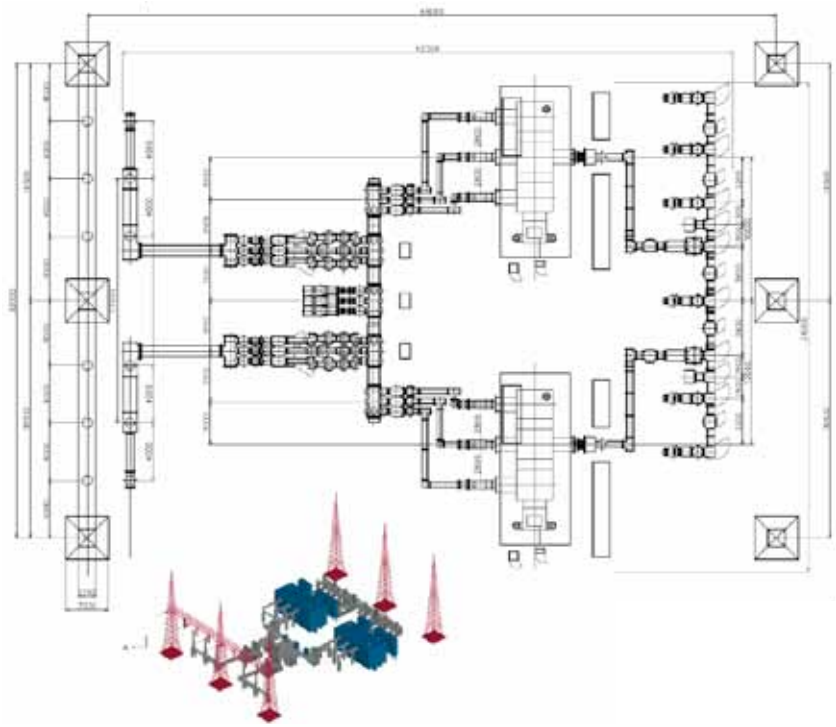

Figure 5.14 Diagram of the electrical utility master substation.

The European region sample site developed for the *Reference Design Report* was also a somewhat mountainous region located near CERN, although it was not subject to the constraints of the more mountainous Japanese sites. Vertical shafts will still be used to access the underground complex and surface structures at the shaft locations are still being considered. Specific site investigation has not yet begun with the exception of the development of preliminary geologic profiles along the alignment of accelerator complex.

Figure 5.15 shows a schematic transverse section of the proposed alignment of the European sample site. The geology at this site is primarily a sandstone/ molasse rock, which favours a fully lined tunnel construction method with a tunnel boring machine.

Another European site that is being considered is located in a rural area of the Russian Federation in the northern Moscow region near the town of Dubna and the Joint Institute for Nuclear Research. *Figure 5.16* shows the initial proposed alignment north of the city of Taldom. While the actual design is at a very preliminary stage, some geologic site characterisation and soil boring work has been completed that verifies the consideration of this site and the potential for future conceptual design work. *Figure 5.17* shows a schematic transverse section of the proposed alignment of the Dubna site. Unlike the deep tunnel designs that are currently being considered in Japan, at CERN and in the Americas region, the Dubna site design would incorporate a relatively shallow bored tunnel configuration with surface support buildings. The site is relatively uniform in surface elevation compared to the Asian and CERN sites and the tunnel would be bored in an impermeable soil-based stratum rather than in the deeper rock.

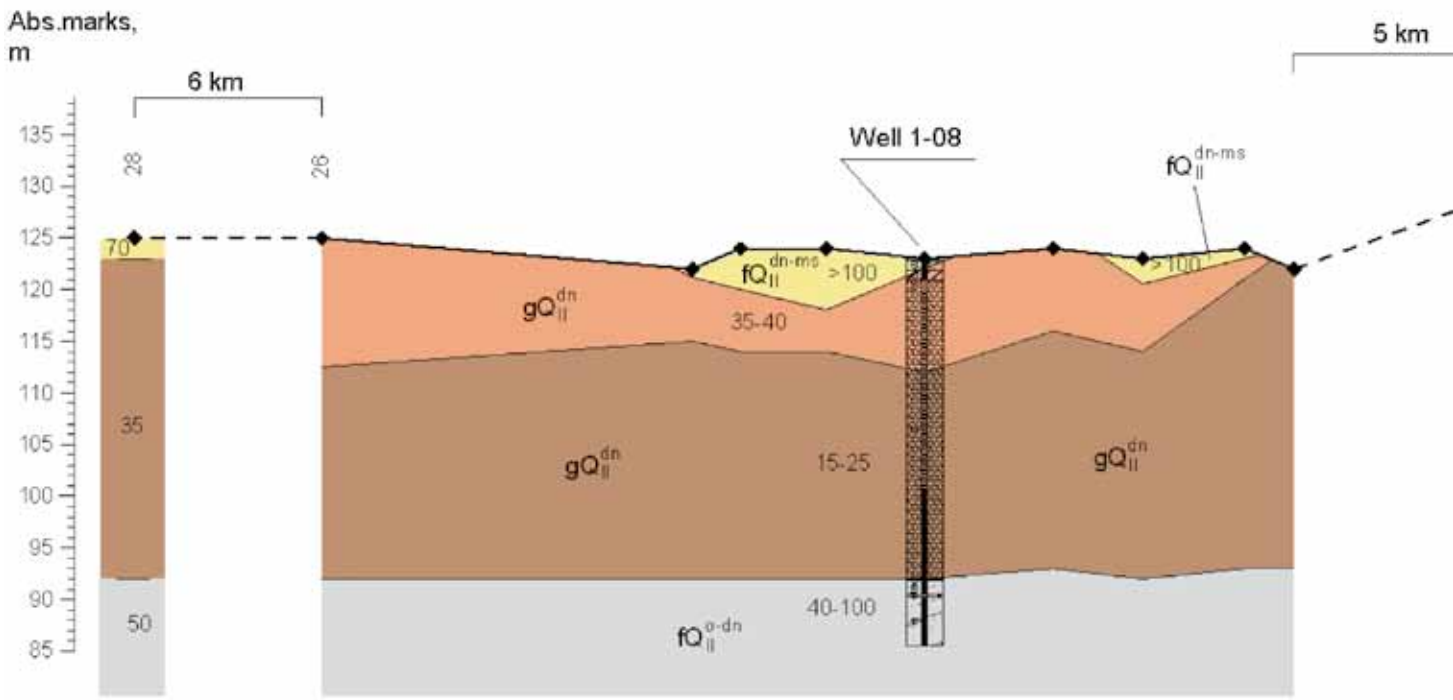

Figure 5.17 A geology study near Dubna in the Moscow, Russia region.

Figure 5.15 Tunnel geology of the CERN region.

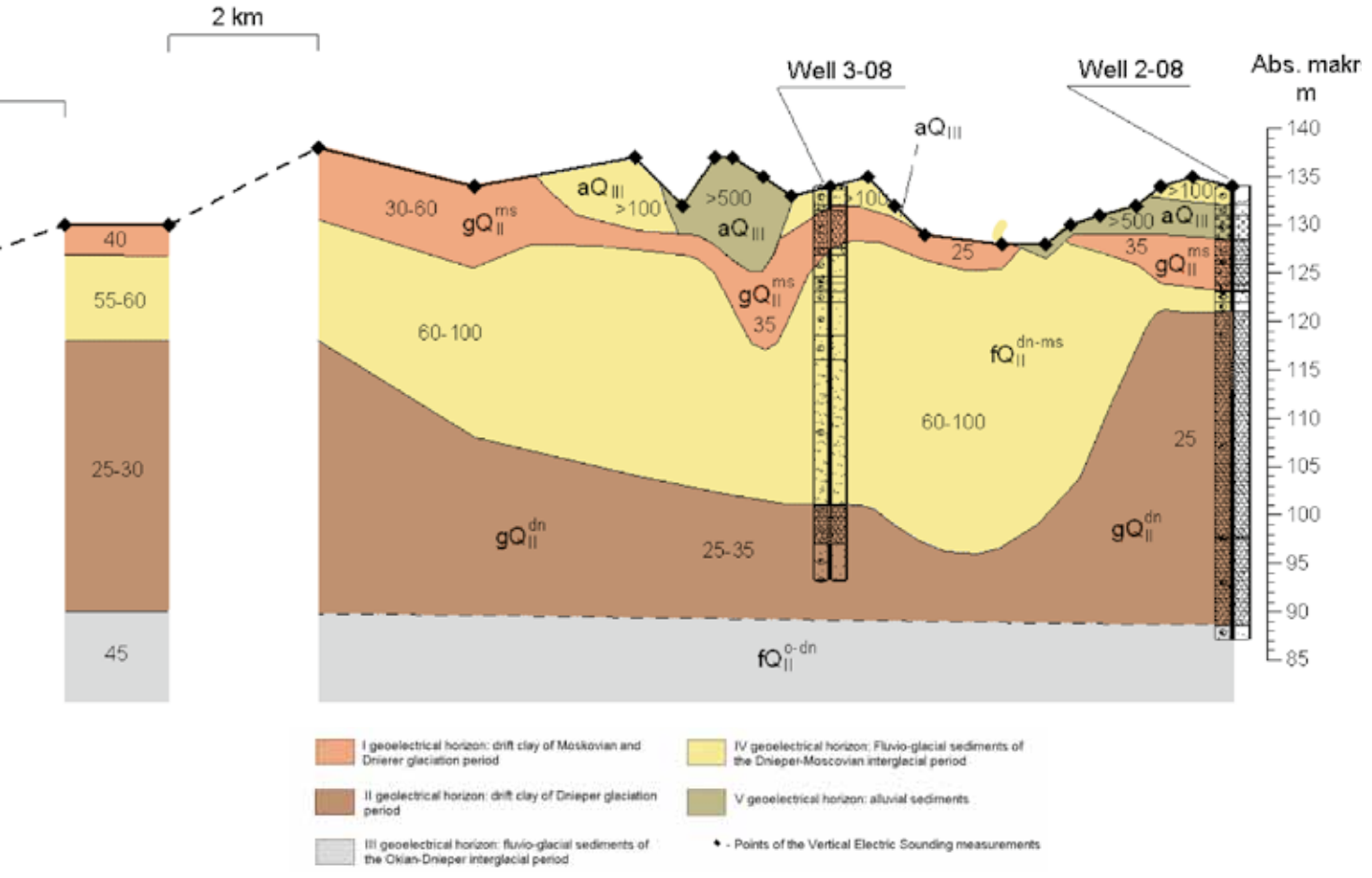

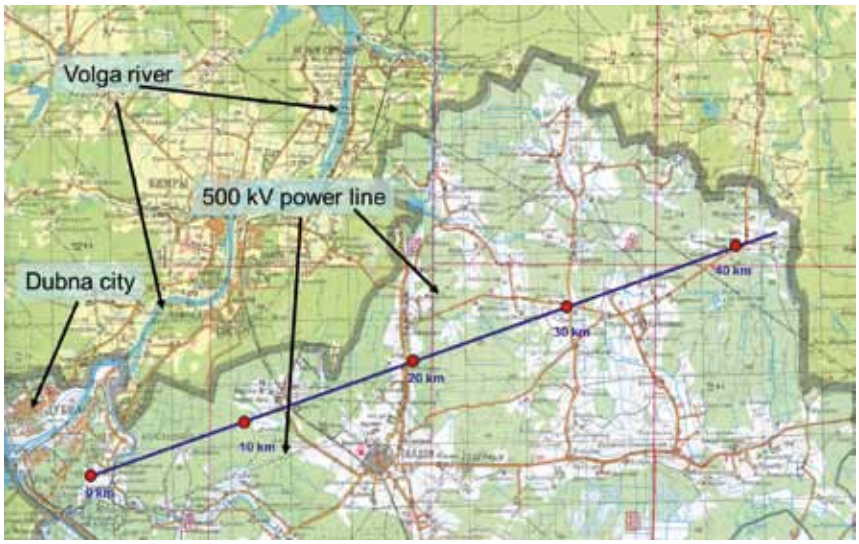

Figure 5.16 The linear collider alignment near Dubna in the Moscow, Russia region.

Figure 5.18 is taken from a cost study that was completed in the Americas region that compared deep-, shallow-bored and cut-and-cover site conditions and tunnel configurations. This schematic perspective view shows a possible configuration for the conditions found at the Dubna site.

In the Americas region the sample site that was used for the *Reference Design Report* was a site in northeastern Illinois near Fermilab. This site is also relatively uniform in elevation along the machine alignment. However, due to the favourable geologic conditions of the limestone bedrock, a deep-tunnel configuration is the preferred solution for this site. The Americas region has continued to be a full partner in the global effort to develop an updated baseline with respect to the previous reference design. While the preliminary design is well developed, there has been limited actual site investigation up to this point in the Technical Design Phase. There is, however, a great deal of local experience in tunnel construction in the limestone bedrock as a result of the Deep Tunnel Wastewater project recently constructed in the greater metropolitan Chicago area. Experience gained from this project has been incorporated into the design for the Americas sample site.

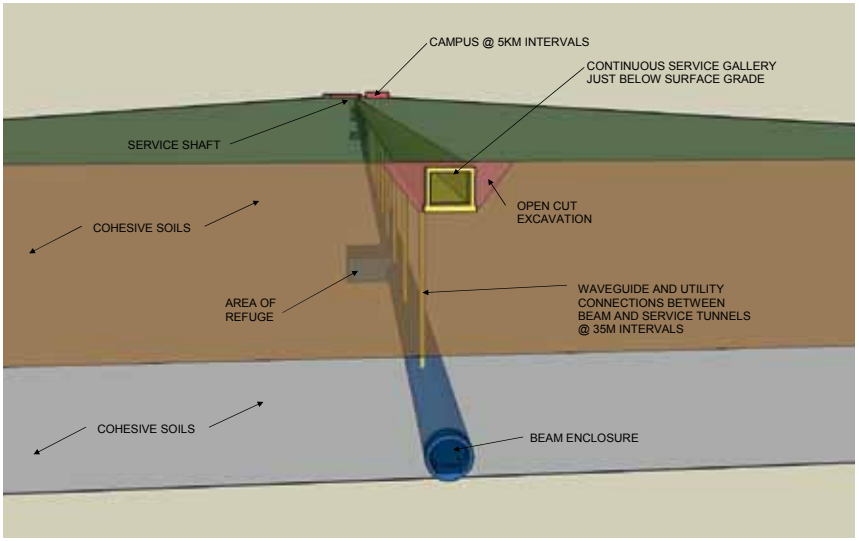

Figure 5.18 Tunnel schematic cross-section near Dubna in the Moscow, Russia region.

Figure 5.19 shows a schematic transverse section along the proposed alignment for the Americas sample site. The dolomite limestone bedrock is a very uniform geologic layer and is also relatively dry, which lends itself to the use of tunnel boring machines and drill-and-blast methods for the construction of underground tunnels and caverns.

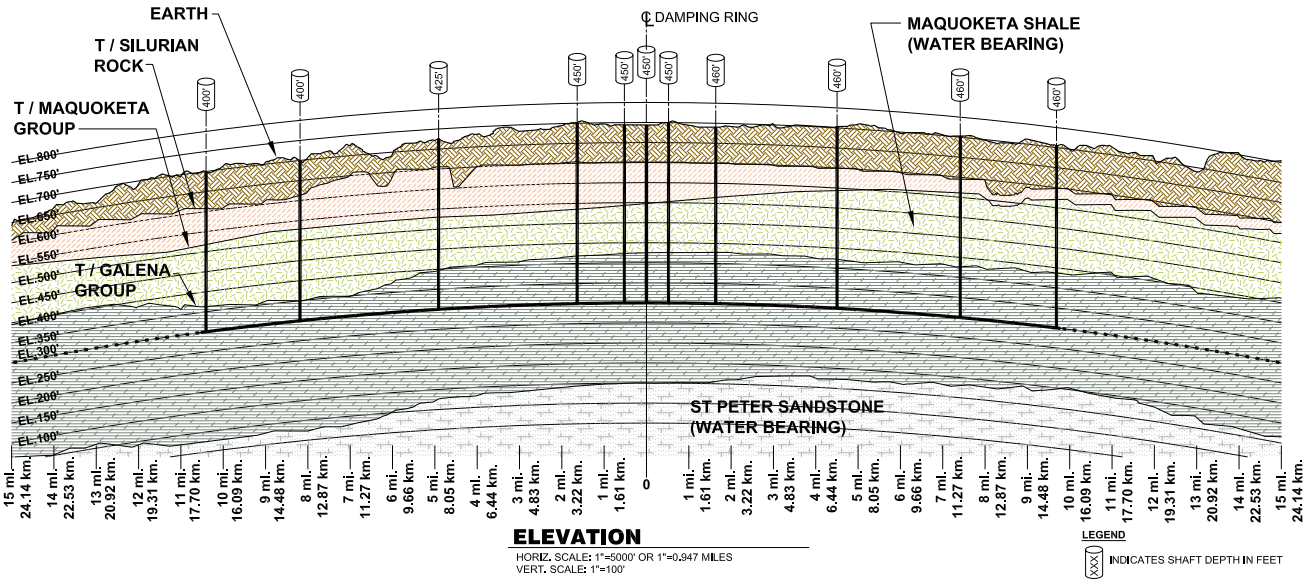

Figure 5.19 Tunnel geology of the Americas region sample site.

A schematic perspective view of the single deep-tunnel solution, also taken from the Americas tunnel configuration study, is shown in *Figure 5.20*. The uniform elevation of the Americas region sample site allows for the construction of surface buildings for utilities and other equipment at and around each vertical shaft location. Variations on the preliminary work for these surface campuses will necessarily depend on exact site selection, which may occur at a later date. However, conceptual work has been completed to develop general schemes and land requirements should this site be considered in the future. *Figure 5.21* shows a plan view of one of the surface campus layouts at a vertical access shaft. Included in this layout is space for cryogenic and high-level RF accelerator support equipment as well as process water cooling and conventional electrical power equipment. *Figure 5.22* shows the same layout in isometric form superimposed on a generic aerial photograph.

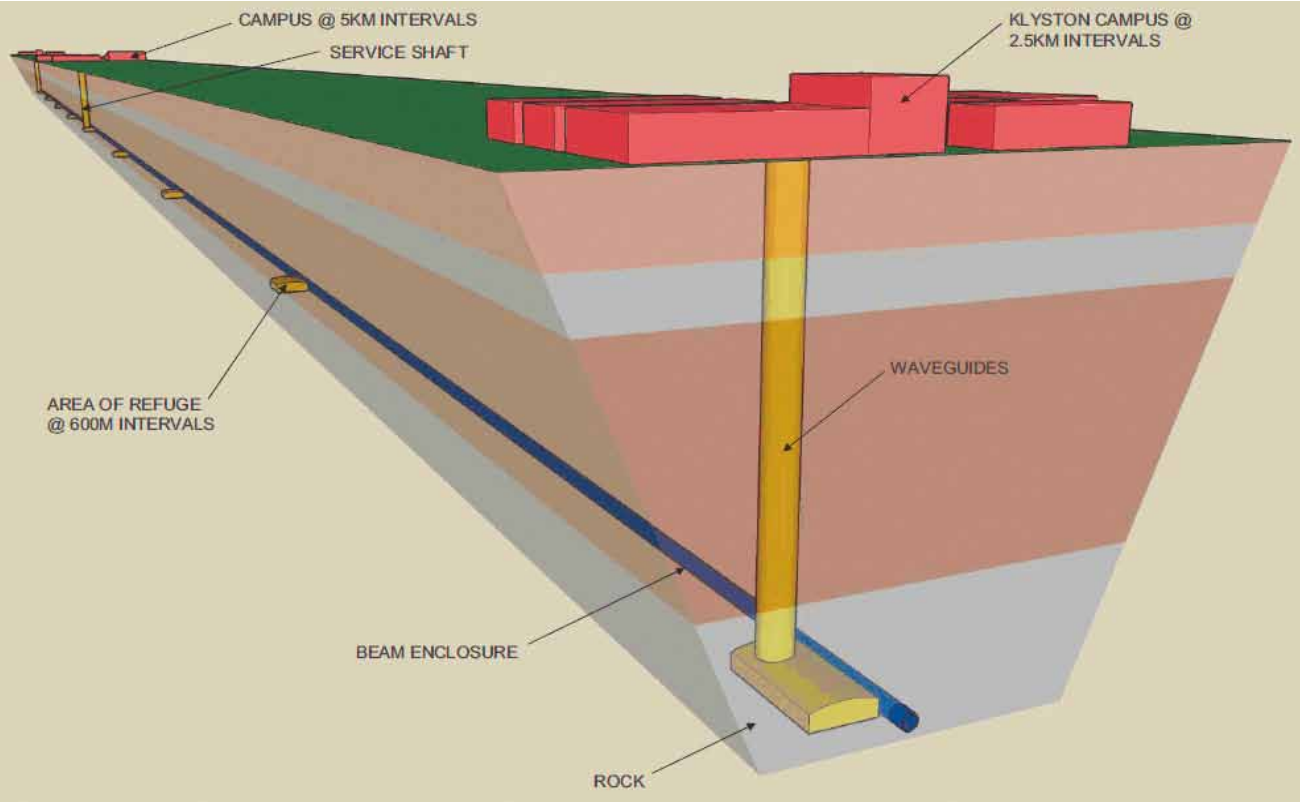

Figure 5.20 Tunnel cross-section schematic for the Americas region.

Variations on the preliminary work for these surface campuses will necessarily depend on exact site selection, which may occur at a later date. However, conceptual work has been completed to develop general schemes and land requirements should this site be considered in the future. *Figure 5.21* shows a plan view of one of the surface campus layouts at a vertical access shaft. Included in this layout is space for cryogenic and high-level RF accelerator support equipment as well as process water cooling and conventional electrical power equipment. *Figure 5.22* shows the same layout in isometric form superimposed on a generic aerial photograph.

Figure 5.21 Building floor plan of the klystron cluster surface support.

Figure 5.22 Aerial view of the klystron cluster surface support building.

The actual site selection process for the ILC project will begin in the coming years. However, preliminary work to investigate the potential of various sites located in all parts of the world provides a global approach to understanding the relative costs for each of the different design approaches and conditions that are likely to be encountered for each of the various sites being considered.

06

TOWARDS THE TECHNICAL DESIGN REPORT

6.1 A focus on mass production and cost

Phase 2 of the Technical Design Phase (TDP) will see a major focus on cost-effective mass-production scenarios for the superconducting radiofrequency (SCRF) cavity and cryomodule systems. As the primary cost driver for the ILC, establishing a defendable and realistic cost for the industrial manufacture of some 2,000 cryomodules will be by far the most critical issue facing the Global Design Effort (GDE) as it prepares for the *Technical Design Report* (TDR) at the end of 2012.

In order to establish an internationally agreed cost estimate for the cryomodules, several key themes will need to be developed:

- Cavity and cryomodule gradient specification and projected production yield
- Flexible technical specification based on a plug compatibility concept (interface definition and specifications)
- Production process and industrialisation models
- Models for international cooperation including in-kind contributions

Several issues go beyond just production engineering. For example, understanding the need to maintain flexibility in the industrialisation models to support in-kind contributions is seen as a high priority. As a result, understanding how the production of cryomodules might be divided among contributing nations (or regions) must be factored into the production models. At the same time, a strong emphasis on mass-production techniques must be adopted to maximise the expected significant cost-reduction factor associated with large-volume production. A further desire is to maintain as far as possible global competition between possible vendors, with a view to reduced cost to the ILC project. Last (but not least), a cost-effective approach to risk mitigation needs to be developed, one that does not place too stringent performance guarantees on vendors that would likely increase the costs.

Early in the Technical Design Phase, the concept of plug-compatible design was introduced for the components of the cryomodule (specifically the cavity package). A set of interface definitions have been internationally agreed upon that, in principle, would allow alternative component designs to be assembled in the same cryomodule. During the current R&D phase, plug compatibility has allowed parallel development of technologies such as cavities, tuners, and high-power couplers. This has allowed regional teams to develop in-house design expertise, effectively promoting local innovation, while maintaining global cooperation and sharing advanced technology.

The concept of plug compatibility can now be directly translated to the mass-production models (construction), where it will:

- support competition between multiple suppliers, promoting cost reduction, while allowing variants within a common design envelope;
- allow for multiple (in-kind) contributors, each of which may arrive at a different cost-optimised design, maximising the benefit of local industrial capability and experience;
- encourage intellectual interest from each contributor to promote regional, national or institutional centres for integration and test of the cryomodule or any of its subcomponent packages.

The published cost estimate in the RDR was firmly based on the original European-based industrial studies performed for the TESLA proposal in 2000 *[6-1]*. These studies were based on a single-vendor model for the production of 20,000 cavities (about 1,700 cryomodules) in a five-year time scale (two years for setup and pre-production, three years for peak production). While these studies represent a solid basis for one particular industrial model, it is now necessary that the GDE produce its own updated estimate given the progress in the last ten years. Specifically,

- The last ten years of R&D have seen the establishment of SCRF technology in both the Americas and Asian regions, and a European-centric estimate must now be reviewed.
- The governance issues mentioned above (in-kind contributions leading to distributed mass-production) should be considered and the possible impact on the costs quantified. This suggests moving away from the single-vendor model used in the RDR estimate (but does not necessarily exclude it).
- Production risk should be more carefully considered, which would also tend towards a multiple-vendor model.

Finally, the recent experience of the European X-ray Free-Electron Laser (or European XFEL) mass-production will need to be factored in, as this will be the largest production and deployment of the technology within the TDR timescale. However, at approximately 5% of the ILC production requirement, care needs to be taken in extrapolating these costs.

Many of the key issues mentioned above are driven primarily by politics, which is at this stage difficult to predict. Exactly how the mass-production of cryomodules will be divided amongst possible contributors (in some form of in-kind model) will only be exactly known at the time of approval. However, the GDE needs to be prepared to answer the inevitable questions that will be asked, which will require the development of more than one mass-production model (and ultimately cost estimate). Therefore it is necessary to develop cost estimates in all three regions based on a limited set of in-kind contribution scenarios. Approaches to mass-production in each region will need to be studied that take into account the differences in local industry technical expertise, markets and cost. This will likely result in different technical approaches to mass-production, each cost-optimised for the specific scenarios considered and the local regional industrial environment.

In developing the models and associated cost estimates it will be necessary to

- review the existing manufacturing process, and understand the primary cost-drivers (information from the European XFEL will be extremely useful in this respect),
- look for the most cost-effective production technology and approach towards aggressive cost-reduction for large-scale mass production; this includes R&D towards cost-effective production techniques and possible modifications to the cryomodule design (design for manufacture), and
- communicate with regional industry and laboratories, with a view to developing cost-effective manufacturing, testing and quality control models.

The role of the large regional laboratories is seen as central to cost-effective mass production. In particular, these labs would provide testing and quality control facilities, and possibly act as the primary integrator of sub-components delivered by industry. Such a model is similar to the approach adopted by

CERN for the LHC dipole mass production. Performance guarantees would then be the responsibility of the central labs; this is seen as key to reducing to a minimum vendor risk, and thereby reducing the costs. The central labs – acting as regional production centres – are then directly responsible for delivering complete cryomodules (for example) to the future ILC lab. While other mass-production models exist, the lab-based regional centre model is clearly one that would fit naturally with a globally distributed cryomodule production, driven by in-kind contributions. For all models considered, an important aspect is to maintain global market competition between vendors. A primary GDE goal for the Technical Design Phase is the development of industrial capability in all three regions, but this should be seen as developing a global competition base, rather than guaranteeing regionally centred contracts to local industries.

To facilitate the development of the mass-production models, and to prepare the way for cost estimates based on industrial quotes, a series of visits to established cavity and cryomodule manufacturers in all three regions was made in 2009, primarily to establish contact and to gauge first-hand the scale of the production facilities. This was followed by an industrial workshop on SCRF cavity industrialisation, held in Kyoto in 2010 *[6-2]*. The GDE now plans to make a second visit to the vendors in 2011, specifically to begin discussions on mass-production and ultimately producing tentative cost-estimates for cavity production based on a well-defined process specification ('build to print'). The industrial feedback received will then be factored into GDE updated cost estimate for the TDR.

6.2 Consolidating R&D

Following the completion of the *Reference Design Report* in 2007, the focus of the ILC Global Design Effort shifted to component and system development and performance demonstrations. In keeping with a worldwide three-region strategy, the foremost principle of the GDE, the work has been started and carried out evenly in each region by the global partnership team. A summary R&D plan that explains the effort, including tables showing where the work is done, has been kept updated and published semi-annually since mid-2008.

The primary objective of the R&D is to reduce technical risk and find ways to reduce project cost. Also, since the timescale of ILC construction is unknown, the GDE promotes and is constantly in search of alternate strategies for various aspects of the design, including subsystems and components. Through that, the project is kept updated and does not become frozen as can often happen in long-term high-technology projects.

During the second half of the Technical Design Phase the GDE will take stock of risk-reduction and cost-saving R&D work and assess what is useful and appropriate for inclusion in the *Technical Design Report* to be published in 2012. In this section, we summarise these efforts and outline what may be included in the TDR. In some cases, work will continue beyond the publication of the TDR and this is also outlined.

GDE Research and Development work can be divided into three categories: high-technology scientific and engineering studies, beam-based studies and component and sub-system design development.

6.2.1 High-technology scientific and engineering studies aimed at expanding the state-of-the-art frontier

Superconducting radiofrequency process and test infrastructure in several institutions was commissioned successfully during the Technical Design Phase. To provide the greatest return, these facilities were designed and constructed to address a variety of challenges inherent in the emergent technology. While each one is built to satisfy ILC project-specific R&D goals, each also includes enough flexibility to serve the goals of other projects. This strategy, applied globally, resulted in both redundancy and diversity.

Research and development goals (chapter 2) are arranged to focus attention on three aspects of the technology: 1) the basic nine-cell niobium sheet metal cavity, 2) the cryomodule assembly and 3) the operation of a system based on several cryomodules at full ILC main-linac beam intensity. A fourth focus of the R&D is on mass-production aspects of the cavities and cryomodules. For the latter, each of the three regions adopted a different approach – production of roughly 600 cavities for the European XFEL, development of a pilot plant for industrialisation studies in Asia, and studies of longer-term improvements to the basic process in America. During the Technical Design Phase, we will see results from each of the four focal points. Each of these will be included in the TDR, especially the analysis of mass-production techniques.

Notwithstanding this global progress, much of the infrastructure has just been commissioned and full system tests, especially, will not be started until after 2012. While we expect the primary objectives of linac system testing to be achieved in time for the TDR, the potential of the multi-cryomodule high-current test linacs to demonstrate new cost-saving designs will not be realised by then. The highest post-2012 priority for these installations will be to subject the new technology to a value engineering cycle, together with regional industrial partners. A component of this effort will be in support of the 1 TeV energy upgrade for the ILC. We expect 1 TeV upgrade-related R&D to address issues in each of the four focal points, and hope for performance (and cost) breakthroughs in cavity gradient, cryomodule and coupler design, system integration and industrialisation and mass-production.

6.2.2 Beam-based studies based at ILC purpose-built test facilities

Three beam test facilities were constructed with ILC beam parameters in mind and presently devote substantial operations time to ILC R&D. These are CesrTA (Cornell, Americas) for studies of the electron-cloud coherent instability, ATF/ATF2 (KEK, Asia) for studies of precision beam optics and tuning, and TTF/FLASH (DESY, Europe) for studies of high-current superconducting linac operation. It is fitting for investments of this size that the primary goals of each test facility have very little overlap with the goals of the other two. At each one, beam studies are carried by a global collaboration. Initial results from each – electron cloud mitigation strategies from CesrTA, low-emittance tuning from ATF, and full beam current tuning from FLASH operations – will be a highlight of the TDR. It is not expected, however, that the full suite of studies will be complete by the end of 2012; the work will continue beyond then.

Each of the ILC test facilities has unique capabilities and will be useful for accelerator science and technology development well beyond the ILC. This is particularly true for ATF/ATF2, the only accelerator test facility built to study manipulation of ultra-low-emittance beams. Beyond the publication of the TDR, ATF/ATF2 will be valuable for development of precision magnets, instrumentation and alignment technology, coupled with development of iterative beam tuning procedures. TTF/FLASH studies are closely linked to preparations for the operation of the European XFEL, which should begin in 2014. Beam-based feedback loops, especially those intended for control of SCRF cavity fields, will continue to be a critical focus at FLASH because the long bunch trains enable precision performance and stability.

6.2.3 Component and sub-system design development

Through the development of the *Reference Design Report* from 2005 to 2007 and during the Technical Design Phase, development work on the baseline design (and alternate designs), has been strongly supported by the GDE. Examples of this include the polarised electron source laser and gun system, the positron source target and matching device, the damping ring fast injection and extraction kicker, the linac Marx modulator (alternate), the beam delivery and machine-detector interface superconducting final doublet magnet and the conventional facilities and siting development for sites with varied topography. At present, midway through the TDP, plans for reviewing and evaluating the work done are in progress. Criteria to be applied are performance, anticipated cost, needs and plans for additional development and interface to various systems.

For the TDR, technical subsystem choices made through the review process will reflect the state-of-the-art ILC accelerator R&D. In some cases, especially with projects that are close to completion, selections made for the technical design will assume the work to be successful. In addition, to make sure the design is kept dynamic and flexible following the TDR, we will promote work on new and promising technology and develop links to the teams doing that work. One way that will be done is through the collaboration with the CLIC study group, centred at CERN. This group has chosen to work on less well established technologies with tighter tolerances and that require more elaborate demonstration schemes. Nevertheless, we expect their design report, scheduled to be published around 2016, to include significant results that can be adapted to the ILC design.

6.3 The Project Implementation Plan

While the technical information relating to the ILC will be detailed in the *Technical Design Report*, there is additional information that will be useful to any collaboration member considering a possible bid to host. The Project Implementation Plan (PIP) will seek to provide, at an outline level, this kind of non-technical information emphasising areas where the GDE could reasonably be expected to possess an informed opinion. Examples include such topics as technical requirements for sites or in-kind contribution models. At this time there is no requirement for a highly detailed proposal, which would rapidly become out of date. Thus the PIP has the goal of establishing a general framework for considerations that should prove more enduring. The PIP will be produced on the same schedule as the TDR.

Many aspects of project implementation start from the basic project organisation, and the GDE will produce governance and funding recommendations in the PIP. This will be a summary of a more detailed GDE report on this subject. Specific proposals for organisation charts and the like are not warranted at this time. That will depend on the ultimate project management team. A synopsis of the project team and member state roles and responsibilities will be given in the PIP.

A sufficient number of large multinational projects have been completed to date that there seems to be a tacit understanding on the role of a host state, so this should not be too controversial. For example, land acquisition and services to the site boundary should not be a project cost. Civil construction and on-site utilities, which is part of the construction project, are generally accepted be a host responsibility. The host state must also agree to certain legal and quasi-legal conditions such as international access. The PIP will review the anticipated host state responsibilities.

In the absence of any additional information, then, a project schedule based on an LHC-like installation effort for the main linac recommends itself. Some progress in this direction was made at the ALCPG09 workshop. This in turn would establish tunneling requirements. This input together with a 'traditional' start on the low-energy systems will provide sufficient information to develop a nominal project schedule. We intend to develop a crude high-level resource-loaded schedule based on the Technical Design Phase 2 cost estimate. This will provide guidance as to the natural project funding profile and will be part of the PIP.

Most scenarios involve substantial in-kind contributions, and outlining the appropriate interface points in the PIP would serve to furnish examples of the kind of technical contributions that collaboration members could be expected to provide. The exact details of member state contributions will, of course, only be determined during the final project negotiations. The use of in-kind contributions also implies that there will be an outsourcing of technical design and associated quality assurance activities. The PIP will outline the suggested respective roles of the project and the member state collaborators in this regard.

While the design of the ILC is not site-specific, there are requirements for the site that will not be expected to change significantly. The PIP will describe the major site requirements such as footprint, power needs, tunnel penetrations,

central campus layout and so on. The GDE will provide different technical solutions to enable different site topographies to be considered. We expect the final ILC design to be site dependent to some degree. The actual site-selection process will be specified by the ILC Steering Committee. We do expect to include a summary in the PIP for the sake of completeness.

We do not expect all technical work to cease by the end of 2012. The phase two plan of the Superconducting Radiofrequency Test Facility at KEK is scheduled to run to (at earliest) 2014. The Fermilab-based string test is completed in 2012 but routine operations would only start in 2013 and would continue for several years at least. Cryomodule and cavity value engineering will remain a highly leveraged item and it is reasonable to assume that positron production will remain a topic of interest. The Super-KEKB (2013) will incorporate several of the CesrTA electron cloud-mitigation techniques. The anticipated technical programme for the subsequent several years will be described in the PIP.

6.4 Beyond the *Technical Design Report*

This interim report focuses mainly on the ILC R&D progress and accomplishments since the *Reference Design Report* was published. It marks a halfway point toward completion of the ILC Technical Design Phase, which will be documented at the end of 2012 in a *Technical Design Report*. The TDR will be a complete report that contains all that will be needed to propose the ILC to collaborating governments, including the technical design, costing and an implementation plan. The design has evolved significantly since the RDR, reflecting a more optimised and coherent design that balances cost, risk and performance. In addition, by the end of 2012 the key R&D demonstrations will have been completed and the project will be ready to be proposed at any time after the TDR.

The GDE will have accomplished its mandate once the TDR is published, reviewed and accepted by our oversight committees (around mid-2013). Nevertheless, there will still be important R&D still to be continued, and improvements in the design will undoubtedly result. In fact, the ILC design will continue to evolve until the project is approved for construction.

Guidance from LHC results is very much sought. The first extended LHC run will take place during the coming two years, during TDR completion. The most significant results are expected during the post-2012 period. The LHC physics results will both sharpen the physics motivation and help guide the choice of machine parameters, including the initial energy. The ILC design must remain flexible enough to respond to this emerging physics. At present, the biggest unknown is determining what energy a lepton collider will be required to match LHC physics. If the ILC reach of about 1 TeV is a good match, then the ILC is clearly the right machine to propose based on maturity of the technology and achievable physics parameters. However, if much higher energy is required, other approaches like CLIC or a muon collider will be required; both will require more R&D before a project can be proposed.

After the TDR, the highest priority will continue to be developing high-gradient SCRF through research that may substantially increase the gradient, such as developing different cavity shapes. On a systems level, the Superconducting Radiofrequency Test Facility programmes at KEK and the superconducting radiofrequency test accelerator in the New Muon Lab at Fermilab will just be coming to fruition and a several-year programme of research and testing will follow. There will also be continuing R&D in other areas, including positron source R&D, final focus tests at ATF2, assuming the ATF continues to run, and other endeavours. Perhaps the largest unfinished task that has to be completed is a value engineering study, after which the final engineering design can proceed and the construction begun.

It will be possible to carry out the post-TDR programme at a somewhat reduced support level compared to the present programme, but it must be done in a fashion poised to ramp up as soon as commitments are made for an ILC construction project. The post-TDR R&D programme will be carried out by a successor organisation to the GDE; the ILC Steering Committee and International Committee for Future Accelerators are in discussions as to how to structure such a new organisation. The GDE management is providing input for that process. All agree that whatever successor organisation is created there will need to be continuity of key personnel and core expertise, as well as the ability to maintain a global process for setting priorities and making decisions.

Although the future of the ILC R&D programme following the TDR is presently unclear, we remain ready to submit a very strong construction proposal whenever governments are receptive to considering a future large global project in particle physics.

References

[6-1] TESLA proposal.

[6-2] http://ilcagenda.linearcollider.org/conferenceDisplay.py?confId=4530

AUTHOR LIST

Ned Arnold[1], Sebastian Aderhold[16], Chris Adolphsen[44], Robert Ainsworth[28], Yasuo Ajima[31], Mituo Akemoto[31], Javier Alabau[21], Maria Alabau Pons[9], David Alesini[24], James Alexander[15], John Amann[44], Deepa Angal-Kalinin[45], Robert Apsimon[28], Sakae Araki[31], Tug Arkan[18], Alexander Aryshev[31], David Asner[7], Valeri Ayvazyan[16], Nicoleta Baboi[16], Sha Bai[22], Ian Bailey[34], Philip Bambade[11], Serena Barbanotti[18], Barry Barish[5], Marco Battistoni[18], Victoria Bayliss[46], Paul Bellomo[44], Douglas Bett[28], Wilhelm Bialowons[16], Michael Billing[15], Grahame Blair[28], Cesar Blanch[21], Benoit Bolzon[9], Stewart Boogert[28], Laura Boon[42], Gary Boorman[28], Angelo Bosotti[23], Axel Brachmann[44], Tom Bradshaw[46], Amanda Brummitt[46], Yulian Budagov[26], Benjamin Bullock[15], Craig Burkhart[44], Philip Burrows[28], Geoff Burton[46], John Byrd[36], Sergio Calatroni[9], Joseph Calvey[15], Simon Canfer[46], Steve Carr[46], Paul Carriere[15], Harry Carter[18], John Carwardine[1], Christine Celata[36], Mark Champion[18], Stephane Chel[8], Jia-er Chen[41], Glenn Christian[28], Wojciech Cichalewski[16], Jim Clarke[45], Paul Coe[28], Norbert Collomb[45], Ben Constance[28], Zachary Conway[15], Lance Cooley[18], Charlie Cooper[18], Laura Corner[29], Mike Courthold[46], Anthony Curtis Crawford[15], James Crittenden[15], Francis Cullinan[28], T.S. Datta[25], Michael Davis[28], Stefano De Santis[36], Lawrence Deacon[28], Jean-Pierre Delahaye[9], Theo Demma[24], Yury Denisov[26], Andrey Dudarev[26], Gerald Dugan[15], Nicholas Eggert[15], George Ellwood[46], Eckhard Elsen[16], Atsushi Enomoto[31], Fabien Eozenou[8], Grigory Eremeev[27], Bart Faatz[16], Angeles Faus-Golfe[21], John Flanagan[31], Mike Foley[18], Michael Forster[15], Josef Frisch[44], Lars Froehlich[16], Shigeki Fukuda[31], Masafumi Fukuda[31], Yoshisato Funahashi[31], Miguel Furman[36], Fumio Furuta[31], Wei Gai[1], Jie Gao[22], Mingqi Ge[15], Nicolas Geffroy[12], Rongli Geng[27], Eliana Gianfelice-Wendt[18], Camille Ginsburg[18], Mariusz Grecki[16], Shlomo Greenwald[15], Jeffrey Gronberg[37], Susanna Guiducci[24], Hayg Guler[38], Kazufumi Hara[31], Katherine Harkay[1], Elvin Harms[18], Mike Harrison[4], Donald Hartill[15], Hitoshi Hayano[31], Olaf Hensler[16], Aeyoung Heo[33], Leah Hesla[18], Stefan Hesselbach[17], Norio Higashi[31], Matthew Hills[46], Andy Hocker[18], Georg H. Hoffstaetter[15], Robert Holtzapple[6], Yosuke Honda[31], Katja Honkavaara[16], Walter Hopkins[15], Kenji Hosoyama[31], Jung-Yun Huang[40], Andrew Hutton[27], Woon-Ha Hwang[40], Alexander Ignatenko[16], Hitoshi Inoue[31], Yoshihisa Iwashita[32], Wojciech Jamuzna[16], Michael Jenkins[34], Kay Jensch[16], Andréa Jeremie[12], James Jones[45], Nirav Joshi[28], C.K. Joshi[43], Eiji Kako[31], Yoshio Kamiya[48], Raimund Kammering[16], Ken-ichi Kanazawa[31], Pavel Karataev[28],

[1] ANL
[2] Bhabha Atomic Research Centre
[3] BINP Novosibirsk
[4] BNL
[5] California Institute of Technology
[6] California Polytechnic State University
[7] Carleton University
[8] CEA/Irfu
[9] CERN
[10] CNRS/IN2P3
[11] CNRS/LAL
[12] CNRS/LAPP
[13] CNRS/LLR
[14] Cockcroft Institute/ University of Liverpool
[15] Cornell University
[16] DESY
[17] Durham University
[18] Fermilab
[19] Hamburg University
[20] Hiroshima University
[21] IFIC (CSIC-UV)
[22] IHEP
[23] INFN Milano
[24] INFN-LNF
[25] IUAC
[26] JINR
[27] JLab

Vladimir Kashikhin[18], Hiroaki Katagiri[31], Valery Katalev[16], Shigeki Kato[31], Michael P. Kelly[1], Robert Kephart[18], Jim Kerby[18], Timergali Khabiboulline[18], Jin-Sung Kim[15], EunSan Kim[33], HyoungSuk Kim[33], SeungHwan Kim[33], Arkadiy Klebaner[18], Peter Kneisel[27], Yuji Kojima[31], Sachio Komamiya[48], Yoshinari Kondo[31], Waldemar Koprek[16], Denis Kostin[16], Anatoly Krasnykh[44], David Kreinick[15], Benjamin Kreis[15], Dirk Kruecker[16], Kiyoshi Kubo[31], Vic Kuchler[18], Kiran Kulkarni[2], Tatsuya Kume[31], Shigeru Kuroda[31], Mickaël Lacroix[11], Briant Lam[44], Andrea Latina[9], Jerry Leibfritz[18], Konstantin Lekomtsev[28], Yulin Li[15], Lutz Lilje[16], Wanming Liu[1], Xianghong Liu[15], Kexin Liu[41], Jesse Livezey[15], Florian Loehl[15], J. Lucas[45], Alexey Lyapin[28], Oleg Malyshev[45], Fabio Marcellini[24], Mika Masuzawa[31], Axel Matheisen[16], Toshihiro Matsumoto[31], Douglas McCormick[44], Robert Meller[15], Shinichiro Michizono[31], Alexander Mikhailichenko[15], Shekhar Mishra[18], Don Mitchell[18], Takako Miura[31], Wolf-Dietrich Moeller[16], Stephen Molloy[28], Gudrid Moortgat-Pick[19], Dawn Munson[36], Sergei Nagaitsev[18], Takashi Naito[31], Hirotaka Nakai[31], Hiromitsu Nakajima[31], Tomoaki Nakamura[48], Chris Nantista[44], Olivier Napoly[8], Janice Nelson[44], Laurence Nevay[29], Shuichi Noguchi[31], Kazuhito Ohmi[31], Norihito Ohuchi[31], Daisuke Okamoto[47], Toshiyuki Okugi[31], Masahiro Oroku[48], John Osborne[9], Joe Ozelis[18], Hasan Padamsee[15], Carlo Pagani[23], Mark Palmer[15], Yannis Papaphilippou[9], Rocco Paparella[23], Yong Jung Park[40], Brett Parker[4], Ewan Paterson[44], Jacques Payet[8], Shilun Pei[44], Gregg Penn[36], Colin Perry[28], Daniel Peterson[15], Tom Peterson[18], Paulo Pierini[23], Tom Piggott[37], Yuriy Pischalnikov[18], Mauro Pivi[44], Freddy Poirier[16], S. Postlethwaite[45], Eduard Pratt[16], Pravin Rai[2], Pantaleo Raimondi[24], Tor Raubenheimer[44], Charles Reece[27], Kay Rehlich[16], Yves Renier[9], Javier Resta Lopez[29], Nathan Rider[15], Sabine Riemann[16], Cécile Rimbault[11], Bob Rimmer[27], Louis Rinolfi[9], James Rochford[46], Marc Ross[18], Allan Rowe[18], Amit Roy[25], Perrine Royole-Degieux[10], David Rubin[15], Giovanni Rumolo[9], Takayuki Saeki[31], David Sagan[15], Kenji Saito[31], Tomoyuki Sanuki[47], Masato Sato[31], Polepalle Styamurthy[2], Motoaki Sawabi[31], Anthony Scarfe[39], Andreas Schaelicke[16], Joern Schaffran[16], Warren Schappert[18], P. Schilling[16], Felix Schlander[16], Holger Schlarb[16], Christian Schmidt[16], M. Schmoekel[16], Siegfried Schreiber[16], Daniel Schulte[9], Duncan Scott[45], Andrei Seryi[30], James Shanks[15], Valery Shemelin[15], Kyo Shibata[31], Tetsuo Shidara[31], Gregory Shirkov[26], Toshiro Shishido[31], John Sikora[15], Stefan Simrock[16], Waldemar Singer[16], Brian Smith[18], Steve Smith[44], Tonee Smith[44], Nikolay Solyak[18], Kiran Sonnad[15], Cherrill Spencer[44], Martin Staack[16], Rich Stanek[18], Taikan Suehara[31], Yusuke Suetsugu[31], Ryuhei Sugahara[31], Christina Swinson[29], Cosmore Sylvester[18], Jaroslaw Szewinski[16], Mauro Taborelli[9], Tsuyoshi Tajima[35], Tohru Takahashi[20], Rika Takahashi[31], Tateru Takenaka[31], Tao Tang[44], Toshiaki Tauchi[31], Owen Taylor[46], Akio Terashima[31], Nobuhiro Terunuma[31], Jeff Tice[44], Vikas Tiwari[2], Nobukazu Toge[31], Rogelio Tomas[9], Grigori Trubnikov[26], Kiyosumi Tsuchiya[31], Kenji Ueno[31], Junji Urakawa[31], David Urner[29], Andrei Ushakov[16], Alessandro Variola[11], Marco Venturini[36], Marc Verderi[13], Reine Versteegen[8], Bernard Visentin[8], Nicholas Walker[16], Dou Wang[22], Lanfa Wang[44], Min-Huey Wang[44], Faya Wang[44], Matthew Warden[29], Barbara Warmbein[16], Ken Watanabe[31], Yuichi Watanabe[31], Stephen Watson[46], Hans Weise[16], Manfred Wendt[18], Glen White[44], Tim Wilksen[16], Ingo Will[49], Kay Wittenburg[16], Walter Wittmer[44], Torsten Wohlenberg[16], Andrzej Wolski[14], Mayling Wong-Squires[18], Mark Woodley[44], Mike Woodward[46], Seiya Yamaguchi[31], Youhei Yamaguchi[48], Akira Yamamoto[31], Yasuchika Yamamoto[31], Takashi Yamanaka[48], Yiton Yan[44], Jacqueline Yan[48], Hakutaro Yoda[48], Kaoru Yokoya[31], Jiyuan Zhai[22], Min Zhang[22], Feng Zhou[44], Frank Zimmerman[9], Konstantin Zolotarev[3].

[28] John Adams Institute for Accelerator Science and Royal Holloway, University of London
[29] John Adams Institute for Accelerator Science and University of Oxford
[30] John Adams Institute for Accelerator Science, University of Oxford and Royal Holloway, University of London
[31] KEK
[32] Kyoto University
[33] Kyungpook National University
[34] Lancaster University
[35] LANL
[36] LBNL
[37] LLNL
[38] LLRL
[39] Manchester University
[40] PAL
[41] PKU
[42] Purdue University
[43] RRCAT
[44] SLAC
[45] STFC, Daresbury Laboratory
[46] STFC, Rutherford Appleton Laboratory
[47] Tohoku University
[48] Tokyo University
[49] TU Berlin

design: form one® visual communications | www.form-one.de

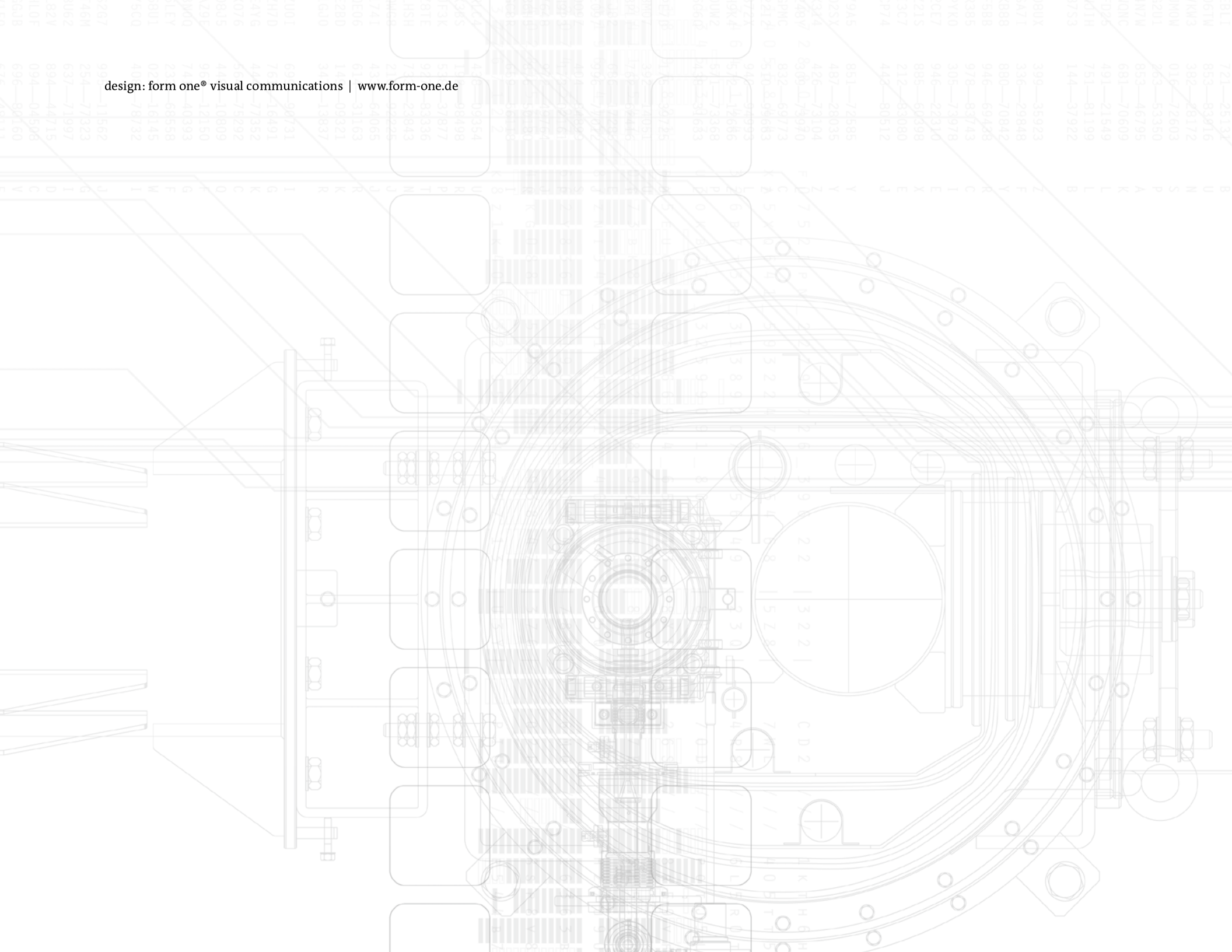

ISSUED BY . . . . ilc international linear collider

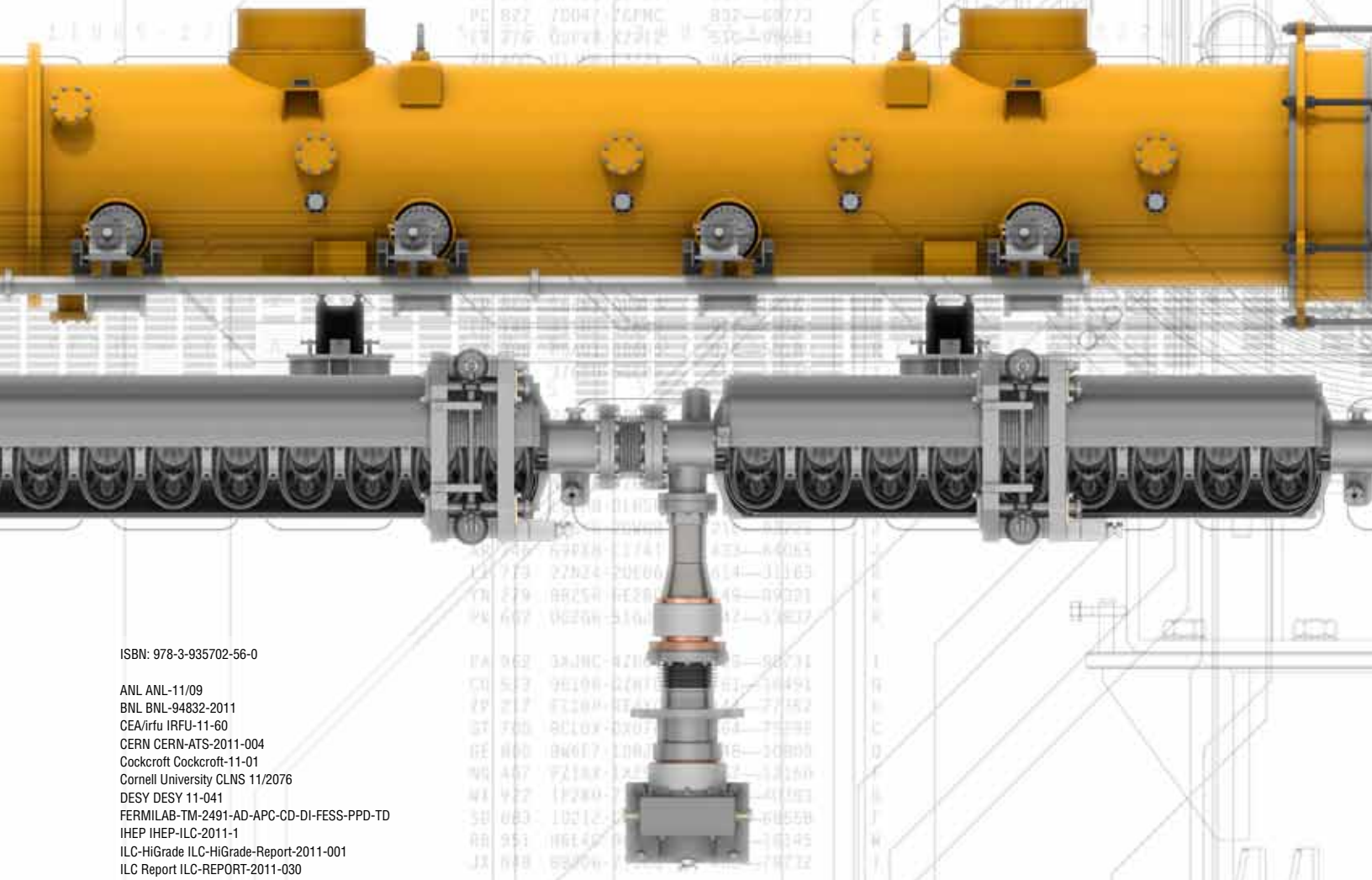

ISBN: 978-3-935702-56-0

ANL ANL-11/09
BNL BNL-94832-2011
CEA/irfu IRFU-11-60
CERN CERN-ATS-2011-004
Cockcroft Cockcroft-11-01
Cornell University CLNS 11/2076
DESY DESY 11-041
FERMILAB-TM-2491-AD-APC-CD-DI-FESS-PPD-TD
IHEP IHEP-ILC-2011-1
ILC-HiGrade ILC-HiGrade-Report-2011-001
ILC Report ILC-REPORT-2011-030
INFN LNF-11/2(NT) 30-03-2011
JAI JAI-2011-001
JINR JINR Dubna-E9-2011-32
JLab JLAB-R-2011-01
KEK KEK Report 2011-1
KNU KNU/CHEP-ILC-2011-1
LLNL LLNL-TR-477656
SLAC SLAC-R-965

INTERNATIONAL LINEAR COLLIDER PHYSICS AND DETECTORS

2011 STATUS REPORT

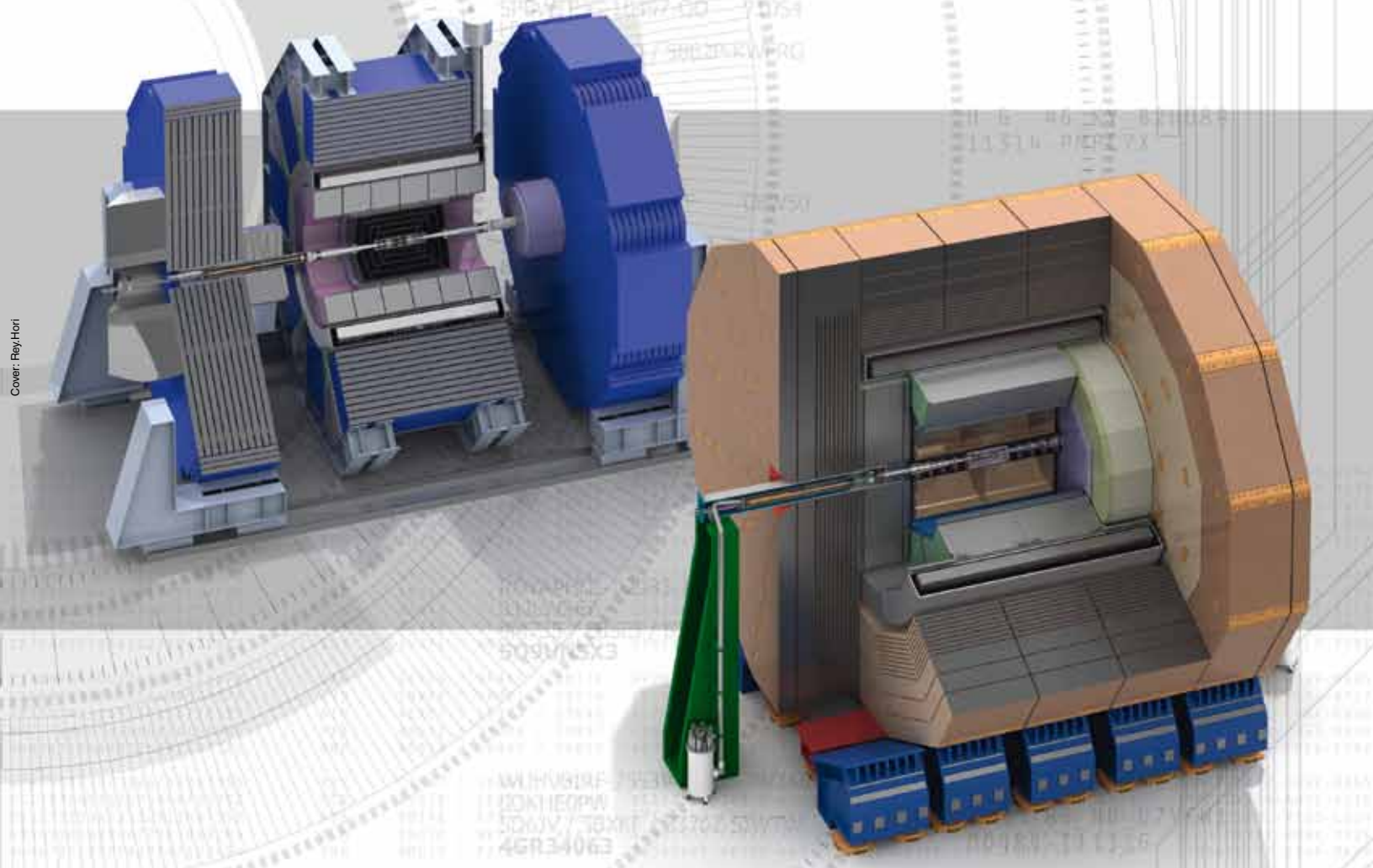

Cover: Rey Hori

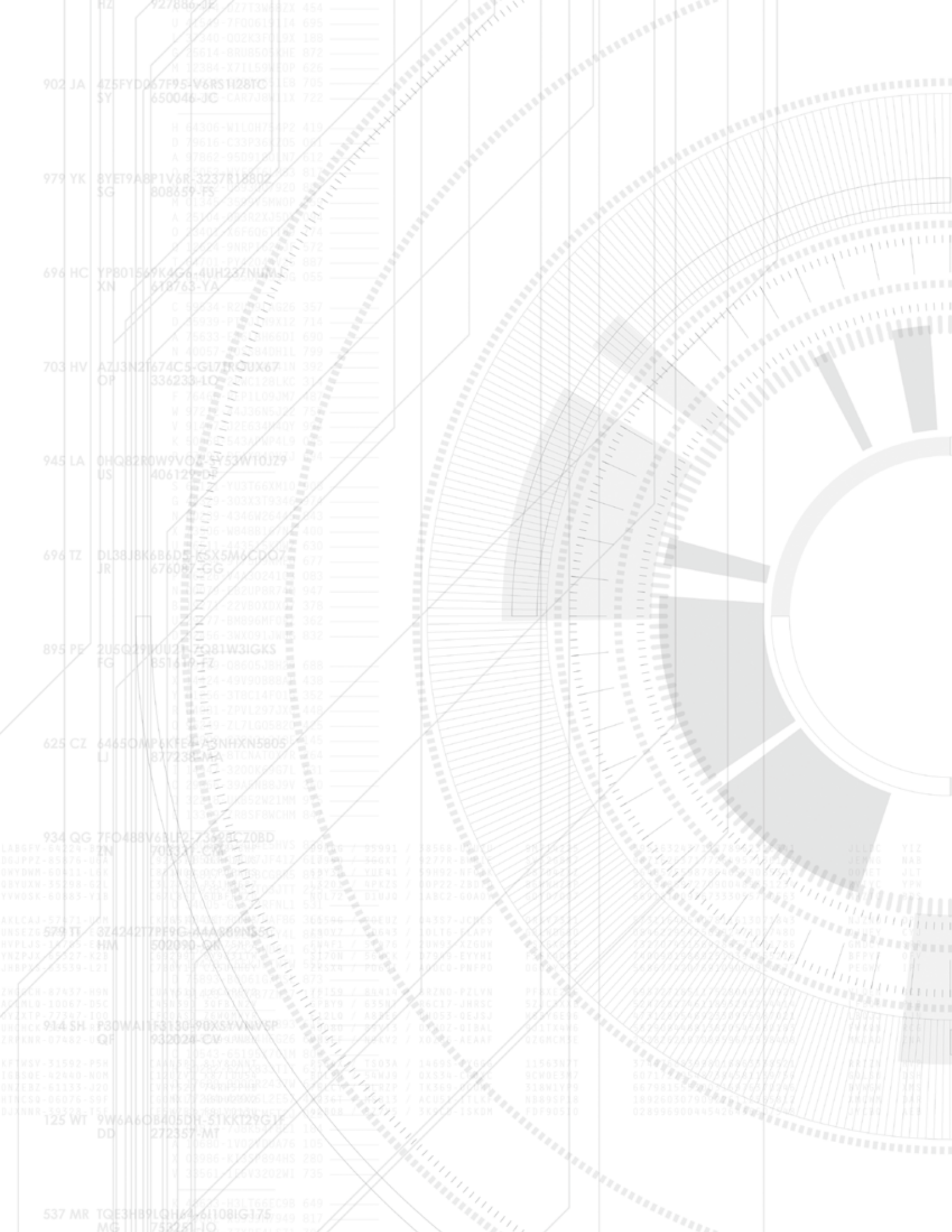

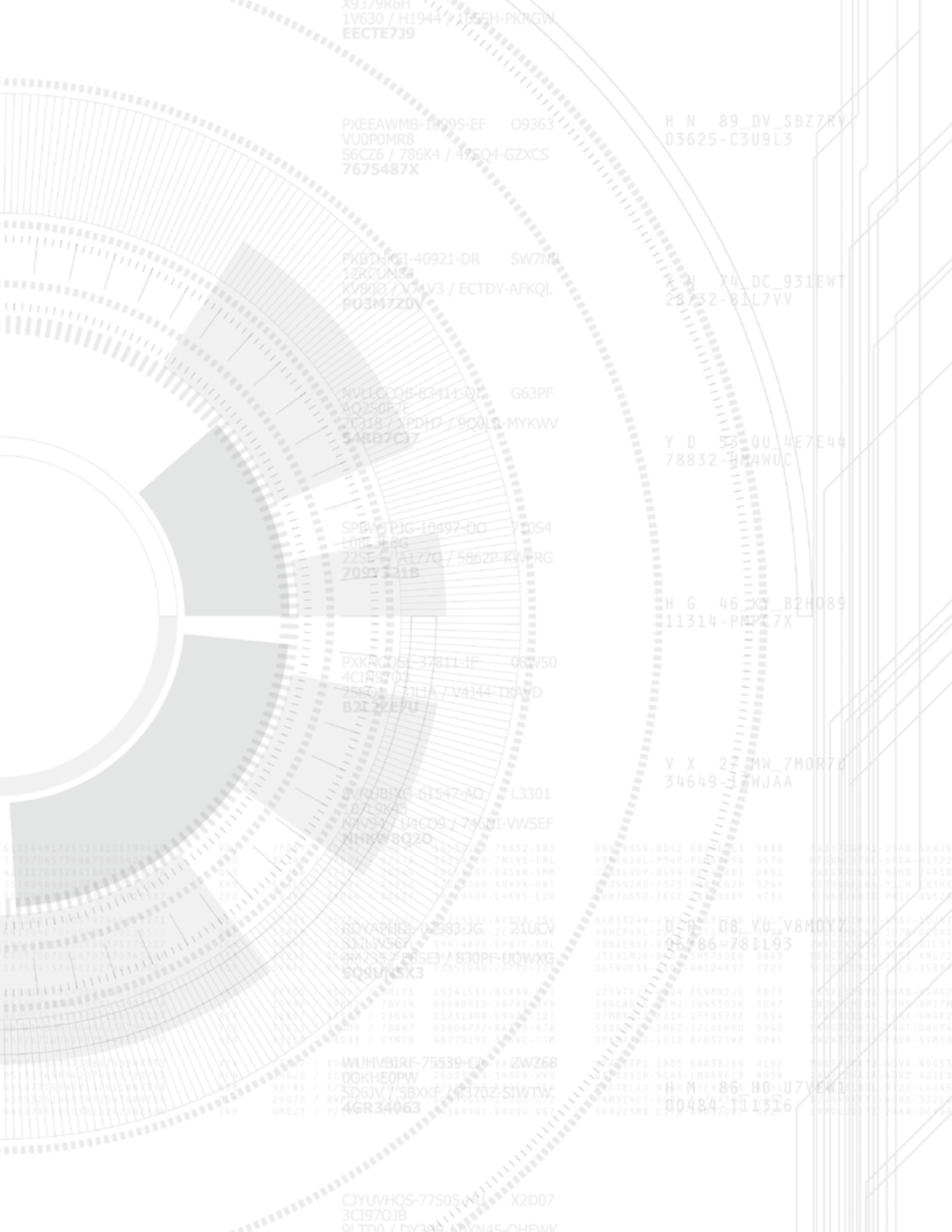

FOREWORD

The studies of physics and detectors for the International Linear Collider are an important parallel element to the effort for the ILC *Technical Design Report*. The studies comprise the physics opportunities, detector requirements, and detector development to achieve the challenging high performance demanded by the physics, as well as integration of detectors into the accelerator. The current phase of this effort began with a call for Letters of Intent (LOIs) in 2007 and will lead to the submission of *Detailed Baseline Design* (DBD) report together with the ILC *Technical Design Report* at the end of 2012. Here we summarise the current status of this process, review what it has accomplished and identify the work that still needs to be completed. This report, titled *International Linear Collider Physics and Detectors: 2011 Status Report,* does just this.

This report begins with a discussion of the outstanding issues in physics that motivate the construction of the ILC. It describes the organisation of the LOI process, the validation of the LOIs by the International Detector Advisory Group, and the results of R&D carried out to support the detector designs. The details of the concept detectors have already been published in the LOIs, which were completed in 2009. This report will, in a complementary way, describe the status of the detector R&D for each individual detector component and the status of the physics simulation infrastructure that has been built for the detector design process. Much of this work is carried out in cooperation between the two detector concept groups. This report describes the five common task groups and two working groups that have organised these cooperative activities.

Many members of the detector concept groups and the common task groups have contributed to this report. Many more people have carried out the actual work that is reviewed. The complete list of members of each detector concept group can be found from the author lists of the published LOIs. The members of the ILC physics and detector organisation are listed at the end of this document.

As we are now nearing the completion of the DBD phase, we are also entering a new stage of our preparation process. The experiments at the Large Hadron Collider at CERN, Switzerland, are accumulating data and are extending our knowledge of the physics of the teraelectronvolt energy scale. The LHC results may confirm the standard model of electroweak symmetry breaking or they may deliver something completely new. In either case, we believe, the ILC will be critical to resolve the questions that the LHC programme will bring forward. In any scenario, we will need very high-quality detectors and excellent technical and simulation capabilities. This report describes the status of our work in pursuit of that goal.

Sakue Yamada, ILC Research Director

EDITOR LIST

James E. Brau
University of Oregon, USA

Juan Fuster
IFIC-Valencia, Spain

Leah Hesla
Fermilab, USA

Monika Illenseer
DESY, Germany

Perrine Royole-Degieux
CNRS/IN2P3, France

Rika Takahashi
KEK, Japan

Barbara Warmbein
DESY, Germany

Sakue Yamada
KEK and University of Tokyo, Japan

Hitoshi Yamamoto
Tohoku University, Japan

Min Zhang
IHEP, China

CONTENTS

01

ILC PHYSICS

The International Linear Collider is designed as the next step in elementary particle physics beyond the Large Hadron Collider at CERN, Switzerland. It will continue the exploration of the distance scale of 10^{-18} metres – 1 one-thousandth of the size of an atomic nucleus – and the energy scale of several hundred gigaelectronvolts, or GeV – a few hundred times the rest energy or mass of the proton. Our current understanding of particle physics points to this distance scale as the key to the origin of the masses of the known elementary particles. It suggests that here, also, we will discover the particles that make up the dark matter of the universe. The ILC will bring new high-precision tools that will help us to solve these mysteries.

1.1 The current state of particle physics

At present, we know of two types of particles that we call elementary. The first are the matter particles. These include the electron and two heavier particles with the same interactions, the muon and the tau. These three particles and the massless, neutral, and elusive neutrinos are collectively called leptons. Matter particles also include the quarks, the basic constituents of strongly interacting particles such as the proton and neutron. In all, there are six types of leptons and six types of quarks. Only the electron and the u (up) and d (down) type quarks are found in atoms. The muon, the tau, and the remaining four quarks – s (strange), c (charm), b (bottom), and t (top) – are produced in high-energy reactions and rapidly decay to the less massive species. We do not understand the need for these particles or the pattern of their masses. The bottom quark has a mass about four times the mass of the proton; the top quark has a mass about 180 times the mass of the proton.

The elementary particles of the second type are the bosons, the quanta carrying the basic forces of nature. We know of three forces that operate at very short distances: the strong interactions, which bind quarks together and are responsible, more indirectly, for the structure of atomic nuclei; the weak interactions, which produce radioactive decay processes; and the electromagnetic interactions. The quantum of electromagnetism is the photon; the quanta carrying the strong and weak interactions are the less familiar gluons and W and Z bosons. These particles are similar, and all obey field equations of the form of Maxwell's equations of electromagnetism. The gluons, like the photon, have zero mass, but the W and Z bosons have masses about 90 times the mass of the proton.

The masses of the W and Z bosons give a hint as to the origin of all of the masses of these elementary particles. The equations of electromagnetism and the weak interactions put the W, Z and photon into a perfectly symmetrical relationship. This symmetry is visible in the experimentally determined values of the couplings of the W, Z and photon to quarks and leptons. If the symmetry were exact in all of nature, all three bosons would be massless. The observed pattern of masses follows if the symmetry is broken by an external entity, a new field in nature not otherwise visible. This field is called the Higgs field.

1.2 The hunt for new particles

The Higgs field has associated Higgs particles. These are new particles, ones that do not fit into the above classification. They couple both to leptons and quarks and to the W and Z bosons. It is not understood what force causes the Higgs field to take its required asymmetrical orientation. Models for this force bring in additional particles and fields of unprecedented types. One class of models, theories of supersymmetry related to the proposed superstring unified theories, requires new matter particles with the couplings of the photon and gluon and new force-carrying particles with the couplings of leptons and quarks. These new particles can serve other purposes than completing the theory of mass. A matter particle with the electromagnetic couplings of the photon would be a perfect candidate for the particle that makes up the mysterious dark matter, a neutral and weakly interacting substance, completely outside our current theory of particle physics, which makes up 80 percent of the matter in the universe.

The LHC at CERN is now engaged in the search for these particles. The technique used is to collide protons at extremely high energies. Pairs of quarks or gluons in the protons can annihilate and reform as particles of a completely new type. The rates predicted for these reactions are of the order of one part in ten billion of the rates for typical inelastic proton-proton collisions. Thus, only the most unusual and characteristic final states can be recognised. The events are very complex since they contain, in addition to the new particles, the leftover remnants of the original protons and the particles produced by quarks and gluons radiated from the annihilating pair. We expect that many of the predicted particles, including the Higgs boson, can be discovered in this environment. But, necessarily, most details of their properties will remain obscure.

The ILC will bring new tools to the study of these particles. The ILC will collide electrons and positrons at energies comparable to those of quark and gluon collisions at the LHC. Because electrons and positrons are elementary and couple through simple, point-like interactions, the rates for processes that create new particles are comparable to the total annihilation rate. And since they interact through forces much weaker than the strong interactions at work at the LHC, the annihilations produce events that are relatively free of background debris. That allows these events to be analysed as a whole, making use of all of their details to constrain the new particle properties. It also means that the experimental conditions will be much more benign, allowing the construction of detectors with unprecedented precision in energy and momentum measurement. Realising such unprecedented measurements requires the design and development of new detector technologies. For example, as compared to the detectors designed for LHC events, the ILC detectors will have only one tenth of the amount of obscuring material in front of the calorimeters that measure photon energies.

1.3 Experiment programme at the ILC

1.3.1 Experiments at the ILC: quarks and leptons

The first goal of the ILC programme will be to measure the simplest reactions of electron-positron annihilation into pairs of quarks and leptons. Currently, the measurements of these processes from CERN's former electron-positron collider, LEP, place the strongest constraints on possible substructure of quarks and leptons and are among the strongest constraints on new forces of nature beyond the weak interactions. Experiments at the ILC, at the energy of 500 GeV and full luminosity, will extend these searches by an order of magnitude in the mass of the particles that mediate the new forces. It is possible that new heavy bosons, partners of the W and Z, might be discovered at LHC as resonances in the production of electron or muon pairs. In that case, the ILC at 500 GeV can deliver the complete profile of the new bosons. The precision measurement of the pair production of leptons, of c-type quarks, and of b-type quarks using polarised electron and positron beams allows all couplings of this particle to be determined independently. *Figure 1.1* illustrates the ability of the ILC to discriminate from among a wide variety of possible models.

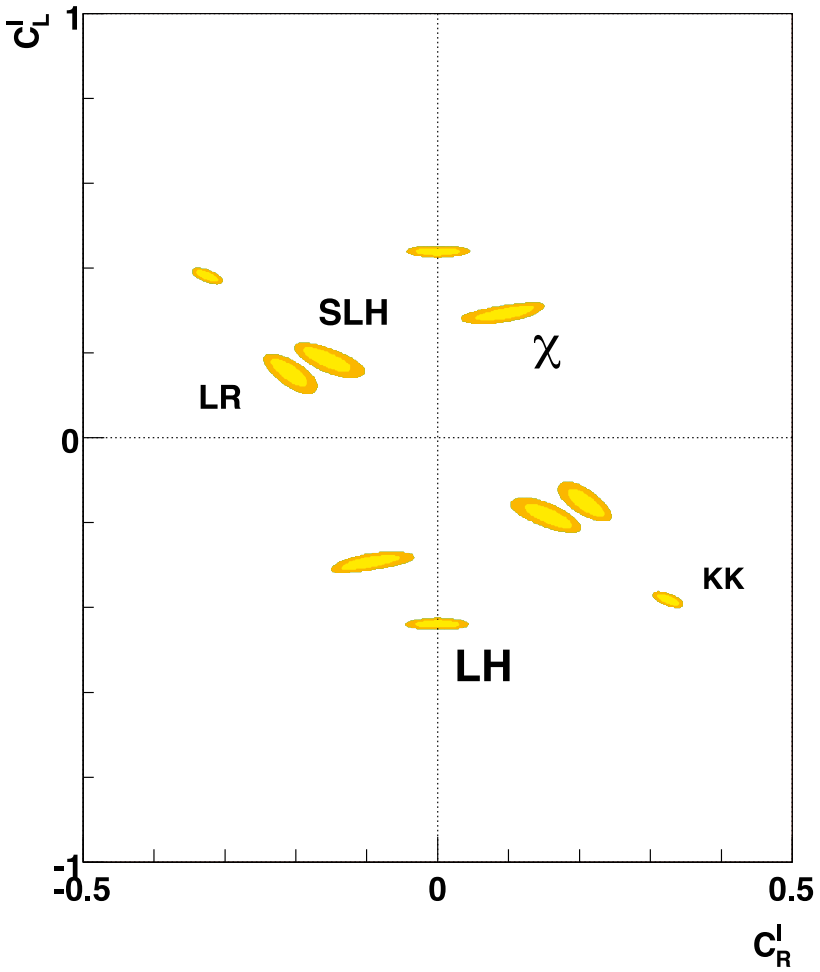

Figure 1.1 The expected ILC measurement of the couplings CL and CR of a Z' boson to left- and right-handed polarised leptons, expressed as an allowed region in the two-dimensional plane of these couplings. The mass of the boson is assumed to be 2 TeV. The various regions represent the expectations for different Z' models that have been discussed in the literature. The ILC experiments will select one of these regions unambiguously. *[1-1]*

1.3.2 Experiments at the ILC: top quark

The heaviest quark, the t or top quark, is the known particle most strongly coupled to the Higgs field and to other possible particles responsible for its symmetry breaking. The ILC will produce hundreds of thousands of top quark pairs. Both the production and decay of the top quark make use of parity-violating interactions sensitive to the particle spin. The use of polarised electron and positron beams will accentuate these effects. In the environment of the ILC, complete events with production and decay of a pair of top quarks can be reconstructed with high precision. The analysis of these events will probe the elementary couplings of this quark to electromagnetic and weak interactions and will, perhaps, reveal this particle's novel couplings or substructure.

1.3.3 Experiments at the ILC: Higgs boson

Although we expect that the LHC experiments will discover the Higgs boson, those experiments will not be able to definitively measure any of the Higgs boson couplings. The simplest model of the Higgs field predicts its couplings to each known particle as a precise value proportional to the mass of that particle. More complex models, for example supersymmetry, predict deviations from this law. At the ILC, large samples of Higgs bosons can be produced in a setting in which the decay of this boson to each possible final state can be recognised in an unbiased way. From these experiments, the presence or absence of a regularity in the set of Higgs boson couplings can be tested at the percent level of accuracy; see *Figure 1.2*. This will provide a definitive test of the simplest model of symmetry breaking in the weak interactions, or crucial clues if the true picture is more complex.

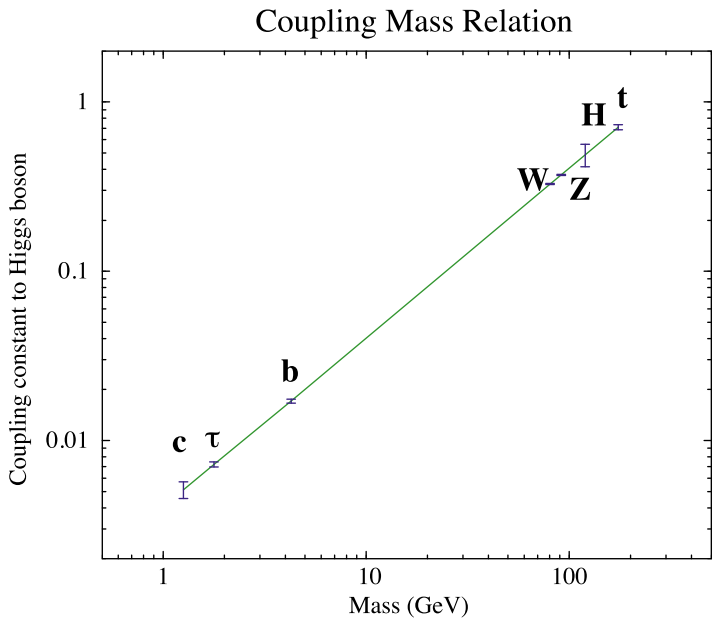

Figure 1.2 ILC expectations for the measurement of the Higgs boson coupling to quarks, leptons, and bosons, in the simplest model. *[1-2]*

1.3.4 Experiments at the ILC: new particles

We may soon know whether the LHC will discover new particles of the type that are predicted in models of weak interaction symmetry breaking and dark matter. In any case, the ILC will be able to make a definitive search for new particles with masses of up to 250 GeV. The ILC will produce these particles as pairs through weak and electromagnetic interactions. In this setting, the magnitude of the production rate, the angular distribution, and the asymmetry with respect to electron beam polarisation will definitively identify each particle's quantum numbers. As with the Higgs particles, the ILC experiments will be able to make unbiased measurements of the decay probabilities to possible final states.

Figure 1.3 shows an expected result from the ILC measurement of the decay of a supersymmetry partner of the W boson. This particle should decay to a quark-antiquark pair plus the supersymmetric partner of the photon, an invisible dark matter particle. The figure shows the distribution of the reconstructed energy of the quark-antiquark system. The detailed shape of this distribution is used to determine the couplings of the new particle. Further constraints on these couplings will be obtained from the angular distributions of the quark and antiquark relative to the electron beam direction, which can be obtained to an accuracy of the order of one degree. As with the top quark, angular asymmetries are enhanced by the use of electron and positron beam polarisation.

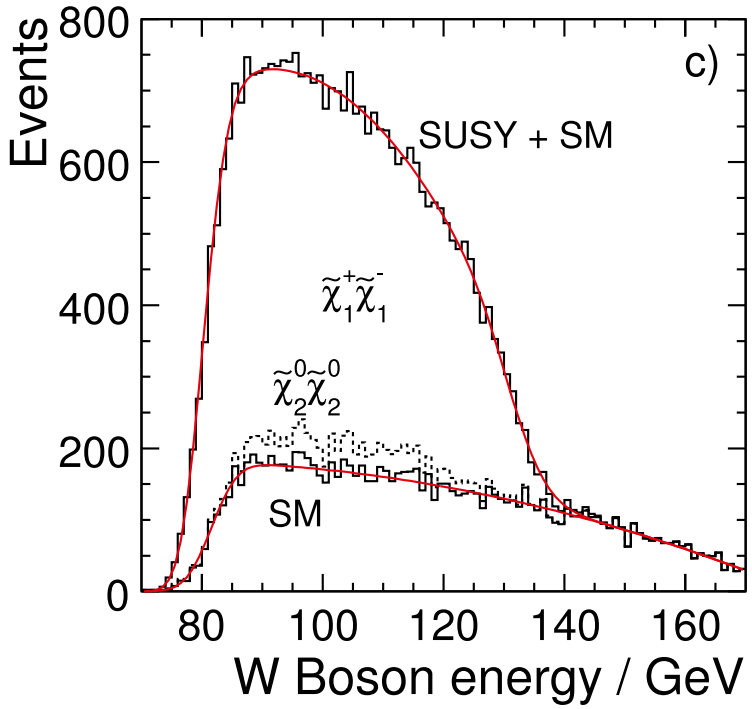

Figure 1.3 Distribution of the energy of the quark-antiquark system produced in the decay of the supersymmetry partner of the W boson, as it would be measured by the ILD detector. *[1-3]*

1.3.5 Experiments at the ILC: dark matter

The complete picture that the ILC will give of new elementary particles will address the question of whether the lightest of these particles makes up the dark matter of the universe. Measurements at the ILC will allow the cosmic density of that particle produced in the early universe and the interactions of that particle with ordinary matter to be predicted from elementary particle data alone. These predictions can then be matched against astrophysical measurements. One specific comparison of an ILC measurement to astrophysics is shown in *Figure 1.4*. This programme could provide a definitive test that we are making dark matter in the laboratory.

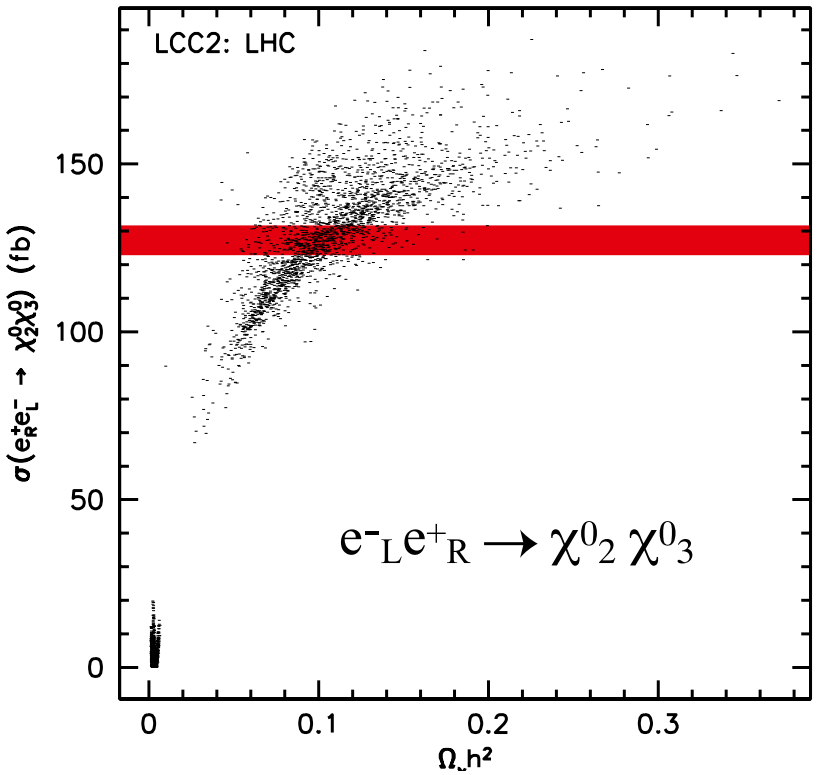

Figure 1.4 Scatter plot of the predictions of models of supersymmetric dark matter consistent with expected LHC data. On the vertical axis is one specific reaction rate that will be measured at the ILC with polarised beams. The horizontal axis is a quantity proportional to the density of dark matter in the universe; the current best value from astrophysics is close to 0.1. The ILC will provide many constraints of this type on the ability of observed new particles to explain dark matter. *[1-4]*

Summary

Elementary particle physicists expect that the CERN LHC will discover new types of elementary particles and will open a new chapter in the physics of the universe. But writing that chapter will require new tools that go qualitatively beyond the capabilities of the LHC. The ILC will provide them.

References

[1-1] Fig. 4a of "Distinguishing between models with extra gauge bosons at the ILC," Stephen Godfrey, Pat Kalyniak, Alexander Tomkins, hep-ph/0511335, presented at the Snowmass 2005 workshop on the ILC.

[1-2] Fig. 2.4 of the GLC report, K. Abe, et al,"GLC project: Linear collider for TeV physics," KEK-REPORT-2003-7, Sep 2003.

[1-3] Fig. 3-3.19(c) of ILD LOI, "The International Large Detector: Letter of Intent," Toshinori Abe (Tokyo U) et al, ILD Concept Group - Linear Collider Collaboration, FERMILAB-LOI-2010-03, FERMILAB-PUB-09-682-E, DESY-2009-87, KEK-REPORT-2009-6. Feb 2010. 189 pp. e-Print: arXiv:1006.3396 *[hep-ex]*

[1-4] Fig. 26(b) of "Determination of dark matter properties at high-energy colliders," Edward A. Baltz (KIPAC, Menlo Park), Marco Battaglia (UC, Berkeley & LBL, Berkeley), Michael E. Peskin, Tommer Wizansky (SLAC). Published in Phys.Rev. D74 (2006) 103521, e-Print: hep-ph/0602187. Expected ILC measurement of the quantity on the vertical axis is superposed on it.

02

DEVELOPMENT AND COORDINATION OF PHYSICS AND DETECTOR STUDIES

The physics and detector studies for the ILC have been organised since 2007 through a process of Expressions of Interest, Letters of Intent, and Detailed Baseline Design (DBD) report. As the plan to develop a technical design for the ILC in 2012 unfolded, the ILC Steering Committee (ILCSC) recognised the importance of defining detailed detector concepts that should be considered in the design of the ILC, particularly in addressing issues of the ILC interaction region. Coordinating with the ILC 2012 plan, the ILCSC initiated a parallel process for technical development of detector design. A Letter of Intent (LOI) process was initiated in 2007 in order to validate detector concepts to be developed by 2012. This LOI process and the framework for conducting it have guided organisational steps towards the detailed detector designs over the past few years. These steps are described briefly in this introduction.

2.1 Call for LOIs

In October 2007, the ILCSC announced a call for letters of intent to produce reference designs for two detectors for the ILC *[2-1]*. The proposed roadmap had been prepared by the World Wide Study Organising Committee (WWS-OC) and approved by the community through the discussion at the Linear Collider Workshop at DESY, Germany in 2007, in which the chairs of the International Committee for Future Accelerators, the ILCSC and the Global Design Effort (GDE) participated.

When the GDE published the ILC *Reference Design Report* in summer 2007, there were four detector concepts described in its detector volume. The call for LOIs was intended to lead the community to form two capable groups that would develop their concepts to a technically advanced stage and produce detailed baseline designs at the same time as the planned completion of the GDE accelerator *Technical Design Report* in 2012[1]. The submitted LOIs were planned to be reviewed by an advisory body called the International Detector Advisory Group (IDAG). In order to conduct the LOI procedure, ILCSC created simultaneously with the call of LOIs the position of research director, who was to set up a management structure and to compose IDAG with the approval of the ILCSC.

A detailed guideline for the preparation of the LOIs was published together with the call. It defined the contents of the LOIs and their lengths. As for the content, it says, “The LOI should contain information on the proposed detector, its overall philosophy, its sub-detectors and alternatives, and how these will work in concert to address the ILC physics questions. The evaluation of the detector performance should be based on physics benchmarks, some of which will be the same for all LOIs based on an agreed-upon list, and some of which may be chosen to emphasise the particular strengths of the proposed detector. It should contain a discussion of integration issues with the machine. It should be developed enough to allow a first preliminary assessment of civil engineering issues like the interaction hall, support halls, etc. It should enable the reader to judge the potential of the detector concept and to identify the state of technological developments for the different components.” Further, “the LOI should include a preliminary cost estimate for the detector. The overall length of the LOI should not exceed 100 pages.”

[1] The call for LOIs was originally planned for engineering designs of two detectors by 2010. The plan was soon modified at the ILCSC meeting in February 2008 due to the financial drawbacks for the activity. The completion of the detailed baseline designs was consequently pushed back to 2012. The due date for LOIs was accordingly extended to the end of March 2009.

The Software Panel of the World Wide Study prepared a list of key benchmarks to be studied for the LOIs. An agreement on the list was reached by end 2007 *[2-2]*.

2.2 The management of detector organisation

The first step for the Research Director was to form the central management, which would include a representative of the detector community of each region. With consultation and agreement of the steering body of each region, the three WWS co-chairs were requested to become the first regional contacts. This choice could be controversial since having representatives of so-called user representatives in the management might cause conflict. At a laboratory that runs an accelerator, such a choice does not happen. However, since the ILC is still in the R&D phase and our effort is to prepare for its realisation, good communication with the detector community would be only helpful. The choice was accepted as a temporary solution over the turn of the year. Jim Brau from North America, Francois Richard[2] from Europe and Hitoshi Yamamoto from Asia joined the management by January 2008.

[2] Juan Fuster took this role in February 2012.

The management started its work by listing possible candidates for IDAG members among the experimental physicists, phenomenology theorists and ILC accelerator experts, considering regional balance. Most candidates had been active in the field of electron-positron collision while some members shifted to other fields in the meantime.

We in the detector management requested Michel Davier to chair the group. With the approval of ILCSC on the possible members and the chair, each candidate was asked to serve. We were pleased that all of these competent candidates accepted and that IDAG could be set up by the end February. The present members are listed in *Table 2.1*. The TILC08 workshop of ILC in Sendai, Japan, in March 2008 was too early for the entire IDAG to meet, but some members were able to attend to collect information on the status of the detector activity and to conduct some preparatory discussions. In particular the chair and the Research Director discussed in some detail the aim of IDAG and how to carry out the LOI process.

Experiment & Detector	Michael Danilov	ITEP
	Michel Davier (Chair)	LAL/Université Paris Sud
	Paul Grannis	Stony Brook University
	Dan Green	FNAL
	Dean Karlen	Victoria
	Sun-Kee Kim	SNU
	Tomio Kobayashi	ICEPP Tokyo
	Weiguo Li	IHEP
	Richard Nickerson	Oxford
	Sandro Palestini	CERN
Phenomenology	Rohini Godbole	IIS
	Christophe Grojean	CEA-Irfu/CERN
	JoAnne Hewett	SLAC
Accelerator	Eckhard Elsen	DESY
	Tom Himel	SLAC
	Nobu Toge	KEK

Table 2.1 International Detector Advisory Group members

2.3 Organisation of detector activity

The management worked in the meantime on the framework to organise the detector activity. The scheme is illustrated in *Figure 2.1.* Much of the detector R&D and physics simulation was carried within the concept groups, which further collaborate with various R&D collaborations for certain components. Each group was expected to design a harmonised detector system along its concept to be outlined in its LOI. Required preparatory work was organised within each group. Nevertheless, it was thought that cooperation among the separate concept groups would be very important during the R&D phase. There were certain tasks like the push-pull studies that could be pursued only with close cooperation among the concept groups and with the accelerator team for the beam delivery system. Also sharing of commonly needed tasks was recommended to optimise the outcomes. In order to facilitate such cooperation and communication among the various concept groups, we planned to create five common task groups (CTG) consisting of members from all the concept groups. Detailed planning of the CTGs was made later together with the representatives of the concept groups.

The Physics and Experiment Board (PEB) was conceived as the decision-making body of the detector and physics community, which would comprise the representatives of the LOI groups, conveners of the CTGs and the management members.

In order to start practical work within this framework, the next step was to identify the concept groups that would submit LOIs in 2009. This was done by a call for Expression of Interest (EOI) to submit LOIs. The announcement was made in February 2008 with a short time window for the due date, the end of March 2008. Three groups responded with the required information, the names of two representatives and the participating institutions. They were ILD (International Large Detector), SiD (Silicon Detector) and Fourth. The ILD was a fusion of two large concept groups, GLD and LDC of the RDR plan, which had similar ideas and decided to make joint efforts for LOI. The representatives of the three groups joined in further discussions for details of the framework. For instance, the five common task groups that were agreed upon were the machine-detector interface (MDI) group, engineering tools group, detector R&D group, software group and physics group. The concept groups were requested to send their members for these common task groups so that they could be formed by end of May 2008. The MDI group was supposed to make a link to the beam delivery system group of the GDE and had to be set up as soon as possible. As for the physics common task group, we wished to invite theory members, too.

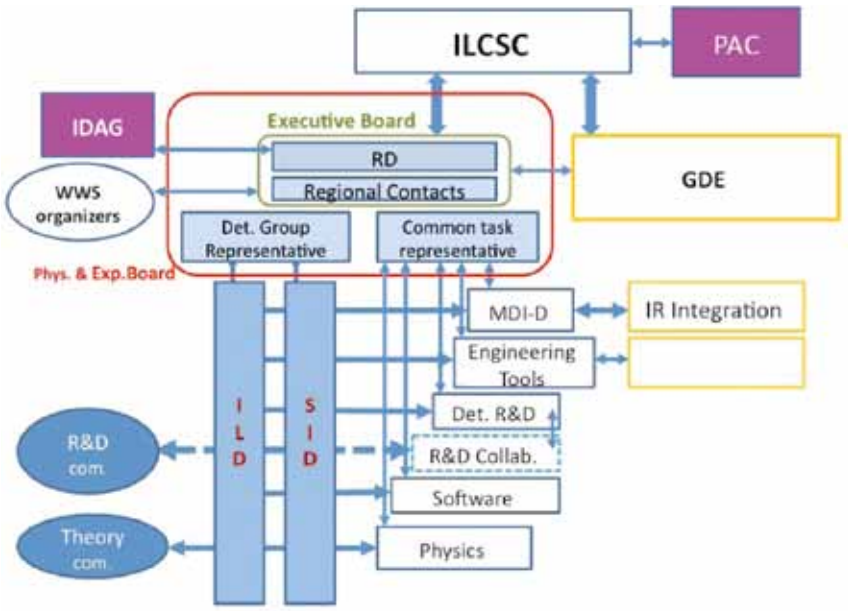

Figure 2.1 The organisation chart of the detector activity. Image: Sakue Yamada

During the European Committee for Future Accelerators (ECFA) workshop in Warsaw, Poland, in June 2008, the management met face to face for the first time with the concept representatives and with many of the common task members to clarify the detailed plan of the LOI process. Also the management could be informed of the situation of each concept group's possible issues in preparing LOIs. After the workshop, we nominated the conveners and deputies of all the common task groups, and the PEB could meet with full membership. The activity of each common task group is described later in this report.

Through the discussions with the detector groups, we became aware of the important roles played by the independent ("horizontal") R&D collaborations. Close cooperation with these groups was crucial to achieve the R&D goals of each concept group. So the detector management decided to invite representatives of major horizontal collaboration groups for calorimetry and tracking to join the R&D common task group for better communication.

2.4 IDAG beginnings

The first IDAG meeting was also held during the ECFA workshop in June 2008. Through face to face discussions, the detector management and IDAG discussed the role of IDAG for the validation process. A common understanding was reached about what features were required for validation of an LOI and its group. Specifically, IDAG would examine whether (1) the overall concept had an expected goal and performance suited to the physics programme of the ILC and (2) the proposing group had the scientific and technical ability to reach its goal.

Since this meeting, IDAG has met and interviewed the concept groups at each linear collider workshop. The second meeting was held in Chicago, US, during the American Linear Collider Physics Group (ALCPG) workshop in November 2008, where IDAG began to organise its validation of LOIs. The members divided tasks in two ways: each member would review the LOI of one of the groups, and each would review one particular topic for all of the LOIs, either key detector components or physics performance. This matrix of horizontal and vertical tasks ensured a thorough review engaging the IDAG membership in careful consideration of the concepts. At the Chicago meeting IDAG also issued a set of additional requirements, which were more concrete than those given in the LOI guideline, and they were to be answered in the submitted LOIs.

IDAG continued its preparation through telephone meetings until the LOI due date in order to update itself on the current status of the major detector components.

2.5 The LOIs

The three Letters of Intent were submitted as expected from the ILD, SiD and Fourth groups by the due date. As the allowed length of the LOIs was limited and could not include all detailed information, all groups submitted additional material and more information in separate documents to cover the details of their preparatory studies. IDAG began their examination for validation immediately and sent specific questions to each of group regarding its LOI contents.

During the TILC09 workshop in Tsukuba, Japan in April 2009 each concept group made two presentations on its LOI, one for the detector concept, design philosophy or optimisation principle, components and structure, and the other for its expected performance on the benchmark reactions. These presentations were attended by many people of the community and

IDAG members. Each concept group was interviewed separately by IDAG, where they answered IDAG's questions on the LOIs. Based on this interview IDAG issued further questions to the groups, which were to be answered at a special IDAG meeting in June 2009, held in Orsay, France; the final interviews with the concept groups led to the start of the final IDAG discussions and recommendations. IDAG began its written summary of their validation conclusions and recommendations.

It should be stressed that from the submission of the EOIs in March 2008 until the last interview with IDAG in June 2009, the members of the three concept groups devoted very large efforts in the preparation of the LOIs and presenting the concepts to IDAG, along with written answers to formal IDAG questions. IDAG also made very concentrated effort to examine carefully the huge amount of material in a short period.

2.6 IDAG recommendation and validation

IDAG sent the Research Director a recommendation for validation in August 2009. The conclusion that ILD and SiD be validated was presented by the Research Director during the ILCSC meeting a few days later and was approved. During the ALCPG workshop in Albuquerque, US, in September 2009, the IDAG examination process and the validation were reported by the chair *[2-3]*.

The validation made a clear milestone for the next step. In Albuquerque, there was a preliminary meeting between the management and available IDAG members, including the chair, about how to monitor the progress of the validated groups towards the detailed baseline design. In order to check the progress in detail we agreed that IDAG would examine the activity of each common task group, too. The idea was that common effort of the two groups would become more important and the expertise of IDAG would be helpful to strengthen it.

Following validation the organisation of the detector activity was modified: the PEB membership was reorganised to include members of the validated groups and the common task members. The CTGs were also reorganised with increased membership from ILD and SiD.

2.7 Planning for the detailed baseline designs

For the validated groups, the next step was to prepare a detailed plan to reach the final goal. In order to guide the planning, we agreed in the PEB meeting to prepare a list of the expectations for the DBD. The nine items on the list included subjects such as

- completion of R&D for critical detector components for their feasibility proof,
- defining a detailed baseline design of the detector system,
- setting up a realistic model of the detector for physics simulation,
- completion of studies of a push-pull scheme and integration into the interaction region,
- making physics simulations for a new set of benchmark reactions including some at 1 TeV.

New physics benchmark reactions were investigated by the physics CTG, which would best illustrate the ability of ILC for the expected new physics. The CTG proposed a list by the end of 2009, which also included a few reactions at 1 TeV. The high-energy case was included in view of the optional upgrade of ILC[3].

Each group submitted a time schedule by October with a caveat that it was made under the assumption that necessary resources would become available in due course. While certain anticipation for resources was included in the submitted LOIs, it was recognised that resources were not secured for the entire period or for all the tasks, and efforts had to be made by participating institutions. The first detailed planning assumed that such efforts would be successful.

The tentative planning towards the completion of the DBD and the expected role of IDAG were reported to ILCSC in February 2010 at Brookhaven National Laboratory, US. ILCSC extended the mandate of IDAG until the end of the ILC's technical design phase to monitor the progress of the detector groups. ILCSC also recognised the limited resources of the detector groups, in particular, the need of engineering support.

The first monitoring of the progress of the validated groups by IDAG was made during LCWS10 in Beijing, China in March 2010. By this time, both groups had tried to refine the first work plan in view of the updated scope for resources. The detector groups expressed uneasiness about the sign of declining resources all over the world and the lack of engineering support required for the integration studies. We revisited the planning in view of the projected resources and decided that all nine items to be referenced in planning would be retained while the level of accomplishment for each item would be adjusted according to the available resources. However, the minimum requirement should be satisfied. The difficulty and the corresponding strategy were understood by IDAG.

[3] The list was reconsidered later by a subgroup including representatives of the two groups and software common task groups for priority and work sharing. An updated list, which classifies the new benchmarks, was completed after careful study in January 2011.

2.8 Other working groups

In addition to the original five standing common task groups, we subsequently created some new working groups to solve specific tasks as they appeared and needed to be handled intensively in a relatively short period. These were organised in cooperation with the two detector groups and relevant common task groups as well. A good example is the SB2009 working group, which was organised soon after the ALCPG workshop in Albuquerque in order to evaluate the effects on experiments and the resulting physics consequences of the proposed SB2009 accelerator parameters. This working group communicated with the accelerator team systematically and organised necessary works among the participating bodies. The details of the activity are described later. There was a working group to study and arrange the work plan for the new benchmarks. It was led by the physics common task group and worked with the representatives of the two groups and the software common task group. It completed its work with a report on the list of priority- and work-sharing for each possible physics channel. Currently we have a new short-term working group to study a common costing method between the two groups.

The CLIC (Compact Linear Collider study)-ILC joint working group was initiated in early 2010 following discussions during the ILCSC meeting in Hamburg, Germany. It surveys ongoing cooperation and looks for further synergies between the two linear collider detectors. Before this working group was formed, there had already been much grassroots cooperation since 2008. This has become more intensive since CLIC deployed the two ILC concepts for its detectors. Now we observe an overlap of the members who prepare both CLIC *Conceptual Design Report* and the ILC DBD. The current situation is reported later in a separate chapter.

2.9 A way to go

Having passed through the midway point to publishing the DBD, the detector groups are continuing their efforts and making progress towards the detailed baseline design. We intend to be ready by the end of 2012 for the next step with the completed DBD, hoping that some new signal will be obtained at LHC by that time. We are also keen on how the completed DBD will become useful for the realisation of the project and for more advanced design studies.

The R&D for detector components, some of which are conducted in cooperation with R&D collaborations, are advancing, and crucial integration work like the push-pull study is approaching the pursued milestone. Also, more realistic simulation studies are being prepared. Many efforts are organised, led or carried out by the common task groups. IDAG monitors all these advancements regularly and gives us helpful advice. In the following sections, more details of these ongoing activities are described.

References

[2-1] Shin-ichi Kurokawa, http://ilcdoc.linearcollider.org/record/15684/files/CallForLOI.pdf, 4 October 2007

[2-2] http://ilcdoc.linearcollider.org/record/14681/files/Benchmark_Reactions_for_the_ILC_LOI.pdf

[2-3] http://ilcdoc.linearcollider.org/record/23970/files/IDAG_report_090816.pdf

03

DETECTOR R&D AND INTEGRATION

3.1 Detector concepts at the ILC

The International Linear Collider will be built to investigate properties of nature at very high energy with very high precision. This puts the highest demands not only on the accelerator, but also on the detectors. Currently the interaction region at the collider is designed to house two detectors, operated in a push-pull scheme to share the available luminosity. In an internationally coordinated effort two concept groups, which have formed over the last few years, propose detectors for experiments at this machine. Together with focused R&D groups they advance the state-of-the-art in detector technology to make them usable for these sophisticated experiments.

Both the ILD (International Large Detector) and the SiD (Silicon Detector) concepts are based on the paradigm of particle flow, an algorithm by which the reconstruction of both charged and neutral particles is accomplished by an optimised combination of tracking and calorimetry. Since, on average, a large fraction (roughly 60%) of the energy of a jet is in the form of charged hadrons, one can achieve a better measure of the energy deposited in the calorimeter by these particles using their tracking information. This requires that individual tracks be able to be followed from the tracking system into the calorimeter and their clusters of energy deposition be associated with the followed track. Once the association between charged tracks and their energy clusters has been made, those clusters can be removed from further consideration. It then remains to measure the energies of the other clusters deriving from neutral hadrons and photons, with allowance made for (minimum ionising) muons in the calorimeter. The photons have their energy measured in the first electromagnetic section of the calorimeter system and the neutral hadrons in the second hadronic section. The detailed use of individual tracks and energy clusters in the calorimeter demands a small cell size or high granularity. The net result is then improved charged particle and jet energy resolutions.

3.1.1 The SiD detector concept at the ILC

The SiD detector *(Figure 3.1)* is a compact detector designed to make precision measurements of physics variables and to be sensitive to a wide range of possible new phenomena. The design represents an optimised balance between cost and physics performance. The choice of silicon for the entire tracking system ensures that SiD is robust to beam backgrounds or beam loss. It provides superior charged particle momentum measurement and eliminates hits from tracks not in time with the main beam collisions. The SiD calorimetry is optimised for excellent jet energy measurement using the particle flow technique. The complete tracking and calorimeter systems are contained within a superconducting solenoid, which has a 5-tesla (T) field magnitude appropriate to the overall compact design. The coil, in turn, is located within a layered iron structure that returns the magnetic flux and is instrumented to allow the identification of muons. All aspects of the SiD detector are the result of intensive and leading edge research conducted to raise its performance to unprecedented levels. Members of SiD have been developing the detector design for several years, and will continue to work towards a baseline definition of the detector in 2012.

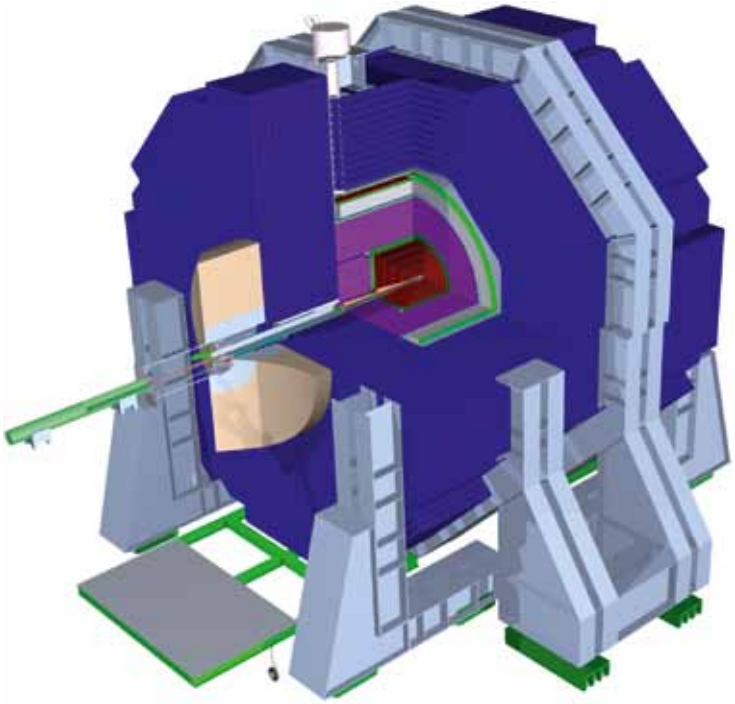

Figure 3.1 Three-dimensional view of the SiD detector.
Image: SiD

3.1.2 The ILD detector concept at the ILC

ILD detector *(Figure 3.2)* has been optimised for excellent jet energy resolution over a wide solid angle and for high-precision reconstruction of exclusive final states. A major goal in the design has been the event reconstruction within the particle flow paradigm. The detector is relatively large to improve the separation between neutral particles, has a sizeable magnetic field to separate charged from neutral particles and to sweep away low-momentum backgrounds and is optimised for highly efficient, precise particle reconstruction, in particular very robust, redundant pattern recognition of particles in the tracker and in the calorimeter.

The calorimeter plays a central role in the reconstruction of the complete event properties. A system of unprecedented granularity is proposed for ILD, both for the electromagnetic and the hadronic sections. The complete calorimeter is located inside the magnet. The flux from the coil is returned through an iron yoke, which is instrumented to serve as a muon filter in addition. It is complemented by a system of small, precise and radiation hard calorimeters in the very forward direction, used to complete the solid angle coverage, and to measure precisely the luminosity of the collider.

The tracker inside the calorimeter is a combination of a powerful large-volume time projection chamber (TPC) and an extensive silicon tracking system. The TPC provides up to 200 space points per particle, allowing efficient and highly redundant pattern recognition. It is combined with silicon tracking stations, both inside and outside of the TPC and covering the end plate, to provide addition high precision points. Located close to the beam pipe is a high-precision vertex detector.

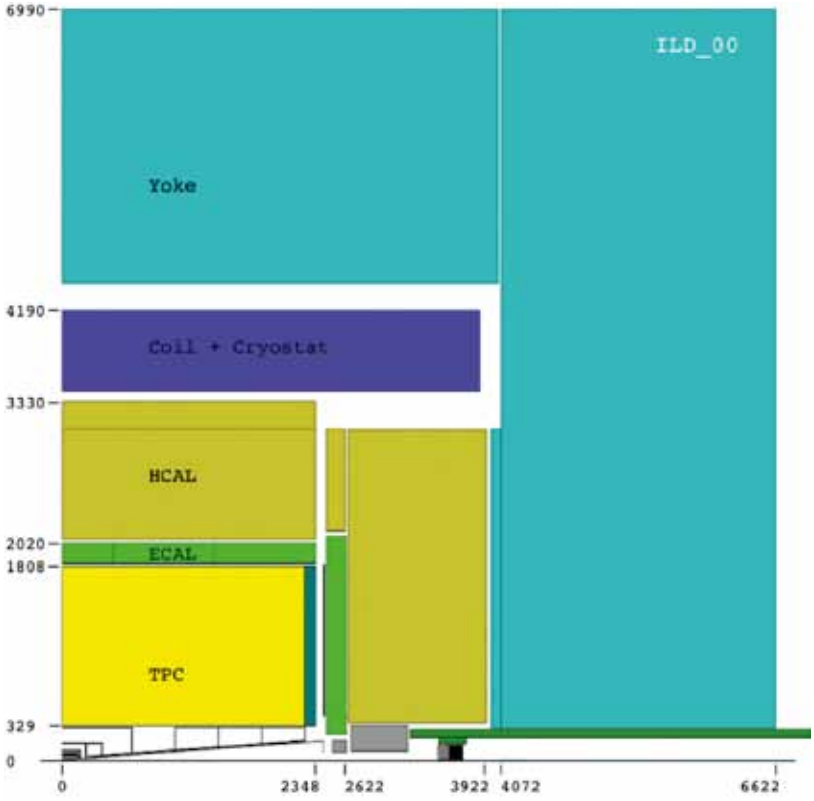

Figure 3.2 Quadrant view of the ILD detector model. The interaction point is in the lower left corner. Image: ILD

The ILD study group formed in 2007. It is a loose organisation with some 700 people from all three regions who signed the latest document, the Letter of Intent for ILD. The goal of the group is to prepare a coherent and integrated design of a detector for the ILC that meets the physics requirements in a way that is well balanced between cost and performance. The group closely cooperates with a number of detector R&D groups that develop technologies and sub-detector concepts for a detector at the ILC.

3.2 The vertex detector

To unravel the underlying physics mechanisms of new observed processes, the identification of heavy flavours will play a critical role. One of the main tools for heavy flavour identification is the vertex detector. The physics goals dictate an unprecedented spatial three-dimensional point resolution and a very low material budget. The running conditions at the ILC impose the readout speed and radiation tolerance. These requirements are normally in contradiction. High granularity and fast readout compete with each other and tend to increase the power dissipation. Increased power dissipation in turn leads to an increased material budget. The challenges on the vertex detector are considerable and significant R&D is being carried out on both the development of the sensors and the mechanical support.

The difficulty and novelty of the sensors drive the investigation of many different sensor designs worldwide and a wide array of sensor technologies is being considered. One architecture, which has been successfully employed before at an electron-positron collider, is based on a pixel-based charged-coupled device (CCD) technology. The new technologies are based on buried-channel CCDs with the charge collected from the thin epitaxial silicon layer. Typically only part of this epitaxial layer is depleted, and electrons created in this layer diffuse and are eventually collected in potential wells – the buried channel. The electrons generated during the passage of a charged track can spread over several pixels by diffusion and can serve to improve the position resolution. As the epitaxial layer is relatively thin, CCD-based pixel detectors have yielded the highest-performance vertex detector yet constructed. The new technologies are based on very small pixels, down to 5 × 5 micrometres square (μm^2) in size.

The depleted field effect transistor (DEPFET) detector is another major branch of sensor R&D. It combines the sensor and readout amplifier into the pixel FET structure such that the signal charge is collected on the internal gates of the transistors. Readout is performed by cyclically enabling transistor rows by a combination of steering and readout application-specific integrated circuits (ASICs) mounted at the ends and along the edges of the sensors. DEPFETs have the potential to be one of the technologies with the lowest power consumption. This technology, the development of which originated within the ILC community, is currently being developed for the vertex detector for the BELLE-II detector at KEK in Japan.

Another technology is the monolithic active pixel sensor (MAPS) architecture, which integrates, on the same substrate, the detector element with the processing electronics. This ability could prove very powerful for the demanding performance of vertex detectors. These devices can now be fabricated using standard CMOS processes available through many commercial microelectronics companies. The ability of the monolithic CMOS sensors to provide charged particle tracking has been demonstrated on a series of prototypes that have been successfully employed as tracking stations for the test beams at CERN in Switzerland and DESY in Germany.

There are two technologies for integrated detector and readout where the different functionalities are implemented in separate silicon tiers. The silicon-on-insulator (SOI) technology separates the detector element from the electronics tier through a thin buried oxide layer. Prototype devices

have been fabricated for imaging applications. A second technology is the 3-D vertical integrated silicon technology. This technology utilises vertical integration of several layers of electronics, where each layer can be as thin as 7 microns. The layers are electrically connected using micron-sized vertical metal connections called vias. The detecting element can be one of the layers or can be a separate layer optimised for the specific application, interconnected using the same bonding techniques.

An integral part of the development of a high-performance vertex detector is R&D in the support materials. Different groups are studying an array of low-mass materials such as various reticulated foams and silicon-carbide materials. An alternative approach that is being pursued very actively is the embedding of thinned, active sensors in ultra low-mass media. This line of R&D explores thinning active silicon devices to such a thickness that the silicon becomes flexible. The devices can then be embedded in, for example, Kapton structures, providing extreme versatility in designing and constructing a vertex detector.

Closely related to the material budget is the issue of power delivery. Higher power consumption in general increases the material budget because of the higher cooling requirements. The vertex detector designs assume that the power can be pulsed during bunch trains. Careful studies need to be carried out to evaluate the sensitive trade-off between ease of cooling and functionality, which requires more power and material budget.

The vertex detector for SiD uses a barrel-disk layout. The barrel section consists of five silicon pixel layers with a pixel size of 20 x 20 μm^2. The forward and backward regions each have four silicon pixel disks. In addition, there are three silicon pixel disks at a larger distance from the interaction point to provide uniform coverage for the transition region between the vertex detector and the outer tracker. This configuration provides for excellent hermeticity with uniform coverage and guarantees good pattern recognition capability for charged tracking and excellent impact parameter resolution over the whole solid angle. The layout of the vertex detector provides for stand-alone tracking capability, which in turn allows for a very compact tracking volume enabling an economic choice for a high-granularity calorimeter.

To provide for a very robust track-finding performance, the SiD detector has as its baseline choice for the vertex detector a sensor technology that provides putting a time stamp on each hit with sufficient precision to assign each hit to a particular bunch crossing. This significantly reduces the effective backgrounds. Two technologies are being researched. The first is a CMOS-based monolithic pixel sensor called chronopixel. The main goal for the design is a pixel size of about 10 x 10 μm^2 with 99% charged-particle registration efficiency. The second, more challenging technology, is the 3-D vertical integrated silicon technology.

The vertex detector for ILD is not required to have the time resolution to separate different beam bunches (approximately 700 nanoseconds apart) thanks to the very powerful track reconstruction capability of other tracking detectors, such as strip inner tracking detectors and TPC, surrounding the vertex detector. Therefore, it has a wider variety of options for the sensor

technology than the SiD detector concept. The technologies presently considered promising and the R&D under way are CMOS sensors, DEPFETs, fine-pixel CCDs (FPCCD), and in-situ-storage image sensors (ISIS). Recently, CMOS sensors exploiting vertical integration technology have also been developed.

There are two ideas of the sensor configuration of the ILD vertex detector as shown in *Figure 3.3*: the five-single-layer option and the three-double-layer (for a total of six layers) option. In both cases, pixel sensor layers surround the beam pipe coaxially and no forward disk, as is seen in SiD, exists. The angular coverage is $|\cos\theta| < 0.97$ for the innermost layer and $|\cos\theta| < 0.9$ for the outermost layer. R&D efforts for realising light material detectors with these sensor configurations as well as R&D for various sensor technologies are ongoing.

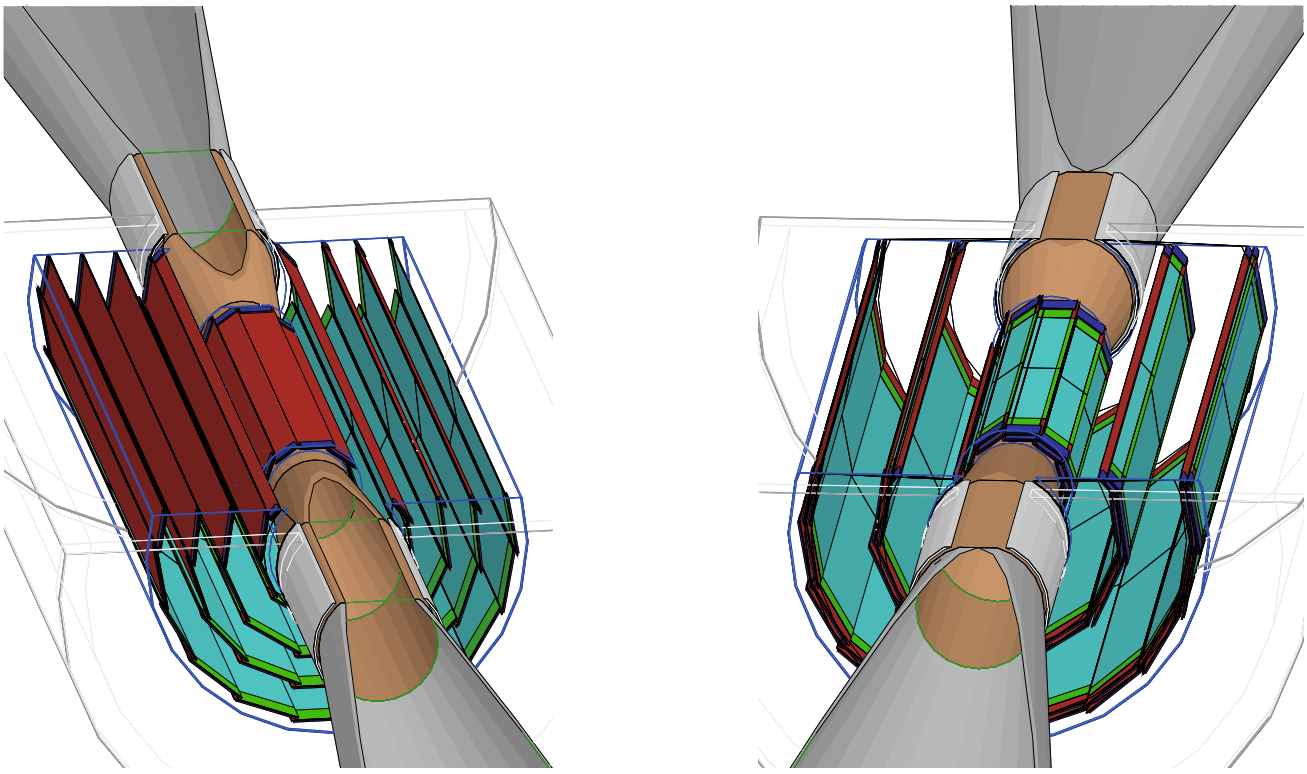

Figure 3.3 Vertex detector geometries for ILD. Left: five-single-layer option. Right: three-double-layer option. Image: ILD

3.3 Tracking for the linear collider detectors

The tracking system is a central part of the detector concepts at the ILC. The particle flow algorithm requires excellent tracking with superb efficiency and two-particle separation. The requirements from precision measurements, in particular in the Higgs sector, place high demands on the momentum resolution. The main performance goals of the tracker imposed by the physics are summarised in *Table 3.1*. The two ILC detector concepts, ILD and SiD, follow different philosophies in tracking. We shall briefly describe the SiD and ILD tracking systems, summarise their simulated performance and, in each case, give an overview of the R&D status.

Momentum resolution (~4 T)	$\delta(1/pt) \sim 2 - 5 \times 10^{-5}$/GeV/c all tracking detectors
Solid angle coverage	Up to $\cos\theta \sim 0.98$
Material budget	~0.10 – 0.15 X_0 to the ECAl in r ~0.20 – 0.25 X_0 in z
Performance	~99% all tracking
Background robustness	Full efficiency with 1% occupancy
Background safety factor	Trackers will be prepared for 10-times-worse backgrounds at the linear collider start-up

Table 3.1 An overview of goals for the performance of linear collider tracking.

3.3.1 SiD tracking

The design of the tracking system of the SiD detector is driven by the combined performance of the pixel detector at small radius, the tracker at large radius and the electromagnetic calorimeter for the identification of minimum ionising track stubs. With the choice of a 5-T solenoidal magnetic field, in part chosen to control the electron-positron pair background, the design allows for a compact tracker design. The technology of choice is silicon strip sensors arrayed in five nested cylinders in the central region and four disks following a conical surface with an angle of 5 degrees with respect to the normal to the beamline in each of the end regions for precision tracking and momentum measurement. The geometry of the end caps minimises the material budget to enhance forward tracking. The detectors are single-sided silicon sensors, approximately 10×10 cm^2 with a strip pitch of 50 µm. The end caps utilise two sensors bonded back-to-back for small angle stereo measurements. With an outer cylinder radius of 1.25 metres and a 5-T field, the charged track momentum resolution will be better than $\sigma(1/p_T) = 5 \times 10^{-5}$ (GeV /c)$^{-1}$ for high momentum tracks. *Figure 3.4* shows an isometric view of the SiD tracking system and the material budget as a function of the polar angle.

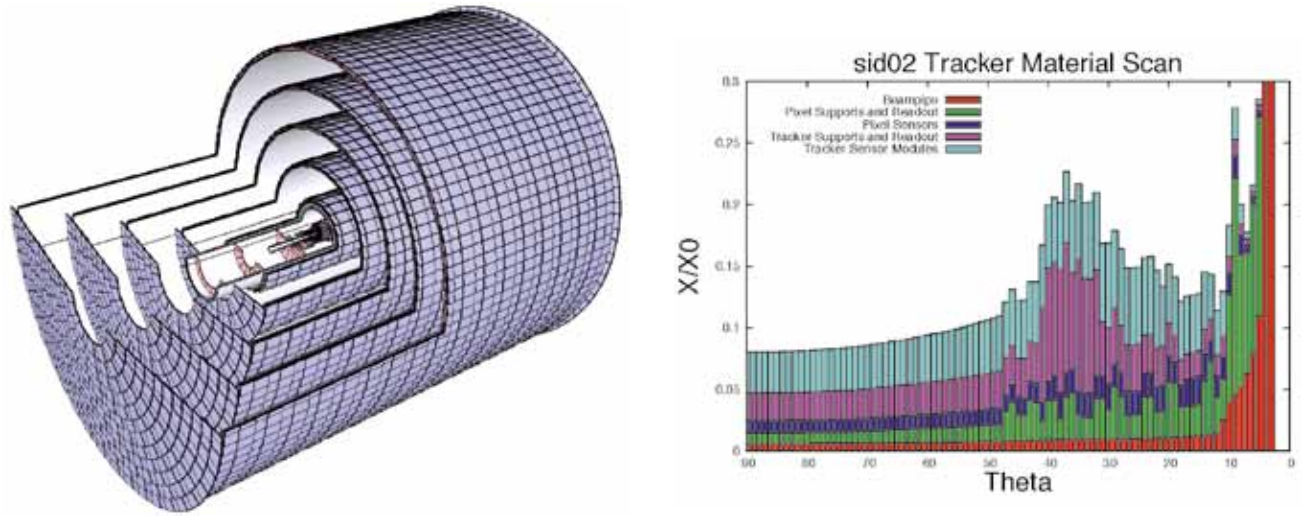

Figure 3.4 Isometric view of the SiD tracking system (left) and total material budget of the tracking system as function of the polar angle (right). The different detector components are indicated. Images: SiD

Status of R&D for SiD tracking

The design of a tracking system at the ILC must minimise the material in front of the calorimeter that might compromise particle-flow jet reconstruction. Furthermore, establishing and maintaining the alignment for the tracker is critical. Even with the largest feasible magnetic field, the tracking volume is quite large, demanding optimised tracker components that facilitate mass production. Finally, the tracker must be robust against beam-related accidents and aging and all these requirements must be maintained within a push-pull scenario.

The silicon modules are supported on a sandwich of pre-impregnated carbon fibre composite around a Rohacell core. The support structures are barrels in the central regions and cones in the forward region. Each support cone is supported off a barrel. Finite element analyses show that these structures meet the static rigidity requirements. It is expected that openings will be cut in the support structures to reduce material once module mounting locations are known. These openings not only reduce the number of radiation lengths, but also reduce the weight to be supported. Openings may also be needed for an optical alignment system. Prototype structures will be built to confirm that the support structures will meet the requirements. Also, dynamic tests will be carried out in a magnetic field with pulsed power.

The tracker employs a modular, hybrid-less design for the silicon readout modules to meet the stringent material budget requirements. This unique design relies on the gold stud bump-bonding of a 1024-channel readout chip directly to the silicon sensor, the signals of which are routed to the readout chip using a double metal layer. Prototype sensors and readout chips with a reduced channel count have been characterised. The readout chips meet the specifications. Initial prototype readout modules have revealed some areas for further study in the bonding of the readout chip and cable to the sensor. Work on the design of a lightweight module frame is in progress.

The bunch structure at the ILC allows for power-pulsing, that is, the readout is current-starved between bunch trains. This makes active cooling unnecessary and allows the tracker to be air-cooled. Ongoing studies demonstrate that the power budget can be met and that the mechanical stability can be maintained with pulsed power in a high magnetic field environment. With judicious routing of power leads, Lorentz forces can be largely cancelled. Such designs, however, need to be simulated and tested to ensure that all design specifications within a 5-T magnetic field with power pulsing can be met. To date studies of signal communication have not been carried out. Such studies are foreseen once full prototype modules and ladders are available.

The unprecedented track momentum resolution demands minimising systematic uncertainties in sub-detector relative alignments. The fact that the two ILC detectors will swap places on the beamline puts a premium on alignment stability and in situ alignment monitoring that does not depend on tracks. Development work is expected to occur to demonstrate that the goals for structural stability will be achieved in a tracker system meeting the material budget. The SiD tracker is considering two alignment methods, one based on frequency-scanning interferometry (FSI) and one based on infrared-transparent silicon sensors (ITSS).

The FSI system incorporates multiple interferometers fed by optical fibres from the same laser sources, where the laser frequency is scanned and fringes counted, to obtain a set of absolute lengths. With a test apparatus precisions better than 100 nanometres (nm) have been attained using a single tunable laser when environmental conditions are carefully controlled. Precisions under uncontrolled conditions (e.g., air currents, temperature fluctuations) were, however, an order of magnitude worse with the single-laser measurements. Hence a dual-laser FSI system is foreseen for the tracker, which employs optical choppers to alternate the beams introduced to the interferometer by the optical fibres. By using lasers that scan over the same wavelength range but in opposite directions during the same short time interval, major systematic uncertainties can be eliminated. It will be important to monitor tracker distortions during the push-pull operations, not only for later track reconstruction, but also to ensure that no damage-inducing stresses are inadvertently applied to the tracker components.

The second method exploits the fact that silicon sensors have a weak absorption of infrared (IR) light. Consecutive layers of silicon sensors are traversed by IR laser beams, which play the role of infinite momentum tracks. Then the same sophisticated alignment algorithms as employed for track alignment with real particles can be applied to achieve relative alignment between modules to better than a few microns. This method employs the tracking sensors themselves, with only a minor modification to make them highly transparent to infrared light. Since IR light produces a measurable signal in the silicon bulk, there is no need for any extra readout electronics. The development of a prototype system that demonstrates the ability to achieve and maintain the required alignment tolerances will be a major focus of future R&D.

3.3.2 ILD tracking

The ILD concept has chosen a combination of continuous tracking and discrete tracking, the former being a TPC central tracker and the latter being layers of silicon detectors. This combination has been chosen to provide a robust system with superb pattern recognition ability due to the large and redundant number of points provided and the complementary strength of silicon and gaseous tracking.

The interaction point is surrounded by a multi-layer pixel-vertex detector (VTX) followed by a system of strip and pixel detectors. In the barrel, two layers of silicon strip inner tracking detectors (SIT) are arranged to bridge the gap between the VTX and the TPC. In the forward region, a system of silicon pixel and silicon strip forward tracking disks (FTD) provides low angle tracking coverage.

A large volume TPC with up to 224 points per track provides continuous tracking for a large volume. The TPC is optimised for excellent three-dimensional point resolution and minimum material in the field cage and in the end plate. It also provides particle identification capabilities based on the energy loss of particles per unit of distance (dE/dx).

A system of Si-strip detectors provides additional high-precision space points, which improve the tracking measurements and provide additional redundancy in the regions between the main tracking volume and the calorimeters. It consists of the silicon internal tracker (SIT) between the vertex detector and TPC, the end cap tracking detector (ETD) behind the end plate of the TPC, and the silicon external tracker (SET) between the TPC and the electromagnetic calorimeter (ECAL) The performance of the ILD tracking system is illustrated in *Figure 3.5*.

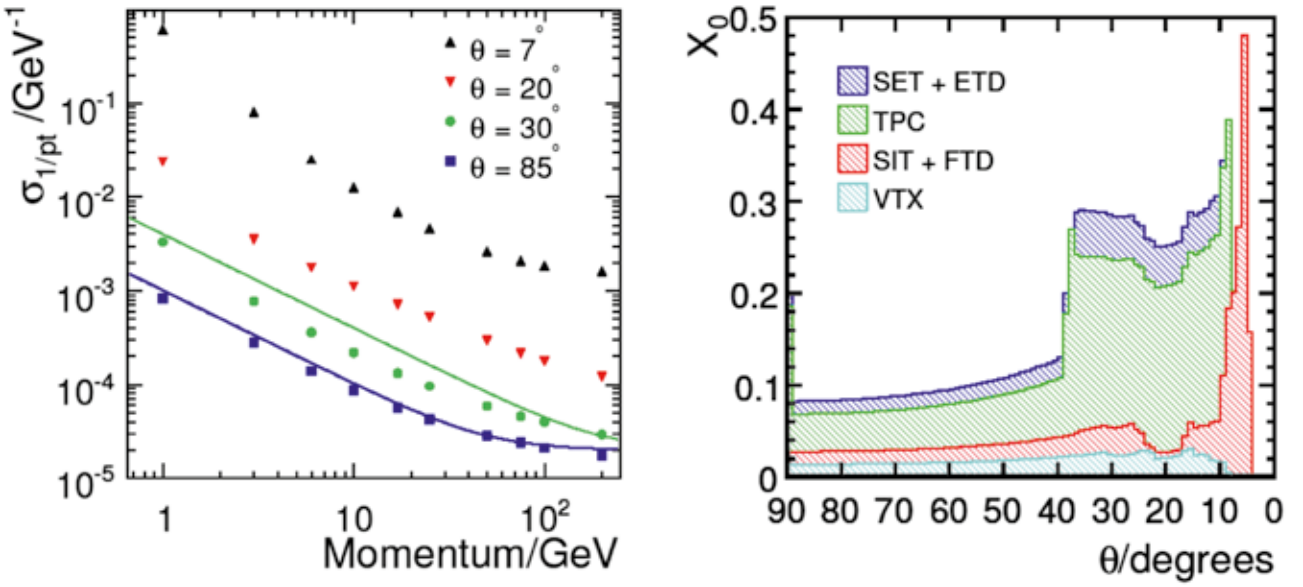

Figure 3.5 Left: transverse momentum resolution in the ILD detector concept for different angles relative to the beam. The lines show the resolution goals parametrised as $\sigma\{1/p_T\} = 2\times10^{-5} \oplus 1\times10^{-3}/(p_T \sin\theta)$. Right: total amount of material in the tracker as a function of the polar angle. Indicated are the different detector components in the ILD tracker. Images: ILD

The time projection chamber in ILD

The TPC for the ILC (see *Figure 3.6)* is based on a lightweight field cage, read out by micro-pattern gas detectors (MPGD) at either end. MPGDs have been chosen since they promise better performance than the more traditional wire chamber readout, are robust, lightweight and comparatively cheap. They lend themselves well to a system with small readout pads as it is needed for a high spatial resolution. In addition MPGD provide a significant suppression of the flow of positive ions back into the drift field, a major obstacle for a TPC, which needs to be operated continuously throughout an ILC bunch train. In addition, the well proven method of a gate will be foreseen to eliminate the remaining backflow.

The international linear collider-TPC collaboration (LC-TPC collaboration) is carrying out a comprehensive research programme to develop and establish the TPC as a possible solution for a tracker at the ILC. During the first phase of the work the fundamental principles of an MPGD-TPC have been established, gas properties have been measured, the achievable point resolution is understood, the resistive anode charge-dispersion technique has been demonstrated, and CMOS pixel readout technology has been demonstrated. The option of wire chamber-based gas amplification has been ruled out and a micro-mesh gaseous detector (or Micromegas, a fine micromesh structure) with standard pads has been ruled out as well.

The second phase of the work is currently ongoing. The main focus here is on the design, construction and operation of a large prototype and is expected to take another two to three years. The main goal of this work is to establish and demonstrate a large TPC readout with MPGDs in a realistic setting and with magnetic field. Both gas electron multiplier (GEM) and Micromegas readout technologies are studied. They are state-of-the-art technologies to detect electrons with gas amplification and fine-grain sensors. An important ingredient will be the demonstration that the field homogeneity can be controlled at the required level. Tests with the large prototype and different readout schemes will continue. The TPC will be upgraded to a lightweight end cap and exposed to electron and possibly hadron beams. A much improved readout system will be tested, one that is more compact and will include facilities for power pulsing. A conceptual design of a TPC will be prepared for the *Detailed Baseline Design Report.* Cabling, power pulsing and active carbon dioxide (CO_2) cooling will be studied as well.
The third phase, the final design and building phase, will commence once the ILC project gets the green light. The three phases described above overlap naturally; for example, certain aspects of the design have already started in preparation for the detailed baseline document.

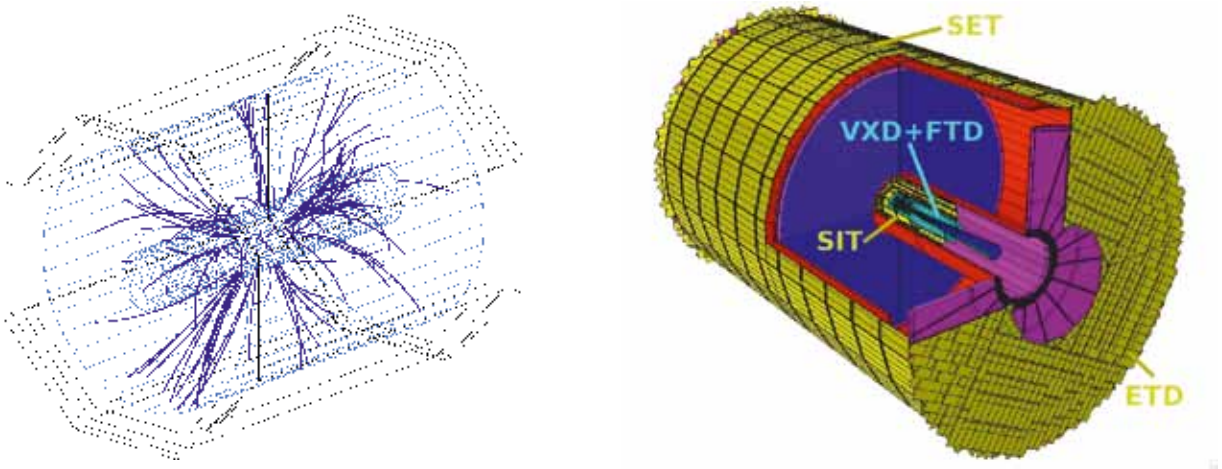

Figure 3.6 Three-dimensional view of the ILD time projection chamber after removal of machine background using a simple algorithm (left) and the silicon tracking system (right). VXD: vertex detector; FTD: forward tracking disks; SIT: silicon internal tracker; ETD: tracker behind the TPC end cap; SET: silcon external tracker. Images: ILD

Silicon tracking in ILD

The silicon tracking system in ILD is a combination of pixel and strip detectors. The forward direction, below the acceptance of the TPC, is covered by a number of pixel disks followed by disks instrumented with crossed-strip detectors. In total, seven stations will provide robust and powerful tracking. In the central region and behind the endplate of the TPC, strip detectors provide high-precision points inside and outside the TPC. The same strip sensor technology and sensor size (except for the FTD disks) is used throughout the system to simplify the system layout and maintenance. A view of the system is shown in *Figure 3.6*.

Significant development work is ongoing to provide sensors and readout systems for this large and complex system. The ladders are realised in deep sub-micron technology. An intense effort is underway to develop edgeless sensors, which would make the tiling of the sensors into a detector much simpler and help reduce the material budget. The integration of the pitch adapter and the readout onto a module made of one or a few sensors are studied to minimise the complexity and the amount of material. Challenging R&D is actively pursued on the front-end readout chip that must fully process the signals from a large number of channels up to and including digitisation. Modern deep sub-micron CMOS technology has been chosen to optimise the performances of the on-detector front-end electronics.

A major goal for the overall design of the system is to provide a lightweight support structure, minimising the material budget but still maintaining the overall tolerances. Studies into the use of new and advanced materials are underway in close cooperation with the Large Hadron Collider (LHC) experiments at CERN, Switzerland, which face similar problems.

Another challenge is to ensure that the system can be aligned quickly and precisely. The chosen scheme uses two different types of laser monitoring systems. One shines an IR laser through the ladders and provides a relative alignment between ladders. Another aligns a complete system relative

to another sub-detector, for example the TPC, through the use of an interferometry system. In addition, the final alignment will be accomplished using tracks from physics events. The capability of the system to provide precise timing will add another powerful tool to help combine information from the silicon tracker and the time projection chamber.

First prototypes of most of the individual parts of the system have been developed and tested with beam. Part of the programme is a combined test of silicon tracking detectors and the time projection chamber in the presence of a magnetic field. The next two years will be devoted to building a complete realistic prototype system, which will be the basis for a realistic conceptual design of the silicon tracking system.

3.4 Calorimetry

3.4.1 Overall design requirements

The baseline designs for the ILD and SiD detectors incorporate the elements needed to successfully implement the particle flow approach, introduced earlier. This imposes a number of basic requirements on the calorimeter systems. The entire central calorimeter system must be contained within the solenoid in order to reliably associate tracks to energy deposits. The electromagnetic and hadronic sections of the calorimeter must have imaging capabilities that allow both efficient track-following and correct assignment of energy clusters to tracks. These requirements imply that the calorimeters must be finely segmented both longitudinally and transversely. In order to ensure that no significant amount of energy can escape detection, the calorimeter system must extend down to small angles with respect to the beam pipe and must be sufficiently deep to prevent significant energy leakage. Since the average penetration depth of a hadronic shower grows with its energy, the calorimeter system must be designed for the highest-energy collisions envisaged.

The mechanical design of the calorimeter must consist of a series of modules of manageable size and weight to ease detector construction. The boundaries between modules must be as small as possible to prevent significant un-instrumented regions. Module boundaries, which do not project onto the interaction point, avoid the non-detection of high-momentum particles. The detectors must have excellent long-term stability and reliability, since access during the data-taking period will be extremely limited, if not impossible.

3.4.2 Electromagnetic calorimeter design requirements

For the efficient identification of individual jet components, it is important that the electromagnetic energy depositions of electrons and photons be as compact as possible to avoid overlaps and confusion. This implies the use of a dense absorber material and minimal active shower sampling gaps between the absorber layers, imposing significant design constraints. The energy resolution of the electromagnetic calorimeter should make a negligible contribution to the overall jet energy resolution. The calorimeter should provide efficient identification of electrons and photons and allow the reconstruction of neutral pions in jets and tau lepton decays to improve jet energy resolution and to discriminate between different tau final states. Due to the narrow size of electromagnetic showers in the ECAL, it is important that module boundaries do not project onto the interaction point.

3.4.3 Hadronic calorimeter requirements

The hadronic calorimeter (HCAL) must be divided into a sufficient number of layers that hadronic showers can be well identified and associated with charged tracks, or identified as a the result of a neutral particle, as appropriate. The radial space for the hadronic calorimeter is therefore divided into alternating layers of steel absorber and active sections, with the need to keep the latter as thin as possible to prevent the increase of lateral shower size and keep the overall detector volume compact. There must also be a fine transverse segmentation to allow efficient charged track following for the particle flow algorithm. Within the detector modules, the active layers should have a good uniformity of response and a reliable monitoring and control system.

3.4.4 The SiD and ILD calorimeter systems

The combined SiD electromagnetic and hadronic calorimeter systems consist of a central barrel part and two end caps (*Figure 3.7)*. The entire barrel system is contained within the volume of the cylindrical superconducting solenoid. The electromagnetic calorimeter has silicon active layers between tungsten absorber layers. The structure has 30 layers in total, the first 20 layers having a thinner absorber than the last ten layers. This configuration attempts to compromise between cost, electromagnetic shower radius, sampling frequency, and shower containment. The total depth is 26 radiation lengths (X_o). The hadronic calorimeter has a depth of 4.5 nuclear interaction lengths (λ), consisting of alternating steel plates and active layers. The baseline choice for the active layers is glass resistive plate chambers, but several other technologies are also being prototyped and evaluated.

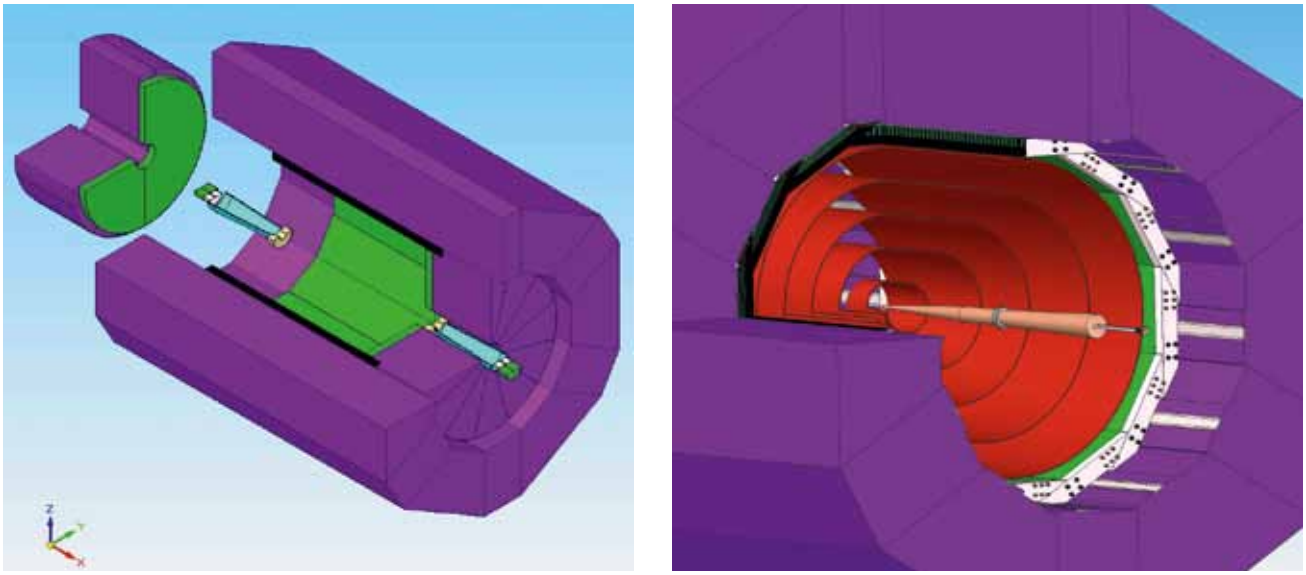

Figure 3.7 The SID calorimeter system. Images: SiD

The hadronic calorimeter is split into three along the beam direction, and into 12 azimuthal sections, giving reasonably sized modules for individual construction while keeping the number of boundaries between modules (and hence dead regions) to a minimum. Each end cap hadronic calorimeter will be in the form of a plug that is split along a vertical median line.

The ILD calorimeter design is guided by similar principles. The main parameters, such as the aspect ratio, inner radius, depth and granularity, have been optimised using a particle flow algorithm package called Pandora. Both electromagnetic and hadronic sections with tungsten and steel, respectively, as absorbers, are situated inside the solenoid as in SiD, however ILD uses a shorter barrel and larger end caps and has an eight-fold azimuthal symmetry. The ECAL (*Figure 3.8)* is segmented into 30 sampling layers corresponding to 24 X_0. The HCAL has 48 layers and a total depth of 5.5 λ, in addition to the ECAL. Several baseline technologies are considered for the instrumentation of the active layers: silicon pad diodes or scintillator strips with a transverse segmentation of 0.5 to 1 cm for the ECAL and 3 x 3 cm^2 scintillator tiles or gaseous devices with a segmentation of 1 x 1 cm^2 for the HCAL.

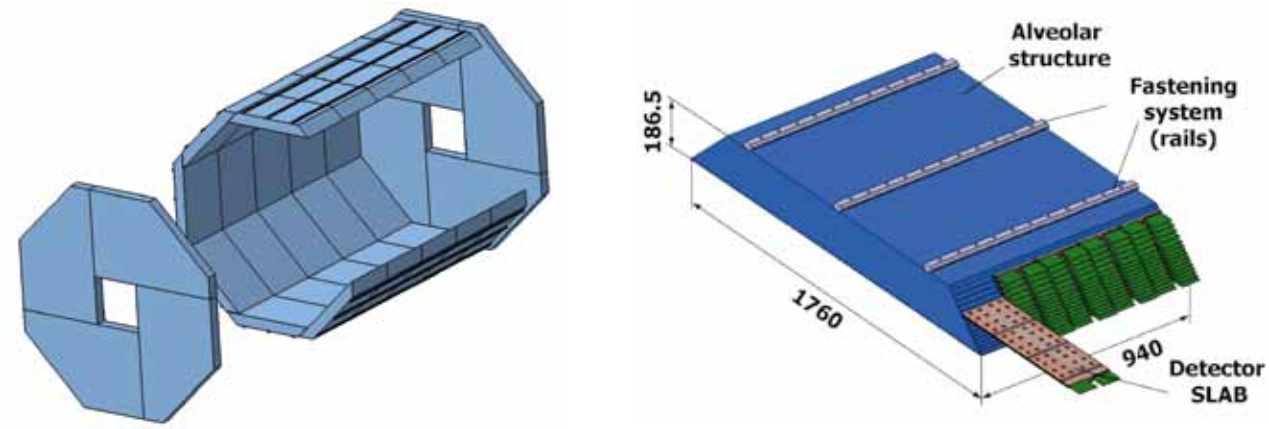

Figure 3.8 The ILD ECAL structure and details of a barrel module. Images: ILD

3.4.5 Electromagnetic calorimeter R&D

The requirements described above have given rise to the design of sampling electromagnetic calorimeters with tungsten absorbers because of its small Moliere radius and short radiation length. The active layers must be thin (to limit the size of the calorimeter's effective Moliere radius) with a highly segmented readout to provide the required transverse granularity.

The CALICE (Calorimeter for Linear Collider Experiment) collaboration presently pursues three technologies for the active part of the calorimeter: one based on matrices of silicon pad sensors, the second on strips of scintillator readout by compact photo-detectors and the third based on silicon pixel sensors with a digital readout.

The silicon-based approach uses matrices of 5 x 5 square millimetre (mm^2) pads made in 300- to 500-micron-thick high-resistivity silicon, fully depleted by a reverse bias voltage of around 200 volts (V). The advantages of this technology are its compactness, the ease of implementing high transverse granularity, and the stability of its response with respect to environmental factors. The scintillator-based option is based on 45 x 5 x 2 mm^3 scintillator strips individually read out by novel Geiger mode multi-pixel photo-sensors, so-called silicon photo-multipliers (SiPM), e.g. multi-pixel photon counter (MPPC) devices (*Figure 3.9).* The small size of the MPPC, its dynamic range and excellent photon-counting capabilities and its insensitivity to magnetic fields make it a very suitable detector for this application. The cost of this approach may be less than for a silicon-based ECAL.

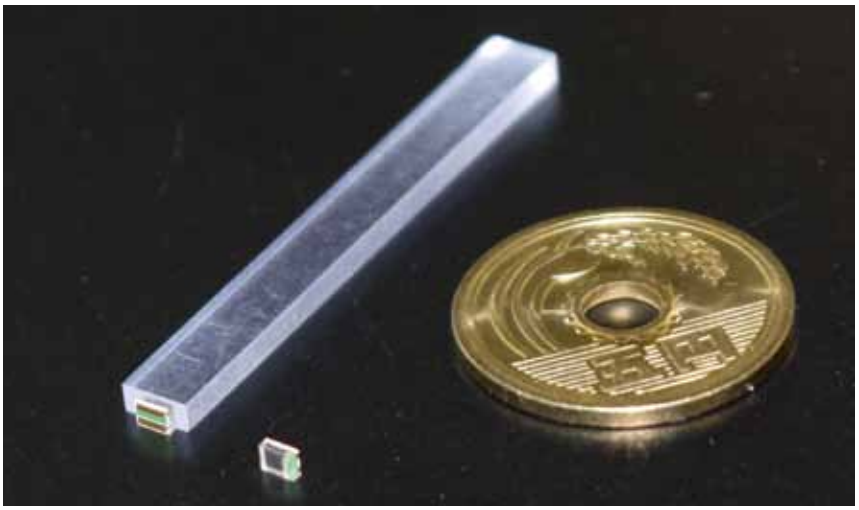

Figure 3.9 5 x 45 x 2 mm^3 scintillator strip and MPPC sensor. Image: CALICE

Prototype calorimeters of these two types have been constructed and tested in particle beams over a number of years. A 30-layer silicon-tungsten (SiW) prototype with almost 10,000 channels in a volume of 18 x 18 x 20 cm^3 has been tested *[3-1]*. A scintillator-based prototype consisting of more than 2,000 scintillator strips in 30 detection layers has also been produced and tested *[3-2]*. The measured performance, in terms of response linearity and energy resolution, of both these prototypes is in line with the expectations from detector simulation and sufficient for the requirements of a detector at a future linear collider.

The groups developing these two technologies are now working closely together on the development of a second-generation prototype, which will address technological questions of the integration of these technologies into a full detector in order to prepare for a detailed detector design. The possibility of a hybrid ECAL design with a mix of scintillator and silicon layers is also under study, with the development of dedicated reconstruction algorithms for such a detector.

Figure 3.10 Mechanical structure of technical prototype. Image: CALICE

A tungsten-carbon fibre composite mechanical structure (a slightly scaled-down version of a barrel module for ILD) has been constructed (*Figure 3.10)*. It will host detection layers based on both detector technologies. Several approaches to leakless water-based detector cooling are being tested. The front-end ASICs designed to read out the PIN detectors and SiPM devices (SKIROC2 and SPIROC2 respectively), including their power-pulsing capabilities, have been produced and are being tested. Studies of the integration process, including the manufacture of dedicated printed circuit boards (PCBs) to host the detection elements and front-end electronics (active sensor units) and their interconnection are also underway (*Figure 3.11)*. Further development of the detection elements (PIN matrices, scintillator strips and MPPCs) are continuing, with a move to 5-mm granularity for improved physics performance, and design developments (working closely with industrial partners) for lower cost and simpler detector construction. The CALICE data acquisition system is being developed to read out these and other calorimeters, and to be scalable to detectors required for a linear collider.

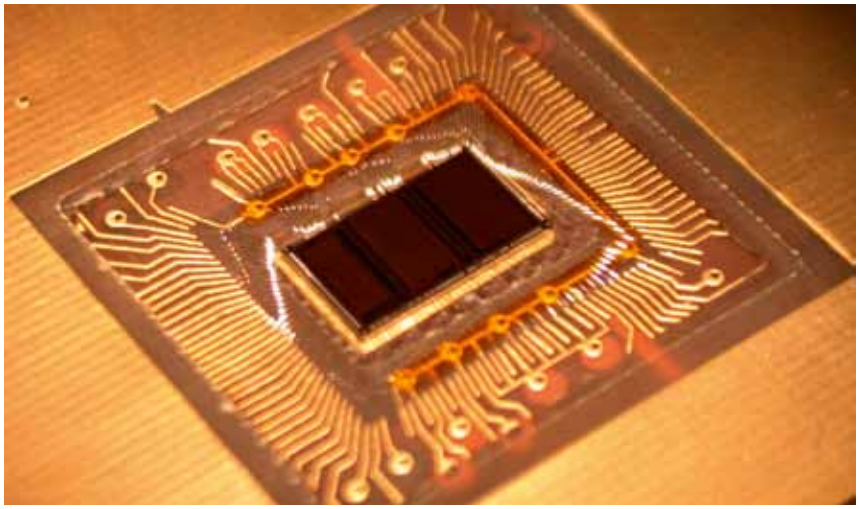

Figure 3.11 SKIROC2 chip bonded on detector PCB (active sensor unit). Image: CALICE

Progress is continuing on understanding the key issues surrounding the development of CMOS sensors, which could be used in a binary pixel readout ECAL. The R&D effort has concentrated on measuring the minimum ionisation particle efficiency of various sensor types and studying the density of particles in the electromagnetic shower downstream of tungsten, using data collected at a series of test beams carried out with pion and electron beams at CERN and DESY. Preliminary results demonstrate the significant improvements afforded by a new CMOS process called INMAPS that was developed during the project *[3-3]*. Work is continuing on the measurement of the electromagnetic shower density, an essential input to the choice of pixel size.

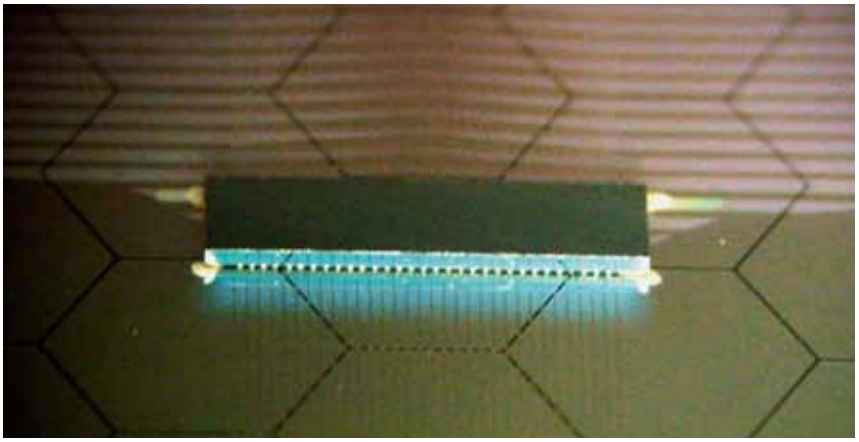

Figure 3.12 A prototype (256-channel) KPiX chip bump-bonded to a sensor. Hexagonal pixels are 13 mm^2. Image: SiD

The SiD ECAL R&D (carried out outside the CALICE collaboration) makes use of innovations in interconnect technologies that combine readout electronics and silicon sensors into a dense, highly segmented imaging electromagnetic calorimeter which, as discussed above, is required to fully exploit the ILC physics potential. The key developments include a fully integrated readout of silicon sensors with 1024 13-mm^2 pixels and interconnect technologies that make small 1- to 1.25-mm readout gaps possible, thus preserving the compact showers in tungsten. The current R&D status is that the technological steps are nearly complete: Having evaluated a series of smaller prototypes, the 1024-channel readout chip (KPiX) is currently in fabrication; the silicon sensors with 13-mm^2 pixels are in hand; and reasonable interconnect technology choices have been identified. After successful system tests, a full-depth module will be constructed for evaluation, which is planned in a test beam at SLAC. *Figure 3.12* is a photograph of a (256-channel) prototype KPiX readout chip affixed to a silicon sensor via bump bonding. *Figure 3.13* shows a flexible Kapton cable being affixed to a prototype sensor. The flex cable, sensor, and KPiX chip fit within the roughly 1-mm gap between tungsten layers.

Figure 3.13 Bonding of a flex cable to a prototype sensor. The cutout is for the KPiX chip. Image: SiD

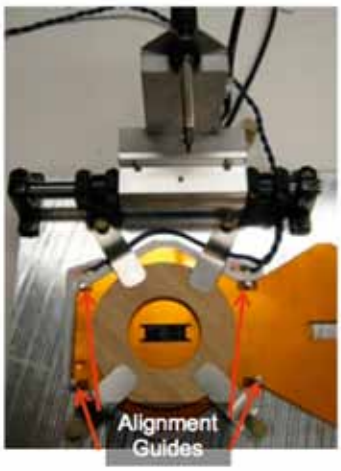

3.4.6 Hadronic calorimeter R&D

The R&D for the hadronic calorimeter of ILD and SiD is pursued in the framework of the worldwide CALICE collaboration. The goals are to establish the new technologies necessary to realise fine granularity, to validate the shower simulations at the detailed level required for particle flow reconstruction and to test these algorithms with real data. Once such a proof of principle is achieved in beam tests of first generation physics prototypes, the system design challenges are tackled with technological prototypes with the aim of demonstrating that the enormous channel densities can be accommodated in a large detector system without large dead spaces for cables, supplies and supports degrading the detector performance.

Both ILD and SiD groups foresee sampling calorimeters with stainless steel as absorbers and are considering different technologies for the active readout layers. These are based either on scintillator tiles of about 3 x 3 cm^2, optically read out by SiPMs (analogue readout, AHCAL) or on gaseous devices with gas amplification micro-structures with even finer 1 x 1 cm^2 segmentation and digital 1- or 2-bit readout (DHCAL). Resistive plate chamber (RPC), gas electron multiplier (GEM) and Micromegas technologies are under study.

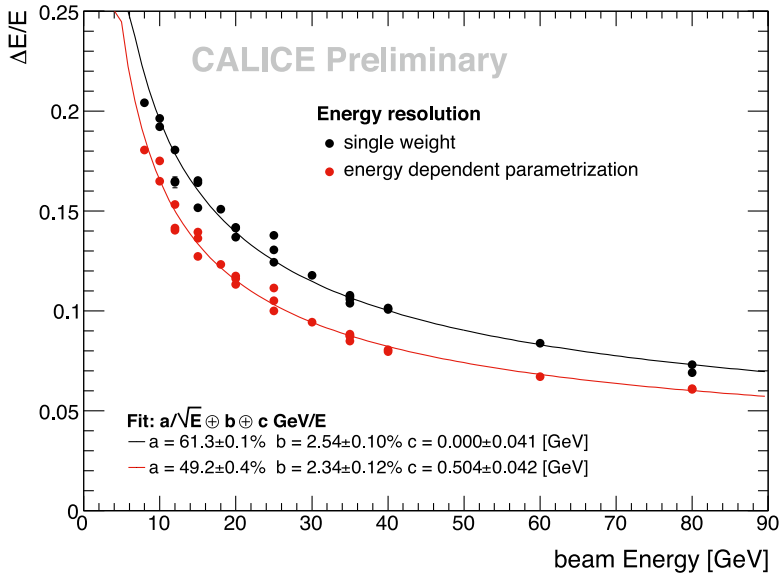

Figure 3.14 Hadronic energy resolution of the scintillator AHCAL prototype, without and with cell energy weighting. Image: CALICE

A cubic-metre-sized prototype of the AHCAL has been extensively tested at CERN and Fermilab in conjunction with silicon tungsten and scintillator tungsten electromagnetic calorimeters. The SiPM technology has proven to be robust and stable and has been chosen for applications in other high-energy physics experiments, for example Belle, CMS and T2K. The calorimeter has performed according to simulation-based expectation, with a resolution for single hadrons of 49%/√E (*Figure 3.14*). The detector shows very good imaging capabilities. For example, tracks are visible inside hadronic showers and used for calibration as well as for detailed feedback to refine the simulation models.

The high granularity and consequent low occupancy allows the use of event mixing techniques to study the performance of the Pandora particle flow algorithm with test beam data. The observed degradation of energy reconstruction for a neutral particle, as the distance to nearby charged particle showers decreases, is well reproduced by simulation; see *Figure 3.15*. This lends strong support to the jet energy performance prediction for the full detector, based on the same algorithm and critically depending on the particle separation power.

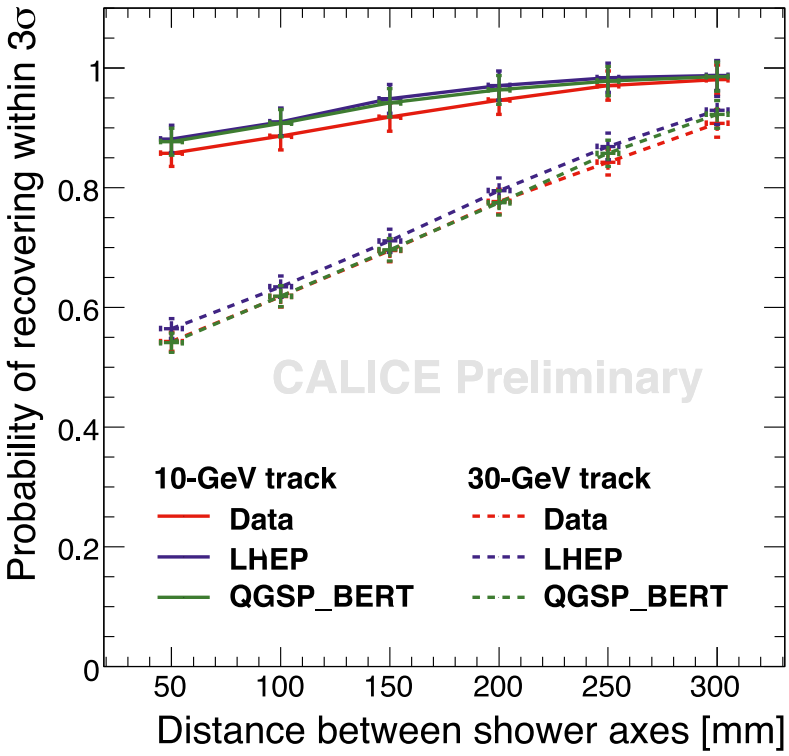

Figure 3.15 Reconstruction quality as function of distance to a nearby shower, in SiW ECAL plus scintillator AHCAL test beam data and simulation. Image: CALICE

An intensive effort is underway to establish the exciting concept of digital calorimetry with gaseous devices for the ILC. Following encouraging performance with a tabletop prototype, the first RPC-based full cubic-metre-sized system, with almost 400,000 channels, was assembled and exposed to hadron beams in the autumn of 2010 for the first time. The imaging resolution of the device is superior, as can be seen from the first events recorded, *Figure 3.16*. A comprehensive test beam programme is in full swing in 2011, including tests in conjunction with the SiW ECAL prototype and different devices. It will deliver the data set to establish the calorimetric and particle flow performance in time for the DBD.

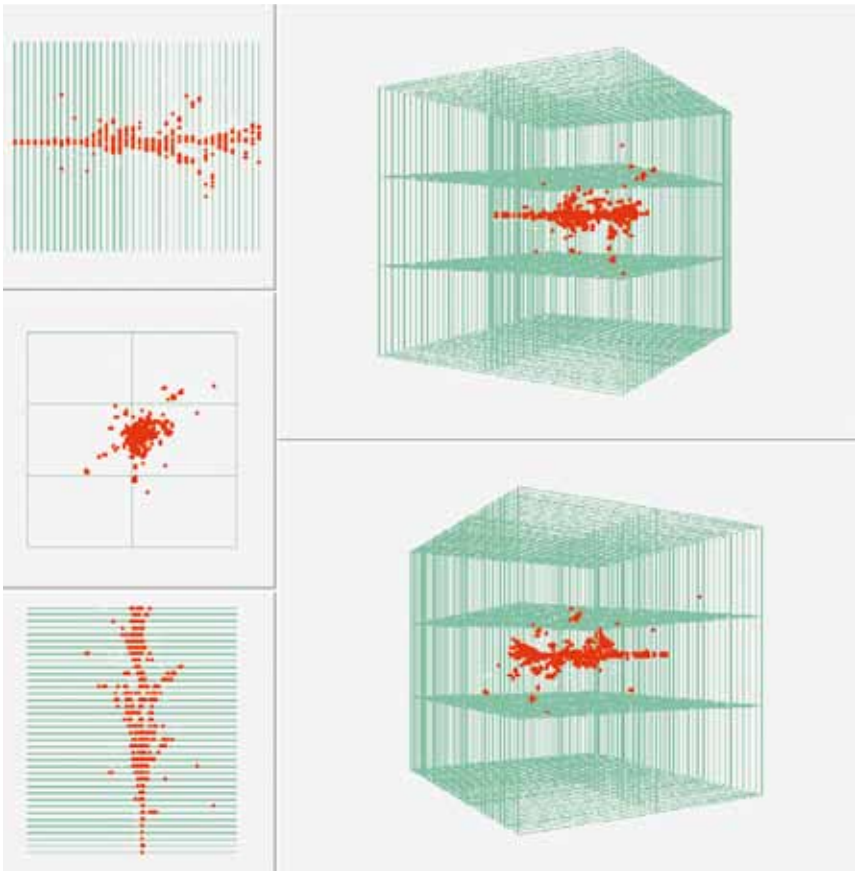

Figure 3.16 Online displays of test beam events in a cubic meter RPC DHCAL prototype. Image: CALICE

In order to handle the high granularity in a full collider detector, the front-end electronics must be integrated into the detector volume and the data be digitised as early as possible. The feasibility depends crucially on the development of ultra-low power, highly integrated micro-electronics ASICs. The 'ROC' chip family, for example, uses common building blocks for the use with different calorimeter technologies for AHCAL, DHCAL and ECAL. The first electronics modules of the second-generation chips have been tested in the beam with tiles and SiPMs as well as with gaseous devices, and full new AHCAL, ECAL and RPC DHCAL prototypes are in preparation.

Glass RPCs are the forerunner in integrating the new, highly integrated power-pulsed readout electronics. It was shown to function well in magnetic fields of more than 3 T. Square-metre planes were tested and a full stack is underway. This will allow tests of 2-bit readouts, expected to improve the resolution for higher particle energies. R&D on other gaseous techniques, GEMs and Micromegas, is being followed with vigour, too. Limited resources currently do not permit exploiting each of them at full cubic-metre scale, but this is also not necessary at this stage. Instead, small stacks and large areas have been successfully tested. Thereby the specific features of the calorimetric response are studied and their understanding in terms of simulations is validated. At the same time for each of them critical technical issues for extrapolating to larger systems are actively addressed.

Conclusion

Altogether, this programme will establish technology options for a feasible particle flow calorimeter with well understood strengths and weaknesses. The next step will be to validate the system performance and interplay of the highly integrated prototypes.

3.5 Very forward calorimeters

Two special calorimeters are foreseen in the very forward region of the ILC detectors - LumiCal for the precise measurement and BeamCal for the fast estimation of the luminosity. For beam tuning a pair monitor is considered, positioned just in front of BeamCal. LumiCal is a precision device with challenging requirements on the mechanics and position control. BeamCal, positioned just outside the beam pipe, is exposed to a large amount of low-energy electron-positron pairs originating from beamsstrahlung. These depositions, useful for a bunch-by-bunch luminosity estimate and the determination of beam parameters, require radiation hard sensors.
The detectors in the very forward region have to tackle relatively high occupancies, requiring dedicated front-end electronics.

3.5.1 Design of the very forward region

A sketch of the very forward region of the ILD detector, as an example, is shown in *Figure 3.17*.

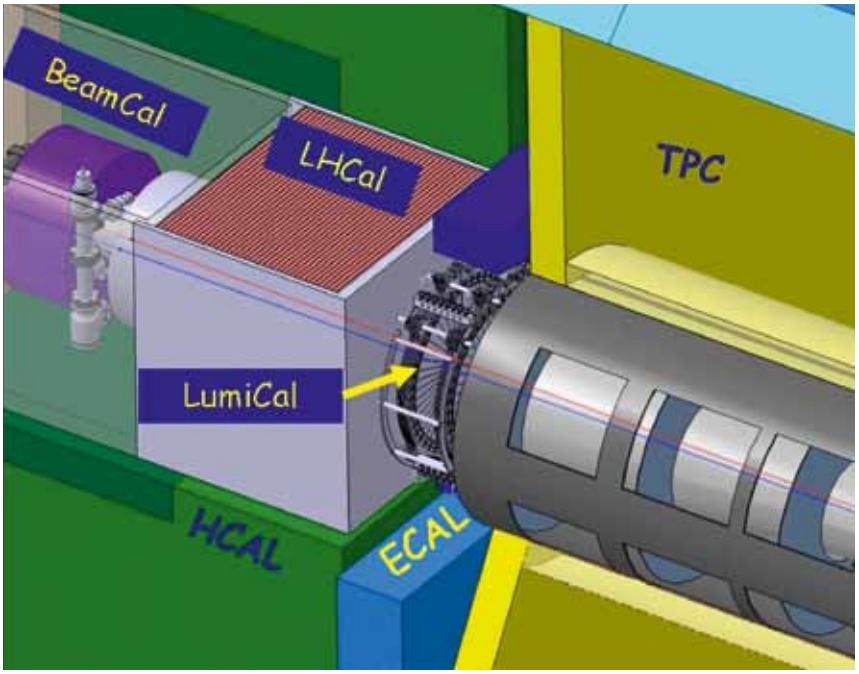

Figure 3.17 The very forward region of the ILD detector. LumiCal, BeamCal and LHCAL are carried by the support tube. Image: ILD

LumiCal and BeamCal are cylindrical electromagnetic calorimeters centred on the outgoing beam. BeamCal is placed just in front of the final focus quadrupole and LumiCal is aligned with the electromagnetic calorimeter endcap.

Both devices are designed as cylindrical sensor-tungsten sandwich calorimeters, consisting of 30 absorber disks, each 3.5 mm thick and corresponding to one radiation length, interspersed with sensor layers. Each sensor layer is segmented radially and azimuthally into pads. The granularity is optimised using Monte Carlo simulation.

Front-end ASICs are positioned at the outer radius of the calorimeters. BeamCal covers polar angles between 5 and 40 milliradians (mrad) and LumiCal between 31 and 77 mrad. The design of the very forward region of the SiD detector is very similar.

3.5.2 Sensor R&D

The challenge of BeamCal is to find sensors tolerating about one megagray (MGy) of dose per year. So far polycrystalline chemical vapour deposition (CVD) diamond sensors of 1 cm^2 and larger sectors of GaAs (gallium arsenide) pad sensors, as shown in *Figure 3.18* (left), have been studied. Since large-area CVD diamond sensors are extremely expensive, they may be used only at the innermost part of BeamCal. At larger radii GaAs sensors appear to be a promising option. Sensor samples produced using the liquid encapsulated Czochralski method and doped with tin and tellurium as shallow donors and chromium as a deep acceptor have been studied in a high-intensity electron beam. The charge collection efficiency is measured as a function of the absorbed dose. It decreases with growing dose; however signals of minimum ionising particles are visible up to a dose of 600 kilograys. The leakage current of a pad at room temperature before irradiation is about 200 nanoamps (nA) at an applied voltage of 50 V. After exposure of a dose of 1.2 MGy, leakage currents of up to a factor 2 larger were found, still tolerable for the application. Prototypes of LumiCal sensors of similar shape have been designed and manufactured by Hamamatsu Photonics. The pitch of the p-type pads on n-type silicon is 1.8 mm. All pads have a leakage current of a few nA and a depletion voltage of about 40 V. The capacitances range from 8 to 20 picofarads.

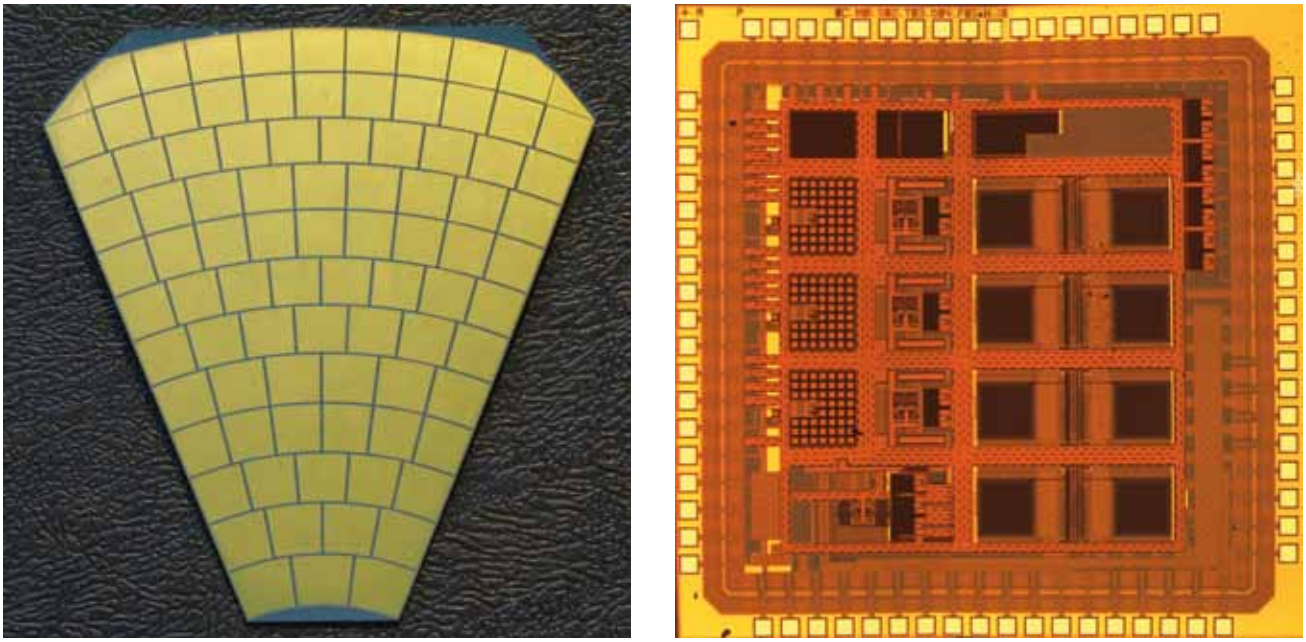

Figure 3.18 A prototype of a GaAs sensor with pads of 8 x 8 mm^2 size (left) and a 4-channel ASIC (right). Left image: G. Shelkov, FCAL, JINR. Right image: A. Abulselme, FCAL, Stanford University

ASIC developments

Since the occupancy in BeamCal and LumiCal is relatively large they must be read out after each bunch crossing. Therefore special front-end and analogue-to-digital converters (ADC) that match the timing of the ILC have been developed. The BeamCal ASICs, designed for 180-nm technology, will be able to handle 32 channels. A prototype, containing 4 channels, is shown in *Figure 3.18* (right). Two modes of operation require a front-end circuit capable of a wide performance envelope: high slew rate for standard data-taking and low noise for calibration. In standard data-taking all data from a full bunch train must be recorded to be read out between bunch trains. Because of its reliability, density and redundancy, a digital memory array will be used to store the data from all collisions in each bunch train. This choice requires a sampling rate of 3.25 megahertz per channel, which is achieved by 10-bit, successive approximation analogue-to-digital converters.

The ASICs for LumiCal, designed in 350-nm CMOS technology, have to tackle in addition a larger range of input capacitances due to a large variation of pad sizes. The chosen front-end architecture comprises a charge-sensitive amplifier, a pole-zero cancellation circuit and a shaper. The ADC is designed using pipeline technology. The first prototype ADC, shown in *Figure 3.19* (left), consists of an input sample and hold circuit, nine pipeline stages and digital correction circuitry. In addition, the power-switching feature is also implemented.

Prototypes have been tested for both BeamCal and LumiCal. The results confirm that the ASICs match the requirements derived from the detector performance necessary for the physics programme.

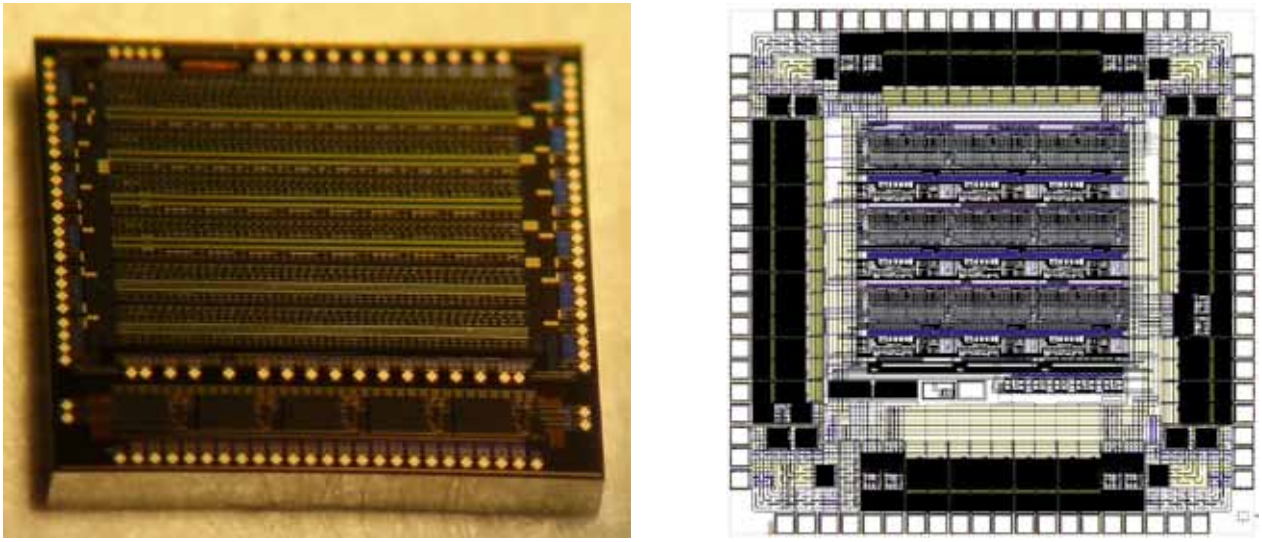

Figure 3.19 Prototypes of the ADC ASIC for LumiCal (left) and for the Pair Monitor (right). Left image: M. Idzik, FCAL, University of Science and Technology, Cracow. Right image: FCAL, Tohoku University.

First fully functional sensor plane

In summer 2010 a sensor for BeamCal and a sensor for LumiCal were assembled with front-end ASICs and investigated in the 4-GeV electron beam at DESY. Several millions of triggers have been recorded, exposing several pads and sensor edges to the beam. Studies of signal-to-noise, cross talk, sensor homogeneity and edge effects are ongoing. Preliminary results, as shown in *Figure 3.20*, are promising.

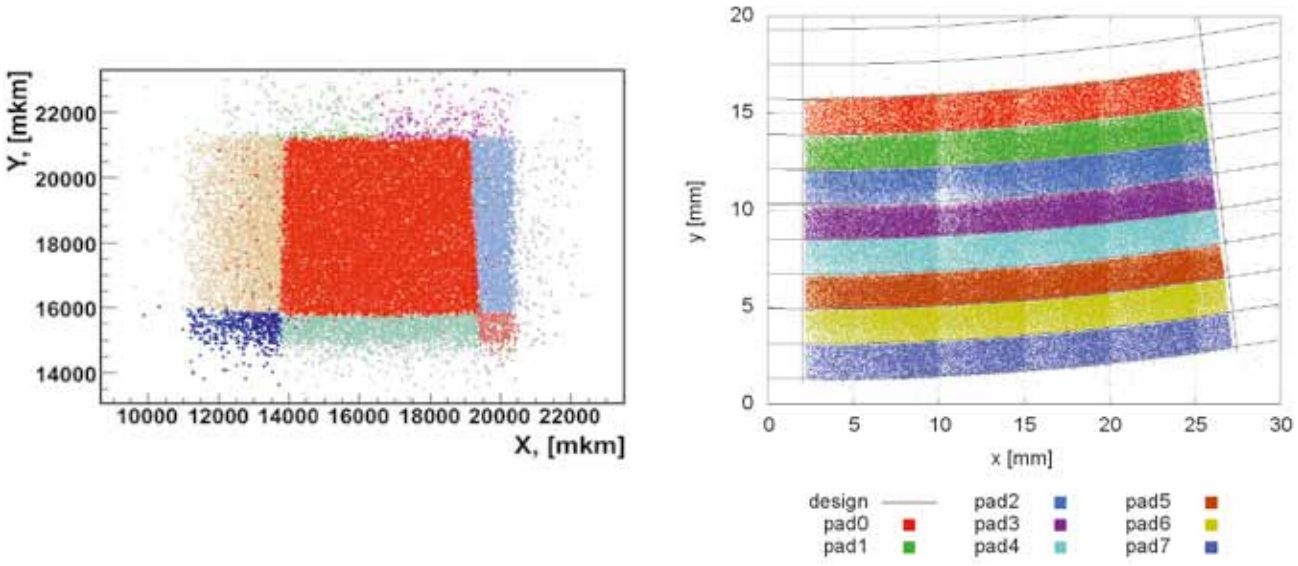

Figure 3.20 Predicted beam particle impact points are compared with the signal on the pad crossed by the beam particle. Left: BeamCal. Right: LumiCal. Each color is assigned to a certain pad. Left image: O. Novgorodova, FCAL, DESY Zeuthen. Right image: S. Kulis, FCAL, University of Science and Technology, Cracow.

3.6 Magnet coil

3.6.1 ILD magnet coil

Since the *Reference Design Report* (RDR), the main progress done on the ILD coil has been to confirm the main coil parameters: design field of 3.5 T in a 6.9-m warm bore and on a 7.35-m coil length to perform 3-D magnetic calculations (including the yoke) and to study various options for the coil design. Starting from the basic ILD design, which is based on the Large Hadron Collider CMS detector configuration, a few possibilities have been studied in detail: improve the magnetic field homogeneity by adding extra current in specific locations of the winding and/or add an anti-DID (detector-integrated dipole, *Figure 3.21)* to compensate the effects of the crossing angle on the beams.

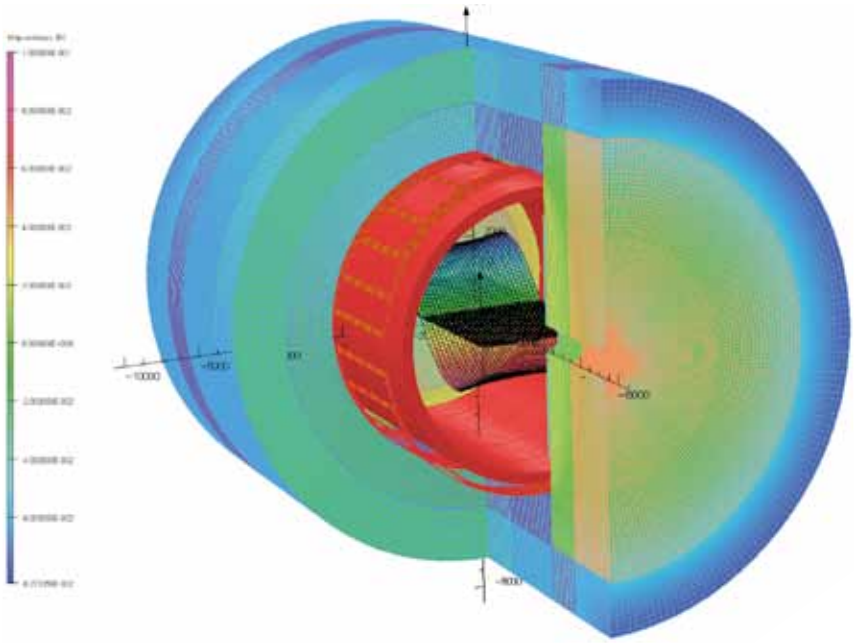

Figure 3.21 Anti-DiD in ILD. Image: Olivier Delferriere

3.6.2 SiD magnet coil

Since the RDR, the SiD superconducting solenoid still retains the CMS solenoid design philosophy and construction techniques, using a slightly modified CMS conductor as its baseline design. Superconducting strand count in the coextruded Rutherford cable was increased from 32 to 40 to accommodate the higher 5-T central field. Many iron flux return configurations have been tested in two dimensions to reduce the fringe field. An Opera 3-D calculation with the DID coil has been completed. Calculations of magnetic field with a 3-D ANSYS program are in progress. These will have the capability to calculate forces and stress on the DID as well as run transient cases to check the viability of using the DID as a quench propagator for the solenoid. Field and force calculations with an iron end cap HCAL were studied. The field homogeneity improvement was found to be insufficient

to pursue this option. Conceptual DID construction and assembly methods have been studied. The solenoid electrical power system, including a water-cooled dump resistor and grounding, was established. Significant work has been expended on examining different conductor stabiliser options and conductor fabrication methods. This work is pursued as a cost- and time-saving effort for solenoid construction.

3.6.3 R&D common programme

An R&D common programme for the improvement of the conductor of the ILD and SiD detector magnets has been proposed and started among various laboratories in Europe, Japan and the US. The main goal is to improve the mechanical behaviour of the conductor without degrading too much the function of the electrical stabiliser. Several ways are foreseen: extrusion with Al/micro-doped alloy, alumina fibres, and carbon nanotube technology.

3.7 The ILD and SiD muon systems

The return yoke for ILD and SiD is instrumented with position sensitive detectors to serve as both a muon filter and a tail catcher. The total area to be instrumented is very significant, with several thousand square metres of area. Technologies that lend themselves to low-cost large-area detectors are therefore under investigation. Particles arriving at the muon system have seen large amounts of material in the calorimeters and encounter significant multiple scattering inside the iron. Spatial resolutions of a few centimetres are therefore sufficient. Occupancies are low, so strip detectors are possible. In the ILD and SiD concepts, solutions exist that extend the technologies for the hadronic calorimeter – either scintillator or resistive plate chambers – to the muon system so that synergies exist for the two systems. Simulation studies have shown that ten or more layers of sensitive detectors yield adequate energy measurements and good muon-detection efficiency. The efficiency to find muons in semi-leptonic bottom decays is shown in *Figure 3.22* (left).

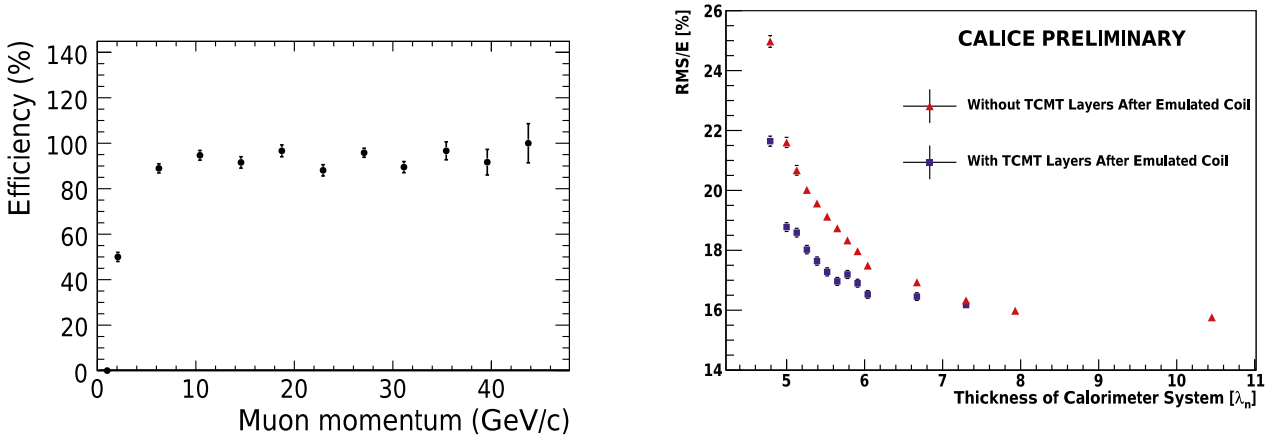

Figure 3.22 Left: muon-finding efficiency in hadronic b-decays as simulated for the ILD detector. Right: resolution improvement for 20-GeV pions using the muon tracker as a tail catcher, measured with CALICE test beam data. The red triangles show the energy resolution as a function of calorimeter thickness. The blue squares show the resolution for a system including a leading calorimeter, an emulated magnet coil, and post-coil sampling with the tail catcher as function of the depth of the forward edge of the emulated coil. The resolution is calculated with the root-mean-square of the energy distribution to account for non-Gaussian tails. The coil is emulated by omitting layers of the tail catcher from the energy measurement. The maximum depth of the full calorimeter system including the tail catcher is 11 proton interaction lengths. Left image: DESY. Right image: CALICE.

The detector R&D that is being pursued has to do with the principles of operation for both resistive plate chambers and readout of wavelength-shifting (WLS) fibres embedded in extruded strip scintillators using pixellated photon detectors (PPDs), or SiPMs.

The R&D on RPCs centres on understanding their long-term efficiencies with about 9-kilovolt direct current voltages applied for long periods of time in a radiation environment, such as is expected in the forward and backward regions of the linear collider interaction region. The strip scintillator/PPD readout R&D has centred on calibration using zero, one and two photoelectron response from spontaneous not-beam-associated signals and on measurement of the attenuation due to subsequent passage of the light pulses through the WLS before they reach the PPD. Because the PPDs have better photoelectron conversion efficiency from light pulses, the observed number of photoelectrons exceeds what is possible with multi-anode photomultiplier vacuum tubes. The list of future R&D includes examples of how to deal with thousands of channels and their specification and background noise in a cost-effective way using integrated circuitry. In the short time we have before the publication of the detailed baseline design, we will need to prioritise our work to attack important problems, such as dealing with many fewer instances of large energy deposits for muons than for hadrons, with the possibility for local tracking of muons.

3.8 Data acquisition

The detectors at the ILC will be built to perform high-precision experiments in a high-luminosity environment. As one of the major components, the data acquisition (DAQ) has to be designed to achieve this by dead-time-free data recording without compromising on possible rare or yet unknown physics processes. Because of the bunched operation mode of the ILC, a DAQ system without a hardware trigger was adopted for both the ILD and the SiD detector concepts *[3-4]*. The data are processed and stored in the front-end readout electronics of the different detectors for a full bunch, that is, for up to 3,000 collisions during a timespan of about 1 millisecond (ms). In the time between bunch trains, on the order of 200 ms, the data are then collected from the front end by an event-building network and are further processed in a software event filter based on commercial processing units. The processed data are finally sent to permanent storage according to physics and calibration needs. This concept will assure the needed flexibility and scalability and will be able to cope with the expected complexity of the physics and detector data without compromising efficiency or performance.

In addition, the ILC physics goals require higher precision in energy and momentum resolution and better impact parameter resolution than any other collider detector built so far. Improved accuracy can only be achieved by a substantially larger number of readout channels than in previous detectors. The increased calculations numbers of readout channels for the ILC detectors will require signal processing and data compression already at the detector electronics level as well as high bandwidth for the event-building network to cope with the data flow. To reduce the power consumption and hence the need for large cooling power, it is proposed to switch off power to parts of the front-end electronics in the time between trains.

For both detector concepts, prototypes of the front-end readout electronics for the different detector technologies have been designed and fabricated *[3-5]* to be used in test beams for verification of the detector design as well as of the electronics design. An essential part of these tests is the demonstration of the power pulsing scheme.

The DAQ systems emerging from the test beam systems began recently to address more and more the issues of system control and integration as well as slow control and monitoring (*Figure 3.23)*. First designs like the EUDAQ and the CALICE DAQ Version 2 or the SiD DAQ try to integrate different detector systems into a common integrated DAQ system.

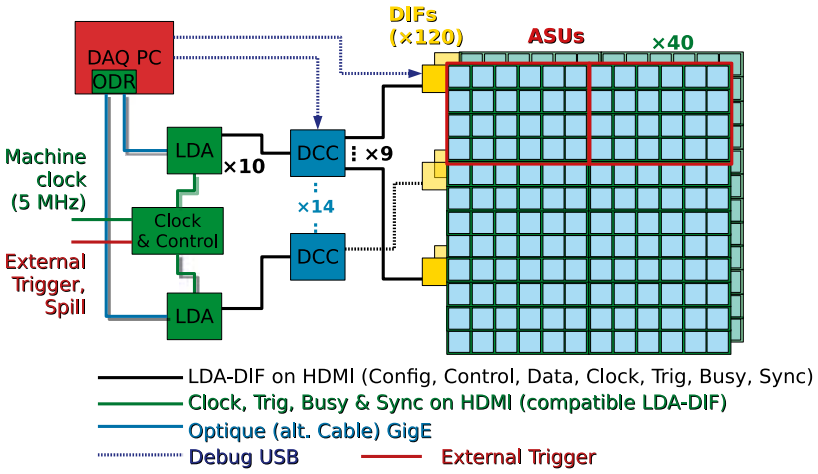

Figure 3.23 Calice DAQ scheme. Only the detector interface is detector-specific. All other components, such as the data concentrator card (DCC), the link data aggregator (LDA) and the off-detector receiver card (ODR) are common. Images: Vincent Boudry

3.9.1 The push-pull system

The push-pull system for the two detectors was only conceptual at the time of RDR's publication, and since then the engineering design has progressed significantly. A time-efficient implementation of the push-pull model of operation sets specific requirements and challenges for many detector and machine systems, in particular the interaction region (IR) magnets, the cryogenics, the alignment system, the beamline shielding, the detector design and the overall integration. The minimal functional requirements and interface specifications for the push-pull IR have been successfully developed and published *[3-4]*, to which all further IR design work on both the detectors and machine sides are constrained.

The push-pull design needs to accommodate two detector concepts, ILD and SiD, that are different in their design, dimensions and mechanical characteristics (such as mechanical rigidity). The different sizes provide particular challenges for the beamline shielding elements, referred to as the 'pacman' shielding. An example of a design of the pacman shielding that ensures compatibility with both detectors is illustrated in *Figure 3.24*.

3.9 The machine-detector interface

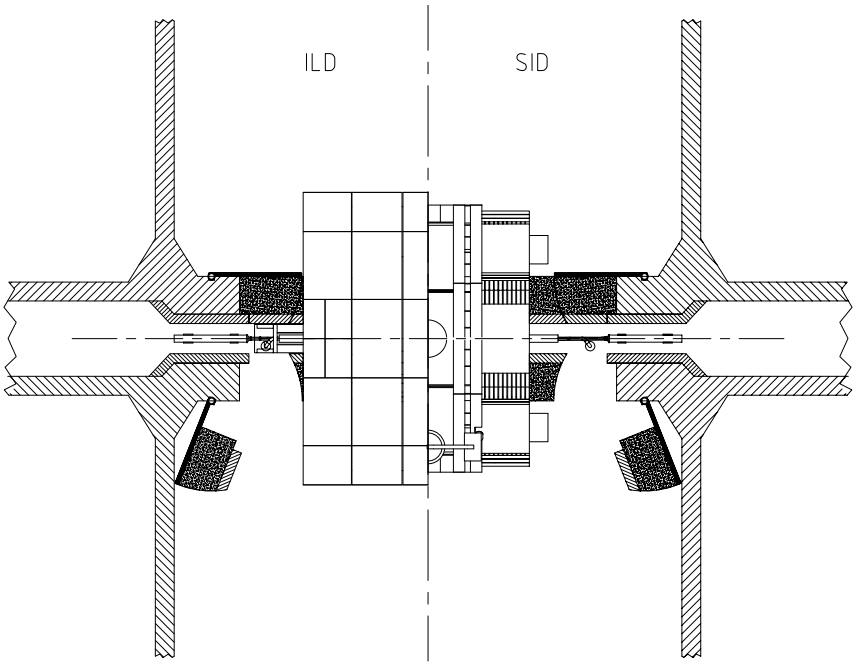

Figure 3.24 Design of the beamline shielding compatible with two detectors of different sizes. Image: Marco Oriunno

The detector motion and support system has to be designed to ensure reliable push-pull operation, allowing a hundred moves over the life of the experiment, while preserving internal alignment of the detector's internal components and ensuring accuracy of detector positioning. The motion system must be designed to preserve structural integrity of the collider hall floor and walls. Moreover, the motion and support system must be compatible with the tens-of-nanometre-level vibration stability of the detector. If situated in seismic regions, the system must also be compatible with earthquake safety standards. Two different approaches for the detector support system are currently being considered, a roller and a platform-based system.

The approach for the design of the detector motion system, and in particular the use of a platform, is currently being investigated. The criteria for selection of the common design will be based on engineering considerations and on vibration stability analysis of the entire system (detector together with its support and motion system). The selection is planned to happen in the near future.

SiD in a push-pull configuration

The more compact and rigid SiD detector can naturally be supported by an eight-leg structure as shown on *Figure 3.25* or sit upon a rigid platform. As its half-height is 1.7 m less than that of ILD, either extra-long legs or an extra thick platform will be required. With the magnetic field turned on and the end cap doors sucked into the central barrel, SiD is very stiff. The last quadrupole lens package, QD0, is designed to rest on a magnetically insensitive mover system, which in turn rests on cylinder-shaped cutouts in the doors, which are only marginally larger than the diameter of the QD0 cryostat. This design emphasises maximal hermeticity and rapid push-pull detector exchange. The forward calorimeter (FCAL) package (LumiCal,

BeamCal and masking) will be a logical cantilevered extension of the QD0 cryostat. A frequency-scanning interferometer (FSI)-based alignment system will align the opposing QD0/FCAL packages to the tunnel-mounted QF1 cryostats that complete the final doublet telescope and ensure precision LumiCal positioning with respect to the interaction point. The same FSI system will guarantee vertex and tracking detector alignment after each push-pull operation without the need to reacquire beam-based alignment data. This design requires that all mechanical systems mounted on the detector be vibration-free. While still under study, interaction point vacuum is assumed achievable via QD0 cryo-pumping without external pumps or non-evaporative getter (NEG) coating systems.

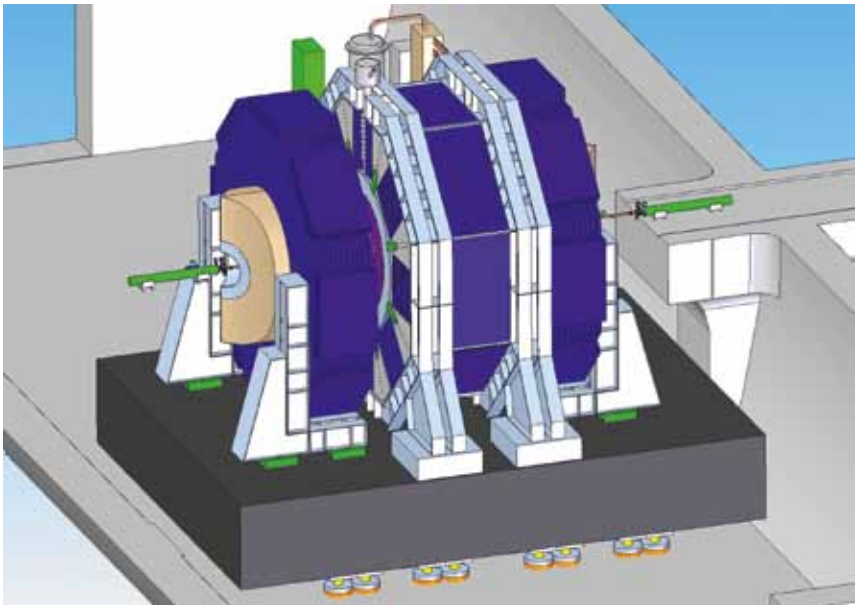

Figure 3.25 Possible detector motion system for the SiD. Image: Marco Oriunno

ILD in a push-pull configuration

The ILD detector is somewhat larger than SiD and is also designed to be assembled from slices in a similar way to the Large Hadron Collider CMS detector. The ILD detector motion system foresees the use of a rigid platform on which the entire detector can be placed. The platform will preserve detector alignment and will distribute the load evenly onto the floor. Such an approach is illustrated in *Figure 3.26.* The platform will carry also some of the detector services like electronic racks. Cables and cryogenic lines will be routed to the platform in flexible cable chains that move in trenches underneath the platform itself. The platform itself will move on air pads that allow linear and rotational movements on the floor. In combination with a simple positive indexing mechanism, the platform with the detector can be positioned quickly within the required precision of 1 mm with respect to the beam axis.

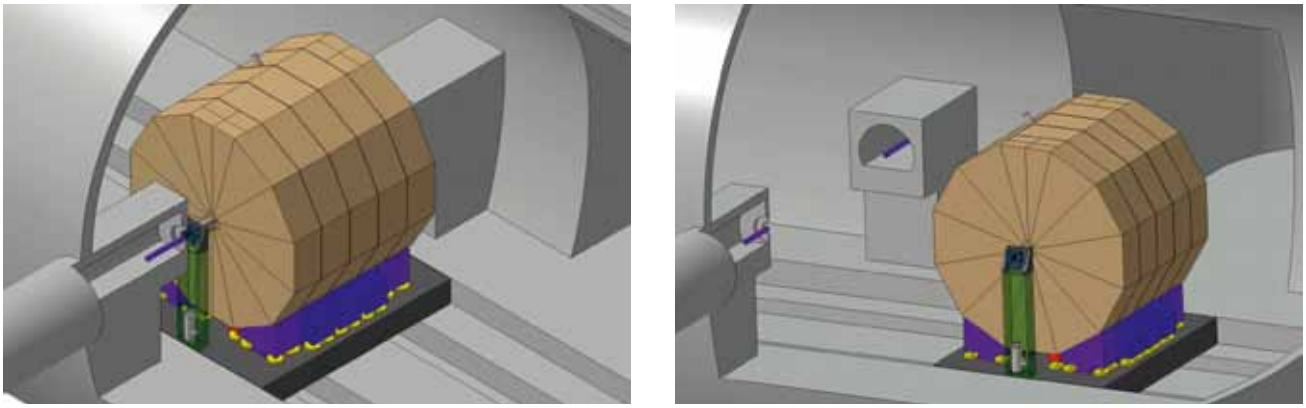

Figure 3.26 Possible platform support concept for the ILD. Left: on the beamline. Right: off the beamline. Images: Marco Oriunno

3.9.2 Vibration analysis

The main causes of luminosity losses in the beam delivery system are the naturally occurring ground motion, mechanical vibration sources and wake field effects. The most acute effects are the relative jitter of the final focussing magnets, which need mechanical stabilisation at about the 50-nm level, with the residual effect being compensated by beam feedback systems for collision optimisation. Mechanical vibrations generated by technical systems, such as HVAC and cryogenics, will be mitigated by design, placing them in appropriate locations of the experimental area. Ground vibrations are site-dependent and a careful design of the detector support and final focussing system is required. A comprehensive database of ground motion vibrations for different sites around the world that host accelerator facilities is available. The ILD and SiD collaborations are working together towards the simulation and benchmarking of the respective detectors in order to guarantee the required level of stability. Preliminary results show that both detectors can achieve the goals by means of mechanical passive stabilisation of the QD0 systems, in conjunction with the interaction point feedback system. Further studies are necessary to understand the coupling with the QF1 magnets, which will be mechanically independent from the QD0 during the push-pull operations.

A possible solution for the transport of the detectors in the push-pull is a reinforced concrete platform. The stability requirements of a platform solution are under study and a first mechanical design is in progress. Because of the intrinsic uncertainty related to the nonlinearity and the damping factors of large reinforced concrete structures, an experimental benchmark with comparable structures was required. An experimental characterisation of the dynamic behaviour of the large reinforced concrete shielding slab of the CMS access shaft, which is so far the closest existing example of a push-pull platform, has been made.

References

[3-1] CALICE collaboration, Design and Electronics Commissioning of the Physics Prototype of a Si-W Electromagnetic Calorimeter for the International Linear Collider, 2008_JINST_3_P08001; CALICE collaboration, Response of the CALICE Si-W Electromagnetic Calorimeter Physics Prototype to Electrons, NIM A608 (2009) 372.

[3-2] S. Uozumi, "Performance of the Scintillator-Strip Electromagnetic Calorimeter Prototype for the Linear Collider Experiment," talk at CALOR2010, Beijing.

[3-3] P. Dauncey, "Performance of CMOS sensors for a digital electromagnetic calorimeter," PoS (ICHEP 2010) 502.

[3-4] B. Parker et al., ILC-Note-2009-050.

04

PHYSICS AND SIMULATION UPDATES

4.1 Software

The ILD (International Large Detector) simulation has been performed with a model implemented in a full simulation framework called Mokka. The model used for the Letter of Intent (LOI) study is shown in *Figure 4.1*. Most of the sub-detectors in this model have been implemented, including a significant amount of engineering detail such as material structures, electronics and cabling as well as dead materials and cracks with detailed cell structures of calorimeters. This provides a reasonable estimate of the material budget, which is crucial for a realistic demonstration of detector performances. The update of the model is now in progress for the detailed baseline design (DBD). The new features to be implemented in the new model include additions of services and support structures between sub-detectors, catching up the evolution of the computer-aided design (CAD) model of ILD and implementations of wafer and support structures of silicon trackers, which had been approximated by cylinder and disks in the current ILD model.

Simulated ILD events have been reconstructed by a set of realistic event reconstruction programs called Marlin. Reconstruction processors in Marlin include the Kalman filter-based charged track reconstruction processors of Marlin Reco, PandoraPFA processor for reconstructions of particle flow objects, and LCFIVertexing for flavour tagging through reconstructions of secondary and tertiary vertices. According to our study, these programs perform charged particle reconstruction with efficiency better than 99% in top-antitop pair events with background hits overlaid, with jet energy resolution of 3% for jets with energy between 100 to 200 gigaelectronvolts (GeV), and with excellent flavour tagging efficiency. Improvements of reconstruction and analysis tools are in progress following the update of simulator model for the Detailed Baseline Design (DBD) report.

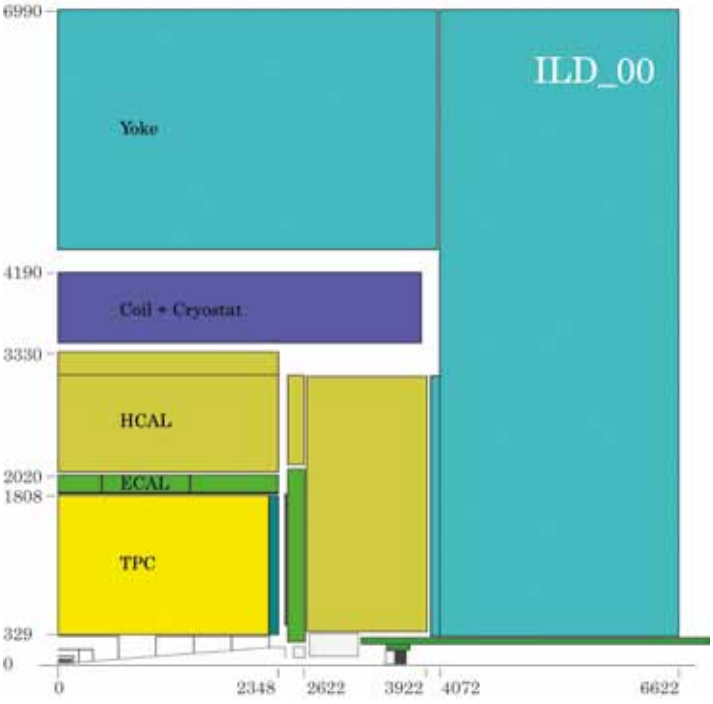

Figure 4.1 The ILD detector model as implemented in Mokka. From the inside to the outside, the detector components are the vertex detector, silicon strip inner tracker, time projection chamber (TPC), silicon external tracker, electromagnetic calorimeter (ECAL), hadronic calorimeter (HCAL), and yoke. In the forward region the forward tracking disks, endcap tracking detector, LumiCal (LCAL), LHCAL and BeamCal (BCAL) are shown. Image: Akiya Miyamoto

Using the fast and flexible detector simulation package developed by the American Linear Collider Simulation and Reconstruction Physics Group, more than 50 different detector designs were modeled before selecting the baseline design for SiD (Silicon Detector). Since that time, the fully detailed geometry has been implemented in a model called sidloi3. All of the tracker elements are therefore modelled as planar silicon wafers with their attendant support structures. The readout geometry is simplified, but reflects the gross amount and general distribution of the materials. The calorimeters are modelled as polygonal staves in the barrel region or planes in the end caps with interleaved readouts. The complexity of this detector model does not lend itself to a simple textual description. We therefore present a few figures to give an indication of the detail implemented in this model. See *Figure 4.2*.

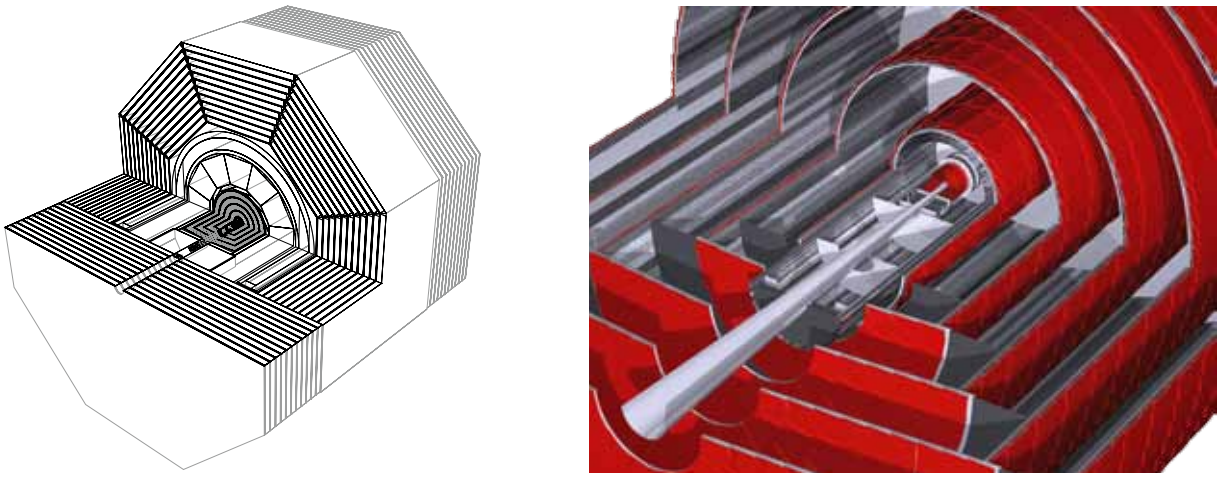

Figure 4.2 SiD as implemented in the simulation program showing the complexity of the design implemented for the DBD studies. Left: complete detector. Right: tracker. Images: Norman Graf

Digitisation involves a detailed simulation of the ionisation generation in the sensitive layer of the sensor, charge collection, signal formation and signal processing. This has two major goals during the detector design phase: optimising sensor parameters and comparing different sensors, and providing an estimation of the full detector performance. Very detailed but flexible simulation of the response of silicon detectors is possible, including variable readout dimensions (e.g. pixels or strips), various media, electric and magnetic field maps, detailed energy loss simulation using specialised code, electronics response, including electronics noise or inefficiencies, propagation of the signal to readout and digitisation of the signal. The reconstruction software has been modified as necessary to accommodate the changes in geometry, and the tracking continues to show excellent efficiency and resolution. A binding between the simulation output and the PandoraPFA package has also been released. Production simulation and reconstruction will take place on the worldwide network of computers (namely, 'Grid') using a submission tool called Dirac

4.2 Benchmark modes

The physics case for the ILC operating at a centre-of-mass energy of 500 GeV and its complementarity to that of the Large Hadron Collider has been well established (see documents on Tesla Test Facility R&D *[4-1]*, the *Reference Design Report* (RDR) *[4-2]*, and studies on ILC-LHC physics cases *[4-3]*). However, realising the full potential of the ILC places stringent requirements on the performance of the detectors. Compared to the previous generation of electron-positron machines (LEP at CERN and SLC at SLAC National Accelerator Laboratory) the detector at the ILC needs to deliver an order of magnitude better momentum resolution, a factor two to three better jet energy resolution and a factor three better impact parameter resolution. Since the *Reference Design Report,* much of the work of the detector and physics community has focussed on demonstrating that the full physics reach of the ILC can be achieved based on detailed simulations of the ILD and SiD detector concept designs. In order to demonstrate the physics reach with realistic detector simulations and a full event reconstruction chain, several physics benchmark processes were identified and studied in detail. These studies, summarised below and described in detail in the ILD *[4-4]* and SiD *[4-5]* LOI documents, were rigourously reviewed by the International Detector Advisory Group. As a result of this process, it was demonstrated that the full physics potential of the ILC could be realised with realistic and technically feasible detector designs operating in the ILC beam conditions. It should be noted, however, that the prime motivation for the study of the benchmark modes is to demonstrate the capabilities of detectors; they are not intended as a list of physics highlights of ILC.

The physics benchmark channels were studied for both the ILD and SiD detector concepts with both concepts leading to broadly similar physics sensitivities. The highlights of these studies are described below. For reasons of space, for each physics benchmark process, only the studies from one of ILD or SiD is shown. In all cases, all Standard Model (SM) backgrounds were simulated and included in the analysis.

4.2.1 Higgs production and mass measurement

The precise determination of the properties of the Higgs boson (H) is one of the main goals of the ILC regardless of its nature, whether it fits in the SM or is described by some other model. Of particular importance are the Higgs boson mass, m_H, and its branching ratios. Electroweak data and direct limits from searches at LEP and at the Tevatron favour a relatively low value for m_H. Hence the ILC benchmark studies assumed m_H = 120 GeV. To assess the physics reach a data sample of 250 inverse femtobarns (fb^{-1}) recorded at a centre-of-mass energy of E_{CM} = 250 GeV was assumed. In this case, the dominant Higgs production process is that of Higgsstrahlung, $e^+e^- \rightarrow HZ$. A particularly clean signature is obtained for the case where $Z \rightarrow \mu^+\mu^-$ and $Z \rightarrow e^+e^-$. Here the distribution of the invariant mass recoiling against the reconstructed Z provides a precise measurement of m_H, independent of the Higgs decay mode. In particular, the $\mu^+\mu^-X$ final state provides a particularly precise measurement as the e^+e^-X channel suffers from larger experimental uncertainties due to bremsstrahlung. It should be noted that it is the capability to precisely reconstruct the recoil mass distribution from $Z \rightarrow \mu^+\mu^-$ that defines the momentum resolution requirement for an ILC detector.

The ILD analysis is outlined below. The first stage in the event selection is the identification of leptonically decaying Z bosons. Candidate lepton tracks with transverse momentum (p_T) greater than 15 GeV, are identified. Candidate leptonic Z decays are then selected from oppositely charged pairs of identified leptons using a mass window around m_Z. Background from $e^+e^- \rightarrow$ leptons is rejected using cuts on transverse momentum of the di-lepton system and the acoplanarity of the two tracks. Additional cuts are used to reject background from lepton pair production with initial and final state radiation. Backgrounds from $e^+e^- \rightarrow ZZ$ and $e^+e^- \rightarrow WW$ are suppressed using a multivariate likelihood based on the acoplanarity, the polar angle, the transverse momentum and the invariant mass of the di-lepton system.

The reconstructed recoil mass distributions, calculated assuming the ZH is produced with four-momentum (E_{CM}, 0, 0, 0), are shown in *Figure 4.3*. In the e^+e^-X-channel final state radiation and Bremsstrahlung photons are identified and used in the calculation of the $e^+e^-(ng)$ recoil mass. Fits to signal and background components are used to extract m_H. Based on this model-independent analysis of Higgs production in the ILD detector, it is shown that m_H can be determined with a statistical precision of 40 megaelectronvolts (MeV) (80 MeV) from the m^+m^-X (e^+e^-X) channel. When the two channels are combined, an uncertainty of 32 MeV is obtained. The corresponding model-independent uncertainty on the Higgs production cross-section is 2.6%. Similar results were obtained from SiD. It should be emphasised that these measurements only used the information from the leptonic decay products of the Z and are independent of the Higgs decay mode. As such this analysis technique could be applied even if the Higgs decayed invisibly.

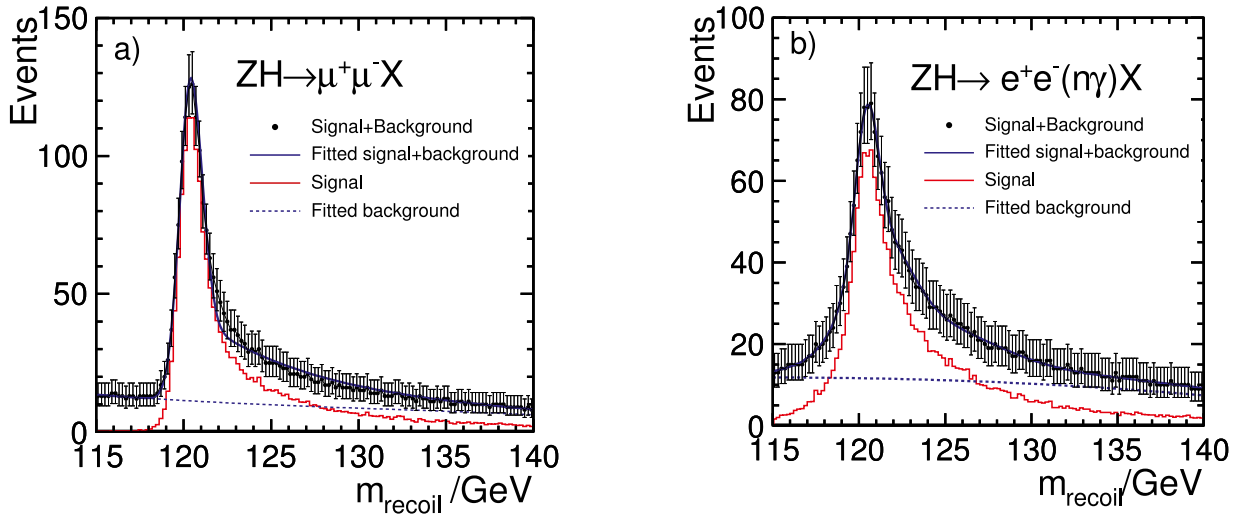

Figure 4.3 Results of the model-independent analysis of the Higgsstrahlung process $e^+e^- \rightarrow HZ$ in which $Z \rightarrow \mu^+\mu^-$ (left) and b $Z \rightarrow e^+e^-$(ng) (right). The results are shown for $P(e^+, e^-)$ = (+30 %, -80 %) beam polarisation. Images: Mark Thomson

It is worth noting that for the m^+m^-X channel the width of the recoil mass peak is dominated by the beam energy spread. In the above study Gaussian beam energy spreads of 0.28% and 0.18% are assumed for the incoming electron and positron beams respectively. For ILD the detector response leads to the broadening of the recoil mass peak from 560 MeV to 650 MeV. The contribution from momentum resolution is therefore estimated to be 330 MeV. Although the effect of the detector resolution is not negligible, the dominant contribution to the observed width arises from the incoming beam energy spread rather than the detector response. This is no coincidence; the measurement of m_H from the $\mu^+\mu^-X$ recoil mass distribution determines the momentum resolution requirement for a detector at the ILC.

4.2.2 Higgs branching fractions

A precise measurement of the absolute branching ratios of the Higgs bosons is an important test of the Higgs boson hypothesis and provides a window into effects beyond the SM. With an SM branching ratio of 3%, the decay of a 120-GeV Higgs boson into a pair of charm quarks challenges the flavour tagging and calorimeter capabilities of an ILC detector.

At E_{CM} = 250 GeV, a 120-GeV Higgs boson is produced primarily through $e^+e^- \rightarrow ZH$, where the largest branching fraction (BF) Z boson decay modes are $Z \rightarrow \nu\nu$ and $Z \rightarrow qq$, q = u,d,s,c,b. The main signal event topology therefore consists of either two or four jets, with at least two of the jets originating from charm quarks. The primary background arises from $e^+e^- \rightarrow qq$, $e^+e^- \rightarrow ZZ$ and $e^+e^- \rightarrow WW$ events. In addition, the $H \rightarrow cc$ decays have to be separated from $H \rightarrow bb$ decays (SM BF = 68%) or $H \rightarrow gg$ (SM BF = 5%). The SiD analysis, based on an assumed integrated luminosity of 250 fb^{-1} with initial state polarisations of +80% for the electron beam and -30% for the positron beam, is presented here. ILD obtained similar results. Events are first classified into the candidate decay topology. Events with reconstructed charged leptons of energy greater than 15 GeV are rejected. If the visible energy lies between 90 and 160 GeV the event is classified as a candidate $H\nu\nu$; events with visible energy above 170 GeV are classified a candidate Hqq. The candidate $H\nu\nu$ (Hqq) are forced into two (four) jet topologies using the Durham algorithm. Cuts are then applied to reduce the main non-Higgs SM backgrounds. The cut variables include the H candidate di-jet invariant mass, the number of charged tracks in a jet, the event thrust, the angle of the thrust axis with respect to the beamline, the angle between the two jets from the Z candidate and the maximum energy of any isolated photon.

Finally, for the surviving events in each of the final state topologies, two neural net (NN) variables are calculated. The first, to reject non-Higgs background, is trained using all Higgs decays as signal and all SM processes as background ($NN_{SM\text{-}Higgs}$). The second, which identifies $H \rightarrow cc$ decays, is trained using $H \rightarrow cc$ as signal and all other Higgs decays as background ($NN_{Higgs\text{-}signal}$). The input variables to the neural nets include all cut variables as well as three different charm flavour-tag variables. *Figure 4.4* shows, for the four-jet analysis, the distributions for one of the three flavour tag variables and the neural net variable $NN_{Higgs\text{-}signal}$. For 250 fb^{-1} a total 1292 (1930) events survive the final cuts of $NN_{SM\text{-}Higgs\,1} > 0.2$ and $NN_{Higgs\text{-}signal} > 0.3$ in

the two- (four-) jet selections. The purity of the final sample is about 40% with the background being roughly equally divided between Higgsstrahlung process with H → bb and other SM processes. The H → cc branching fraction is obtained by dividing the measured signal cross-section by the total. For the analysis described above, the simulated H → cc branching fraction is determined to be 3.3 ± 0.4% and 3.3 ± 0.2% for the Z → νν and Z → qq respectively.

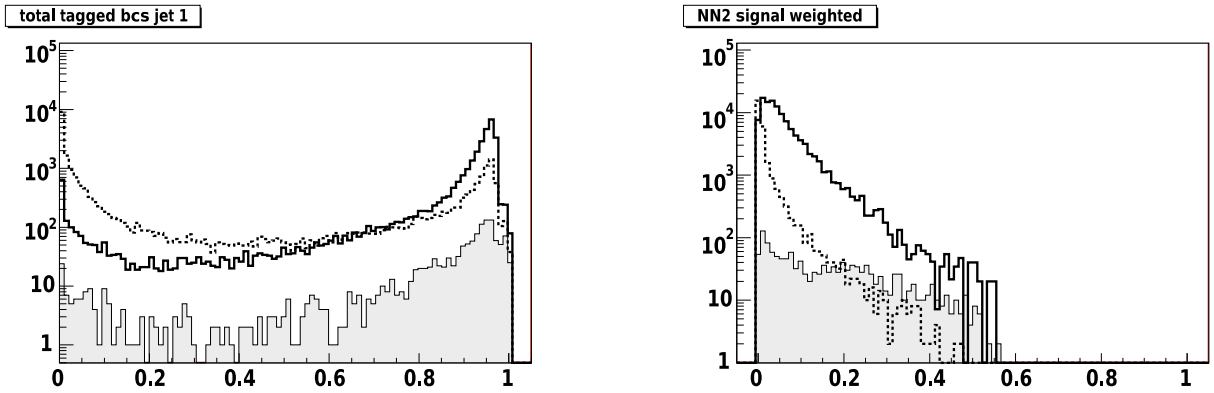

Figure 4.4 Distributions of flavour tag variable 'charm with only b-quark background' (left) and $NN_{Higgs\text{-}signal}$ (right) for hadronic mode events. The solid curves are the Standard Model background, dashed are background Higgsstrahlung events, and filled histograms are ZH → qqcc. Images: Mark Thomson

4.2.3 Top mass measurement from direct reconstruction

Top physics will form an important part of the scientific programme at the ILC. In particular, the top mass, m_t, and top width, Γ_t, can be determined with high precision. The measurement of m_t and Γ_t from the direct reconstruction of $e^+e^- \rightarrow t\bar{t}$ events was studied for the detector LOIs. Similar results were obtained by ILD and SiD. The results with the full ILD detector simulation and event reconstruction are shown here. Two main decay topologies were considered by ILD: fully hadronic, $t\bar{t} \rightarrow (bqq)(bqq)$ and semi-leptonic, $t\bar{t} \rightarrow (bqq)(bln)$, decay topologies. Results were obtained for an integrated luminosity of 500 fb^{-1} at E_{CM} = 500 GeV.

The analysis depends on excellent jet energy resolution and high-performance flavour tagging. In the ILD study, events with an isolated lepton are considered to be candidates for the semi-leptonic analysis; otherwise they are assumed to be candidates for the fully hadronic analysis branch. In the fully hadronic branch, the event is reconstructed as six jets that are combined to form W bosons and, when combined with a b quark jet, top quarks. The two b-jets originating directly from the top quark decays are identified using the flavour-tagging information. The four remaining jets are considered as the decay products of the two Ws. The combination of the four jets into two di-jets that gives the smallest value of $|m_{ij}-m_W|+|m_{kl}-m_W|$ is chosen to form the two Ws (where m_{ij} and m_{kl} are the di-jet masses for a given jet pairing). Out of two possible combinations to pair the W bosons with the b-jets, the one that yields the smallest mass difference is chosen.

The first step in the semi-leptonic branch is to remove the identified lepton and to force the remainder of the event into four jets. The two b-jets are identified using flavour-tagging information. The two remaining jets are assigned to the hadronically decaying W. The identified lepton and the neutrino are assigned to the leptonically decaying W boson, with the three-momentum of the neutrino defined as the missing momentum. The chosen pairing of the W bosons with the b-jets is that which yields the smallest reconstructed top mass difference. For each analysis branch, background events are rejected using a multi-variate likelihood technique. Finally, a kinematic fit is applied in order to improve the final top mass resolution. The reconstructed mass distributions in the two event topologies are shown in *Figure 4.5*.

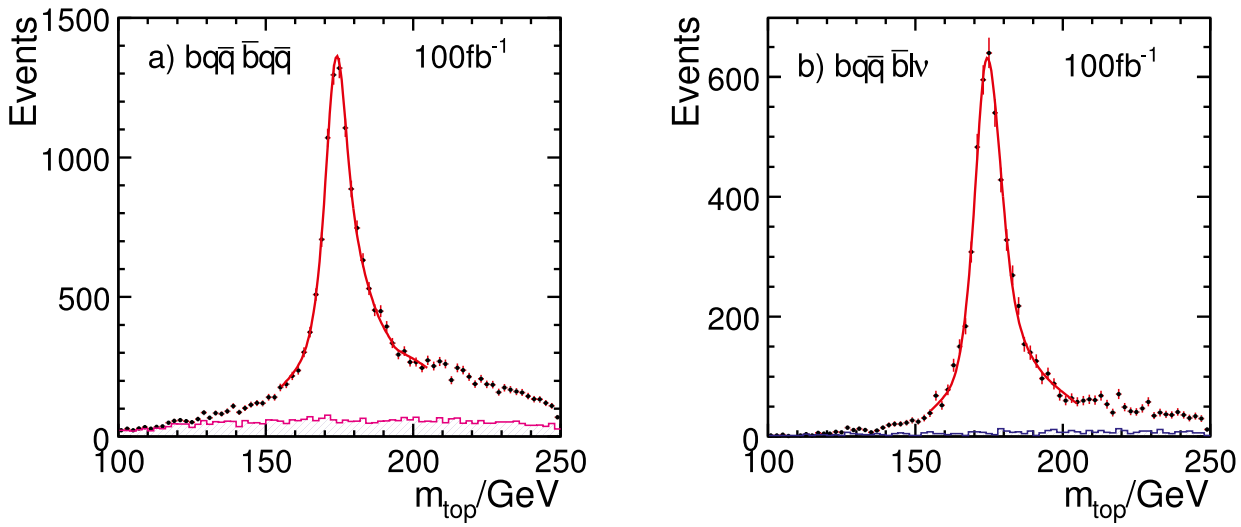

Figure 4.5 Reconstructed top mass distributions in fully hadronic and semi-leptonic events as simulated and reconstructed in the ILD detector concept. Images: Mark Thomson

For an integrated luminosity of 500 fb^{-1} it was shown that the cross-section (s) of $e^+e^- \rightarrow tt$ can be determined with a statistical uncertainty of 0.4% using the fully hadronic decays only. The invariant mass spectra are fitted with the convolution of a Breit-Wigner function and an asymmetric double Gaussian, the latter representing the detector resolution. The combinatoric background and the background from other processes are described by a 2nd-order polynomial. For an integrated luminosity of 500 fb^{-1} leads to uncertainties of 30 MeV on m_t and 22 MeV on Γ_t. Both ILD and SiD also studied the prospect to measure the top quark forward-backward asymmetry; a precision of about 2% was demonstrated.

4.2.4 Tau decay identification and tau polarisation in $e^+e^- \rightarrow \tau^+\tau^-$

The analysis of full energy tau leptons at E_{CM} = 500 GeV would be an important part of the physics programme at the ILC if, for example, a Z' is discovered at the LHC. Through interference with the Z/g* amplitudes, the couplings of the Z' to left- and right-handed tau leptons can be determined by measuring the tau angular distribution and polarisation. As a detector benchmark the identification of 250-GeV tau leptons and their decay modes pushes the tracker and calorimeter capabilities of the detector. Tightly collimated low-multiplicity jets must be reconstructed in terms of the underlying charged hadron and π^0 constituents. It provides a challenging test for particle flow reconstruction.

The SiD event selection for full energy tau pair events requires 2 and 6 charged tracks and that the visible energy be in the range of 100 to 450 GeV. Jet clustering is applied to the reconstructed particles and exactly two jets, each with $|\cos\theta| < 0.95$ where θ is the polar angle with respect to the beam axis, are required. The opening angle between the two jets must be more than 178^o. Events with two muons or two electrons are rejected. This procedure selects 72% of tau pair events where the energy of each tau is at least 240 GeV. The SM background is 2.4% of the selected event sample. For 250 fb^{-1}, the tau polarisation can be measured with a statistical precision of 0.28%. The forward-backward asymmetry, A_{FB}, is measured by fitting the t^- angular distribution, with the result A_{FB}=0.5038 ± 0.0021 for 250 fb^{-1} (assuming 80% left-handed electron polarisation and 30% right-handed positron polarisation).

The SiD particle flow algorithm was modified to identify tau decay modes. All calorimeter hits were clustered and assigned to the nearest tau jet. Photon identification was performed. All remaining clusters were assigned to tracks. The total calorimeter energy assigned to the track was required to be consistent with the track momentum. Neutral pions were formed from pairs of photons satisfying 60 MeV < m_{gg} < 180 MeV. The purity and efficiency of the tau decay mode identification is summarised in *Table 4.1*.

Table 4.1 Tau decay mode purity and efficiency

Decay mode	Correct ID	Wrong ID	ID eff	ID purity	SM bgnd
$e\nu\nu$	39602	920	0.991	0.977	1703
$\mu\nu\nu$	39561	439	0.993	0.989	1436
$\pi\nu$	28876	2612	0.993	0.917	516
$\rho\nu$	55931	8094	0.790	0.874	1054
$a_1\nu$, $a_1 \rightarrow \pi^+\pi^0\pi^0$	18259	11140	0.732	0.621	847
$a_1\nu$, $a_1 \rightarrow \pi^+\pi^-\pi^-$	21579	2275	0.914	0.905	141

The optimal observable technique is used to measure the mean tau polarisation, P_t, using the $e\nu\nu$, $\mu\nu\nu$, $\pi\nu$, and $\rho\nu$ decay modes giving P_t = -0.611 ± 0.009, where the error is purely statistical. Similar decay mode identification efficiencies and measurement statistical precisions were obtained by the ILD concept group.

4.2.5 SUSY gaugino mass reconstruction

The above benchmark processes represent precision tests of the Standard Model including the Higgs sector. In addition, the ILC has sensitivity to many Beyond the Standard Model processes. One much discussed extension to SM is supersymmetry (SUSY). As part of the physics benchmark studies, both ILD and SID investigated the SUSY 'point 5' scenario with non-universal soft SUSY-breaking contributions to the Higgs masses. In this model the lowest mass chargino, $\chi_1^{\pm}$, and the second lightest neutralino, χ_2^0, are not only nearly mass degenerate, but decay predominantly into $W^{\pm}\chi_1^0$ and $Z\chi_1^0$, respectively. For this SUSY benchmark point, the gaugino masses are: $m(\chi_1^0)$ = 115.7 GeV, $m(\chi_1^{\pm})$ = 216.5 GeV, $m(\chi_2^0)$ = 216.7 GeV, and $m(\chi_3^0)$ = 380 GeV. The SUSY point-5 scenario was chosen solely because it provides a suitable benchmark test of the di-jet mass reconstruction capability of a detector at the ILC. From an experimental point of view the reconstruction of the gaugino masses is particularly challenging as both $e^+e^- \rightarrow \chi_1^+\chi_1^- \rightarrow W^+W^-\chi_1^0\chi_1^0 \rightarrow qqqq\chi_1^0\chi_1^0$ and $e^+e^- \rightarrow \chi_2^0\chi_2^0 \rightarrow ZZ\chi_1^0\chi_1^0 \rightarrow qqqq\chi_1^0\chi_1^0$ result in final states consisting of four jets and missing energy. Distinguishing between these two processes requires the ability to accurately reconstruct the di-jet invariant mass distribution from the decays of W and Z bosons. This capability drives the jet energy requirement for the ILC detectors.

The event selection starts by forcing events into four jets. A cut-based pre-selection retains events consistent with a four-jet plus missing energy topology. All three possible di-jet associations to two bosons are considered. A kinematic fit that constrains the two boson masses to be equal is applied; in terms of mass resolution this is essentially equivalent to taking the average mass of the two di-jet systems. After a number of cuts used to reject the majority of the SM background, ILD obtained the mass distribution shown in *Figure 4.6*, left. The contributions from WW and ZZ final states are clearly distinguishable. By cutting the invariant mass, samples of $e^+e^- \rightarrow \chi_1^+\chi_1^- \rightarrow W^+W^-\chi_1^0\chi_1^0$ and $e^+e^- \rightarrow \chi_2^0\chi_2^0 \rightarrow ZZ\chi_1^0\chi_1^0$ can be isolated. The gaugino masses are then reconstructed from the endpoints of the energy reconstructed energy spectra of the reconstructed W and Z, as shown in *Figure 4.6*, right. For the analysis of simulated events in the ILD detector, statistical precisions of 2.4 GeV, 0.9 GeV, and 0.8 GeV are obtained for the masses of the $\chi_1^{\pm}$, χ_2^0 and χ_1^0 respectively.

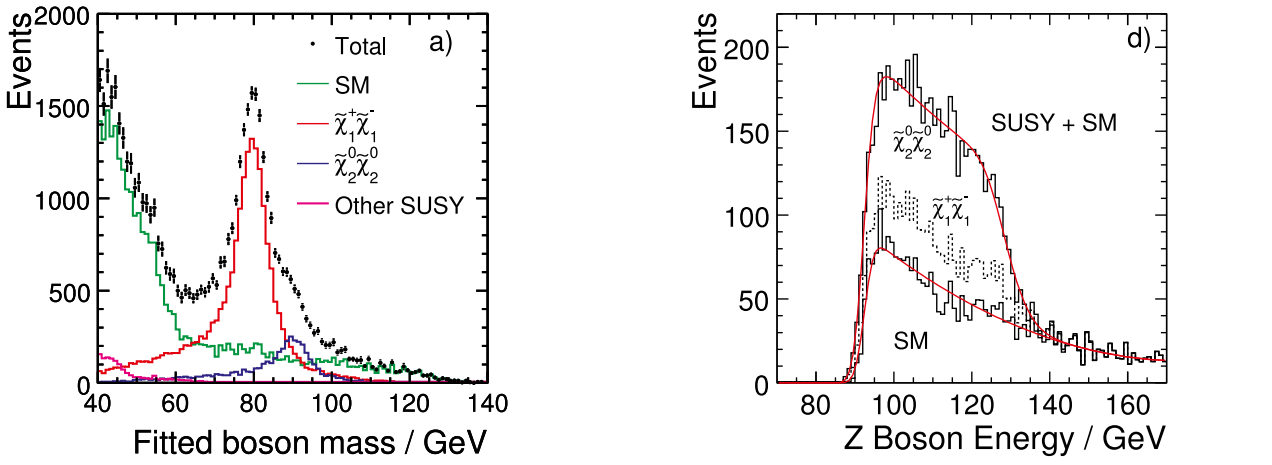

Figure 4.6 Left: distribution of reconstructed di-jet invariant masses from gauge boson decays in chargino and neutralino production. Right: reconstructed energy of select Z bosons and a fit to determine the χ_2^0 and χ_1^0 masses. Images: Mark Thomson

4.2.6 Squark production

In addition to the ILC benchmark channels both SiD and ILD studied a number of other physics processes. One such example is the study of squark production. Measurements of the neutralino relic density point to a small mass difference between the next-to-lightest SUSY particle (NLSP) and the lightest neutralino, assuming that the lightest neutralino makes up most of the dark matter in the universe. Motivated by this, SiD studied the case that the b squark was the NLSP and considered four different b squark and neutralino mass points of ($m_{bsquark,}$ $m_{neutralino}$) = (230,210); (240,210); (230,220); (240,220) GeV. The b squark mass determines the b squark pair production cross-section of 1.3 fb, 0.4 fb for b squark masses of 230 GeV and 240 GeV, respectively, at E_{CM} = 500 GeV. The mass difference between the b squark and neutralino determines the energy of the b-jets, which, for the model parameters considered here, are less than 30 GeV. At these b-jet energies the b-tagging efficiency is relatively low (10-30%).

The analysis proceeds by applying the Durham k_T jet algorithm with k_T^{min} = 10 GeV to the reconstructed particles. Events are required to have exactly two jets. The SM background is suppressed by requiring that the total visible energy be less than 80 GeV and by applying cuts on the event acoplanarity, jet polar angles and the number of reconstructed particles. In addition an event is rejected if a photon or electron with an energy greater than 300 MeV is detected in the SiD luminosity calorimeter. Following the selection cuts, a neural net algorithm is applied using the above cut variables as well as the total number of charged particles and a b-jet flavour tag variable. *Figure 4.7* shows the NN output for signal and background. Also shown is the statistical significance of the signal, $S/(S+B)^{1/2}$, for the mass point ($m_{bsquark,}$ $m_{neutralino}$) = (230,210) GeV as a function of the number of signal events passing the final NN cut as the NN cut is varied. A luminosity of 1,000 fb^{-1} is assumed. The other mass points ($m_{bsquark,}$ $m_{neutralino}$) = (240,210); (230,220); (240,220) GeV can all be excluded at the 95% confidence level.

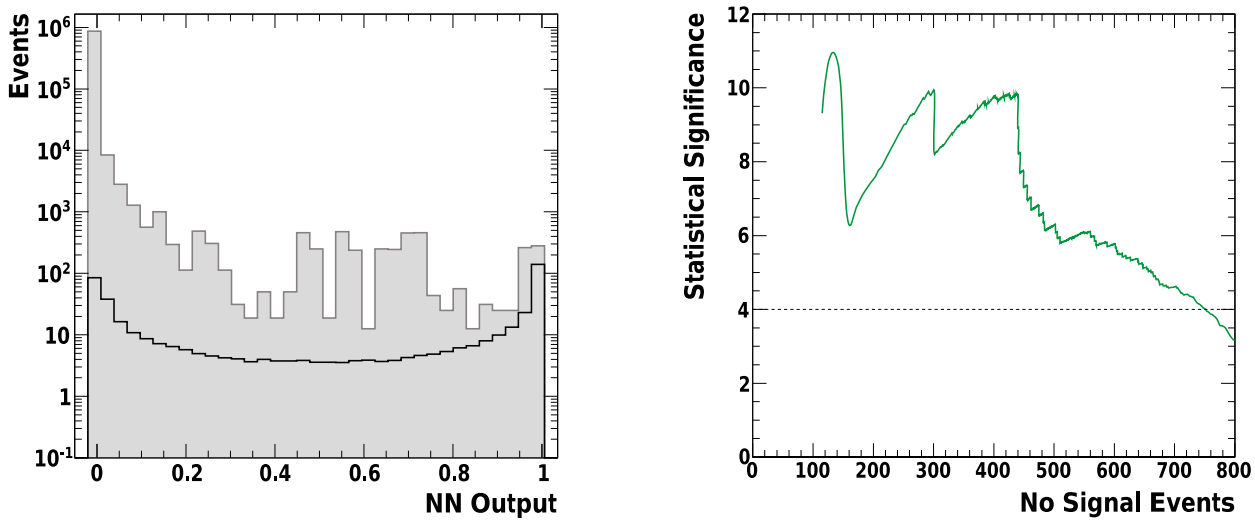

Figure 4.7 Left: final neural net output for the b squark mass of 230 GeV and lightest neutralino mass of 210 GeV (black) and SM background (filled histogram). Right: statistical significance versus the number of signal events passing the final NN cut as the NN cut is varied. Large variations are due to SM events with large weights. Images: SiD

4.2.7 Strong electroweak symmetry breaking

If strong electroweak symmetry breaking is realised in nature, the study of the WW scattering processes is particularly important. At the ILC the WW → WW and WW → ZZ vertices can be probed via the processes $e^+e^- \rightarrow qqq\nu\nu$ where the final state quarks arise from the decays of two W bosons or two Z bosons. Separating the two processes through the reconstruction of 4 jets requires an excellent di-jet mass reconstruction and thus provides a test of the jet energy resolution of an ILC detector. While not an official benchmark channel, this process was studied in detailed by the ILD concept group at E_{CM} = 1 TeV.

The analysis is relatively straightforward. Cuts are applied to remove the majority of the SM background, then events are forced into four jets and of the three possible jet-pairings, the one that minimises the product of $|m_{ij}-m_{W/Z}|$ and $|m_{kl}-m_{W/Z}|$ is chosen. The two processes WW → WW and WW → ZZ are separated using the reconstructed invariant mass distributions shown in *Figure 4.8*. The contributions from the WW$\nu\nu$ and ZZ$\nu\nu$ final states are clearly resolved as a result of the excellent jet energy resolution of the ILD detector. Fits to the anomalous quartic (4^{th}-order) gauge boson couplings (a_4 and a_5) were obtained from a binned maximum likelihood fit to the two-dimensional distribution of the boson polar angle in the reference frame of boson pair and the jet polar angle in the reference frame of each boson, giving a 90% confidence level sensitivity of $-1.38 < a_4 < +1.10$ and $-0.92 < a_5 < +0.77$.

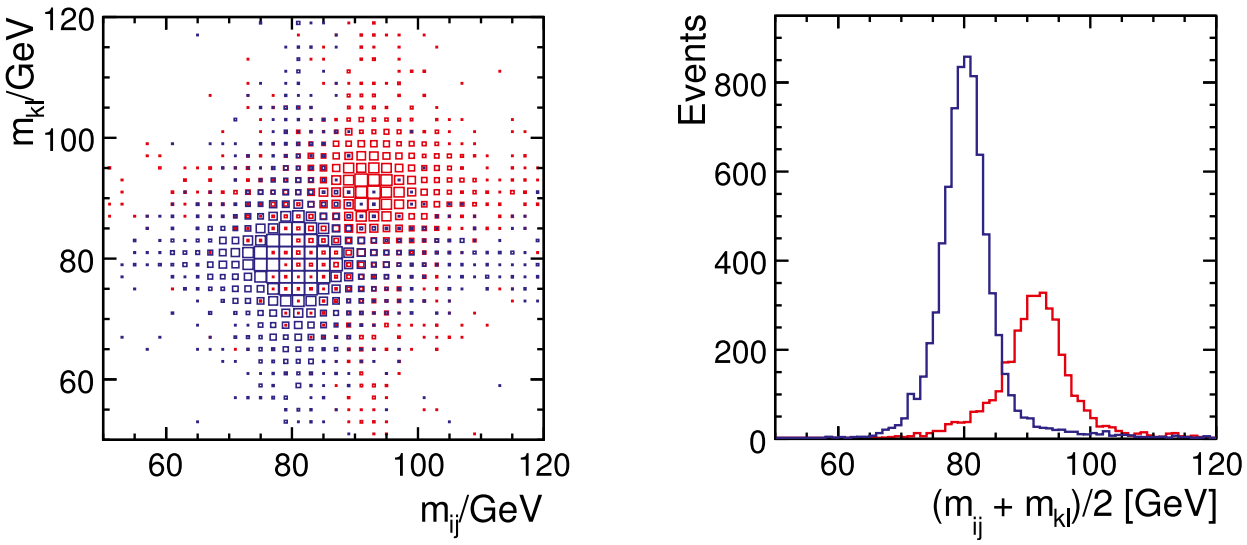

Figure 4.8 Left: the two di-jet masses. Right: the mean di-jet mass in $e^+e^- \to qqqqvv$ simulated events reconstructed in the ILD detector. Images: Mark Thomson

Towards the detailed baseline designs

As shown above, both the ILD and SiD detector concepts meet the basic requirements to carry out the ILC physics programme expected at energies up to 500 GeV. It should be emphasised that this has been demonstrated with full simulations and with full Standard Model backgrounds. Some 50 million events were generated at 250 GeV and 500 GeV, which amounted to more than 50 terabytes of simulated data for each for the two detector concepts. This is an unprecedented achievement for detector optimisation studies in the 0th stage.

The two LOI detector concept groups are now trying to further the level of realism in their detector simulations by implementing details of the detector system including various detector services such as power lines, cooling lines, and support structures, which had been represented only as a bulk of dead material with a density averaged over a relatively wide region. They are also planning to overlay beam-induced backgrounds in a more realistic way. These improvements will not only enhance the precision of the detector simulations, which is already very good, but also help establish the validity of the detector concepts at higher energies, say at 1 TeV.

It is very difficult to predict the physics scenarios at 1 TeV, since the terascale physics will take more concrete shape only after the discoveries at the LHC. Nevertheless, we need to prepare ourselves for the machine upgrade to 1 TeV by considering typical situations where the different aspects of the detector performance will have to be tested. For this purpose a new set of benchmark processes, primarily meant for the detector validation at 1 TeV, is being decided. The new set will include complicated final states such as those from $e^+e^- \to ttH$, eight jets or six jets plus an isolated lepton, as well as final states populating more in the forward-backward regions such as from $e^+e^- \to \nu\nu H$ and $e^+e^- \to WW$. There will be also some 500-GeV processes for the comparisons with the LOI studies. The results from these simulation studies will comprise the main body of the analysis section of the DBD document.

4.3.1 Standard Model physics

Higgs self-coupling

Most aspects of the SM Higgs physics are part of the benchmarks. However, one important and very challenging aspect is the Higgs self-coupling. The observation and measurement of coupling can be seen as the ultimate test of whether an observed Higgs particle is the SM Higgs or something different. It is potentially measurable from the final state ZHH. However, the results of the LOI studies were inconclusive. The expected cross-section is very low, and the background from $t\bar{t}$ is large. The aim of the current studies is to bring together expertise from all needed topics (jet-finding, flavour-tagging, kinematic fitting, theory) into a ZHH task-force and thereby be in the position to have definite answer on the feasibility of such a measurement by the DBD.

Top physics

Another SM topic only partly covered by the benchmarks is top physics. Here ongoing studies will address couplings, mass and forward-backward asymmetries. The last was addressed as a benchmark for the LOI. The LOI benchmark analysis was more aimed at detector performance studies, and thus it concentrated on fully hadronic decays to see if a detector can handle highly complicated events. A more sensitive mode is when one top decays semi-leptonically. In this mode, there is no ambiguity in separating top from anti-top, and a study on it with full simulation has been initiated.
Furthermore, recent theoretical advances shows that there is a very important quantum chromodynamic enhancement of the top pair cross-section near threshold. The implications of this effect are now under study, including the development of an event-generator that takes this effect into account. It is quite probable that the result of such a study will be to indicate a different running scenario than what was previously assumed to be optimal. For example, it seems probable that the study of the top-Higgs coupling can very well be done at E_{CM} = 500 GeV, contrary to what is assumed for the benchmark study of the channel (to be done at 1 TeV). With one inverse attobarn (ab^{-1}) of integrated luminosity at 500 GeV, a significant signal of the top-Yukawa coupling could be attained.

Gauge bosons

While WW production at 1 TeV is a benchmark study, the ZZ, Weν and Zee channels are being studied at 1 TeV. In addition, the LOI studies on the ILC capabilities to measure deviations from the SM predictions for triple-gauge couplings are being continued, in particular the impact of the modified beam parameters.

4.3 Ongoing physics analyses beyond benchmark reactions

4.3.2 New physics

Supersymmetry

Supersymmetry (SUSY) may provide a rich spectrum of kinematically accessible new particles at the ILC. It might also yield new sources of violation of conservation laws, for example, charge parity violation or flavour violation. New particles might be short- or long-lived, depending on the SUSY breaking mechanism and whether R-parity is conserved or not. Hence, various SUSY scenarios are under study.

The signals for SUSY consist of a complex mixture of dominant and subdominant processes, often with identical visible final states. An extended study of the popular SPS1a' is planned. In SPS1a', which is an mSUGRA-type model, all sleptons, neutralinos up to χ_3 and the lighter chargino can be produced at a 500-GeV ILC. For the LOI, certain channels were studied (smuons and staus), but no evaluation of the complete exploration was done. In particular, the combined precision on the lightest supersymmetric particle (LSP) mass from all channels is quite important to estimate, as it tends to enter into many other measurements.

A study of the possibly existing long-lived, heavy, charged particles, in particular the long-lived staus, is also ongoing. These types of models are particularly interesting because they are of the type that the LHC quite likely would be able to observe at an early stage.

Another class of SUSY models under study is bi-linear R-parity-violating SUSY. In such models, the neutral fermions (neutrinos) mix with the neutral bosinos (neutralinos), yielding a relation between neutrino masses and SUSY, and LSP decays to Standard Model particles. The LSP lifetime is long, so the decay vertex is expected to be well separated from production vertex.

Another search, extended beyond the LOI study, is a model-independent weakly interacting massive particle (WIMP) search in $e^+e^- \rightarrow n\gamma$ + invisible. WIMPs are possible candidates for dark matter. The SUSY LSP is a WIMP, but many other new physics models also predict the existence of such objects. Different models predict different spins of the WIMPs, different Lorentz structures and different decay modes. If they can pair annihilate into e^+e^-, then the reverse process can be detected at the International Linear Collider. In this case the two neutral (undetected) WIMPs are accompanied by an initial state radiation (ISR) from the incoming electron or positron, giving a photon recoil mass distribution that has a characteristic onset. The location of the onset and shape of the recoil mass distribution depends on the WIMP mass and spin. Experimentally, the WIMP signal has to be resolved from the large irreducible ISR background from $e^+e^- \rightarrow \nu\nu+n\gamma$ events. Assuming that the total cross-section for WIMP pair annihilation into SM fermion pairs is known from cosmological observations, the ILC sensitivity can be expressed in terms of the WIMP pair branching fraction into e^+e^-. It is found that the WIMP can be detected over a wide range of theory assumptions.

Other new physics: little Higgs and extra dimensions

Several non-SUSY models of new physics are also under study:

1. The little Higgs model shares several features with SUSY: It predicts a number of new states, some of which might be directly observable at a 500-GeV linear collider. If the model predicts that T-parity is conserved – some little Higgs models do, some don't – the lightest of these new T-odd states is stable and is a WIMP-type dark matter candidate. However, the quantum numbers of the new states are different from the SUSY case: In the simplest little Higgs model, the new states occur when extending the SM SU(2) doublets to SU(3) triplets so that the new states are left-handed quarks and leptons. One also obtains new heavy gauge bosons, and typically the heavy photon A_H is the WIMP. Ongoing studies of a scenario with a little Higgs model with T-parity have analysed heavy photon and SM particles, so a simultaneous fit of the masses of W_H , Z_H and A_H gives the vacuum expectation value <f>, which in turn implies that the ILC can determine the relic abundance to a level comparable to what the Planck mission will be able to do from the observation of the cosmic microwave background.
2. Models with extra dimensions are also being studied. In particular, the possibility of the existence of a 100-GeV-scale right-handed neutrino (N) has been considered. In the SM, the lightness of the neutrino can be understood by the seesaw mechanism, but then the N must be ultra-heavy. However, in compact extra-dimensional models, this is not so: An N would not need to be heavier than 100 GeV to explain the lightness of the ordinary neutrino. In addition, an infinite number of such states is expected as Kaluza-Klein (KK) excitations. At the ILC, the N could be produced together with an SM neutrino. In the decay process, the N is expected to have interacted with the Higgs field – transforming it to a virtual ν, which then decays to a W or a Z and an ordinary lepton. Due to neutrino mixing (the Pontecorvo-Maki-Nakagawa-Sakata mixing matrix), the ordinary lepton does not need to have the same flavour as the neutrino initially produced together with the N. If the N decays via a W*, all decay products will be observable and it can be fully reconstructed. A case where the masses of the first three KK modes are 150, 450 and 750 GeV, respectively, has been studied at E_{CM} = 500 and 1000 GeV. The cross-sections depend on the model of neutrino mixing, but the first KK mode would be observable in any case, while all three would be so at 1 TeV. In addition, by studying the number of events with different final state leptons, it would be possible to separate different models.

References

[4-1] T. Behnke et al., TESLA Technical Design Report, DESY 2001-011, ECFA 2001-209, March 2001.

[4-2] ILC project, International Linear Collider Reference Design Report, 2007, ILC-REPORT-2007-001.

[4-3] LHC/LC study group, G. Weiglein et al., Phys. Rept. 426, 47 (2006).

[4-4] The International Large Detector, Letter of Intent, March 2009, DESY 2009-87, KEK 2009-6.

[4-5] SiD Letter of Intent, March 2009, https://silicondetector.org/display/SiD/LOI.

05

COMMON TASK GROUPS

5.1 The Machine-Detector Interface Common Task Group

The Machine-Detector Interface (MDI) Common Task Group (CTG) has been established to deal with all topics that are common to the machine and the detector design. Strong interdependencies exist at a linear collider between both push-pull detectors and between the detectors and the machine itself. Therefore the MDI CTG is a forum of information exchange for the SiD (Silicon Detector) and the ILD (International Large Detector) as well as for the respective groups of the ILC machine design team. The task group currently comprises six members, three from ILD and three from SiD, and usually meets together with the technical area leaders of the ILC beam delivery system[4] to enable a well functioning communication on common work and related information between all three parties.

The paramount challenge in the design of the interaction region of the ILC is the development of an engineering design for a realistic push-pull system. The idea of using one common beam line with two interchangeable detectors has never been realised at a major particle collider so far, so it is new territory for all involved experts.

[4] Current members: K. Buesser (convener, DESY, ILD), P. Burrows (deputy convener, Oxford, SiD), Alain Hervé (University of Wisconsin, ILD), T. Markiewicz (SLAC, SiD), M. Oriunno (SLAC, SiD), T. Tauchi (KEK, ILD); regular guest: A. Seryi (Oxford, GDE-BDS)

5.1.1 Design process

Figure 5.1 displays the flow diagram of the path towards an engineering design of the interaction region. The starting point is a set of functional requirements that define the ground rules for a friendly coexistence of two detectors and the machine in the push-pull scenario. These ground rules have been worked out in the discussions of the MDI CTG together with the ILC Global Design Effort (GDE) Beam Delivery System Group (BDS) and have been published in the Interaction Region Interface Document *[5-1]*.

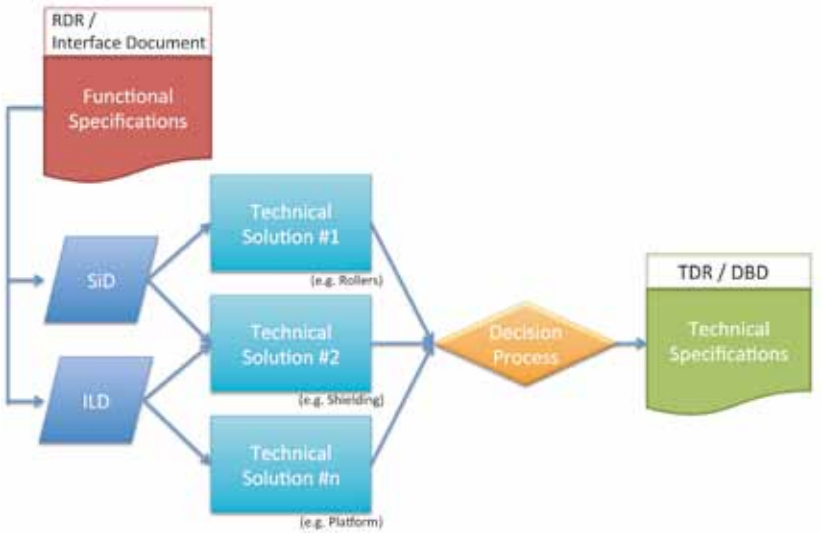

Figure 5.1 Towards an engineering design. Image: Karsten Buesser

The detector concept groups are designing technical solutions for the detector integration with the interaction region that need to fulfil these functional requirements. While some of those technical solutions might be common from the start for both detectors, for example, a common design of the shielding in the underground hall, some might be different, such as the design of the detector motion systems where SiD prefers a rollers and ILD a platform. In the end, the technical solutions need to be evolved so that a decision could be taken for the common design. The detailed engineering requirements form then the basis of the *Technical Design Report* and the detailed baseline design (DBD).

The MDI CTG started this process after the publication of the ILC *Reference Design Report* (RDR). Major milestones were the publication of the interaction region Interface Document and the Letters of Intent (LOI) of the detector concepts in 2009.

5.1.2 Interaction Region Interface Document

The Interaction Region Interface Document is a major deliverable of the MDI CTG. It was published in 2009 and has the approval of the detector concepts and also of the GDE project managers. The document lists requirements that stem from the technical and physical boundary conditions of the machine design. It includes geometrical boundaries, like the required floor space of the underground experimental hall or the height of the beam above the floor. It also covers safety and working requirements like limits on the allowed magnetic fields or about the radiation environment. Emphasis has been placed on the requirements defined by the ILC beam operations. Vacuum conditions and the requirements on the support and alignment of the final focus magnets are of paramount importance to a successful operation of the ILC.

5.1.3 Push-pull design study

The technical work on the engineering design and the technical specifications of the interaction region are the focus of the MDI group since the publication and validation of the Letters of Intent. The most important topic is the engineering design of a realistic push-pull system for both detectors. As the required engineering resources are not controlled by the MDI CTG, but exist mainly within the detector concept and machine groups, a comprehensive work plan needed to be established in close cooperation with the participating laboratories and universities. Following a request by the ILC Steering Committee, which offered help in finding additional resources, the MDI/Beam Delivery System (BDS) Group has developed a work plan for a design study on the push-pull system. An important milestone will be the choice of a common detector motion system (platform or rollers) that is envisaged for the first half of 2011.[5] *Figure 5.2* shows a possible underground hall layout with the detectors in push-pull configuration with rollers and with platforms.

[5] In March 2011, it was decided that the detector motion system will use platforms.

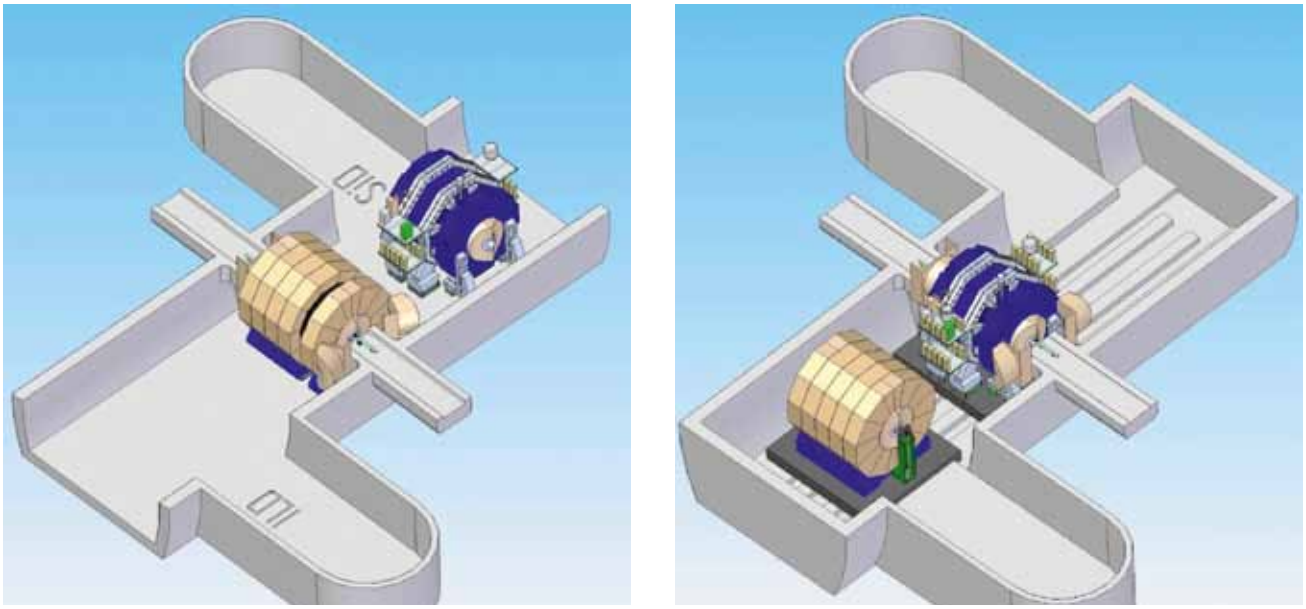

Figure 5.2 Underground hall with both detectors in push-pull configuration: roller-based system (left) and platform-based system (right). Image: Marco Oriunno

5.2 Engineering Tools Common Task Group

As the two detectors concepts, ILD and SiD, will be placed in a common experimental area and will share some services and constraints, it is necessary to ensure the compatibility of their engineering tools and that they are working with the same basis data. This is the purpose of the Engineering Tools CTG.

An additional goal of the Engineering Tools CTG is to propose and validate the use of the future ILC common tools.

The group concentrated its work on the selection of a document server specifically devoted to the repository and exchange of engineering documents in a consistent way with the International Linear Collider's existing tools. This system is to be used as a support tool for the coordination of the engineering process and will facilitate the informational workflow during of the lifecycle of the project within the constraints of an international project.

Thus the decision was to follow the recommendations of GDE and to use the ILC EDMS (electronic document management system), led by the DESY EDMS team *(Figure 5.3)*.

Figure 5.3 Foreseen system breakdown structure for the detectors EDMS

An adequate system breakdown structure describing the main components of the two detectors has been created and is to be implemented on the ILC EDMS with a common level corresponding to the design of the two detectors in the experimental hall.

This common node should contain 2-D drawings for both detectors in order to have reference dimensions and ease the studies concerning the experimental hall (cavern design, motion system, services). It will become the repository to exchange technical notes and data for detectors common studies.

5.3 The Detector R&D Common Task Group

The Detector R&D CTG was created out of a desire to work across the detector concept groups and coordinate activities between these groups and the horizontal detector R&D collaborations, such as CALICE (CAlorimetry for the LInear Collider with Electrons) and LC-TPC (A Time Projection Chamber for a future Linear Collider). It was realised that many issues in the area of detector development are common and are better addressed, not in a competitive, but in a collaborative common framework. This holds especially true for the area of detector R&D. The proposed detectors for the ILC call for highly sophisticated technologies that have not yet reached a level of maturity to prove that the concept can be employed in a large-scale experiment. Moreover, the resources dedicated to the detector R&D are scarce. The Detector R&D CTG was formed to coordinate cooperation of detector R&D among various parties and to maintain contact with detector R&D collaborations. The synergistic and mutually supportive efforts in the area of detector R&D are illustrated in *Figure 5.4*. A shared test beam infrastructure is used to independently characterize silicon detectors and a time projection tracking chamber, where each will benefit from the studies of the other.

The Detector R&D CTG is composed of representatives from the ILC collaborations, the horizontal detector R&D collaborations and dedicated detector technology groups. The group acts as a forum for all detector development that is being carried out within the ILC community, facilitating their communication. Furthermore, the group acts as a strong advocate of support for its activities and the research activities of its members. It is also a resource of the ILC management that can be called upon to carry out specific tasks, such as surveys in certain areas of R&D as well as reporting at various advisory and review panels.

The overarching goal of the Detector R&D CTG is to help the concept groups be ready by 2012 to make a realistic proposal for detectors that can execute the precision-physics programme. Collaboration readiness means that the technologies are well understood and proven to be scalable; it does not imply a fully engineered design. Because of the structure of the collaborations and their funding this group does not coordinate existing activities of the separate R&D collaborations.

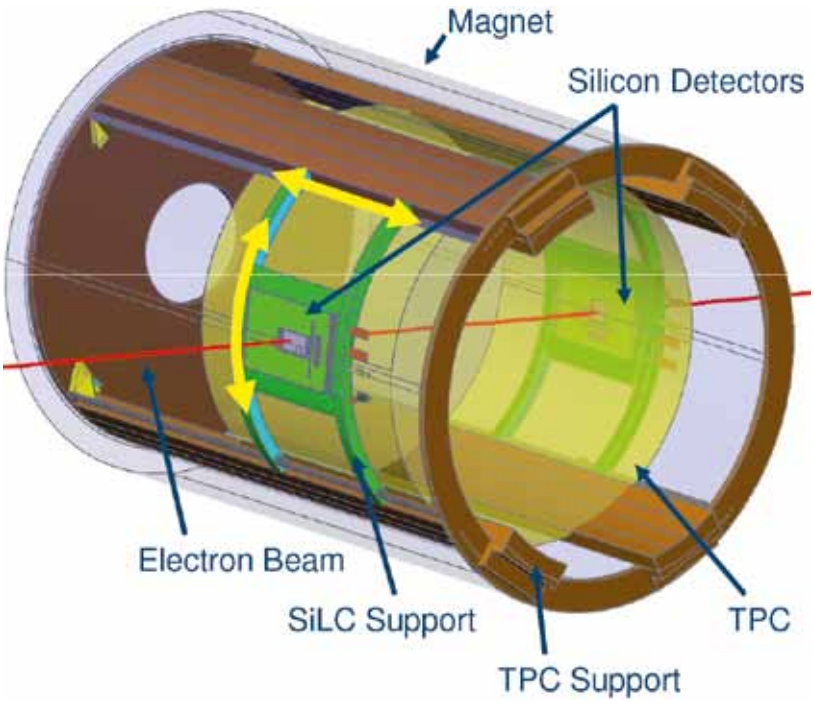

Figure 5.4 Example of a synergistic effort between different detector development efforts characterising a silicon and time projection chamber tracking system in a shared test beam infrastructure. Image: SILC Collaboration

The support for the development of new detector technologies has fluctuated significantly over the last few years. The R&D is often considered to be far enough in advance of any defined future project that the importance and need for this effort has struggled, and continues to struggle, to be formally recognised by the agencies. As a result, the funding situation has been relatively unstable and the size of the community engaged in the project has ebbed and waned with the real and perceived level of support. The detector development programme currently faces an immediate problem beyond 2012. Efforts could be severely curtailed or even stopped beyond 2012, which would be a significant loss of its decade-long investment in the development of new technologies. The Detector R&D CTG continues to strongly argue for stable strong support for its activities beyond 2012.

A sustained, stable and strategic investment in the area of detector development is critical, not only for the ILC, but for the viability of the field as a whole. Many R&D initiatives from within the ILC detector groups have already found their way into other projects, some beyond high-energy physics. For example, the DEPFET sensor technology for an ILC vertex detector is currently being deployed for the Belle-II vertex detector at KEK in Japan and is also being considered for a large-area Cherenkov telescope studying air showers. The development work for a micro-pattern-gas detector time projection chamber (TPC) has been implemented in the TPC for the T2K experiment at Japan's J-PARC, shown in *Figure 5.5*. Large-scale application of silicon photomultipliers was proven for the first time in the context of R&D for the ILD concept detector and has subsequently been chosen for the T2K detector and the upgrades of the CMS detector of LHC at CERN and the Belle kaon and muon end cap identification system. Another example is the 3-D vertically integrated silicon technology, which is being considered for the CMS upgrade experiment. The development of CMOS pixel detectors has found its way into nuclear and heavy-ion physics experiments. The Detector R&D CTG made a systematic survey of these spin-off cases *[5-2]*. The field of particle physics is a highly integrated field and the importance of investments in the development of new detector technologies and detector systems for any facility is unquestioned for the sustained viability of the field. The Detector R&D CTG has recently proposed that a plan be developed to coordinate the detector R&D on a broad international basis, leading to a more stable, coherent, efficient and cost-effective way to carry out research and development for future projects.

Figure 5.5 Micromegas readout plane for the near detector of the T2K experiment, the development of which fully originated out of R&D carried out for the ILC. Image: T2K Collaboration

Two other lepton colliders, albeit with a different timescale than the ILC, are being considered, namely the Compact Linear Collider (CLIC) and the muon collider. The Detector R&D CTG tries to maintain close links with the activities related to these projects, given the large overlap in technical requirements. When topics can be identified that serve all the projects, common workshops are organised. There is in particular an active participation of physicists performing CLIC-related detector studies within the CALICE, LC-TPC and forward calorimetry FCAL collaborations.

To provide infrastructure to the community is another area that the Detector R&D CTG tries to address. Beam tests of prototype detectors are an essential element in bringing a technology from the concept stage to the detector stage. Facilities for beam tests are scarce and are subsequently heavily subscribed. The Detector R&D CTG provides the individual detector groups a forum to optimise use of all available resources, and to discuss areas of concern.

5.4 Software Common Task Group

The Software CTG is charged with coordinating tools and databases common to the detector concepts and code compatibility for simulation studies. It is also charged with working on any common software issues for ILC detector studies. For the detailed baseline design studies, the Research Director has requested that the ILD and SiD groups develop a realistic detector simulation model, including faults and limitations, and perform simulation and re-analysis of some LOI benchmark processes and analyses of newly defined processes at 1 TeV, including realistic backgrounds. This is the main target of current software activities in SiD and ILD and making this effort coherent is the goal of the Software CTG *[5-3]*.

For the LOI, the common generator samples were produced primarily at SLAC; small signal samples were produced at DESY and KEK. The Standard Model samples were produced using an event generation program, Whizard *[5-4, 5-5]* at the centre-of-mass energy of 250 and 500 GeV. The processes consisted of final states of 2 to 6 fermions and 0 to 4 gammas (γ) by collisions of e^+e^-, $e^{+/-}\gamma$ and γγ. We adopted StdHep *[5-6]* as the common file format. Using the same input event samples has been extremely useful to understand the results of the benchmark studies, especially when differences were seen.

For DBD studies, new samples have to be generated for benchmark studies with updated generator code. In order to share the work involved in the generator code preparation and the sample production, a generator sub-working group was formed in early 2010. A member from the CLIC study group joined soon thereafter, and thus the group is now working together as the Linear Collider Generator Group. The group agreed to use Whizard 1.95 and Pythia 6.422 for the DBD samples with some minor exceptions. The interface to Whizard 1.95 for linear collider physics has been updated, which includes a proper treatment of the polarisation in τ decay, use of the CKM matrix, preparation of a luminosity function for new ILC beam parameters, and use of LEP-tuned parameters for quark fragmentation. New features such as storing initial particles' information, colour flow and spin information in output files and the ability to generate many processes at once will be implemented soon. The systematic production of the generator samples will start in 2011.

For easy communication at the software level and sharing of software tools among the linear collider community, a common persistence format and a common event data model are essential. To this end, Linear Collider Input/Output (LCIO) *[5-7]* has been developed and has been used by ILD and SiD for the infrastructure of their simulation and reconstruction. LCIO has been used since the pre-LOI period, which led to the successful development and use of cross-concept group software packages such as PandoraPFA *[5-8]* and LCFIVertexing *[5-9]*.

When the LOI studies were completed in 2009, requests from users were collected, and an effort to upgrade LCIO from version 1.0 to 2.0 was launched. A list of new features planned includes (1) random access to event data, (2) the support of ROOT dictionary and IO with ROOT format, (3) extension of track data model for 2-D devices and improved treatment of kink and curl tracks, (4) preservation of additional generator information such as spin, colour and others. Features (1) and (2) have been implemented and (3) is in preparation, involving discussions among software experts. LCIO version 1.51 was released in autumn 2010, and a release of version 2.0 is expected in 2011.

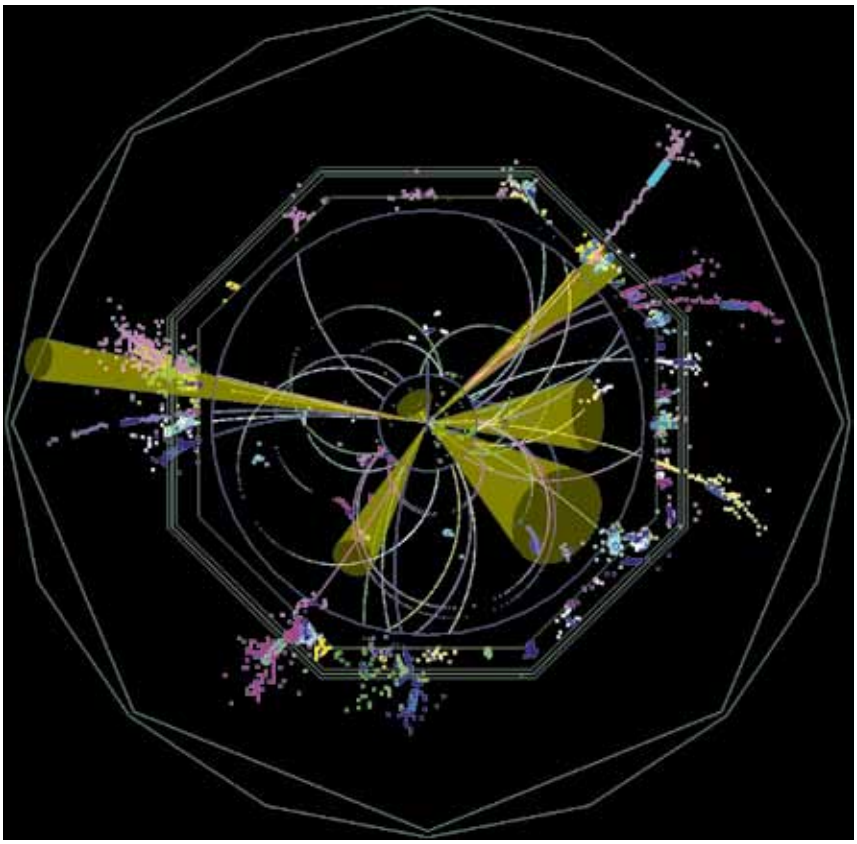

Figure 5.6 A typical 6-jet event simulated and reconstructed by the ILD software. Calorimeter and tracker hits grouped to the same particle flow objects are painted with the same colour and reconstructed jets are indicated by cones. Image: ILD

Despite differences between the detector concepts, ILD and SiD use many of the same software tools. The Software CTG acts as a contact between the two groups on software tools, such as geometry infrastructure, particle flow analysis (PFA), vertexing and kinematical fitting. Faced with the request from the Research Directorate to implement detailed detector models for simulation, the two detector groups desired a program with unified geometry tools to support detector simulations, event reconstruction and physics analyses. Such a program has been underway since 2010 in Europe under the aegis of the Advanced European Infrastructures for Detectors at Accelerators, including people outside the ILC community. The PandoraPFA program, which performs PFA very efficiently, has been rewritten to make it more modular and less framework- and geometry-dependent. It has been used to analyse SiD events simulated by the new SiD geometry for DBD study. A typical 6-jet event simulated and reconstructed by ILD is shown in *Figure 5.6*. The LCFIVertexing package has been widely used in the linear collider community to bring out the best performance of vertex detectors in ILC experiments. The code was originally developed in the UK, but it is now maintained by a Japanese group and work is in progress to improve the performance, especially in multi-jet environments. In order to encourage the broader use of common software tools, communication among people participating in software developments is crucial. In addition to presentations at various workshops, the Software CTG organised a dedicated linear collider software meeting in May 2009 at CERN and a second in July 2010 at DESY. It plans to continue these meetings in the coming years.

5.5 Physics Common Task Group

The Physics CTG was added to the Physics and Experiments Board in the autumn of 2008. The purpose of this group is to develop the understanding of the physics goals and opportunities of the ILC, building on the work done for the physics volume of the *Reference Design Report.* One goal of this group is to assess changes in the ILC capabilities as a result of changes in the design and schedule of the machine. However, its main purpose is to take into account progress in our understanding of elementary particle physics, especially from results from the Large Hadron Collider experiments. It is often said that the ILC will follow the LHC and build on the discoveries made by that machine. Ideally, this connection should be made in concrete and specific terms. This is the primary goal of the Physics CTG.

The LHC is now well into the early phase of its operation. It has been running at an energy 3.5 times that achieved by the Tevatron collider at Fermilab, and the event samples analysed so far by the LHC experiments are approaching those of the Tevatron experiments. The search for the rare events that signal the appearance of the Higgs boson and other new particles has just begun. As the data samples increase, the search for new particles will sharpen. The Physics CTG has been preparing for this search by enumerating scenarios for new physics that can be discovered relatively early in the LHC programme and analysing the experiments at the ILC that these discoveries will call for. Though the Higgs boson will be relatively difficult to discover if its mass is below 130 GeV, as preferred by other data, there is a significant chance that the Higgs boson will be seen before the end of 2012. The current estimate of the sensitivity of the LHC to the Standard Model Higgs boson is shown in *Figure 5.7.*

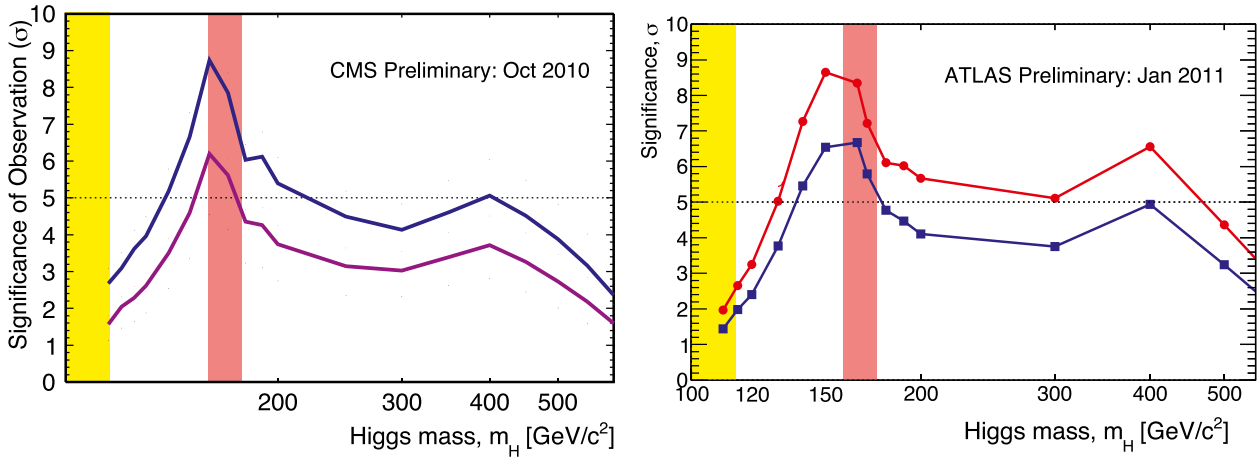

Figure 5.7 Expected significance of the observation of the Standard Model Higgs boson as a function of the mass of that particle, as estimated by the CMS and ATLAS collaborations for different levels of integrated luminosity at the LHC *[5-10, 5-11].* Observation at 5 sigmas is the conventional criterion for a particle discovery. The curves give the estimates for 2 inverse femtobarns (fb^{-1}) (purple), 5 fb^{-1} (blue), and 10 fb^{-1} (red). The vertical bands are the exclusion regions for the Standard Model Higgs boson by the Tevatron as of early 2011 (red) and LEP (yellow). Each experiment accumulated over 5 fb^{-1} of data in 2011. Left image: CMS. Right image: ATLAS.

The Physics CTG has also carried out a number of other studies for the ILC programme. It has discussed the programme of a photon collider based on the ILC in the light of new understanding of constraints on the properties of the Higgs boson and the LHC capabilities for Higgs boson measurements. The group has also participated in the analysis of the SB2009 revision of the ILC baseline design, emphasising in particular the maintenance of the ILC capabilities for precision measurement. It has discussed progress in the ILC capabilities for Higgs boson studies and, in particular, the measurement of the characteristic self-coupling of the Higgs boson field. It has also participated, with members of the Software CTG and representatives of the two concept groups, in defining the new full simulation studies that should be done for the 2012 detailed baseline design.

References

[5-1] ILC-Note-2009-050.

[5-2] ILC-REPORT-2011-034, http://ilcdoc.linearcollider.org/record/35252.

[5-3] http://www.linearcollider.org/wiki/doku.php?id=swctwg:swctwg_home.

[5-4] W. Kilian, T. Ohl, J. Reuter, WHIZARD: Simulating Multi-Particle Processes at LHC and ILC, http://arxiv.org/abs/0708.4233.

[5-5] M. Moretti, T. Ohl, J. Reuter, O'Mega: An Optimizing matrix element generator, LC-TOOL-2001-040-rev, http://arxiv.org/abs/hep-ph/0102195.

[5-6] http://cepa.fnal.gov/psm/stdhep/.

[5-7] LCIO: A Persistency framework for linear collider simulation studies. F. Gaede, T. Behnke, N. Graf, T. Johnson, In the Proceedings of 2003 Conference for Computing in High-Energy and Nuclear Physics (CHEP 03), La Jolla, California, 24-28 Mar 2003, pp TUKT001. e-Print: physics/0306114.

[5-8] Particle Flow Calorimetry and the PandoraPFA Algorithm, M. A. Thomson, NIMA 611 (2009) 25-40.

[5-9] The LCFIVertex package: Vertexing, flavour tagging and vertex charge reconstruction with an ILC vertex detector, D. Bailey, et al., NIMA 610 (2009) 573-589.

[5-10] CMS Note 2010/008 and http://twiki.cern.ch/twiki/bin/view/CMSPublic/PhysicsResultsHIG.

[5-11] ATLAS collaboration, report ATL-PHY-PUB-2011-001 (2011), http://cdsweb.cern.ch/record/1323856/.

06

WORKING GROUPS

6.1 SB2009 Working Group

The value of energy variability of the linear collider, enabling threshold scans, has been emphasised as critical as long as the linear collider has been advocated. The ILC Steering Committee (ILCSC) 'scope document' *[6-1]* included variable energy operation and good luminosity in its specification of the linear collider requirements.

To meet these crucial requirements, the Global Design Effort (GDE) developed the design presented in the *Reference Design Report* (RDR), with energy variability over the 200- to 500- gigaelectronvolt (GeV) centre-of-mass energy range and with electron polarisation of at least 80%.

Last year, in preparing for the next major design phase, moving from the RDR to the *Technical Design Report* at the end of 2012, the GDE initiated a process to evolve the ILC design to improve the optimisation of cost to performance-to-risk with major changes that will improve these tradeoffs. An early set of these changes in the form of a straw man baseline, SB2009, was presented in a plenary session at the September 2009 Linear Collider Workshop of the Americas in Albuquerque, USA (ALCPG) *[6-2]*.

In the months following the Albuquerque meeting, the specific parameters of SB2009 were presented. Two sets of parameters were presented, one assuming travelling focus operation at the interaction point, achieving a luminosity of 10^{34} $cm^{-2}s^{-1}$ at 500-GeV centre-of-mass energy, and parameters without the travelling focus. Among the changes from assumed RDR parameters were reduced low centre-of-mass energy luminosities, increased beamsstrahlung and associated background pairs and increased energy beam spread. Research Director Sakue Yamada established a physics and detectors SB2009 Working Group to study the impact of the design changes on the physics performance, convened by Jim Brau. The working group membership includes T. Barklow, M. Berggren, J. Brau, K. Buesser, K. Fujii, N. Graf, J. Hewett, T. Markiewicz, T. Maruyama, D. Miller, A. Miyamoto, Y. Okada, M. Thomson and G. Weiglein, and has benefitted from contributions by P. Grannis and H. Li. The Working Group identified issues of concern and risk for the physics programme and developed a plan of studies to measure the impact. The most significant concern was the reduced luminosity for lower energies, as illustrated in *Figure 6.1*.

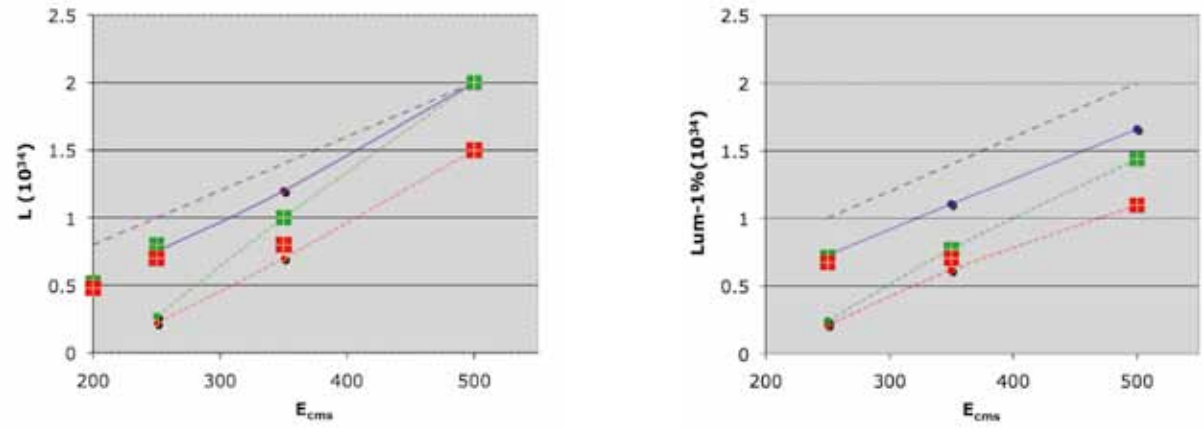

Figure 6.1 Left: luminosity versus centre-of-mass energy (ECMS). Right: luminosity restricted to the peak at full energy allowing less than 1% loss of the full collision energy. Red squares: New ILC, no travelling focus. Green squares: New ILC, travelling focus. Red dots: 2009 straw man ILC, no travelling focus. Green dots: 2009 straw man ILC, travelling focus. Violet dots: 2007 RDR. Dashed line: reference line showing luminosity proportional to energy. The RDR parameters are unofficial. SB2009 parameters were presented in 2009. Parameters labeled 'New ILC' were determined in 2010 following the Beijing Linear Collider Workshop. Image: Jim Brau

In the early months of 2010, leading up to the Beijing Linear Collider Workshop (March 2010), the study group prepared analyses of a few benchmarks. These established quantitatively that the low-energy performance of SB2009 had a serious negative impact on optimal performance at lower energies, such as at and just above the threshold for Z-Higgs (210 to 350 GeV), an assumed key operating point for the measurement of Higgs properties. The optimal operating point for the Z mass measurement appeared to be 350 GeV, rather than the 250 GeV assumed for the RDR parameters. Threshold scans for new lower mass states were also significantly affected.

The studies included:

1. Backgrounds (M. Berggren , T. Maruyama)
2. Higgs mass and cross-section measurements (H. Li)
3. Stau measurements (M. Berggren)
4. Low-mass SUSY scenario (P. Grannis)

Figure 6.2 shows the resulting electron-positron pair distributions *[6-3]*. The SB2009 parameters were found to have a small impact on the margin between the pairs and beam pipe. Compared to the RDR parameters, the total energy per bunch crossing in pairs for SB2009 was found to increase from 215 teraelectronvolts (TeV) to 635 TeV with the travelling focus. The number of electrons and positrons increased from 85,500 to 203,000, with average energies increased from 2.5 GeV to 3.1 GeV. A related study showed increased, but manageable, backgrounds in the vertex detector *[6-4]*.

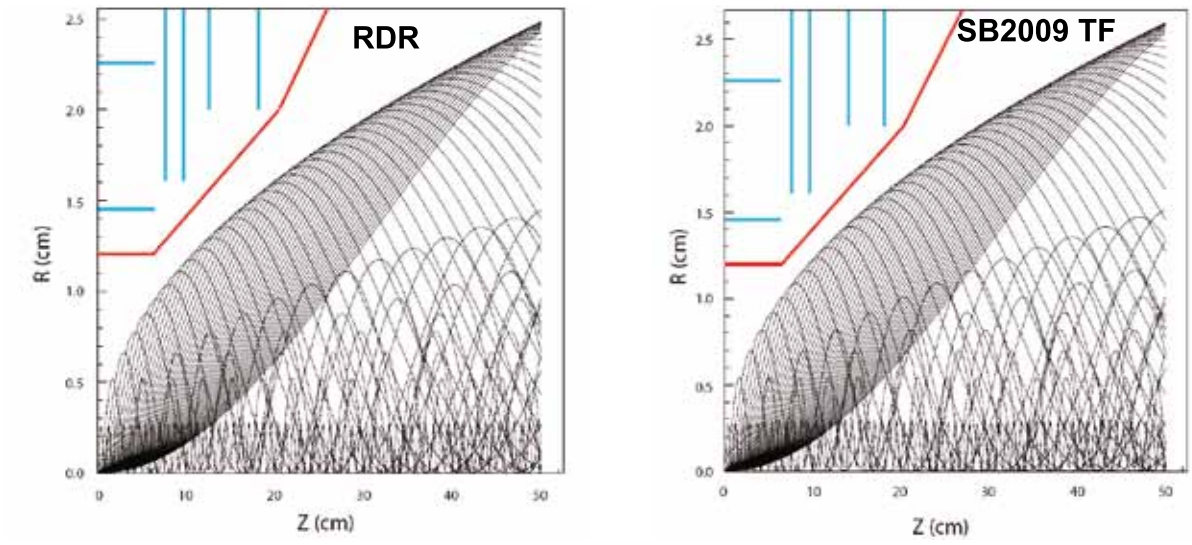

Figure 6.2 Distribution of beam pairs near the interaction point relative to the SiD beam pipe and vertex detector for the RDR beam parameters (left) and SB2009 with travelling focus (right). Image: Takashi Maruyama

The results of these studies were also presented at the Beijing Linear Collider Workshop.

Responding to these comments from the physics community, the GDE began investigating concepts that could improve the low-energy luminosity by increasing the operating rate of the design above the nominal 5 hertz and by improving the final quad doublet focusing system. These new designs matured over the summer months of 2010, and in the autumn of 2010 the GDE provided new baseline (NB) parameters to the SB2009 Working Group.

The Working Group repeated its studies of physics performance, noting that the new parameter set largely restored the performance of the RDR. The Higgs mass and cross-section measurement study *[6-5]* are summarised in *Table 6.1*. The operation at each energy is normalised to correspond to a constant period of time. The Higgs mass precision is improved from 43 to 29 megaelectronvolts (MeV) compared to the RDR when operating at 250 GeV with the travelling focus. The cross-section precision is also improved from 3.9% to 3.4%.

Beam parameters	L_{int} (fb^{-1})	ε	S/B	M_H (GeV)	σ (fb) (δσ/σ)
RDR 250	188	55%	62%	120.001 ± 0.043	11.63 ± 0.45 (3.9%)
RDR 350	300	51%	92%	120.010 ± 0.087	7.13 ± 0.28 (4.0%)
NB w/o TF 250	175	61%	62%	120.002 ± 0.034	11.67 ± 0.42 (3.6%)
NB w/o TF 350	200	52%	84%	120.003 ± 0.106	7.09 ± 0.35 (4.9%)
NB w/ TF 250	200	63%	59%	120.002 ± 0.029	11.68 ± 0.40 (3.4%)
NB w/ TF 350	250	51%	89%	120.005 ± 0.093	7.09 ± 0.31 (4.4%)

Table 6.1 Results based on NB beam parameters, assuming a beam polarisation of e^-: –80%; e^+: +30%, compared with those of RDR beam parameters. *[6-5]*

Higgs branching ratio studies have also been completed *[6-6]*.

A study of staus at the SPS1a' point (a supersymmetry benchmark point *[6-7]*) was repeated with the new beam parameters *[6-8]*. Three impacts of the SB2009 parameters were evaluated: increased background pairs in the BeamCal (beam calorimeter) could induce more γγ background; the overlaid beam background on the signal could reduce efficiency; and with a reduced number of events in the peak and a more spread-out peak, the precision of the mass measurement could be affected. The study found a degradation of 15 to 20% in mass and cross-section errors operating at the full 500-GeV centre-of-mass energy.

A run scenario study for the first 1,000 inverse femtobarns of data at the 500-GeV ILC first performed in 2002 was repeated with the new beam parameters. A SUSY working point (Snowmass 2001 SM2, *[6-9]*), although ruled out by current data to some level, has a very rich spectrum of supersymmetric particles, or sparticles, that are accessible at the 500-GeV (and below) ILC. The SUSY portion of the programme was composed of runs at the full 500-GeV energy to produce all accessible sparticle pairs and obtain a rough estimate of the masses through measurements of endpoint energies of observable final state particles, followed by dedicated scans across the thresholds for several of the sparticle pairs to obtain a more accurate determination. The importance of a $t\bar{t}$ threshold scan and of the critical need to measure the Higgs boson properties was recognised in the study. The selected energies of operation included a run above 500 GeV aimed at studying the $\tilde{\chi}_1^+\tilde{\chi}_2^-$ reaction, assuming that a tradeoff between energy and luminosity could be achieved. It also included a run with electron-electron operation to study the sharp threshold for selectron R-pair production. Both of these were included in part as a reminder that such special operating conditions may be required by the physics. The details are provided in *[6-10]*.

Table 6.2 presents the estimated sparticle mass precisions (in GeV) for luminosities at approximately the full centre-of-mass energy (labelled E_{CM} scaling), the RDR parameter sets, and the new baseline parameters (labelled NB). NB precisions are presented with and without the travelling focus (TF) and assume use of the full luminosity (full L), or just the luminosity within 1% of the full collision energy (peak L).

As expected, the changes in sparticle mass precision expected in the RDR parameter set differ little from those with the E_{CM} luminosity scaling. The precisions are typically only a few percent worse than with E_{CM} scaling, and at worst are roughly 10% larger. Similarly the full luminosity with travelling focus new baseline parameters (NB TF full L) at any energy show little degradation of mass precision. But the mass precisions degrade by up to around 25 to 30% for the other parameter sets, either considering only the luminosity within 1% of the nominal energy (NB TF peak L), without travelling focus (NB no TF full L), or just peak luminosity without travelling focus (NB no TF peak L).

Table 6.2 Estimated total sparticle mass precisions (in GeV) for all parameter sets considered, including cases with no travelling focus and the cases considering only the luminosity within 1% of the nominal energy (peak L).

sparticle	E_{CM} scaling	RDR	NB TF full L	NB TF peak L	NB no TF full L	NB no TF peak L
$selectron_R$	0.02	0.02	0.02	0.02	0.02	0.02
$selectron_L$	0.20	0.21	0.21	0.25	0.25	0.28
$smuon_R$	0.07	0.07	0.07	0.08	0.08	0.09
$smuon_L$	0.51	0.52	0.53	0.62	0.61	0.70
$stau_1$	0.64	0.82	0.73	0.78	0.78	0.81
$stau_2$	1.10	1.25	1.25	1.34	1.35	1.39
$sneutrino_e$	~1	~1	~1	~1	~1	~1
$sneutrino_\mu$	~7	~7	~7	~7	~7	~7
$sneutrino_\tau$	--	--	--	--	--	--
$\tilde{\chi}_1^0$	0.07	0.07	0.07	0.08	0.08	0.09
$\tilde{\chi}_2^0$	0.12	0.14	0.14	0.15	0.15	0.15
$\tilde{\chi}_3^0$	8.50	8.50	8.50	10.02	9.81	11.49
$\tilde{\chi}_4^0$	--	--	--	--	--	--
$\tilde{\chi}_1^+$	0.18	0.19	0.21	0.24	0.24	0.25
$\tilde{\chi}_2^+$	4.00	4.00	4.00	4.71	4.62	5.41

6.2 CLIC-ILC collaborations on detectors

One of the seven working groups was created in 2008 to foster cooperation between the Compact Linear Collider (CLIC) Study and ILC detector collaborations and was under the responsibility of S. Yamada and F. Richard from the ILC side. It is fair to say that before this initiative was taken, many contacts occurred between the CLIC physics and detector study and the two LOI detector groups, SiD (Silicon Detector) and ILD (International Large Detector). CLIC has signed Memoranda of Understanding (MOUs) with several international R&D detector collaborations, in particular CALICE (CAlorimeter for the LInear Collider with Electrons), LC-TPC (a Time Projection Chamber for a future Linear Collider) and FCAL (Forward CALorimetry). CLIC has also developed active contacts with the ILC software group, adopting the reconstruction strategy developed around the particle flow ideas.

This bottom-up approach is sound and should continue. It was proposed to provide ILCSC with an overall picture of the ongoing collaborations and to organise a joint working group on CLIC-ILC general detector issues composed of the main players.

This joint group has met on a bimonthly basis since March 2010 and has produced a chart summarising its primary actions. The group is composed of: S. Yamada (Research Directorate chair), L. Linssen (CLIC/CERN co-chair), M. Demarteau (R&D panel of the RD, SiD), F. Richard (RD Executive Committee, ILD)[6], F. Sefkow (CALICE / ILD nominated by CLIC), M. Stanitzki (SiD), M. Thomson (ILD).

[6] In January 2011 F. Richard was replaced by J. Fuster.

6.2.1 From ILC to CLIC detectors

CLIC has adapted the two ILC detector concepts for its current conceptual design phase. As with the ILC, the CLIC detectors SiD and ILD would also be operated in a push-pull scheme. However, CLIC researchers have identified some specific aspects of the detector scheme that justify significant variances with respect to the SiD and ILD standard versions.

CLIC requires increased HCAL (hadron calorimeter) absorption length to contain more energetic jets produced in the multi-TeV regime. Since the radius of the superconducting solenoid coil cannot be significantly increased, CLIC has chosen to use a tungsten absorber for the barrel HCAL, which gives a higher stopping power for the same thickness. This allows for a calorimeter depth of 7.5 λwithout any significant change in the inner bore radius of the solenoid. CLIC has also increased the depth of the steel HCAL end cap of the two detectors. To reduce cell occupancies in the vertex detector due to background from incoherent pairs, the inner radius of the vertex barrel was increased to 31 millimetres (mm) and 27 mm for CLIC_ILD and CLIC_SiD respectively. In view of the higher rates from beam-induced background and the more stringent stability requirements for the forward focusing quadrupole at CLIC, important design changes were implemented in the very forward region of both detectors. A vertical cut of the CLIC_ILD and CLIC_SiD detectors as presented in the CLIC conceptual design report is shown in *Figure 6.3*.

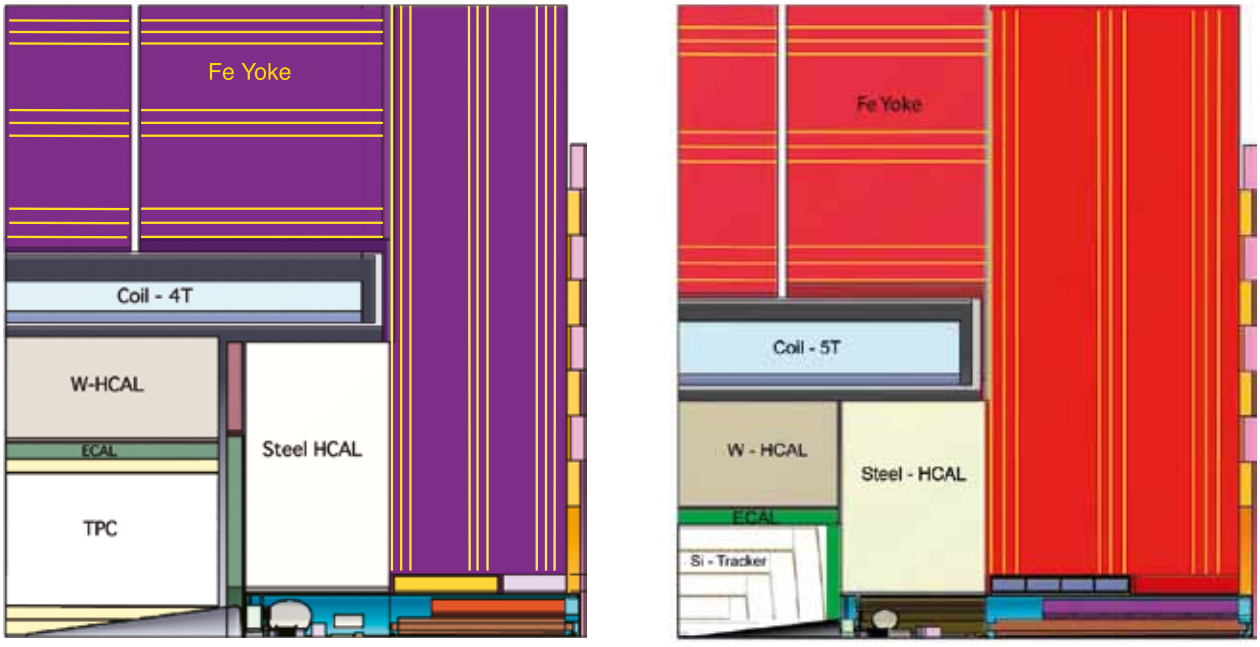

Figure 6.3 ILD (left) and SiD (right) versions used for the CLIC Conceptual Design Report. Image: CLIC CDR

With these modifications, the particle flow algorithm used for the CLIC_ILD version gives very good performances as shown below in *Table 6.3* and *Figure 6.4*.

E_{jet}	root-mean-squared 90%/E_{jet}
45 GeV	3.7%
100 GeV	3.0%
250 GeV	3.0%
500 GeV	3.2%
1 TeV	3.5%
1.5 TeV	3.6%

Table 6.3 Jet energy resolution for various jet energies in the barrel region of the CLIC_ILD detector

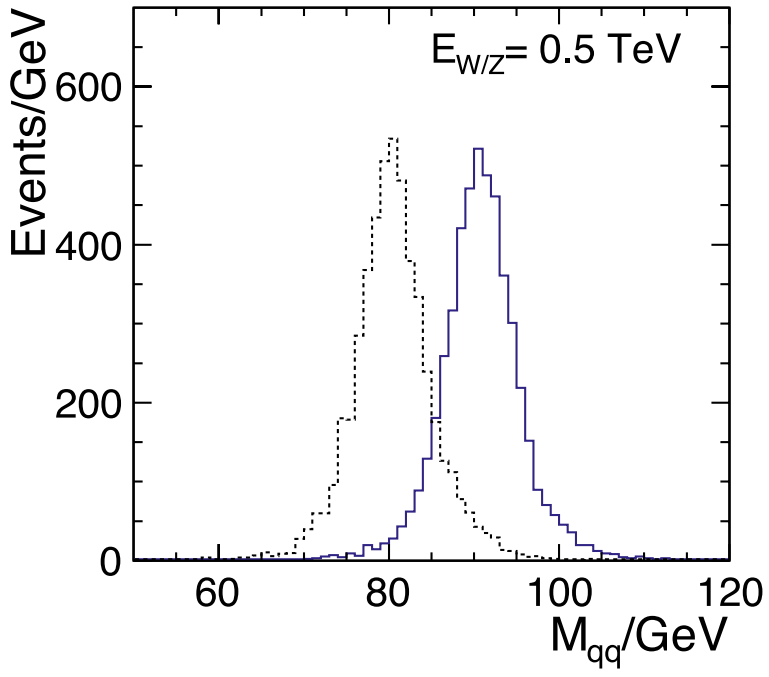

Figure 6.4 Jet-jet mass separation for 500-GeV W and Z decays. Image: Mark Thomson

An essential difference between CLIC and ILC lies in the time structure. While ILC has several hundred nanoseconds (ns) between bunch crossings, CLIC works with bunch crossings separated by only 0.5 ns over a 312-ns bunch train duration for CLIC operating at 3 TeV. The ability to separate interesting physics events from beam-induced background imposes very challenging timing requirements on the various sub-detectors. As described in the CLIC Conceptual Design Report, the calorimeters with fine granularity allow for a very effective background suppression at CLIC by applying precise timing cuts on reconstructed particle flow objects. Therefore supplementary R&D is needed for the readout of the CLIC detectors, with time-stamping capabilities of 10 ns for ECAL (electromagnetic calorimeter) and for all silicon tracking and vertex detectors, while a 1-ns hit time resolution will be required for HCAL. Needless to say, ILC would also benefit from such improvements.

6.2.2 Content of CLIC-ILC collaborations

The main topics covered are:

- Core software development: frameworks, geometry description, tracking, particle flow algorithms, event overlays, grid tools
- Beam-induced background studies
- Detector performance studies and detector optimisation for high energies (at 3-TeV and 1-TeV centre-of-mass energies), for example, for particle flow and tracking
- Event generation and physics benchmarking
- Engineering studies and cost assessment
- Solenoid studies and conductor R&D (with CMS (Compact Muon Solenoid) expertise)
- Electronics developments (CERN expertise)
- HCAL beam tests (tungsten absorbers)

The CLIC-ILC collaboration proceeds through mini-workshops, gathering specialists from both collider groups:

- Software workshop: Following the May 2009 workshop, a follow-up workshop was held on 5 July 2010 at DESY. Contacts: F. Gaede, N. Graf, A. Miyamoto, D. Schlatter.
- Monte Carlo generators: a member of the CLIC study has recently joined the ILC common data sample subgroup. This is an ongoing cooperation, so no new initiative from this working group is required. Contacts: T. Barklow, M. Berggren, A. Miyamoto, S. Poss.
- Power delivery and power pulsing: a common ILC-CLIC workshop was held at Orsay in May 2011.
- Extended ILC-CLIC collaboration on push-pull and experimental hall: in this area common meetings take place on a regular basis.

ILD and SiD are also very actively collaborating on the CLIC Conceptual Design Report on detectors, in particular by providing more than half of the editors.

CALICE has performed beam tests on hadron calorimetry with a tungsten absorber using the analog HCAL developed for ILC.

Figure 6.5 Test setup for the CLIC W-HCAL. Left image: *CERN Bulletin*. Right image: CERN LCD.

6.2.3 Common workshops

An important step in the CLIC-ILC collaboration has been the October 2010 workshop organised at CERN, Switzerland, under the European Committee for Future Accelerators Study of Physics and Detectors for a Linear Collider. For the first time, both CLIC and the ILC were equal partners in organising the event, which covered all linear collider activities: theory, instrumentation, machine and machine-detector interfaces.
There were approximately 500 registered participants with a large fraction of non-European attendees *[6-11]*.

Future annual linear collider collaboration meetings, under the responsibility of the Worldwide Study Organizing Committee, will cover all ILC and CLIC aspects. The latest meeting took place in Granada, Spain, from 26 – 30 September 2011.

References

[6-1] "Parameters for the Linear Collider" document (URL - http://www.fnal.gov/directorate/icfa/para-Nov20-final.pdf), updated 20 November 2006.

[6-2] N. Walker, "Design Considerations for the ILC," (URL - http://ilcagenda.linearcollider.org/materialDisplay.py?contribId=29&sessionId=2&materialId=slides&confId=3461), Sep 28, 2009.

[6-3] T. Maruyama, "SiD beampipe and pairs edge," private communication, 16 March 2010.

[6-4] M. Berggren, "Beam pair-background in with SB2009 and RDR from GuineaPig," Jan 15, 2010.

[6-5] H. Li, "Impacts of the New Baseline ILC Design on the Higgs Recoil Mass Analysis Based on a Fast Simulation of the ILD," 10 October 2010.

[6-6] H. Ono, "ZH branching ratio study @ 350 GeV," 19 October 2010.

[6-7] J.A. Aguilar-Saavedra et al, Eur. Phy. J C46 (2006) 43.

[6-8] M. Berggren, private communication, March 7, 2010; P. Bechtle et al., "Prospects for the study of the stau-system in SPS1a' at the ILC," DESY-09-124, July 2009.

[6-9] B.C. Allanach et al, hep-ph/0202233

[6-10] P. Grannis, "Sparticle mass precision with revised ILC luminosity estimate," revised 10 December 2010; arXiv:hep-ex/0211002.

[6-11] International Workshop on Linear Colliders 2010, 18-22 October 2010, Geneva, Switzerland, https://espace.cern.ch/LC2010/default.aspx.

07

APPENDIX

ACKNOWLEDGEMENT

We acknowledge the support of BMWF, Austria; MinObr, Belarus; FNRS and FWO, Belgium; NSERC, Canada; NSFC, China; MPO CR and VSC CR, Czech Republic; FP7 European Commission, FP6 European Commission, European Union; HIP, Finland; CNRS/IN2P3, CEA-DSM/IRFU, France; BMBF, DFG, HGF, MPG and AvH Foundation, Germany; DAE and DST, India; ISF, Israel; INFN, Italy; MEXT and JSPS, Japan; CRI (MST) and MOST/ KOSEF, Korea; FOM and NWO, The Netherlands; NFR, Norway; MNSW, Poland; ANCS, Romania; MES of Russia and ROSATOM, Russian Federation; MON, Serbia and Montenegro; MSSR, Slovakia; MICINN and CPAN, Spain; SRC, Sweden; STFC, United Kingdom; DOE and NSF, United States of America.

AUTHOR LIST

Tim Barklow
SLAC, USA

Ties Behnke
DESY, Germany

Mikael Berggren
DESY, Germany

James E. Brau
University of Oregon, USA

Karsten Buesser
DESY, Germany

Philip Burrows
University of Oxford, UK

Marty Breidenbach
SLAC, USA

Catherine Clerc
LLR, École polytechnique, CNRS / IN2P3, France

Wes Craddock
SLAC, USA

Marcel Demarteau
ANL, USA

Guenter Eckerlin
DESY, Germany

Gene Fisk
Fermilab, USA

Ray Frey
University of Oregon, USA

Keisuke Fujii
KEK, Japan

Norman Graf
SLAC, USA

Gunther Haller
SLAC, USA

Daniel Jeans
LLR, École polytechnique, CNRS / IN2P3, France

Francois Kircher
CEA, France

Wolfgang Lohmann
DESY, Germany

Tom Markiewicz
SLAC, USA

Takeshi Maruyama
SLAC, USA

Akiya Miyamoto
KEK, Japan

Michael Peskin
SLAC, USA

Francois Richard
LAL, Université Paris-Sud, CNRS / IN2P3, France

Bruce Schumm
UCSC, USA

Felix Sefkow
DESY, Germany

Yasuhiro Sugimoto
KEK, Japan

Mark Thomson
University of Cambridge, UK

Jan Timmermans
DESY, Germany and NIKHEF, The Netherlands

Andrew White
UTA, US

Sakue Yamada
KEK and University of Tokyo, Japan

Vishnu Zutshi
NIU, USA

Members of Physics and Experiment Board

Ties Behnke (ILD)
James Brau (Regional Contact for Americas)
Karsten Buesser (Machine Detector Interface CTG)
Katherine Clerc (Engineering Tool CTG)
Marcel Demarteau (Detector R&D CTG)
Juan Fuster (Regional Contact for Europe, since February 2011)
John Jaros (SiD)
Akiya Miyamoto (Software CTG)
Michael Peskin (Physics CTG)
Francois Richard (Regional Contact for Europe, till January 2011)
Yasuhiro Sugimoto (ILD)
Sakue Yamada (Research Director)
Hitoshi Yamamoto (Regional Contact for Asia)
Andrew White (SiD)

Members of the Common Task Groups

Machine Detector Interface CTG

Karsten Buesser (convener)
Philip Burrows (deputy)
Marco Oriunno
Toshiaki Tauchi

Engineering Tool

Catherine Clerc (convener)
Kurt Krempetz
Marco Oriunno (deputy)
Hiroshi Yamaoka

Detector R&D

Dhiman Chakraborty
Marcel Demarteau (convener)
John Hauptman
Ronald Lipton
Wolfgang Lohmann
Timothy Nelson
Burkhard Schmidt
Aurore Savoy-Navarro
Felix Sefkow
Tohru Takeshita
Jan Timmermans
Andrew White
Marc Winter

Software

Frank Gaede
Norman Graf (deputy)
Tony Johnson
Akiya Miyamoto (convener)

Physics

Tim Barklow
Stewart Boogert
Seong Youl Choi
Klaus Desch
Keisuke Fujii (deputy)
Youanning Gao
Heather Logan
Klaus Moenig
Andrei Nomerotski
Michael Peskin (convener)
Aurore Savoy-Navarro
Georg Weiglein (deputy)
Jae Yu

LETTERS OF INTENT SIGNATORIES

The following are signatories to the Letters of Intent of the ILD groups. Names are listed as given in the official signatories list. Institute names are abbreviated to save space.

ILD (International Large Detector)

Toshinori Abe[142], Jason M. Abernathy[145], Halina Abramowicz[101], Marek Adamus[3], Bernardo Adeva[43], Konstantin Afanaciev[5], Juan Antonio Aguilar-Saavedra[111], Carmen Alabau Pons[39], Enrique Calvo Alamillo[13], Hartwig Albrecht[16], Ladislav Andrieck[71], Marc Anduze[63], Steve J. Aplin[16], Yasuo Arai[53], Masaki Asano[143], David Attie[49], Derek J. Attree[109], David Bailey[135], Juan Pablo Balbuena[41], Markus Ball[39], James Ballin[32], Mauricio Barbi[138], Roger Barlow[14, 135], Christoph Bartels[16, 128], Valeria Bartsch[109], Daniela Bassignana[41], Richard Bates[127], Sudeb Battacharya[92], Jerome Baudot[47, 114], Philip Bechtle[16], Jeannine Beck[16], Moritz Beckmann[16, 25], Marc Bedjidian[48], Ties Behnke[16], Khaled Belkadhi[63], Alain Bellerive[9], Stan Bentvelsen[81], Thomas Bergauer[86], C. Mikael U. Berggren[16], Matthias Bergholz[7, 17], Werner Bernreuther[88], Marc Besancon[49], Auguste Besson[47, 114], Bipul Bhuyan[33], Otmar Biebel[69], Burak Bilki[131], Grahame Blair[89], Johannes Bluemlein[17], Li Bo[106], Veronique Boisvert[89], A. Bondar[8], Giovanni Bonvicini[154], Eduard Boos[64], Vincent Boudry[63], Bernard Bouquet[60], Joël Bouvier[68], Ivanka Bozovic-Jelisavcic[151], Jean-Claude Brient[63], Ian Brock[108], Andrea Brogna[47, 114], Peter Buchholz[150], Karsten Buesser[16], Antonio Bulgheroni[35], Jochen Bürger[16], John Butler[6], Craig Buttar[127], A. F. Buzulutskov[8], Massimo Caccia[35, 115], Stefano Caiazza[16, 128], Alessandro Calcaterra[59], Allen Caldwell[71], Stephane L. C. Callier[60], Alan J. Campbell[16], Michael Campbell[10], Chiara Cappellini[35, 115], Cristina Carloganu[66], Nuno Castro[111], Maria Elena Castro Carballo[17], Marina Chadeeva[45], Dhiman Chakraborty[83], Paoti Chang[79], Alexandre Charpy[67], Hongfang Chen[139], Shaomin Chen[106], Xun Chen[71], Byunggu Cheon[26], Suyong Choi[98], B. C. Choudhary[124], Sandra Christen[16, 128], Jacek Ciborowski[134, 146], Catalin Ciobanu[67], Gilles Claus[47, 114], Catherine Clerc[63], Cornelia Coca[28], Paul Colas[49], Auke Colijn[81], Claude Colledani[47, 114], Christophe Combaret[48], Rémi Cornat[63], Patrick Cornebise[60], François Corriveau[72], Jaroslav Cvach[44], Michal Czakon[147], Nicola D'Ascenzo[16, 84], Wilfrid Da Silva[67], Olivier Dadoun[60], Mogens Dam[123], Chris Damerell[90], Witold Daniluk[102], Mikhail Daniolv[45], Guillaume Daubard[67], Dörte David[16], Jacques David[67], Wim De Boer[10, 116], Nicolo De Groot[42, 81], Paul De Jong[81], Sijbrand De Jong[42, 81], Christophe De La Taille[60], Rita De Masi[47], Albert De Roeck[10], David Decotigny[63], Klaus Dehmelt[16], Eric Delagnes[49], Zhi Deng[106], Klaus Desch[108], Angel Dieguez[110], Ralf Diener[16], Mihai-Octavian Dima[28], Günther Dissertori[19], Madhu S. Dixit[9, 105], Zdenek Dolezal[11], Ralph Dollan[29], Boris A. Dologoshein[73], Andrei Dorokhov[47, 114], Philippe Doublet[60], Tony Doyle[127], Guy Doziere[47, 114], Marko Dragicevic[86], Zbynek Drasal[11], Vladimir Drugakov[5], Jordi Duarte Campderrós[40], Frédéric Dulucq[60], Laurentiu Alexandru Dumitru[28], Daniel Dzahini[68], Helmut Eberl[86], Guenter Eckerlin[16], Wolfgang Ehrenfeld[16], Gerald Eigen[117], Lars Eklund[127], Eckhard Elsen[16], Konrad Elsener[10], Igor Emeliantchik[5], Jan Engels[16], Christophe Evrard[67], Riccardo Fabbri[16], Gerard Faber[19], Michele Faucci Gianelli[60, 89], Angeles Faus-Golfe[39], Nils Feege[16, 128], Cunfeng Feng[94], Jozef Ferencei[96], Marcos Fernandez Garcia[40], Frank Filthaut[42, 81], Ivor Fleck[150], Manfred Fleischer[16], Celeste Fleta[41], Julien L. Fleury[60], Jean-Charles Fontaine[112], Brian Foster[137], Nicolas Fourches[49], Mary-Cruz Fouz[13], Sebastian Frank[86], Ariane Frey[24], Mickael Frotin[63], Hirofumi Fujii[53], Keisuke Fujii[53], Junpei Fujimoto[53], Yowichi Fujita[53], Takahiro Fusayasu[75], Juan Fuster[39],

Andrea Gaddi[10], Frank Gaede[16], Alexei Galkin[84], Valery Galkin[84], Abraham Gallas[43], Laurent Gallin-Martel[68], Diego Gamba[38], Yuanning Gao[106], Luis Garrido Beltran[110], Erika Garutti[16], Franck Gastaldi[63], Bakul Gaur[150], Pascal Gay[66], Andreas Gellrich[16], Jean-Francois Genat[67, 122], Simonetta Gentile[37], Hubert Gerwig[10], Lawrence Gibbons[15], Elena Ginina[86], Julien Giraud[68], Giuseppe Giraudo[38], Leonid Gladilin[64], Joel Goldstein[119], Francisco Javier González Sánchez[40], Filimon Gournaris[109], Tim Greenshaw[133], Z. D. Greenwood[65], Christian Grefe[10, 108], Ingrid-Maria Gregor[16], Gérald Grenier[48], Philippe Gris[66], Denis Grondin[68], Martin Grunewald[126], Grzegorz Grzelak[146], Atul Gurtu[99], Tobias Haas[16], Stephan Haensel[86], Csaba Hajdu[30], Lea Hallermann[16, 128], Liang Han[139], Peter H. Hansen[123], Takanori Hara[53], Kristian Harder[90], Anthony Hartin[16], Tomiyoshi Haruyama[53], Martin Harz[16], Yoji Hasegawa[95], Michael Hauschild[10], Qing He[87], Vincent Hedbeg[70], David Hedin[83], Isa Heinze[16, 128], Christian Helebrant[16, 128], Hans Henschel[17], Carsten Hensel[24], Ralf Hertenberger[69], Alain Hervé[19], Takeo Higuchi[53], Abdelkader Himmi[47, 114], Kazurayama Hironori[103], Hana Hlucha[86], Bart Hommels[121], Yasuyuki Horii[103], Dezso Horvath[30], Jean-Yves Hostachy[68], Wei-Shu Hou[79], Christine Hu-Guo[47, 114], Xingtao Huang[94], Jean Francois Huppert[67], Yasuhiro Ide[95], Marek Idzik[1], Carmen Iglesias Escudero[43], Alexandr Ignatenko[5], Olga Igonkina[81], Hirokazu Ikeda[50], Katsumasa Ikematsu[53], Yukiko Ikemoto[53], Toshinori Ikuno[144], Didier Imbault[67], Andreas Imhof[128], Marc Imhoff[47, 114], Ronen Ingbir[101], Eiji Inoue[53], Giomataris Ioannis[49], Akimasa Ishikawa[55], Kennosuke Itagaki[103], Kazutoshi Ito[103], Hideo Itoh[53], Masaya Iwabuchi[97], Go Iwai[53], Toshiyuki Iwamoto[142], Editha P. Jacosalem[74], Richard Jaramillo Echeverria[40], Daniel T. D. Jeans[63], Fanfan Jing[106], Ge Jing[139], Stevan Jokic[151], Leif Jonsson[70], Matthieu Joré[60], Tatjana Jovin[151], Daniela Käfer[16], Fumiyoshi Kajino[57], Yusuke Kamai[103], Jochen Kaminski[108], Yoshio Kamiya[142], Alexander Kaplan[16, 129], Frédéric Kapusta[67], Deepak Kar[100], Dean Karlen[105, 145], Nobu Katayama[53], Eriko Kato[103], Yukihiro Kato[54], Alexander Kaukher[149], Kiyotomo Kawagoe[55], Hiroki Kawahara[142], Masanori Kawai[53], Takeo Kawasaki[80], Sameen Ahmed Khan[93], Robert Kieffer[48], Eryk Kielar[102], Wolfgang Kiesenhofer[86], Christian M. Kiesling[71], Martin Killenberg[108], Choong Sun Kim[156], Donghee Kim[58], Eun-Joo Kim[12], Guinyun Kim[58], Hong Joo Kim[58], Hyunok Kim[58], Shinhong Kim[144], Francois Kircher[49], Danuta Kisielewska[1], Claus Kleinwort[16], Tatsiana Klimkovich[88], Hanna Kluge[17], Peter Martin Kluit[81], Makoto Kobayashi[53], Michael Kobel[100], Hideyo Kodama[53], Peter Kodys[11], U. Koetz[16], Els Koffeman[81], Takashi Kohriki[53], Sachio Komamiya[142], Yoshinari Kondou[53], Volker Korbel[16], Katsushige Kotera[95], Sabine Kraml[68], Manfred Krammer[86], Kaloyan Krastev[68], Bernward Krause[16], Thorsten Krautscheid[108], Dirk Krücker[16], Kirsten Kschioneck[16], Yu-Ping Kuang[106], Jan Kuhlmann[16], Hirotoshi Kuroiwa[91], Tomonori Kusano[103], Peter Kvasnicka[11], Carlos Lacasta Llácer[39], Eric Lagorio[68], Imad Laktineh[48], Wolfgang Lange[17], Patrice Lebrun[48], Jik Lee[20], Frank Lehner[16], Tadeusz Lesiak[102], Aharon Levy[101], Bo Li[106], Hengne Li[60], Ting Li[106], Yulan Li[106], Zuotang Liang[94], Guilherme Lima[83], Frank Linde[81], Lucie Linssen[10], Diana Linzmaier[16], Benno List[128], Jenny List[16], Bo Liu[106], Xavier Llopart Cudie[10], Wolfgang Lohmann[17], Amparo Lopez Virto[40], Manuel Lozano[41], Shaojun Lu[21, 71], Angela Isabela Lucaci-Timoce[16], Nick Lumb[48], Bjorn Lundberg[70], Benjamin Lutz[16, 128], Pierre Lutz[49, 60], Thorsten Lux[107], Pawel Luzniak[134], Alexey Lyapin[109], Wengan Ma[139], Lukasz Maczewski[134, 146], Wolfgang F. Mader[100], Manas Maity[152], Gobinda Majumder[99], Nayana Majumdar[92], Akihiro Maki[53], Yasuhiro Makida[53], Judita Mamuzic[151], Dhellot Marc[67], Ivan Marchesini[16, 128], Michal Marcisovsky[44], Carlos Mariñas[39], John Marshall[121], Cornelius Martens[16], Jean-Pierre Martin[113], Victoria J. Martin[125], Gisele Martin-Chassard[60], Celso Martinez Rivero[40], Hans-Ulrich Martyn[16, 88], Hervé Mathez[48], Antoine Mathieu[63], Takeshi Matsuda[16, 53], Hiroyuki Matsunaga[142,] Takashi Matsushita[55], Georgios Mavromanolakis[22, 121], Kirk T. McDonald[87], Paolo Mereu[38], Marcel Merk[81, 153], Mikhail M. Merkin[64], Niels Meyer[16], Norbert Meyners[16], Satoshi Mihara[53], David J. Miller[109], Owen Miller[118], Winfried A. Mitaroff[86], Akiya Miyamoto[53], Hitoshi Miyata[80], Ulf Mjornmark[70], Joachim Mnich[16], Klaus Moenig[17], Andreas Moll[21, 71], Gudrid A. Moortgart-Pick[14, 18], Paulo Mora De Feitas[63], Frederic Morel[47, 114], Stefano Moretti[90, 140], Vasily Morgunov[16, 45], Takashi Mori[76], Toshinori Mori[142], Laurent Morin[68], Sergey Morozov[16, 128], Fabian Moser[86], Hans-Günther Moser[71], David Moya[40], Mihajlo Mudrinic[151], Supratik Mukhopadhyay[92], Takeshi Murakami[53], Luciano Musa[10], Gabriel Musat[63], Tadahi Nagamine[103], Isamu Nakamura[53], Eiichi Nakano[85], Kenichi Nakashima[91], Kazuo Nakayoshi[53], Hideyuki Nakazawa[78], Jiwoo Nam[20], Shinwoo Nam[20], Stanislav Nemecek[44], Carsten Niebuhr[16], Marcus Niechciol[150], Piotr Nieuzurawski[146], Shohei Nishida[53], Miho Nishiyama[95], Osamu Nitoh[104], Ed Norbeck[131], Mitsuaki Nozaki[53], Val O'Shea[127], Martin Ohlerich[17], Nobuchika Okada[53], Alexander Olchevski[52], Bob Olivier[71], Krzysztof Oliwa[102], Tsunehiko Omori[53], Yasar Onel[131], Hiroaki Ono[82], Yoshimasa Ono[103], Yoshiyuki Onuki[103], Wataru Ootani[142], Risto Orava[130], Marius Ciprian

Orlandea[28], Anders Oskarsson[70], Per Osland[117], Dmitri Ossetski[84], Lennart Osterman[70], Cristobal Padilla[107], Mila Pandurovic[151], Hwanbae Park[58], Il Hung Park[20], Chris Parkes[127], Ghislain Patrick[67], J. Ritchie Patterson[15], Bogdan Pawlik[102], Giulio Pellegrini[41], Antonio Pellegrino[81], Daniel Peterson[15], Alexander Petrov[16], Thanh Hung Pham[67], Marcello Piccolo[59], Roman Poeschl[60], Ivo Polak[44], Elena Popova[73], Martin Postranecky[109], Volker Prahl[16], Xavier Prudent[100], Helenka Przysiezniak[62, 113], Jesus Puerta-Pelayo[13], Wenbin Qian[106], Arnulf Quadt[24], Fatah-Ellah Rarbi[68], Alexei Raspereza[16], Lodovico Ratti[36], Ludovic Raux[60], Gerhard Raven[81, 153], Valerio Re[36], Meinhard Regler[86], Marcel Reinhard[63], Uwe Renz[2], Philippe Repain[67], Jose Repond[4], Francois Richard[60], Sabine Riemann[17], Tord Riemann[17], Jordi Riera-Babures[148], Imma Riu[107], Aidan Robson[127], Philipp Roloff`[16, 128], Aura Rosca[28, 155], Christoph Rosemann[16], Janusz Rosiek[146], Robert Rossmanith[116], Stefan Roth[88], Christophe Royon[49], Manqi Ruan[63], Alberto Ruiz-Jimeno[40], Vladimir Rusinov[45], Pavel Ruzicka[44], Dmitri Ryzhikov[84], Juan J. Saborido[43], Iftach Sadeh[101], André Sailer[17], Masatoshi Saito[53], Takayuki Sakumo[95], Toshiya Sanami[53], Tomoyuki Sanuki[103], Sandip Sarkar[92], Rei Sasaki[103], Yutaro Sato[103], Valeri Saveliev[84], Aurore Savoy-Navarro[67], Lee Sawyer[65], Peter Schade[16], Oliver Schäfer[149], Joern Schaffran[16], Andreas Schälicke[17], Jan Scheirich[11], Dieter Schlatter[10], Ringo Sebastian Schmidt[7, 17], Sebastian Schmitt[16], Uwe Schneekloth[16], Heinz Juergen Schreiber[17], K. Peter Schüler[16], Hans-Christian Schultz-Coulon[129], Markus Schumacher[2], Bruce A. Schumm[120], Sergej Schuwalow[17], Rainer Schwierz[100], Felix Sefkow[16], Rachid Sefri[67], Nathalie Seguin-Moreau[60], Katja Seidel[21, 71], Jadranka Sekaric[132], Hiroshi Sendai[53], Ronald Dean Settles[71], Ming Shao[139], L. I. Shechtman[8], Shoichi Shimazaki[53], Nikolai Shumeiko[5], Petr Sicho[44], Frank Simon[21, 71], Klaus Sinram[16], Ivan Smiljanic[151], Nebojsa Smiljkovic[19], Jan Smolík[44], Blanka Sobloher[16, 128], Christian Soldner[71], Kezhu Song[139], Andre Sopczak[61], Peter Speckmayer[10], Evert Stenlund[70], Dominik Stockinger[100], Holger Stoeck[141], Arno Straessner[100], Raimund Ströhmer[69], Richard Stromhagen[16], Yuji Sudo[144], Taikan Suehara[142], Fumihiko Suekane[103], Yusuke Suetsugu[53], Yasuhiro Sugimoto[53], Akira Sugiyama[91], Kazutaka Sumisawa[53], Shiro Suzuki[91], Krzysztof Swientek[1], Hajrah Tabassam[125], Tohru Takahashi[27], Hiroshi Takeda[55], Tohru Takeshita[95], Yosuke Takubo[103], Tomohiko Tanabe[142], Ken-Ichi Tanaka[53], Manubo Tanaka[53], Shuji Tanaka[53], Stefan Tapprogge[51], Evgueny I. Tarkovsky[45], Kazuya Tauchi[53], Toshiaki Tauchi[53], Valery I. Telnov[8], Eliza Teodorescu[28], Mark Thomson[121], Junping Tian[31, 106], Jan Timmermans[16, 81], Maxim Titov[49], Katsuo Tokushuku[53], Shunsuke Tozuka[95], Toru Tsuboyama[53], Koji Ueno[79], Miguel Ullán[41], Satoru Uozumi[55], Junji Urakawa[53], Andriy Ushakov[17], Yutaka Ushiroda[53], Manfred Valentan[86], Isabelle Valin[47, 114], Harry Van Der Graaf[81], Brian Van Doren[132], Rick J. Van Kooten[34], Muriel Vander Donckt[48], Jean-Charles Vanel[63], Pablo Vazquez Regueiro[43], Marco Verzocchi[22], Christophe Vescovi[68], Henri L. Videau[63], Ivan Vila[40], Xavier Vilasis-Cardona[148], Adrian Vogel[108], Robert Volkenborn[16], Marcel Vos[39], Yorgos Voutsinas[47], Vaclav Vrba[44], Marcel Vreeswijk[81], Roberval Walsh[125], Wolfgang Waltenberger[86], Meng Wang[94], Min-Zu Wang[79], Qun Wang[139], Xiaoling Wang[139], Yi Wang[106], David R. Ward[121], Matthew Warren[109], Minori Watanabe[80], Takashi Watanabe[56], Nigel K. Watson[118], Nanda Wattimena[16], Oliver Wendt[16, 128], Norbert Wermes[108], Lars Weuste[71], Katarzyna Wichmann[16], Peter Wienemann[108], Wojciech Wierba[102], Graham W. Wilson[132], John A. Wilson[118], Matthew Wing[109], Marc Winter[47], Markus Wobisch[65], Malgorzata Worek[147], Stefania Xella[123], Zizong Xu[139], Akira Yamaguchi[103], Hiroshi Yamaguchi[91], Hitoshi Yamamoto[103], Hiroshi Yamaoka[53], Satoru Yamashita[142], M. Yamauchi[53], Yuji Yamazaki[55], Mahfoud Yamouni[68], Wenbiao Yan[139], Koji Yanagida[95], Haijun Yang[136], Jin Min Yang[46], Jongmann Yang[20], Zhenwei Yang[106], Yoshiji Yasu[53], Ryo Yonamine[97], Kohei Yoshida[103], Takuo Yoshida[23], Tamaki Yoshioka[53], Chunxu Yu[77], Intae Yu[98], Qian Yue[106], Josef Zacek[11], Jaroslav Zalesak[44], Aleksandr Filip Zarnecki[146], Leszek Zawiejski[102], Christian Zeitnitz[147], Dirk Zerwas[60], Wolfram Zeuner[10, 16], Renyou Zhang[139], Xueyao Zhang[94], Yanxi Zhang[106], Zhiqing Zhang[60], Ziping Zhang[139], Jiawei Zhao[139], Zhengguo Zhao[139], Baojun Zheng[106], Liang Zhong[106], Yongzhao Zhou[139], Chengguang Zhu[94], Xianglei Zhu[106], Fabian Zomer[60], Vishnu Zutshi[83]

[1] AGH Univ. of Science and Technology, Cracow, Poland
[2] Albert-Ludwigs Univ. Freiburg, Freiburg, Germany
[3] Andrzej Soltan Inst. for Nuclear Studies, Warsaw Poland
[4] Argonne National Laboratory, Argonne, USA
[5] Belarusian State Univ., Minsk, Belarus
[6] Boston Univ., Boston, USA
[7] Brandenburg Univ. of Technology, Cottbus, Germany
[8] Budker Inst. for Nuclear Physics, Novosibirsk, Russia
[9] Carleton Univ., Ottawa, Canada
[10] CERN, Geneva, Switzerland
[11] Charles Univ., Prague, Czech Republic
[12] Chonbuk National Univ., Jeonju, Korea

[13] CIEMAT, Madrid, Spain
[14] Cockcroft Inst., Warrington, UK
[15] Cornell Univ., Ithaca, USA
[16] DESY, Hamburg, Germany
[17] DESY, Zeuthen, Germany
[18] Durham Univ., Durham, UK
[19] ETH Zürich, Zürich, Germany
[20] Ewha Womans Univ., Seoul, Korea
[21] Excellence Cluster Universe, Garching, Germany
[22] Fermilab, Batavia, USA
[23] Fukui Univ., Fukui, Japan
[24] Georg-August-Univ. Göttingen, Göttingen, Germany
[25] Gottfried Wilhelm Leibniz Univ. Hannover, Hannover, Germany
[26] Hanyang Univ., Seoul, Korea
[27] Hiroshima Univ., Higashi-Hiroshima, Japan
[28] Horia Hulubei National Inst. of Physics and Nuclear Engineering, Bucharrest-Maguerele, Romania
[29] Humboldt Univ. zu Berlin, Berlin, Germany
[30] Hungarian Academy of Science, Budapest, Hungary
[31] IHEP, Beijing, China
[32] Imperial College London, London, UK
[33] Indian Inst. of Technology, Guwahati, Guwahati, India
[34] Indiana Univ., Bloomington, USA
[35] INFN, Milano, Italy
[36] INFN, Pavia, Italy
[37] INFN, Roma, Italy
[38] INFN, Torino, Italy
[39] Inst. de Física Corpuscular, Valencia, Spain
[40] Inst. de Física de Cantabria, Santander, Spain
[41] Inst. de Microelectrónica de Barcelona, Barcelona, Spain
[42] Inst. for Mathematics, Astrophysics and Particle Physics, Nijmegen, The Netherlands
[43] Inst. Galego de Física de Altas Enerxias, Santiago de Compostela, Spain
[44] Inst. of Physics, Prague, Czech Republic
[45] Inst. of Theoretical and Experimental Physics, Moscow, Russia
[46] Inst. of Theoretical Physics, Beijing, China
[47] Inst. Pluridisciplinaire Hubert Curien, Strasbourg, France
[48] IPNL, Univ. de Lyon, CNRS/IN2P3, Lyon, France
[49] IRFU, CEA Saclay, Gif-sur-Yvette, France
[50] Japan Aerospace Exploration Agency, Sagamihara, Japan
[51] Johannes Gutenberg Univ. Mainz, Mainz, Germany
[52] Joint Inst. for Nuclear Research, Dubna, Russia
[53] KEK, Tsukuba, Japan
[54] Kinki Univ., Higashi-Osaka, Japan
[55] Kobe Univ., Kobe, Japan
[56] Kogakuin Univ., Tokyo, Japan
[57] Konan Univ., Kobe, Japan
[58] Kyungpook National Univ., Daegu, Korea
[59] Laboratori Nazionali di Frascati, Frascati, Italy
[60] LAL, Univ. Paris-Sud, CNRS/IN2P3, Orsay, France
[61] Lancaster Univ., Lancaster, UK
[62] LAPP, Univ. de Savoie, CNRS/IN2P3, Orsay, France
[63] LLR, École polytechnique, CNRS/IN2P3, Palaiseau, France
[64] Lomonosov Moscow State Univ., Moscow, Russia
[65] Louisiana Tech Univ., Ruston, USA
[66] LPC Clermont, Univ. Blaise Pascal, CNRS/IN2P3, Aubière, France
[67] LPNHE, Univ. Pierre et Marie Curie, Univ. Denis Diderot, CNRS/IN2P3, Paris, France
[68] LPSC, Univ. Joseph Fourier, CNRS/IN2P3, Inst. Polytechnique de Grenoble, Grenoble, France
[69] Ludwig-Maximilians-Univ. München, Munich, Germany
[70] Lunds Univ., Lund, Sweden
[71] Max-Planck-Inst. für Physik, Munich, Germany
[72] McGill Univ., Montreal, Canada
[73] Moscow Engineering Physics Inst., Moscow, Russia
[74] MSU-Iligan Inst. of Technology, Iligan City, Philippines
[75] Nagasaki Inst. of Applied Science, Nagasaki, Japan
[76] Nagoya Univ., Nagoya, Japan
[77] Nankai Univ., Tianjin, China
[78] National Central Univ., Chung-li, Taiwan
[79] National Taiwan Univ., Taipei, Taiwan
[80] Niigata Univ., Niigata, Japan
[81] Nikhef, Amsterdam, The Netherlands
[82] Nippon Dental Univ. School of Life Dentistry, Niigata, Japan
[83] Northern Illinois Univ., DeKalb, USA
[84] Obninsk State Technical Univ. for Nuclear Engineering, Obninsk, Russia
[85] Osaka City Univ., Osaka, Japan
[86] Österreichische Akademie der Wissenschaften, Vienna, Austria
[87] Princeton Univ., Princeton, USA
[88] Rheinisch-Westfälische Technische Hochschule, Aachen, Germany
[89] Royal Holloway, Univ. of London, Surrey, UK
[90] Rutherford Appleton Laboratory, Didcot, UK
[91] Saga Univ., Saga, Japan
[92] Saha Inst. of Nuclear Physics, Kolkata, India
[93] Salalah College of Technology, Salalah, Sultanate of Oman
[94] Shandong Univ., Jinan, China
[95] Shinshu Univ., Matsumoto, Japan
[96] Slovak Academy of Sciences, Kosice, Slovakia
[97] Sokendai, Hayama, Japan
[98] Sungkyunkwan Univ., Suwon, Korea
[99] Tata Inst. of Fundamental Research, Mumbai, India
[100] Technische Univ. Dresden, Dresden, Germany
[101] Tel Aviv Univ., Tel Aviv, Israel
[102] The Henryk Niewodniczanski Inst. of Nuclear Physics, Cracow, Poland
[103] Tohoku Univ., Sendai, Japan
[104] Tokyo Univ. of Agricultural Technology, Koganei, Japan
[105] TRIUMF, Vancouver, Canada
[106] Tsinghua Univ., Beijing, China
[107] Univ. Autònoma de Barcelona, Barcelona, Spain
[108] Univ. Bonn, Bonn, Germany
[109] Univ. College London, London, UK
[110] Univ. de Barcelona, Barcelona, Spain
[111] Univ. de Granada, Granada, Spain
[112] Univ. de Haute Alsace Mulhouse-Colmar, Mulhouse, France
[113] Univ. de Montréal, Montreal, Canada
[114] Univ. de Strasbourg, Strasbourg, France
[115] Univ. dell-Insubria in Como, Como, Italy
[116] Univ. Karlsruhe, Karlsruhe, Germany
[117] Univ. of Bergen, Bergen, Norway
[118] Univ. of Birmingham, Birmingham, UK
[119] Univ. of Bristol, Bristol, UK
[120] Univ. of California, Santa Cruz, USA
[121] Univ. of Cambridge, Cambridge, UK
[122] Univ. of Chicago, Chicago, USA
[123] Univ. of Copenhagen, Copenhagen, Denmark
[124] Univ. of Delhi, Delhi, India
[125] Univ. of Edinburgh, Edinburgh, UK
[126] Univ. of Ghent, Ghent, Belgium
[127] Univ. of Glasgow, Glasgow, UK
[128] Univ. of Hamburg, Hamburg, Germany
[129] Univ. of Heidelberg, Heidelberg, Germany
[130] Univ. of Helsinki, Helsinki, Finland
[131] Univ. of Iowa, Iowa City, USA
[132] Univ. of Kansas, Lawrence, USA
[133] Univ. of Liverpool, Liverpool, UK
[134] Univ. of Lodz, Lodz, Poland
[135] Univ. of Manchester, Manchester, UK
[136] Univ. of Michigan, Ann Arbor, USA
[137] Univ. of Oxford, Oxford, UK
[138] Univ. of Regina, Regina, Canada
[139] Univ. of Science and Technology of China, Hefei, China
[140] Univ. of Southampton, Southampton, UK
[141] Univ. of Sydney, Sydney, Australia
[142] Univ. of Tokyo, ICEPP, Tokyo, Japan
[143] Univ. of Tokyo, Inst. for Cosmic Ray Research, Kashiwa, Japan
[144] Univ. of Tsukuba, Tsukuba, Japan
[145] Univ. of Victoria, Victoria, Canada
[146] Univ. of Warsaw, Warsaw, Poland
[147] Univ. of Wuppertal, Wuppertal, Germany
[148] Univ. Ramon Llull, Barcelona, Spain
[149] Univ. Rostock, Rostock, Germany
[150] Univ. Siegen, Siegen, Germany
[151] VINCA Inst. of Nuclear Sciences, Belgrade, Serbia
[152] Visva-Bharati Univ., Santiniketan, India
[153] Vrije Univ., Amsterdam, The Netherlands
[154] Wayne State Univ., Detroit, USA
[155] West Univ. of Timisoara, Timisoara, Romania
[156] Yonsei Univ., Seoul, Korea

LETTERS OF INTENT SIGNATORIES

The following are signatories to the Letters of Intent of the SiD groups. Names are listed as given in the official signatories list. Institute names are abbreviated to save space.

SiD (Silicon Detector)

T. Abe[68], B. Adeva[64], C. Adloff[26], H. Aihara[68], L. Andricek[30], J. P. Balbuena[18], C. Baltay[73], H. R. Band[70], Y. Banda[62], T. L. Barklow[40], A. Belymam[40], E. L. Berger[1], B. Bilki[52], J. Blaha[26], J.-J. Blaising[26], E. E. Boos[33], D. Bortoletto[38], B. P. Brau[53], J. E. Brau[61], M. Breidenbach[40], P. N. Burrows[62], J. M. Butler[3], S. Cap[26], R. Cassell[40], S. Chakrabarti[41], D. Chakraborty[35], M. Charles[52], J. Chauveau[29], M. Chefdeville[26], S. Chen[34], M. Chertok[44], D. C. Christian[10], G. B. Christian[19], S. Cihangir[10], C. Ciobanu[29], R. Coath[39], C. Colledani[21], J. S. Conway[44], W. E. Cooper[10], R. F. Cowan[31], W. Craddock[40], L. Cremaldi[57], J. Crooks[39], N. D'Ascenzo[36], C. Damerell[39], P. D. Dauncey[15], K. De[66], R. De Masi[21], A. de Roeck[7], C. Deaconu[40], M. Demarteau[10], E. Devetak[62], S. Dhawam[73], A. Dieguez[42], A. Dorokhov[21], A. Dragone[40], C. Drancourt[26], J. Duarte[17], T. Dutta[13], A. Dyshkant[35], K. Elsener[7], A. Espargiliare[26], V. Fadeyev[45], A. Farbin[66], A. Faus-Golfe[16], M. Fernandez[17], F. Feyzi[70], P. Fisher[31], H. E. Fisk[10], C. Fleta[18], B. Foster[62], R. Frey[61], J. Fuster[16], A. Gaddi[7], R. Gaglione[26], V. Galkin[36], A. Gallas Torreira[64], D. Gao[65], L. A. Garren[10], Ll. Garrido[42], N. Geffroy[26], H. Gerwig[7], M. Gibson[39], J. Gill[47], J. Goldstein[4], J. Gonzalez[17], N. A. Graf[40], C. Grefe[7], J. Gronberg[27], M. Grunewald[11], V. Guarino[1], J. Gunion[44], G. Haller[40], D. Hedin[35], R. Herbst[40], J. L. Hewett[40], M. D. Hildreth[60], B. Holbrook[44], C. Hu-Guo[21], C. Iglesias Escudero[64], M. Iwasaki[68], J. Jacquemier[26], R. Jaramillo[17], J. A. Jaros[40], W. Jie[65], A. S. Johnson[40], Y. Junfeng[65], J. Kaminski[43], F. Kapusta[29], P. E. Karchin[72], Y. Karyotakis[26], C. J. Kenney[32], G. N. Kim[25], P. C. Kim[40], T. J. Kim[52], W. Klempt[7], K. Krempetz[10], R. Kriske[56], R. K. Kutschke[10], Y.-J. Kwon[74], C. Lacasta[16], M. Laloum[29], R. L. Lander[44], T. Lastovicka[62], G. Lastovicka-Medin[58], C. Li[65], Y.-M. Li[62], L. Linssen[7], R. Lipton[10], S. Liu[65], Y. Liu[65], A. Lopez-Virto[17], X. C. Lou[67], M. Lozano[18], C. Lu[37], H. J. Lubatti[69], P. Lutz[23], D. B. MacFarlane[40], U. Mallik[52], S. Manly[63], C. Mariñas[16], T. Markiewicz[40], C. Martinez-Rivero[17], T. Maruyama[40], J. McCormick[40], K. T. McDonald[37], M. Merkin[33], C. Milstene[72], K. Moffeit[40], G. Moortgat-Pick[22], H.-G. Moser[30], D. Moya[17], U. Nauenberg[47], H. A. Neal[40], T. K. Nelson[40], A. Nichols[39], A. Nomerotski[62], E. Norbeck[52], G. Oleinik[47], Y. Onel[52], D. V. Onoprienko[24], R. Orava[50], M. Oreglia[46], M. Oriunno[40], D. Ossetski[36], A. Pankov[12], A. Para[10], H. Park[25], S. Park[66], R. Partridge[40], M. E. Peskin[40], J. Prast[26], R. Prepost[70], V. Radeka[5], R. Rahmat[57], K. Ranjan[48], J. Repond[1], J. Riera-Babures[71], K. Riles[55], T. G. Rizzo[40], P. Rowson[40], A. Ruiz-Jimeno[17], J. J. Saborido Silva[64], V. Saveliev[36], A. Savoy-Navarro[29], L. Sawyer[28], D. Schlatter[7], B. A. Schumm[45], S. Seidel[59], R. Shivpuri[48], N. Sinev[61], A. J. S. Smith[37], J. Smith[66], P. Speckmayer[7], A. Srivastava[2], M. Stanitzki[39], D. M. Strom[61], J. Strube[39], D. Su[40], Y. Sun[65], G. N. Taylor[54], J. Thom[8], E. Torrence[61], S. M. Tripathi[44], R. Tschirhart[10], R. Turchetta[39], M. Tyndel[39], M. Ullán[18], R. Van Kooten[51], G. S. Varner[49], P. Vazquez Regueiro[64], J. Velthius[4], I. Vila[17], X. Vilasis-Cardona[71], M. Vos[16], G. Vouters[26], V. Vrba[20], S. R. Wagner[47], S. Walston[27], Q. Wang[65], M. Wayne[60], M. Weber[39], H. Weerts[1], H. Wenzel[10], A. P. White[66], S. Willocq[53], M. Winter[21], M. Woods[40], S. Worm[39], D. Wright[27], L. Xia[1], R. K. Yamamoto[31], H.-J. Yang[55], J. Yang[9], R. Yarema[10], J. Yi[65], W. Yonggang[65], J. Yu[66], J. Zhang[1], Q. Zhang[1, 14], Z. Zhang[39], Z. Zhao[65], R.-Y. Zhu[6], V. Zutshi[35]

[1] Argonne National Laboratory, Argonne, USA
[2] Birla Inst. for Technology and Science, Pilani, India
[3] Boston Univ., Boston, USA
[4] Bristol Univ., Bristol, UK
[5] Brookhaven National Laboratory, Upton, USA
[6] California Inst. of Technology, Pasadena, USA
[7] CERN, Geneva, Switzerland
[8] Cornell Univ., Ithaca, USA
[9] Ewha Womans Univ., Seoul, Korea
[10] Fermilab, Batavia, USA
[11] Ghent Univ., Ghent, Belgium
[12] Gomel State Technical Univ., Gomel, Belarus
[13] GSI, Darmstadt, Germany
[14] IHEP, Beijing, China
[15] Imperial College London, London, UK
[16] Inst. de Física Corpuscular, Valencia, Spain
[17] Inst. de Física de Cantabria, Cantabria, Spain
[18] Inst. of Microelectronics of Barcelona, Barcelona, Spain
[19] Inst. of Nuclear Research, Debrecen, Hungary
[20] Inst. of Physics, Prague, Czech Republic
[21] IPHC, Univ. Louis Pasteur, CNRS/IN2P3, Strasbourg, France
[22] IPPP, Durham, UK
[23] IRFU, CEA Saclay, Gif-sur-Yvette, France
[24] Kansas State Univ., Manhattan, USA
[25] Kyungpook National Univ., Daegu, Korea
[26] LAPP, Univ. de Savoie, CNRS/IN2P3, Annecy-le-Vieux, France
[27] Lawrence Livermore National Laboratory, Livermore, USA
[28] Louisiana Tech Univ., Ruston, USA
[29] LPNHE, Univ. Pierre et Marie Curie, Univ. Denis Diderot, CNRS/IN2P3, Paris, France
[30] Max-Planck-Inst. for Physics, Munich, Germany
[31] MIT, Cambridge, USA
[32] Molecular Biology Consortium, Chicago, USA
[33] Moscow State Univ., Moscow, Russia
[34] Nanjing Univ., Nanjing, China
[35] Northern Illinois Univ., DeKalb, USA
[36] Obninsk State Technical Univ. for Nuclear Power Engineering, Obninsk, Russia
[37] Princeton Univ., Princeton, USA
[38] Purdue Univ., West Lafayette, USA
[39] Rutherford Appleton Laboratory, Didcot, UK
[40] SLAC, Palo Alto, USA
[41] SUNY, Stony Brook, USA
[42] Univ. of Barcelona, Barcelona, Spain
[43] Univ. of Bonn, Bonn, Germany
[44] Univ. of California, Davis, USA
[45] Univ. of California, Santa Cruz, USA
[46] Univ. of Chicago, Chicago, USA
[47] Univ. of Colorado, Boulder, USA
[48] Univ. of Delhi, Delhi, India
[49] Univ. of Hawaii, Honolulu, USA
[50] Univ. of Helsinki, Helsinki, Finland
[51] Univ. of Indiana, Bloomington, USA
[52] Univ. of Iowa, Iowa City, USA
[53] Univ. of Massachusetts, Amherst, USA
[54] Univ. of Melbourne, Melbourne, Australia
[55] Univ. of Michigan, Ann Arbor, USA
[56] Univ. of Minnesota, Minneapolis, USA
[57] Univ. of Mississippi, Oxford, USA
[58] Univ. of Montenegro, Podgorica, Montenegro
[59] Univ. of New Mexico, Albuquerque, USA
[60] Univ. of Notre Dame, Notre Dame, USA
[61] Univ. of Oregon, Eugene, USA
[62] Univ. of Oxford, Oxford, UK
[63] Univ. of Rochester, Rochester, USA
[64] Univ. of Santiago de Compostela, Santiago de Compostela, Spain
[65] Univ. of Science and Technology in China, Hefei, China
[66] Univ. of Texas at Arlington, Arlington, USA
[67] Univ. of Texas at Dallas, Dallas, USA
[68] Univ. of Tokyo, Tokyo, USA
[69] Univ. of Washington, Seattle, USA
[70] Univ. of Wisconsin, Madison, USA
[71] Univ. Ramon Llull, Barcelona, Spain
[72] Wayne State Univ., Detroit, USA
[73] Yale Univ., New Haven, USA
[74] Yonsei Univ., Seoul, Korea

design: form one® visual communications | www.form-one.de

ISSUED BY . . . . ilc international linear collider

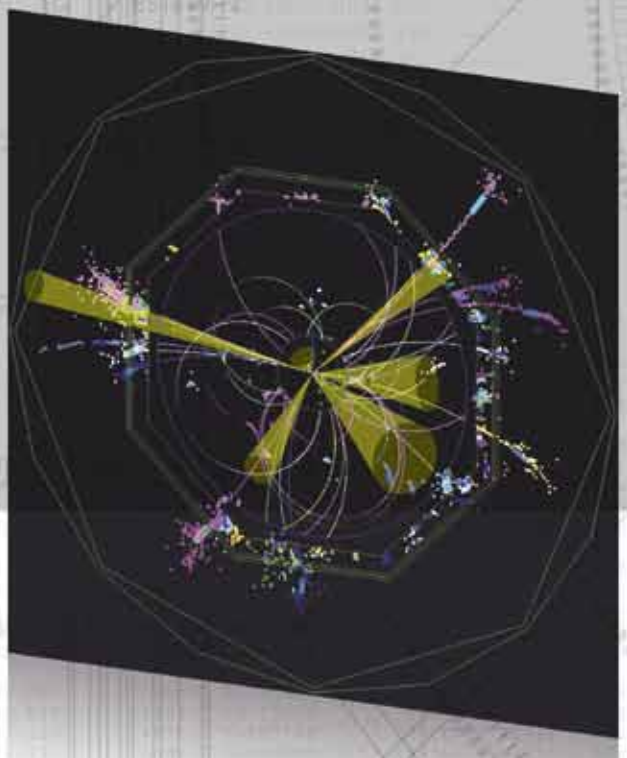

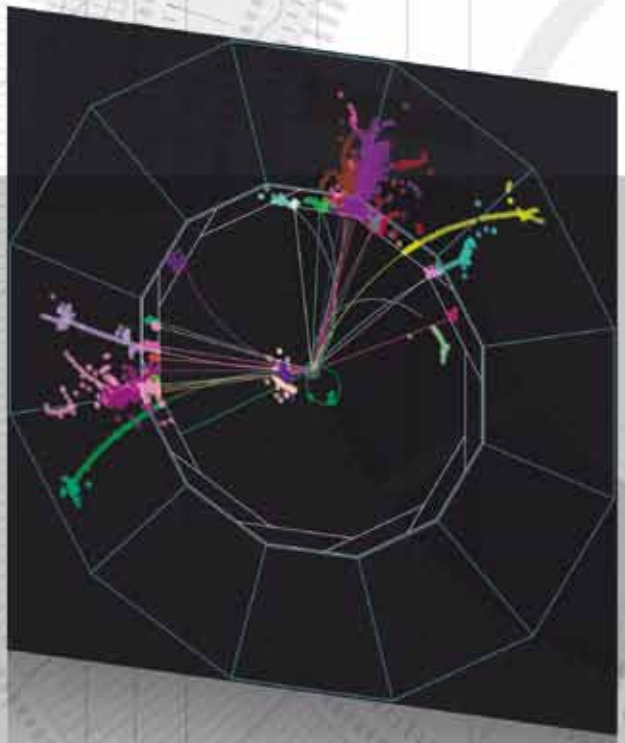

ISBN 978-3-935702-61-4

CERN: CERN-LCD-Note-2011-038
DESY: DESY 2011-190
Fermilab: FERMILAB-FN-0936-PPD
ILC: ILC-REPORT-2011-033
KEK: KEK Report 2011-5
LAL: LAL 11-246
SLAC: SLAC-R-973